

Computational modelling of single and polycrystalline ferroelectric materials

Zur Erlangung des akademischen Grades eines

Doktor-Ingenieur (Dr.-Ing.)

von der Fakultät Maschinenbau
der Technischen Universität Dortmund
genehmigte Dissertation

M. Sc. Dinesh Kumar Dusthakar Kumar Rao

aus Tiruchirappalli, Indien

Referent: Prof. Dr.-Ing. habil. Andreas Menzel

Korreferenten: Prof. Dr. rer. nat. Bob Svendsen

Prof. Dr.-Ing. habil. Jörn Mosler

Tag der Einreichung: 11.07.2017

Tag der mündlichen Prüfung: 30.10.2017

Dortmund, 2017

© Dinesh Kumar Dusthakar Kumar Rao 2017

This work is subject to copyright. All rights are reserved, whether the whole or part of the material is concerned, specifically the rights of translation, reprinting, reuse of illustrations, recitation, broadcasting, reproduction on microfilm or in any other way, and storage in data banks. Duplication of this publication or parts thereof is permitted in connection with reviews or scholarly analysis. Permission for use must always be obtained from the author.

Alle Rechte vorbehalten, auch das des auszugsweisen Nachdrucks, der auszugsweisen oder vollständigen Wiedergabe (Photographie, Mikroskopie), der Speicherung in Datenverarbeitungsanlagen und das der Übersetzung.

Als Manuskript gedruckt. Printed in Germany.

ISBN 978-3-921823-94-1

to my beloved family

Acknowledgements

The research work presented in this thesis has been carried out between June 2012 and December 2016 when I was a Research assistant at the Institute of Mechanics (IOFM), Faculty of Mechanical Engineering, TU Dortmund. During that period I was a part of the project P6 “Microstructural Interactions and Switching in Ferroelectrics” within the Research Unit FOR 1509 “Ferroic Functional Materials: Multi-scale Modeling and Experimental Characterization” funded by the German Research Foundation (DFG).

I wish to express my sincere gratitude to my first advisor Professor Andreas Menzel for giving me the opportunity to pursue a doctoral degree under his guidance and for his supervision of the research activities. I also wish to express my special thanks to my second advisor Professor Bob Svendsen, Chair of Material Mechanics, RWTH Aachen, for his timely suggestions and reviews on the progress of the research work.

My sincere thanks go to Professor Jörn Mosler for his interest in my research work and also for his willingness to serve as the third examiner. I thank Senior researcher Dr. Andreas Zabel, Institute of Machining Technology, TU Dortmund, for agreeing to be the chairman of the examination committee.

I sincerely thank the former members of IOFM, Professor Björn Kiefer, Professor Ali Javili and Professor Ralf Denzer, for sharing their experience and providing inputs during various stages of my research work. Many thanks to the entire team of IOFM with special mention to Dr. Thorsten Bartel, Dr. Richard Ostwald, Karsten Buckmann, Rolf Berthelsen, Christian Sievers, Tim Heitbreder, Matthias Weiss, Markus Schewe, Kerstin Walter and Christina McDonagh for their support over the years. I am deeply indebted to Karsten for all his help and for the fruitful discussions that we had on the subject of mechanics and on life. I would like to extend my thanks to the former members of IOFM, Dr. Maniprakash Subramanian, Dr. Krishnendu Haldar, Dr. Alexander Bartels and Dr. Raphael Holtermann, for their help and support.

I sincerely thank Professor Marc-André Keip, Institute of Applied Mechanics, University of Stuttgart, who inspired me to opt for a doctoral program. His valuable suggestions and the knowledge that he shared with me on the subject of electro-mechanics on various occasions right from my master studies were highly influential throughout my work. I also thank Professor A. Arockiarajan, Department of Applied Mechanics, Indian Institute of Technology Madras, for his inputs from the experimental point of view and also for allowing me to measure some of the experimental data at his Smart Material Characterization Lab.

The contribution of my friends played a vital role in reminding me that there was always time for laugh and leisure activities. I thank Ramya and Maniraj Jeyaraj, Priya and Karthik Muthuk, Pradeep Harikrishnan, Daniel Nierhoff, V. Shrihari, P. Gopinath and S. Dinesh Kumar for their endless support.

Above all, I thank my parents Premalatha and Kumar Rao Dusthakar, my brother Dilip Kumar and my wife Aarthi Bai for their unconditional love and care. They all stood by me and supported me to the fullest extent over these years and encouraged me to complete the thesis even at the times of difficulties. I shall not forget to thank my sweet little daughter Toshaani, who gave a new dimension to my life. This thesis is dedicated to my beloved family.

Dortmund, November 2017

Dinesh Kumar Dusthakar Kumar Rao

Zusammenfassung

Die vorliegende Arbeit befasst sich mit der Entwicklung thermodynamisch konsistenter Materialmodelle zur Beschreibung des makroskopisch nichtlinearen hysteretischen Verhaltens von ferroelektrischen ein- und polykristallinen Materialien. Als erstes wird ein phänomenologisches Materialmodell vorgestellt, welches sowohl zum Verständnis des allgemeinen elektromechanischen Kopplungsverhaltens dient, als auch zur Untersuchung der ratenabhängigen makroskopischen Polarisationsentwicklung in kristallinen ferroelektrischen Festkörpern genutzt wird. Im Anschluss an den phänomenologischen Modellierungsrahmen werden laminatbasierte Modelle entwickelt, bei denen die Volumenfraktionen der tetragonalen ferroelektrischen Varianten als interne Zustandsvariablen in den thermodynamischen Potentialen verwendet werden. Im Kontext der Mittelungsverfahren werden unterschiedliche thermodynamische Potentiale für die verschiedenen laminatbasierten Materialmodelle postuliert. Der Einfluss von sowohl der Belastungsgeschwindigkeit als auch der Höhe der externen Druckspannung auf die Domänenentwicklung und Umklappvorgänge der Polarisation werden in tetragonalen ferroelektrischen Einkristallen unter kombinierter elektromechanischer Belastung mit Hilfe der entwickelten laminatbasierten Modellen simuliert. Zum Schluss werden homogenisierungsartige Verfahren basierend auf Zufallsverteilungen der einzelnen einkristallinen Körnern in einem polykristallinen Verbund im Detail vorgestellt. Die Eigenschaften der zufällig verteilten Körner werden in einem Finite Elemente Rahmen gemittelt, um die Umklappvorgänge der Polarisation und die makroskopische Hysteresekurve einer tetragonalen ferroelektrischen Keramik zu simulieren.

Abstract

The present thesis deals with the development of thermodynamically consistent material models to describe the macroscopic non-linear hysteretic behaviour of ferroelectric single and polycrystalline materials. At first, a phenomenological material model is discussed in order to gain an understanding of the overall electromechanical coupling behaviour as well as to study the rate-dependent macroscopic polarisation evolution in crystalline ferroelectric solids. Following the phenomenological framework, laminate-based models are developed by treating the volume fraction of the tetragonal ferroelectric variants as internal state variables in their thermodynamic potentials. By considering different averaging principles, distinct thermodynamic potentials are postulated for the individual laminate-based material models. The influence of both the loading rate and the magnitude of the external compressive stress on the domain evolution and polarisation switching in tetragonal ferroelectric single crystals under combined electromechanical loading is simulated with help of the developed laminate-based models. Finally, a homogenisation-type strategy based on random orientations of the individual single crystal grains in a polycrystalline aggregate is detailed. The properties of the randomly oriented grains are averaged within a finite element framework to simulate the polarisation switching response and the macroscopic hysteresis curves for a bulk tetragonal ferroelectric ceramic.

Publications

Key parts of this thesis are based on the following main articles, which were either published or submitted during the progress of this thesis.

1. D. K. Dusthakar, T. Bartel, B. Kiefer, A. Menzel and B. Svendsen: *Rate-dependent laminate-based approach for modelling of ferroelectric single crystals*, In Proceedings of the 5th International Congress on Computational Mechanics and Simulation, 1324–1336, 2014 [41].
2. D. K. Dusthakar, A. Menzel and B. Svendsen: *Comparison of phenomenological and laminate-based models for rate-dependent switching in ferroelectric continua*, GAMM-Mitteilungen, 38(1):147–170, 2015 [43].
3. D. K. Dusthakar, A. Menzel and B. Svendsen: *A laminate-based modelling approach for rate-dependent switching in ferroelectric materials*, Proceedings in Applied Mathematics and Mechanics, 15(1):3–6, 2015 [42].
4. D. K. Dusthakar, A. Menzel and B. Svendsen: *Laminate-based models for rate-dependent switching in single crystalline ferroelectrics*, Smart Material Systems and Structures - Modeling and Simulation, Springer-Verlag, (submitted for publication) 2017 [46].
5. D. K. Dusthakar, A. Menzel and B. Svendsen: *Laminate-based modelling of single and polycrystalline ferroelectric materials – application to tetragonal barium titanate*, (In Press), doi: <https://doi.org/10.1016/j.mechmat.2017.10.005>, 2017 [45].

The author of this thesis, in collaboration with other co-authors, contributed essential aspects to the preparation of all the articles listed above. The author of this thesis mainly outlined the theory and detailed the algorithmic framework for articles 1, 3, 4 and 5. With regards to article 2, the author of this thesis prepared the section on the algorithmic framework. For all articles 1 to 5, the author of this thesis carried out the numerical implementation of the material models and generated the necessary simulation results. The experimental hysteresis curves reported in journal article 5 were measured by the author of this thesis at the Smart Materials Lab, Applied Mechanics Department, IIT Madras under the supervision of Prof. A. Arockiarajan and M. Sc. Y. Mohan.

Contents

| | | |
|----------|---|-----------|
| 1 | Introduction | 1 |
| 1.1 | Outline of the present work | 6 |
| 1.2 | Notations used in this work | 7 |
| 2 | Essential balance relations | 9 |
| 2.1 | Electrostatics | 9 |
| 2.2 | Kinematic and stress measures | 12 |
| 2.3 | Balance relations and thermodynamic framework | 13 |
| 2.4 | Finite element approximation | 16 |
| 3 | Phenomenological modelling of ferroelectric materials | 21 |
| 3.1 | Overview of phenomenological models | 21 |
| 3.2 | Rate-dependent phenomenological framework | 25 |
| 3.3 | Algorithmic treatment of the evolution equation | 30 |
| 3.4 | Numerical examples | 31 |
| 3.4.1 | Tests under homogeneous states of deformation | 31 |
| 3.4.2 | Test under inhomogeneous states of deformation | 36 |
| 4 | Laminate-based modelling of single crystalline ferroelectric materials | 39 |
| 4.1 | Overview of micromechanical models | 41 |
| 4.2 | Rate-dependent laminate-based framework | 47 |
| 4.2.1 | Symmetry and material properties of ferroelectric variants | 48 |
| 4.2.2 | Compatibility conditions and averaging principles | 50 |
| 4.2.3 | Thermodynamic model formulation | 52 |
| 4.3 | Algorithmic treatment of the evolution equations | 54 |
| 4.4 | Laminate-based Model 1 | 57 |
| 4.4.1 | Numerical examples | 60 |
| 4.4.2 | Comparison of laminate-based Model 1 and phenomenological model | 68 |
| 4.5 | Laminate-based Model 2 | 76 |
| 4.5.1 | Numerical examples | 79 |
| 4.6 | Laminate-based Model 3 | 86 |
| 4.6.1 | Numerical examples | 88 |
| 4.7 | Laminate-based Model 4 | 94 |
| 4.7.1 | Numerical examples | 96 |

| | | |
|----------|--|------------|
| 4.8 | Comparison of laminate-based Models 2, 3 and 4 | 101 |
| 5 | Laminate-based modelling of polycrystalline ferroelectric materials | 107 |
| 5.1 | Calibration of model parameters | 109 |
| 5.2 | Averaged response of polycrystalline ferroelectrics | 115 |
| 5.3 | Numerical examples | 117 |
| 5.3.1 | Hysteretic response of a polycrystalline block | 118 |
| 5.3.2 | Poling behaviour of a polycrystalline stack actuator | 122 |
| 6 | Summary and outlook | 125 |
| A | Derivations and identification of parameters – phenomenological model | 129 |
| A.1 | Useful derivations for the phenomenological model | 129 |
| A.2 | Identification of isotropic elastic tensor coefficients | 131 |
| B | Derivations – laminate-based formulation | 133 |
| B.1 | Useful derivations for the laminate-based formulations | 133 |
| B.2 | Derivatives of Fischer–Burmeister functions | 135 |
| | Bibliography | 137 |

1 Introduction

Ferroelectric materials, both single crystals and polycrystalline ceramics, are increasingly preferred in industrial and technological applications which require electromechanical sensing and actuating functions. This is due to their exceptional material properties which include high dielectric permittivity values and strong intrinsic electromechanical coupling properties, to name a few. Ferroelectric memory appliances, transducers, multilayer piezoelectric stack actuators and precision electro-optics are some devices employing polycrystalline ferroelectric solids, see Tichý et al. [140]. In recent times, development of thin-film polycrystalline ferroelectrics has made the use of these functional materials possible in integrated semiconductor chips and in non-volatile memories, which include ferroelectric random access memories (FeRAM) and dynamic random access memory (DRAM) capacitors for example, see Scott [128]. A detailed review of the applications related to thin-film ferroelectric materials is provided by Setter et al. [130] and Scott [127]. In order to increase the design efficiency of the functional devices employing ferroelectric materials, the overall macroscopic behaviour based on microscopic effects needs to be predicted well in advance. The present dissertation deals with the thermodynamic consistent material modelling as well as with the numerical implementation for the simulation of the electromechanically coupled material behaviour in tetragonal ferroelectric single and polycrystalline solids.

Both ferroelectric single and polycrystalline solids belong to the class of perovskite, non-centrosymmetric materials. Typical ferroelectric perovskites include, for example, barium titanate (BaTiO_3) and lead titanate (PbTiO_3), in pure compound form, and lead zirconate titanate ($\text{Pb}[\text{Zr}_{1-x}\text{Ti}_x]\text{O}_3$, $0 < x < 1$, or in general PZT), in solid solution form. The unit cell of a ferroelectric perovskite undergoes a phase transition from a non-polar cubic structure to a polar tetragonal phase when cooled below the Curie temperature. The underlying tetragonal unit cells exhibit a lattice distortion and a spontaneous polarisation or electric dipole moment due to the reduction in crystallographic symmetry. In a general three-dimensional setting, there are six equally likely directions in which the unit cells can be oriented or polarised. Moreover, from its default orientation, the direction of the spontaneous polarisation can be switched by the application of sufficiently large external electrical fields or mechanical loads. Multiple regions of uniformly oriented unit cells are termed as domains, and a collection of a number of domains of different orientations constitute a single crystal grain. Within individual single crystal

grains, two arbitrary domains of different configurations are separated by an interface or, in other words, a domain wall. Upon the application of a sufficiently large external electrical field along a particular global crystallographic axis, ferroelectric switching initiates in the crystal, and the randomly oriented domains gradually align along the loading direction. The single crystal is said to be poled and possesses an overall anisotropic symmetry, characterised by macroscopic polarisation and strains. This process is known as poling of the ferroelectric crystal. After the removal of the external electrical fields, the crystal reaches a remnant state described by an irreversible macroscopic remnant strain and a non-vanishing macroscopic remnant polarisation. The poled configuration of the crystal is preserved in its remnant state. A ferroelastic domain switching perpendicular to the loading direction is initiated by the application of a large compressive mechanical stress along a particular crystallographic direction of the crystal. While an externally applied large electrical load induces both 90° and 180° switching of the domains, a purely mechanical loading activates 90° ferroelastic switching only. Note, that a 180° domain reversal induces a polarisation change without any difference in the strain magnitude, whereas a 90° domain switching induces a change in crystallographic shape of the crystal.

A bulk polycrystalline ferroelectric is a compact aggregate of a number of single crystalline grains of various shapes and orientations. Two neighbouring grains are separated from each other by a grain boundary. Due to the, say randomly oriented single crystal grains, the virgin and unpoled polycrystalline ceramic may be considered isotropic on a macroscopic level devoid of a macroscopic remnant polarisation. However, with the application of sufficiently large electrical fields, ferroelectric switching initiates with the reorientation of the domains within the individual grains which transforms, in turn, the bulk ceramic into a macroscopically anisotropic material. After the removal of the externally applied loads, the remnant state of the bulk ceramic is recovered and the poled configuration is characterised by macroscopic remnant polarisation and strains. Upon the application of a sufficiently large external compressive mechanical stress on a poled polycrystalline ferroelectric material along a particular global crystallographic direction, ferroelastic switching is initiated and the domains within the individual single crystal grains switch by 90° . The ferroelastic effects within the individual grains lead to a macroscopic depolarisation of the bulk ceramic. Figure 1.1 shows the optical microstructural images of single and polycrystalline tetragonal BaTiO_3 along with the schematic sketch of a spontaneously polarised tetragonal BaTiO_3 unit cell. The micrographs corresponding to single and polycrystalline BaTiO_3 microstructures are reprinted with the permission from Merz [108] and from Arlt and Sasko [2] respectively. For a more detailed insight into the general theory and properties of ferroelectric materials, the reader is referred to the monographs, for instance by Jona and Shirane [70], Jaffe et al. [66], Lines and Glass [96], Damjanovic [35], Smith [137] as well as by Tagantsev et al. [139].

The 90° and 180° switching phenomena encountered in ferroelectric solids upon the application of a cyclic electrical loading are dissipative in nature and result in a macroscopic non-linear hysteretic material response. The hysteresis plot corresponding to the

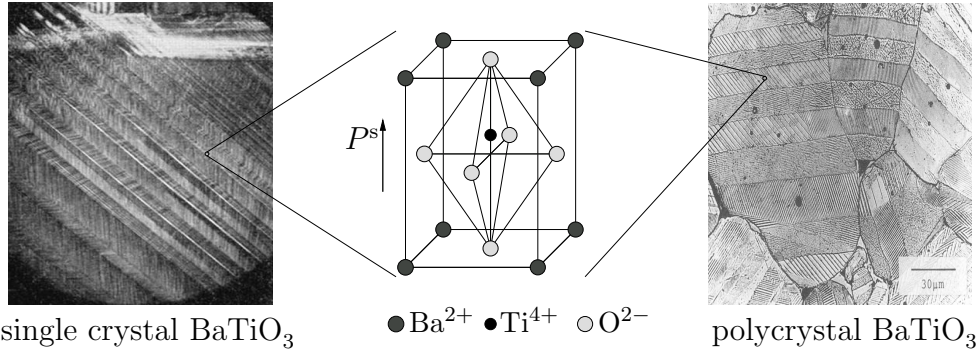


Figure 1.1: Optical observations of the microstructure depicting the different domain configurations in single and polycrystalline materials. The domains within the single crystal (left) and within the individual grains of a polycrystal (right) are a collection of a number of spontaneously polarised tetragonal BaTiO_3 unit cells (sketched in the middle). The single and polycrystalline micrographs are reprinted with the permission from Merz [108] and from Arlt and Sasko [2] respectively.

applied cyclic electric field, along a particular direction, versus the resulting total strain values, also along the loading direction, is termed as the butterfly curve or the strain hysteresis plot. Similarly, the hysteresis loop or the dielectric displacement hysteresis plot denotes the response between the applied cyclic electric field and the resulting dielectric displacement values along the loading direction. Both the butterfly and dielectric hysteresis loops are dependent on the frequency of the applied electrical field, cf. Viehland and Chen [146], Zhou et al. [156], Burcsu et al. [21] and Maniprakash et al. [104]. In addition to the rate-dependent behaviour, the shape of the ferroelectric hysteresis curves is dependent on the magnitude of the compressive mechanical stress applied parallelly to the cyclic electrical load. With respect to the single crystal ferroelectric solids, the effect of the moderate compressive stress along with the cyclic electric field initiates the stress-activated 90° domain switching which, in turn, enhances the magnitude of the resulting total strains along the loading direction, see Shu and Bhattacharya [134], Burcsu et al. [21, 22] and Yen et al. [151]. Thus, the shape of the macroscopic non-linear ferroelectric hysteresis curves is dependent on both the loading rate and external compressive stress magnitude.

In the context of the purely compressive mechanical loading and unloading of ferroelectric single and polycrystalline solids, the macroscopic response between the applied compressive load and the measured total strains along the loading direction is termed as ferroelastic hysteresis curve. Analogously, the mechanical depolarisation hysteresis curve denotes the response between the applied compressive load and the resulting dielectric displacement values. Similar to the rate-dependent ferroelectric hysteretic response, the shape of both the ferroelastic and mechanical depolarisation hysteresis curves is influenced by the compressive loading frequency, cf. Lu et al. [99] and Li and Li [95].

The external stress and electrical rate-dependent hysteretic ferroelectric and ferroelastic material responses as well as the evolving microstructural domain patterns of both single and polycrystalline BaTiO_3 have been studied by many experimentalists

and material scientists over the years. Unlike commercially available polycrystalline ferroelectric ceramics, single crystal ferroelectrics, for example BaTiO_3 , are solution-grown in laboratories with special techniques. These methods include the Remeika method [117], the top-seeded solution growth procedure [119] and the template grain growth process [116, 150], amongst others. This limits the number of research publications focussing entirely on the study of the single crystal BaTiO_3 material behaviour. Nevertheless, the study of BaTiO_3 crystals possessing a single grain structure and hence devoid of grain boundaries and their influences, raises the understanding of the fundamental material behaviour of ferroelectric materials. To name but a few, we refer to the works by Merz [108], Burcsu et al. [21, 22], Shieh et al. [131, 132, 151] and by Li and Li [94, 95] for the experimental investigations on single crystal BaTiO_3 under different loading scenarios. In view of the experimental studies on polycrystalline ferroelectric ceramics, the reader is referred to the monographs [36, 66, 96, 149].

The high magnitude of actuation strains obtained from single crystal BaTiO_3 under combined electromechanical loading is a topic of particular interest. Subjecting a tetragonal BaTiO_3 single crystal to a combined electromechanical load, i.e. an alternating electric field and a constant compressive mechanical load, the actuation strains obtained along the loading direction increase with the moderate increase in the applied stress magnitude. This is due to the enhanced 90° ferroelastic domain switching evident in the crystal due to the combined loading, cf. Burcsu et al. [22], Shu and Bhattacharya [134], Yen et al. [151] and Li and Li [95]. In the experimental work of Burcsu et al. [22], a tetragonal BaTiO_3 single crystal, initially oriented along the [100]-direction, was investigated under combined electromechanical loading. The crystal when loaded with an alternating electric field at 0.05 Hz along with a constant compressive stress of magnitude 3.6 MPa resulted in a hysteretic response with the obtained total strains reaching 0.8% along the loading direction, see Figure 1.2 (left). Furthermore, the high actuation strain response obtained from single crystal ferroelectrics under combined electromechanical loading is dependent on the frequency of the external electrical field. The rate-dependent behaviour of single crystal tetragonal BaTiO_3 under combined electromechanical loading was reported by Burcsu et al. [21]. Figure 1.2 (right), taken from [21], depicts the rate-dependent strain response of a single crystal BaTiO_3 under a cyclic electric field at varying frequencies along with a constant compressive stress of magnitude 1.07 MPa, along the electrical loading direction. The measured magnitudes of the actuation strains, shown in Figure 1.2, corresponding to the tetragonal BaTiO_3 single crystals are found out to be quite high compared to the strain values measured in experiments made on polycrystalline BaTiO_3 ceramics under combined electromechanical loading. The activation of the 90° domain switching due to the applied external compressive stress, along with the subsequent 180° domain switching due to the cyclic electrical load, is reported as the reason for high strain values in BaTiO_3 single crystals. An elaborate study of the [100] and [001]-oriented tetragonal BaTiO_3 crystals under combined electromechanical loading conditions along with detailed description of the considered experimental set up is provided in the doctoral dissertation by Burcsu [20].

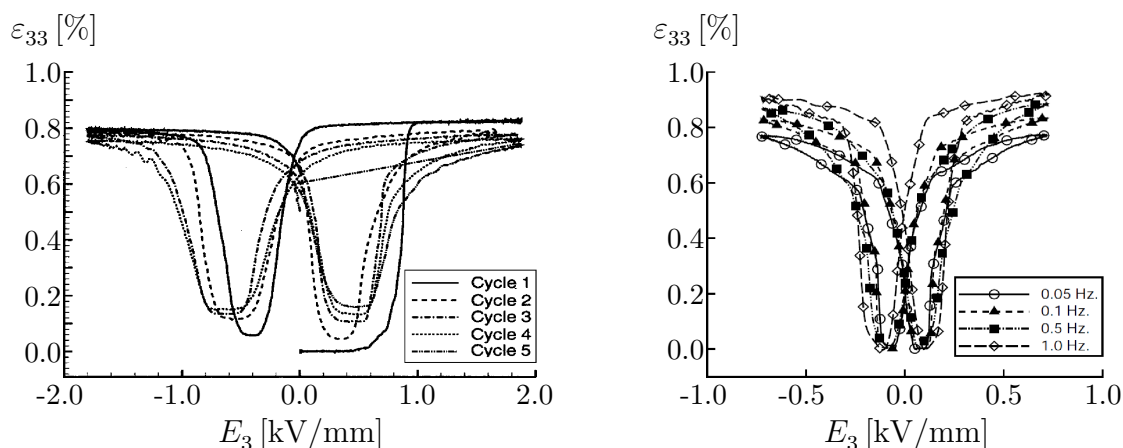


Figure 1.2: Experimental butterfly curves depicting the high actuation strain response of single crystal tetragonal BaTiO_3 under combined electromechanical loading. On the left, butterfly curves measured under a constant compressive stress of 3.6 MPa along with a cyclic electric field at 0.05 Hz, taken from Burcsu et al. [22]. On the right, butterfly curves obtained for a constant compressive stress of 1.07 MPa along with an alternating electric field at varying frequencies, taken from Burcsu et al. [21].

In order to predict the rate and external stress-dependent macroscopic hysteretic response, mathematically sound material models need to be formulated fulfilling thermodynamic relations and restrictions. The underlying modelling approaches can be classified into phenomenological models, micromechanical formulations and approaches such as phase-field methods. A detailed review of the different modelling practices developed for the study of the overall ferroelectric material response is provided by Kamlah [71], Landis [89], Huber [54] and by Potnis et al. [115]. Phenomenological models are considered in order to predict the macroscopic non-linear and dissipative response of ferroelectric solids. In view of ferroelectric solids, these robust phenomenological models are developed in order to gain an understanding of the overall electromechanical coupling behaviour. On the other hand, thermodynamically consistent micromechanical models are formulated in order to simulate the domain evolution and polarisation switching at the unit cell level. The simulation of such effects give a detailed insight into the microscopic phenomena leading to the macroscopic non-linear and hysteretic behaviour in ferroelectrics. Laminate-based models are of particular interest amongst the micromechanically motivated formulations. The major part of this work deals with the development of laminate-based material models to study the rate and external stress-dependent domain evolution and polarisation switching, and hence the macroscopic hysteretic response, in both single and polycrystalline tetragonal ferroelectric BaTiO_3 . Models such as phase-field formulations describe the domain evolution and poling on the microscale by resolving the domains in space and time. These phase-field approaches have recently become increasingly popular in studying the material characteristics, the effect of the grain size as well as the influence of electrode on thin-film polycrystalline ferroelectrics; see the contributions by Zhang and Bhattacharya [153, 154], Schrade et al. [121, 123] and Miehe et al. [113].

1.1 Outline of the present work

The present dissertation deals with the development of thermodynamic consistent material models along with the description of their numerical framework in order to study the macroscopic non-linear hysteretic behaviour of electromechanically coupled ferroelectric single crystals and ceramics. This research work is outlined as follows:

Chapter 2 summarises the essential equations governing the coupled electromechanical response in ferroelectric materials. The basic relations of electrostatics in vacuum and dielectric solids are provided first, followed by the introduction of the kinematic and stress measures assuming geometrically linear theory within the general framework of continuum mechanics. On the basis of the balance laws, the thermodynamic framework for the description of the non-linear and the dissipative behaviour of general ferroelectric solids is detailed. Following the thermodynamic framework, the necessary weak formulations and their approximations as well as the nodal residual equations needed for the finite element framework will be outlined.

Chapter 3 presents a phenomenological material model for the description of the rate-dependent macroscopic polarisation switching evident in ferroelectric solids. Starting with a brief overview of the phenomenological formulations for piezoceramic materials existing in the literature, a rate-dependent macroscopic model is developed by defining a total electric Gibbs energy and a rate-dependent dissipation equation. The evolution equation of the macroscopic remnant polarisation is obtained by fulfilling the necessary conditions of the postulated dissipation relation. By adopting single crystal BaTiO_3 material parameters, representative numerical tests under both homogeneous and inhomogeneous states of deformation will be presented.

Laminate-based formulations based on the mixture theory ansatz form the core of Chapter 4. A brief overview of the existing micromechanical models for the ferroelectric materials in the form of a literature survey is provided. Based on the symmetry considerations and on the material properties of the distinct tetragonal ferroelectric variants, a general laminate-based framework is presented detailing the thermodynamic model formulation. The set of equations defining the evolution of the inequality constrained multi-rank laminate volume fractions is solved by considering a Fischer–Burmeister-type approach. After the general framework and the algorithmic formulation, four distinct laminate-based models are described in detail. The average electric Gibbs energy formulated for the distinct laminate-based models is based on different mixture theory assumptions and averaging formulations. The difference between the four distinct laminate-based models is highlighted by studying the obtained material responses, in terms of the volume fractions evolution and of the hysteresis curves, considering single crystal tetragonal BaTiO_3 material parameters.

Chapter 5 focusses on the computational framework in order to predict the rate-dependent polycrystalline tetragonal BaTiO_3 material response under external loading conditions. The specific computational strategy is based on random initialisation of orientations of the individual single crystal grains within a polycrystalline aggregate. At

first, the model parameters influencing the shape of the hysteresis curves using a particular single crystal laminate-based model, introduced in Chapter 4, are identified by minimising a least-square functional based on available experimental data. Following the calibration of the model parameters, the computational framework and its subsequent implementation within a finite element environment will be elaborated. Apart from solving representative boundary value problems, the obtained polycrystalline tetragonal BaTiO₃ butterfly and dielectric hysteresis curves for a particular loading rate are compared with the recently measured experimental data.

1.2 Notations used in this work

In view of the notations used in this work, the scalar quantities are denoted by italic Latin or Greek letters or by upright sans-serif letters; for example a , B , α , \mathbf{a} . Euclidean vectors or first-order tensors are represented by boldface italic Latin letters, e.g. \mathbf{a} , \mathbf{B} . Likewise, Euclidean second-order tensors are designated by boldface italic Latin or Greek letters, e.g. \mathbf{v} , \mathbf{T} , $\boldsymbol{\sigma}$, $\boldsymbol{\varepsilon}$.

Following Einstein's summation convention, the Euclidean vectors are expressed by their coefficients $(\bullet)_i$ and by Cartesian base vectors \mathbf{e}_i , for $i = 1, 2, 3$, as

$$\{\mathbf{a}, \mathbf{B}\} = \{a_i, B_i\} \mathbf{e}_i.$$

Analogously, the Euclidean second-order tensors are expressed by their tensor coefficients $(\bullet)_{ij}$ and by the Cartesian base vectors as

$$\{\mathbf{T}, \boldsymbol{\sigma}\} = \{T_{ij}, \sigma_{ij}\} \mathbf{e}_i \otimes \mathbf{e}_j,$$

wherein \otimes denotes the standard dyadic product symbol. In particular, $\mathbf{I} = \delta_{ij} \mathbf{e}_i \otimes \mathbf{e}_j$ signifies the second-order identity tensor, wherein δ_{ij} is the Kronecker delta symbol with the properties $\delta_{ij} = 1$ for $i = j$ and $\delta_{ij} = 0$ for $i \neq j$. The symmetric part of an arbitrary second-order tensor \mathbf{A} is introduced as

$$\mathbf{A}^{\text{sym}} = \frac{1}{2} [\mathbf{A} + \mathbf{A}^{\text{t}}],$$

wherein \mathbf{A}^{t} denotes the transpose of \mathbf{A} .

Euclidean third and fourth-order tensors are indicated by boldface upright sans-serif letters, for example \mathbf{a} , \mathbf{B} . These higher-order tensors are expressed by

$$\mathbf{a} = a_{ijk} \mathbf{e}_i \otimes \mathbf{e}_j \otimes \mathbf{e}_k \quad \text{and}$$

$$\mathbf{B} = B_{ijkl} \mathbf{e}_i \otimes \mathbf{e}_j \otimes \mathbf{e}_k \otimes \mathbf{e}_l,$$

wherein a_{ijk} and B_{ijkl} denote the respective third and fourth-order tensor coefficients.

In the context of inner products, the single contraction between two arbitrary vectors \mathbf{a} and \mathbf{b} is denoted as

$$\mathbf{a} \cdot \mathbf{b} = a_i b_i,$$

whereas the single and double contractions between any two arbitrary second-order tensors \mathbf{A} and \mathbf{B} are written respectively as

$$\mathbf{A} \cdot \mathbf{B} = A_{ij} B_{jk} \mathbf{e}_i \otimes \mathbf{e}_k \quad \text{and}$$

$$\mathbf{A} : \mathbf{B} = A_{ij} B_{ij} = \text{tr}(\mathbf{A} \cdot \mathbf{B}^t).$$

Note, the trace of an arbitrary second-order tensor \mathbf{A} is, accordingly, computed as $\text{tr}(\mathbf{A}) = \mathbf{A} : \mathbf{I}$. The inner product rule can be used involving tensors of different orders, wherein the desired number of contractions is characterised by the specified number of dots. In this regard, the double contraction of an arbitrary fourth-order tensor \mathbf{B} with a second-order tensor \mathbf{A} results in

$$\mathbf{B} : \mathbf{A} = B_{ijkl} A_{kl} \mathbf{e}_i \otimes \mathbf{e}_j.$$

The non-standard dyadic products $\overline{\otimes}$ and $\underline{\otimes}$ used in this work are defined as

$$[\mathbf{T}_1 \overline{\otimes} \mathbf{T}_2] : \mathbf{T}_3 = \mathbf{T}_1 \cdot \mathbf{T}_3 \cdot \mathbf{T}_2^t,$$

$$[\mathbf{T}_1 \underline{\otimes} \mathbf{T}_2] : \mathbf{T}_3 = \mathbf{T}_1 \cdot \mathbf{T}_3^t \cdot \mathbf{T}_2^t \quad \text{and}$$

$$[\mathbf{T}_1 \overline{\otimes} \mathbf{v}_1] \cdot \mathbf{v}_2 = \mathbf{T}_1 \cdot \mathbf{v}_2 \otimes \mathbf{v}_1,$$

for all second-order tensors $\mathbf{T}_1, \mathbf{T}_2, \mathbf{T}_3$ and for all vectors $\mathbf{v}_1, \mathbf{v}_2$. Based on the above defined non-standard dyadic product definitions, the fourth-order symmetric identity tensor is introduced as

$$\mathbf{I}^{\text{sym}} = \frac{1}{2} [\mathbf{I} \overline{\otimes} \mathbf{I} + \mathbf{I} \underline{\otimes} \mathbf{I}].$$

2 Essential balance relations

This chapter summarises the fundamental kinematic and balance relations and outlines the coupled thermodynamic framework required to model the behaviour of ferroelectric continua. The present chapter is subdivided into the following four sections. Section 2.1 introduces the fundamental quantities as well as the constitutive relations of electrostatics in both vacuum and dielectric medium. Assuming geometrically linear theory within the general framework of continuum mechanics, Section 2.2 introduces the strain and stress measures required to describe the deformation and internal state of a physical body under the influence of external forces. Following the fundamental notes on electrostatics and kinematics, Section 2.3 summarises the coupled electromechanical balance relations and the thermodynamic framework needed for the description of dissipative ferroelectric materials. Finally, Section 2.4 outlines the necessary weak formulations and their approximations as well as the nodal residual equations required for the finite element framework in order to solve the coupled electromechanical boundary value problems.

2.1 Electrostatics

This section provides the fundamental relations of electrostatics. Without going into the details of the derivations, the basic equations related to the electrostatic theory in both vacuum and dielectric medium will be introduced. For further references with respect to the detailed derivation of the introduced relations, the reader is referred to the monographs on this subject by Landau and Lifshitz [86], Griffiths [52] and Jackson [65].

Electric charge, denoted by q and with coulomb (C) as its SI unit, is the fundamental quantity defining the property of particles. If we assume there are N particles with individual point charges q_i , wherein $i = 1, \dots, N$, then the net charge is an additive measure of the sum of the individual static charges, that is

$$Q = \sum_{i=1}^N q_i. \quad (2.1)$$

A single electric charge or an accumulation of electric charges are either positively or negatively charged. The elementary positively charged particles or protons are denoted by $e^+ \approx 1.6 \times 10^{-19}$ C and the elementary negatively charged particles or electrons are

2 Essential balance relations

represented by $e^- \approx -1.6 \times 10^{-19}$ C. Based on experiments, the electrostatic force \mathbf{f}_1^e exerted by an arbitrary charge q_1 at point \mathbf{x}_1 on a test charge q_0 located at \mathbf{x} is given by Coulomb's law

$$\mathbf{f}_1^e = \frac{q_1 q_0}{4\pi\epsilon_0} \frac{\mathbf{x} - \mathbf{x}_1}{\|\mathbf{x} - \mathbf{x}_1\|^3}, \quad (2.2)$$

wherein $\epsilon_0 \approx 8.854 \times 10^{-12}$ C²/(N m²) is the permittivity of free space. Considering an accumulation of point charges q_1, \dots, q_N , located at $\mathbf{x}_1, \dots, \mathbf{x}_N$, the total electrostatic force of the individual charges on the test charge q_0 is given by

$$\mathbf{F}^e = \sum_{i=1}^N \mathbf{f}_i^e = \sum_{i=1}^N \frac{q_i q_0}{4\pi\epsilon_0} \frac{\mathbf{x} - \mathbf{x}_i}{\|\mathbf{x} - \mathbf{x}_i\|^3} = q_0 \mathbf{E}(\mathbf{x}). \quad (2.3)$$

Here, $\mathbf{E}(\mathbf{x})$ is the total electric field of the individual point charges and is defined as

$$\mathbf{E}(\mathbf{x}) = \sum_{i=1}^N \frac{q_i}{4\pi\epsilon_0} \frac{\mathbf{x} - \mathbf{x}_i}{\|\mathbf{x} - \mathbf{x}_i\|^3}. \quad (2.4)$$

Note, that the total electric field (2.4), measured in V/m, is independent of the influence of test charge q_0 but is written as a function of the location of the test charge. Assuming that the individual point charges q_i are distributed continuously over a volume $\mathcal{V} \in \mathbb{R}^3$, the total electric field is expressed in terms of the charge per unit volume $\rho^v(\bar{\mathbf{x}})$ as

$$\mathbf{E}(\mathbf{x}) = \int_{\mathcal{V}} \frac{\rho^v(\bar{\mathbf{x}})}{4\pi\epsilon_0} \frac{\mathbf{x} - \bar{\mathbf{x}}}{\|\mathbf{x} - \bar{\mathbf{x}}\|^3} d\bar{v}, \quad (2.5)$$

wherein $d\bar{v}$ is the infinitesimal volume element at position $\bar{\mathbf{x}}$. Inserting the definition $\nabla_{\mathbf{x}} [-1/\|\mathbf{x} - \bar{\mathbf{x}}\|] = [\mathbf{x} - \bar{\mathbf{x}}]/\|\mathbf{x} - \bar{\mathbf{x}}\|^3$ in Equation (2.5), one obtains

$$\mathbf{E}(\mathbf{x}) = -\nabla_{\mathbf{x}} \phi(\mathbf{x}), \quad (2.6)$$

wherein $\phi(\mathbf{x})$ is the scalar electric potential and is defined as

$$\phi(\mathbf{x}) = \int_{\mathcal{V}} \frac{\rho^v(\bar{\mathbf{x}})}{4\pi\epsilon_0} \frac{1}{\|\mathbf{x} - \bar{\mathbf{x}}\|} d\bar{v}. \quad (2.7)$$

Furthermore, from Equation (2.6) it follows that the electric field vector is irrotational and that the divergence of the electric field takes a non-zero value, that is

$$\nabla_{\mathbf{x}} \times \mathbf{E}(\mathbf{x}) = \mathbf{0} \quad \text{and} \quad \nabla_{\mathbf{x}} \cdot \mathbf{E}(\mathbf{x}) = \frac{\rho^v}{\epsilon_0}. \quad (2.8)$$

Equation (2.8)₂ is the local form of Gauß's law of electrostatics in free space. Introducing the term electric displacement

$$\mathbf{D}(\mathbf{x}) = \epsilon_0 \mathbf{E}(\mathbf{x}), \quad (2.9)$$

the local form of Gauß's law in free space is reformulated as

$$\nabla_{\mathbf{x}} \cdot \mathbf{D}(\mathbf{x}) = \rho^v. \quad (2.10)$$

The introduced electrostatic relations as well as Gauß's law consider the interactions between the static charges in free space or vacuum. In order to describe the electrostatic phenomena in ferroelectric materials, the above defined fundamental relations need to consider the influence of the material medium. Ferroelectric single and polycrystalline solids which do not conduct electricity fall into the class of non-conducting or insulating materials and are, in general, termed as dielectrics. In contrast to the conducting materials which are composed of free charge carriers responsible for the conduction of electricity, dielectric materials are composed of bound charges, denoted by ρ_b^v , which are bound to the material and can only move to a limited extent from their original position upon the application of an external electric field. Considering an individual atom, a dipole moment \mathbf{p}^e is created due to the separation of the positive and negative charges when the dielectric is subjected to an external potential difference. Assuming N such dipole moments, an overall polarisation at the macroscopic level is obtained as a summation of the finite number of dipole moments per unit volume. The macroscopic polarisation \mathbf{P} of a given volume V is measured in C/m² and is given by

$$\mathbf{P} = \frac{1}{V} \sum_{i=1}^N \mathbf{p}_i^e. \quad (2.11)$$

Note, that the bound charges within the dielectric solid are only responsible for the induced macroscopic polarisation, see [52, 65]. Without further derivations, the relation between the macroscopic polarisation and the bound charges is written as

$$\nabla_{\mathbf{x}} \cdot \mathbf{P}(\mathbf{x}) = -\rho_b^v. \quad (2.12)$$

Furthermore, the induced macroscopic polarisation is also expressed in terms of the electric field as

$$\mathbf{P}(\mathbf{x}) = \epsilon_0 \chi \mathbf{E}(\mathbf{x}), \quad (2.13)$$

wherein χ denotes the electric susceptibility of the material. Decomposing the total charge density per unit volume ρ^v into free and bound charges per unit volume, that is

$$\rho^v = \rho_f^v + \rho_b^v, \quad (2.14)$$

the local form of Gauß's law of electrostatics (2.8)₂ is reformulated using Equations (2.14) and (2.12) as

$$\begin{aligned}\nabla_{\mathbf{x}} \cdot \mathbf{E}(\mathbf{x}) &= \frac{\rho^v}{\epsilon_0} = \frac{\rho_f^v + \rho_b^v}{\epsilon_0} = \frac{\rho_f^v - \nabla_{\mathbf{x}} \cdot \mathbf{P}(\mathbf{x})}{\epsilon_0} \\ \Rightarrow \nabla_{\mathbf{x}} \cdot [\epsilon_0 \mathbf{E}(\mathbf{x}) + \mathbf{P}(\mathbf{x})] &= \rho_f^v.\end{aligned}\tag{2.15}$$

The local form of Gauß's law of electrostatics in dielectric medium reads

$$\nabla_{\mathbf{x}} \cdot \mathbf{D}(\mathbf{x}) = \rho_f^v,\tag{2.16}$$

wherein

$$\mathbf{D}(\mathbf{x}) = \epsilon_0 \mathbf{E}(\mathbf{x}) + \mathbf{P}(\mathbf{x}),\tag{2.17}$$

is the dielectric displacement vector measured in C/m².

2.2 Kinematic and stress measures

Based on the theory of continuum mechanics, this section introduces the kinematic strain measure and the constitutive stress quantity in order to describe the deformation and the internal state of a physical body. For a detailed study on the subject of continuum mechanics and thermodynamics of materials, the reader is referred to the monographs by Müller [114], Ciarlet [33], Šilhavý [147] and by Holzapfel [53].

With reference to the right handed rectangular coordinate axes defined by orthonormal basis vectors $\mathbf{e}_{1,2,3}$ at a fixed origin O , the continuum body occupies a solid domain in a three-dimensional space $\mathcal{B} \in \mathbb{R}^3$ with boundary $\partial\mathcal{B}$ at time t . The physical body consists of material points or particles, wherein each point is identified by a position vector \mathbf{x} with respect to origin O . The velocity of an arbitrary material point at position \mathbf{x} is denoted by

$$\dot{\mathbf{x}} = \partial_t \mathbf{x}.\tag{2.18}$$

The deformation of the physical body under the influence of external electrical and mechanical forces is described by the displacement vector $\mathbf{u}(\mathbf{x}, t)$ corresponding to the individual material points. Under the assumption of geometrically linear theory, i.e. bodies undergoing small or infinitesimal deformations, the second-order linear strain tensor is introduced as the local strain measure. The infinitesimal or linear strain tensor is defined as the symmetric part of the displacement gradient, that is

$$\boldsymbol{\varepsilon}(\mathbf{x}) := \nabla_{\mathbf{x}}^{\text{sym}} \mathbf{u}(\mathbf{x}, t).\tag{2.19}$$

Considering a normal \mathbf{n} of a cutting plane passing through an arbitrary material point $\mathbf{x} \in \mathcal{B}$, the traction vector $\mathbf{t}(\mathbf{x}, \mathbf{n})$ is defined as the force per unit surface area across the cutting plane. The linear dependency of the traction vector with respect to the outward normal is established through Cauchy's stress theorem

$$\mathbf{t}(\mathbf{x}, \mathbf{n}) = \boldsymbol{\sigma}(\mathbf{x}) \cdot \mathbf{n}, \quad (2.20)$$

wherein $\boldsymbol{\sigma}(\mathbf{x})$ denotes the Cauchy stress tensor. The stresses $\boldsymbol{\sigma}(\mathbf{x})$ describe the internal loading state of the physical body under the influence of external forces.

2.3 Balance relations and thermodynamic framework

This section summarises the balance relations as well as the energy and entropy axioms which form the basis for the modelling of ferroelectric crystalline and ceramic solids. The equations are based on the coupled thermodynamic framework for electromechanical problems outlined by, for example, Toupin [141], Eringen [47], Eringen and Maugin [48] and by Bustamante et al. [23].

With respect to closed systems, the conservation of mass states that the mass of the system does not change during the deformation over time. Denoting the mass density by ρ and neglecting the current of free charges, the local form of the conservation of mass is given by

$$\dot{\rho} = 0, \quad (2.21)$$

wherein $\dot{\rho}$ corresponds to the time derivative of the mass density.

The balance of linear momentum states that the sum of all external forces equals the time derivative of linear momentum during the deformation. The local form of the axiom of balance of linear momentum reads

$$\nabla_{\mathbf{x}} \cdot \boldsymbol{\sigma} + \mathbf{b} = \rho \ddot{\mathbf{x}}, \quad (2.22)$$

wherein \mathbf{b} is the vector of body forces and wherein $\ddot{\mathbf{x}} = \partial_t \dot{\mathbf{x}}$ is the acceleration of an arbitrary material point at \mathbf{x} . Note, that the local statement of the balance of linear momentum (2.22) neglects the influence of electrostatic forces on the deformation, i.e. the electrical volume force vector derived from the Maxwell or electrostatic stress tensor is assumed to be approximately equal to zero. In context with the study of the ferroelectric crystals and ceramics, the magnitude of the electrostatic stress tensor is very small in comparison to the mechanical Cauchy stress, see Kamlah [71]. Therefore, the electrically induced volume forces are assumed to vanish while considering the axiom of the balance of linear momentum. Moreover, quasi-static conditions are assumed during the deformation. Due to this assumption, the acceleration of the material points, appearing in Equation (2.22), is approximated to zero, i.e. $\ddot{\mathbf{x}} \approx \mathbf{0}$.

2 Essential balance relations

The axiom of the balance of angular momentum states that the time derivative of the angular momentum with respect to a given point in a body is equal to the sum of all the external moments. A direct consequence of the axiom of the balance of angular momentum is that the Cauchy stress tensor $\boldsymbol{\sigma}(\boldsymbol{x})$ is symmetric, that is

$$\boldsymbol{\sigma} = \boldsymbol{\sigma}^t. \quad (2.23)$$

Following the axioms on the balance of mass and momentum, the balance of energy or the first law of thermodynamics states that the rate of change of the total energy is equal to the sum of the external powers. The total energy is given as the sum of the internal and kinetic energies of the body, and the external power consists of the summation of the mechanical, thermal and electrical powers. The local form of the balance of energy reads

$$\dot{U} = \boldsymbol{\sigma} : \dot{\boldsymbol{\varepsilon}} + \boldsymbol{E} \cdot \dot{\boldsymbol{D}} + r - \nabla_{\boldsymbol{x}} \cdot \boldsymbol{q}, \quad (2.24)$$

wherein U defines the internal energy per unit volume, r denotes the external heat source per unit volume, \boldsymbol{q} represents the heat flux vector and wherein the notation $\dot{\bullet}$ is the time derivative of the corresponding quantity. In Equation (2.24), $\boldsymbol{\sigma} : \dot{\boldsymbol{\varepsilon}}$ corresponds to the rate of the mechanical work and $\boldsymbol{E} \cdot \dot{\boldsymbol{D}}$ relates to the electrical power of the body.

Finally, the axiom of the entropy inequality or the second law of thermodynamics states that the rate of change of entropy of the body is always larger than or equal to the difference between the total heat produced by the internal entropy and the entropy supply due to the heat flux through the surface of the body. Without going into the details of the derivation, the local form of the entropy inequality for a general coupled thermo-electromechanical process assuming isothermal conditions is given by

$$-\dot{U} + \boldsymbol{\sigma} : \dot{\boldsymbol{\varepsilon}} - \boldsymbol{E} \cdot \dot{\boldsymbol{D}} + \vartheta \dot{\eta} \geq 0, \quad (2.25)$$

wherein, ϑ is the absolute temperature and η denotes the volume specific entropy. It is to be noted that the internal energy per unit volume for the coupled dissipative process is written as a function of linear strain tensor $\boldsymbol{\varepsilon}$, dielectric displacement vector \boldsymbol{D} , volume specific entropy η and of a set of internal state variables $\boldsymbol{\nu}$, that is

$$U := U(\boldsymbol{\varepsilon}, \boldsymbol{D}, \eta, \boldsymbol{\nu}). \quad (2.26)$$

The choice of the governing thermodynamic potential depends on the process variables considered. One may arrive at the desired thermodynamic potential starting from the internal energy together with a partial or full Legendre–Fenchel transformation with respect to the particular process variables. Instead of the volume specific internal energy, it is beneficial to introduce the electric Gibbs energy per unit volume for the analysis of global coupled electromechanical boundary value problems. A partial Legendre–Fenchel transformation of the volume specific internal energy is performed with respect to the

dielectric displacement vector and the entropy in order to arrive at the electric Gibbs energy as

$$H(\boldsymbol{\varepsilon}, \mathbf{E}, \vartheta, \boldsymbol{\nu}) = \inf_{\mathbf{D}, \eta} [U(\boldsymbol{\varepsilon}, \mathbf{D}, \eta, \boldsymbol{\nu}) - \mathbf{E} \cdot \mathbf{D} - \vartheta \eta] . \quad (2.27)$$

The electric Gibbs energy is a function of the total linear strain tensor, the electric field vector, the absolute temperature and of the set of internal state variables. Neglecting the influence of the absolute temperature on the deformation, the local form of the entropy inequality (2.25) for dissipative ferroelectric solids is reformulated in terms of the electric Gibbs energy as

$$-\dot{H}(\boldsymbol{\varepsilon}, \mathbf{E}, \boldsymbol{\nu}) + \boldsymbol{\sigma} : \dot{\boldsymbol{\varepsilon}} - \mathbf{D} \cdot \dot{\mathbf{E}} \geq 0 . \quad (2.28)$$

Following the Coleman–Noll procedure of rational thermodynamics, the constitutive quantities, namely the second-order stress tensor and the dielectric displacement vector, are given by

$$\boldsymbol{\sigma} = \frac{\partial H(\boldsymbol{\varepsilon}, \mathbf{E}, \boldsymbol{\nu})}{\partial \boldsymbol{\varepsilon}} \quad \text{and} \quad (2.29)$$

$$\mathbf{D} = - \frac{\partial H(\boldsymbol{\varepsilon}, \mathbf{E}, \boldsymbol{\nu})}{\partial \mathbf{E}} , \quad (2.30)$$

and the reduced dissipation inequality reads

$$\mathcal{D}_{\text{red}} = \mathbf{f}(\boldsymbol{\nu}) \cdot \dot{\boldsymbol{\nu}} \geq 0 , \quad (2.31)$$

wherein $\mathbf{f}(\boldsymbol{\nu})$ is the set of driving forces conjugate to the rate of the set of internal state variables $\dot{\boldsymbol{\nu}}$ identified as

$$\mathbf{f}(\boldsymbol{\nu}) = - \frac{\partial H(\boldsymbol{\varepsilon}, \mathbf{E}, \boldsymbol{\nu})}{\partial \boldsymbol{\nu}} . \quad (2.32)$$

Based on the postulate of maximum dissipation, rate-dependent dissipation functions will be formulated for the phenomenological and laminate-based model formulations in Chapters 3 and 4 respectively. The evolution equations of the set of the internal state variables will be obtained by fulfilling the necessary conditions of the postulated scalar rate-dependent dissipation relations and will be detailed in the forthcoming chapters.

2.4 Finite element approximation

This section reviews the standard finite element approximation procedure considered to solve the quasi-static electromechanical coupled boundary value problems. For a detailed study on the finite element method, the reader is referred to the monographs by, for example, Bathe [17], Hughes [58], Zienkiewicz et al. [157] and Wriggers [148].

Allik and Hughes [1] formulated the finite element setting for piezoelectric solids considering the displacement vector and scalar electric potential as the mechanical and electrical nodal quantities, respectively. Their standard finite element framework was preferred for solving coupled boundary value problems in order to prove the versatility of the thermodynamically consistent material models in a number of research works. To name a few, we refer to the works by Hwang and McMeeking [61, 62], Schröder et al. [124–126], Miehe et al. [111, 112], amongst others. In contrast, an alternative approach favouring the dielectric displacement vector potential instead of the scalar electric potential as the electrical nodal field variable was introduced by Landis [87]. The finite element framework [87] was considered by Kamlah et al. [75] for the numerical simulation of the ferroelectric polycrystalline response. With respect to the numerical implementation of the material models developed in the present research work, the standard finite element procedure for coupled electromechanical problems is followed. Both the displacement vector and scalar electric potential are treated as primary field variables in solving the global boundary value problems, see also Dusthakar et al. [43] in this regard.

The local forms of the governing field equations describing the electromechanically coupled behaviour are the balance of linear momentum and Gauß's law in dielectrics,

$$\nabla_x \cdot \boldsymbol{\sigma} + \mathbf{b} = \mathbf{0} \quad \text{and} \quad \nabla_x \cdot \mathbf{D} - \rho_f^v = 0, \quad (2.33)$$

which must be satisfied at all points within the ferroelectric domain \mathcal{B} . In Equations (2.33)₁ and (2.33)₂, $\boldsymbol{\sigma}$ denotes the second-order (symmetric) stress tensor, \mathbf{D} represents the dielectric displacement vector, \mathbf{b} is the body force vector and ρ_f^v characterises the density of free charge carriers. Assume for simplicity that the electrostatic forces are negligible and that the temperature field remains constant. Furthermore, any contributions of defects and surface charges are assumed to be neglected. The partial differential equations (2.33)₁ and (2.33)₂ are solved with respect to the prescribed Dirichlet and Neumann boundary conditions. The displacements \mathbf{u} and electric potential ϕ corresponding to the Dirichlet boundary conditions are prescribed on the Dirichlet part of the boundaries, that is

$$\mathbf{u} = \bar{\mathbf{u}} \quad \text{on} \quad \partial\mathcal{B}_{\mathbf{u}} \quad \text{and} \quad (2.34)$$

$$\phi = \bar{\phi} \quad \text{on} \quad \partial\mathcal{B}_{\phi}. \quad (2.35)$$

Analogously, the surface tractions \mathbf{t} and the surface free charge density ρ_f^a correspond to the Neumann boundary conditions. These surface quantities are prescribed on the Neumann part of the boundaries, that is

$$\mathbf{t} = \boldsymbol{\sigma} \cdot \mathbf{n} = \bar{\mathbf{t}} \quad \text{on} \quad \partial\mathcal{B}_\sigma \quad \text{and} \quad (2.36)$$

$$-\rho_f^a = \mathbf{D} \cdot \mathbf{n} = -\bar{\rho}_f^a \quad \text{on} \quad \partial\mathcal{B}_D, \quad (2.37)$$

wherein \mathbf{n} denotes the outward normal unit vector. The local form of the governing partial differential equations (2.33)₁ and (2.33)₂, along with the boundary conditions (2.34) to (2.37), form the set of equilibrium equations in the strong form that needs to be solved within the ferroelectric solid domain \mathcal{B} .

Adopting the Galerkin method – based on the principle of virtual work – both the local form of the governing mechanical and electrical equilibrium equations are reduced to their corresponding weak forms. The weak form of the governing mechanical equilibrium equation is derived by multiplying the local form of balance of linear momentum (2.33)₁ with a vector-valued test function $\delta\mathbf{u}$ and integrating over the solid domain \mathcal{B} . Similarly, the weak form of the governing electrical equilibrium equation is arrived by multiplying the local form of Gauß's law in dielectrics (2.33)₂ with a scalar-valued test function $\delta\phi$ and integrating over the solid domain \mathcal{B} . Without further details, the derived mechanical and electrical weak formulations read

$$G_{\mathbf{u}} = \int_{\mathcal{B}} \nabla_{\mathbf{x}} \delta\mathbf{u} : \boldsymbol{\sigma} \, dv - \int_{\partial\mathcal{B}_\sigma} \delta\mathbf{u} \cdot \bar{\mathbf{t}} \, da - \int_{\mathcal{B}} \delta\mathbf{u} \cdot \mathbf{b} \, dv = 0 \quad \text{and} \quad (2.38)$$

$$G_\phi = \int_{\mathcal{B}} \nabla_{\mathbf{x}} \delta\phi \cdot \mathbf{D} \, dv + \int_{\partial\mathcal{B}_D} \delta\phi \bar{\rho}_f^a \, da + \int_{\mathcal{B}} \delta\phi \rho_f^v \, dv = 0. \quad (2.39)$$

Next, the ferroelectric solid domain \mathcal{B} is approximated into \mathcal{B}^h and is further discretised by n_{el} finite elements \mathcal{B}^e , i.e. $\mathcal{B} \approx \mathcal{B}^h = \bigcup_{e=1}^{n_{el}} \mathcal{B}^e$. Each finite element is described by n_{en} distinct nodes and by the interpolation or shape functions $N_I(\mathbf{x})$, defined for the individual nodes I . Following the standard Bubnov–Galerkin procedure, the displacements, the scalar electric potential as well as the virtual displacement and electric potential within each finite element are approximated as

$$\bullet^e(\mathbf{x}) \approx \bullet^{h,e}(\mathbf{x}) = \sum_{I=1}^{n_{en}} N_I(\mathbf{x}) \bullet_I, \quad (2.40)$$

wherein $\{\bullet\} = \{\mathbf{u}, \delta\mathbf{u}, \phi, \delta\phi\}$. Analogously, the virtual displacement and electrical potential gradients, are approximated as

$$\nabla_{\mathbf{x}} \delta\mathbf{u}^e(\mathbf{x}) \approx \nabla_{\mathbf{x}} \delta\mathbf{u}^{h,e}(\mathbf{x}) = \sum_{I=1}^{n_{en}} \delta\mathbf{u}_I \otimes \nabla_{\mathbf{x}} N_I(\mathbf{x}) \quad \text{and} \quad (2.41)$$

$$\nabla_{\mathbf{x}} \delta\phi^e(\mathbf{x}) \approx \nabla_{\mathbf{x}} \delta\phi^{h,e}(\mathbf{x}) = \sum_{J=1}^{n_{en}} \delta\phi_J \nabla_{\mathbf{x}} N_J(\mathbf{x}). \quad (2.42)$$

2 Essential balance relations

Adopting the isoparametric concept, the element geometry is approximated by the same shape functions as considered for the nodal quantities. By inserting the approximations (2.40) to (2.42), the discrete counterparts of the weak form provided in Equations (2.38) and (2.39) within each finite element are approximated as

$$G_{\mathbf{u}}^{h,e} = \sum_{I=1}^{n_{en}} \delta \mathbf{u}_I \cdot \mathbf{r}_I^{\mathbf{u}} = 0 \quad \text{and} \quad G_{\phi}^{h,e} = \sum_{J=1}^{n_{en}} \delta \phi_J r_J^{\phi} = 0, \quad (2.43)$$

wherein the residuals $\mathbf{r}_I^{\mathbf{u}}$ and r_J^{ϕ} corresponding to nodes $I, J = 1, \dots, n_{en}$ read

$$\mathbf{r}_I^{\mathbf{u}} = \int_{\mathcal{B}^e} \nabla_{\mathbf{x}} N_I \cdot \boldsymbol{\sigma} \, dv - \int_{\partial \mathcal{B}_g^e} N_I \bar{\mathbf{t}} \, da - \int_{\mathcal{B}^e} N_I \mathbf{b} \, dv \quad \text{and} \quad (2.44)$$

$$r_J^{\phi} = \int_{\mathcal{B}^e} \nabla_{\mathbf{x}} N_J \cdot \mathbf{D} \, dv + \int_{\partial \mathcal{B}_D^e} N_J \bar{\rho}_f^a \, da + \int_{\mathcal{B}^e} N_J \rho_f^v \, dv. \quad (2.45)$$

The derived residuals are non-linear, with respect to the constitutive relations, and depend on nodal solutions \mathbf{u}_I and ϕ_J . In order to solve them, a method of consistent linearisation is used which reduces the system of non-linear equations to a linearised form which can be solved at each iteration step by means of a Newton–Raphson scheme. The consistent linearisation of the residuals is postulated as

$$\text{Lin}(\mathbf{r}_I^{\mathbf{u}}) = \mathbf{r}_I^{\mathbf{u}} + \Delta \mathbf{r}_I^{\mathbf{u}} = \mathbf{0} \quad \text{and} \quad \text{Lin}(r_J^{\phi}) = r_J^{\phi} + \Delta r_J^{\phi} = 0, \quad (2.46)$$

wherein the nodal increments of the residuals are given as

$$\Delta \mathbf{r}_I^{\mathbf{u}} = \sum_{K=1}^{n_{en}} \mathbf{K}_{IK}^{\mathbf{u}\mathbf{u}} \cdot \Delta \mathbf{u}_K + \sum_{L=1}^{n_{en}} \mathbf{K}_{IL}^{\mathbf{u}\phi} \Delta \phi_L \quad \text{and} \quad (2.47)$$

$$\Delta r_J^{\phi} = \sum_{K=1}^{n_{en}} \mathbf{K}_{JK}^{\phi\mathbf{u}} \Delta \mathbf{u}_K + \sum_{L=1}^{n_{en}} \mathbf{K}_{JL}^{\phi\phi} \Delta \phi_L. \quad (2.48)$$

The entries $\mathbf{K}_{IK}^{\mathbf{u}\mathbf{u}}$, $\mathbf{K}_{IL}^{\mathbf{u}\phi}$, $\mathbf{K}_{JK}^{\phi\mathbf{u}}$ and $\mathbf{K}_{JL}^{\phi\phi}$ in Equations (2.47) and (2.48) correspond to the nodal stiffness contributions and are defined as

$$\mathbf{K}_{IK}^{\mathbf{u}\mathbf{u}} := \frac{d\mathbf{r}_I^{\mathbf{u}}}{d\mathbf{u}_K} = \int_{\mathcal{B}^e} \nabla_{\mathbf{x}} N_I \cdot \frac{d\boldsymbol{\sigma}}{d\boldsymbol{\varepsilon}} \cdot \nabla_{\mathbf{x}} N_K \, dv, \quad (2.49)$$

$$\mathbf{K}_{IL}^{\mathbf{u}\phi} := \frac{d\mathbf{r}_I^{\mathbf{u}}}{d\phi_L} = \int_{\mathcal{B}^e} \nabla_{\mathbf{x}} N_I \cdot \frac{d\boldsymbol{\sigma}}{d\mathbf{E}} \cdot \nabla_{\mathbf{x}} N_L \, dv, \quad (2.50)$$

$$\mathbf{K}_{JK}^{\phi\mathbf{u}} := \frac{dr_J^{\phi}}{d\mathbf{u}_K} = \int_{\mathcal{B}^e} \nabla_{\mathbf{x}} N_J \cdot \frac{d\mathbf{D}}{d\boldsymbol{\varepsilon}} \cdot \nabla_{\mathbf{x}} N_K \, dv \quad \text{and} \quad (2.51)$$

$$\mathbf{K}_{JL}^{\phi\phi} := \frac{dr_J^{\phi}}{d\phi_L} = \int_{\mathcal{B}^e} \nabla_{\mathbf{x}} N_J \cdot \frac{d\mathbf{D}}{d\mathbf{E}} \cdot \nabla_{\mathbf{x}} N_L \, dv. \quad (2.52)$$

The nodal level residuals and their increments are arranged in vector and matrix form, respectively, in order to obtain element level entries. The element-level residual vectors, the stiffness matrices as well as the increments of the primary fields are assembled over n_{el} finite elements to arrive at the corresponding global entries

$$\mathbf{r} := \mathbf{A}_{e=1}^{n_{el}} \begin{bmatrix} \mathbf{r}_e^u \\ \mathbf{r}_e^\phi \end{bmatrix}, \quad \mathbf{K} := \mathbf{A}_{e=1}^{n_{el}} \begin{bmatrix} \mathbf{K}_e^{uu} & \mathbf{K}_e^{u\phi} \\ \mathbf{K}_e^{\phi u} & \mathbf{K}_e^{\phi\phi} \end{bmatrix} \quad \text{and} \quad \Delta \mathbf{d} := \mathbf{A}_{e=1}^{n_{el}} \begin{bmatrix} \Delta \mathbf{u}_e \\ \Delta \phi_e \end{bmatrix}, \quad (2.53)$$

wherein the element-level quantities are denoted with the subscript e . The global system of equations reads

$$\mathbf{r} + \mathbf{K} \cdot \Delta \mathbf{d} = \mathbf{0}, \quad (2.54)$$

which is solved iteratively for the displacement and electric potential increments and the global solution vector \mathbf{d} is updated after each iteration, that is

$$\mathbf{d} \leftarrow \mathbf{d} + \Delta \mathbf{d}, \quad (2.55)$$

until the norm of the global residual vector reaches a given tolerance value, $\|\mathbf{r}\| < \text{tol}$.

3 Phenomenological modelling of ferroelectric materials

This chapter presents a phenomenological material model to study the macroscopic hysteretic response of single crystal ferroelectric solids. The model framework consists of formulating an electric Gibbs energy and a rate-dependent dissipation equation to describe the dissipative ferroelectric material behaviour. The electric Gibbs energy is defined in terms of total strain tensor, electric field vector and additional internal state variables. The macroscopic remnant polarisation of the ferroelectric single crystal is regarded as the only internal state variable. The evolution of the macroscopic remnant polarisation is obtained by solving the particular rate-dependent dissipation equation.

Following the model formulation, the algorithmic treatment to solve the non-linear evolution equation is briefly explained. Considering single crystal tetragonal BaTiO_3 material parameters, the presented model reproduces the characteristic butterfly and dielectric hysteresis curves under cyclic electrical loading. The influence of both the loading frequency and the viscosity parameter is studied under homogeneous states of deformation. The macroscopic material model is further implemented in a finite element environment to solve inhomogeneous boundary value problems. A concise description of the presented phenomenological model along with simulations pertaining to two-dimensional boundary value problems can be found in the work by Dusthakar et al. [43].

3.1 Overview of phenomenological models

This section is devoted to an overview of the existing phenomenological models for ferroelectric materials in literature. Macroscopic models are considered in order to study the overall behaviour of a material. These models are formulated with a reduced number of internal state variables. Thereby, the underlying material response is reproduced with the help of model or fitting parameters. In view of ferroelectric solids, these robust phenomenological models are developed in order to gain an understanding of the overall electromechanical coupling behaviour.

Chen and Percy [29] presented a macroscopic one-dimensional theory for an idealised polycrystalline ferroelectric under dynamic loading conditions. In their work, both the stress and dielectric displacement were assumed to depend on the strain, external electric field, absolute temperature, and on a scalar internal state variable. The effective number

of aligned dipoles per unit volume was considered as the only internal state variable. In addition to the constitutive quantities, the evolution equation for the aligned dipoles due to domain switching was postulated. Their framework provided the complete system of equations needed for a coupled dynamic ferroelectric theory. Based on their framework, numerical computations assuming isothermal and stress-free states were provided in the subsequent work by Chen and Montgomery [28]. The numerical results included the computed butterfly and dielectric hysteresis loops for a PZT 65/35 ceramic. The dielectric hysteresis curve was further compared to the experimental PZT 65/35 data. An extension to a general three-dimensional model formulation was made by Chen [25].

Bassiouny et al. [15] formulated the general thermodynamic framework for macroscopic modelling of coupled ferroelectric materials. Their model formulation was analogous to the plasticity theory and considered the macroscopic remnant polarisation as the internal state variable to capture the dissipative ferroelectric behaviour. Suitable Helmholtz energy, written in terms of the internal state variable, and necessary yield function, in terms of applied loads, were introduced in their framework. Following that work, Bassiouny et al. [16] provided the set of relations describing the poling process of ceramics. In their work, the dipole moment along with the respective rate law were considered to describe the poling of ferroelectric solids. Both the dipole moment and the rate law were in line with the works by Chen et al. [25–31]. Based on the framework developed in [15, 16], the identification of material parameters to fit the macroscopic polarisation hysteresis loop to the experimental data was carried out by Bassiouny and Maugin [13]. The influence of the combined electromechanical loading on the ferroelectric material behaviour was discussed in the subsequent contribution by Bassiouny and Maugin [14]. The macroscopic formulations elaborated in [13, 15, 16] do not account for the prediction of the butterfly hysteresis loop. Nevertheless, the associated thermodynamic framework formed the basis for many constitutive models to describe the behaviour of functionally graded materials.

Zhang and Rogers [155] proposed a one-dimensional macroscopic model to reproduce the polarisation hysteresis loop considering domain switching dynamics. Their modelling approach included the introduction of tangent hyperbolic-type functions in order to capture the basic characteristics of a polarisation hysteresis loop. A polarisation reversal equation was formulated as a tangent hyperbolic function written in terms of the coercive electric field and of an additional material parameter. Along with the external electric field, absolute temperature and total strain, the Helmholtz energy formulated in [155] treated the relative polarisation as an internal state variable to predict the ferroelectric material response.

A multi-axial constitutive model to capture the ferroelectric and ferroelastic behaviour spanning across different length scales was derived by Lynch [101]. The constitutive model framework was motivated from the experimental investigations on different compositions of PZT ceramics by Cao and Evans [24], and on lanthanum doped PZT (PLZT) ceramics by Lynch [100]. In the model by Lynch [101], apart from the reversible strain and dielectric displacement, the Helmholtz energy was written as a function of two in-

ternal state variables, namely the remnant strain and polarisation. Interaction between the internal state variables was described by considering two additional scalar quantities. Along with the set of evolution equations for the scalar quantities, the model [101] provided the set of constitutive equations for the reproduction of strain and polarisation hysteresis curves.

Fan et al. [49] formulated a one-dimensional model to study the stress–strain and stress–dielectric displacement behaviour. Their mechanical model was composed of three Maxwell-type elements arranged in parallel, wherein each element consisted of a frictional slider and a non-linear spring. The resulting ferroelastic hysteresis curves from their mechanical model were presented in comparison with the experimental loops for both hard and soft PZT ceramics.

A phenomenological model to predict the ferroelastic switching response of an unpoled polycrystalline ceramic subject to pure mechanical compressive loading was postulated by Landis and McMeeking [90]. Their constitutive model was formulated to compute the stress and strain states around a crack tip in a ferroelastic material. Three internal state variables were defined with respect to the principal remnant strains to capture the important characteristics of ferroelastic switching behaviour. Cocks and McMeeking [34] developed a uni-axial constitutive model to reproduce the non-linear strain and dielectric hysteresis curves. Their uni-axial model formulated the Helmholtz energy as an additive potential comprising of a reversible and an irreversible part. The average remnant strain and polarisation were treated as internal state variables. The increments of both the average remnant strain and polarisation were determined with the help of the relevant convex yield surface defined in their model. The obtained numerical plots were further compared to the experimental hysteresis loop for PLZT under electrical loading.

A rate-independent one-dimensional model for the description of hysteretic behaviour in ferroelectric ceramics was derived by Kamlah and Tsakmakis [74]. Motivated from the assumptions presented in [15, 34], Kamlah and Tsakmakis [74] considered remnant strain and polarisation as the internal state variables in their formulation. They assumed an additive decomposition of the macroscopic remnant strain into a part induced by remnant polarisation and another part due to ferroelastic switching. Suitable evolution equations for the ferroelastic part of the total strain and for the remnant polarisation were derived based on the theory of incremental plasticity. The resulting numerical strain and dielectric hysteresis curves, both for combined electromechanical and for mechanical compressive loading scenarios, were reported in their work. An extension of the one-dimensional formulation [74] to a general multi-axial model was provided by Kamlah and Böhle [72]. Their three-dimensional model was implemented in a finite element environment to simulate the poling process in a multilayer stack actuator. The solution procedure in [72] was based on a two-step scheme or on a staggered approach in order to overcome global convergence issues.

Landis [88] developed a three-dimensional, multi-axial generalisation of the uni-axial model introduced in [34]. As proposed in the one-dimensional formulation [34], the model by Landis [88] considered the Helmholtz energy to be additively decomposed into a reversible and an irreversible part. The irreversible part of the Helmholtz energy was formulated as a function of the internal state variables, namely the remnant strain tensor and polarisation vector. Satisfying the Clausius–Duhem inequality to ensure that the reduced dissipation remains positive, a convex switching surface was defined such that both the remnant strain and polarisation increments remained normal to the switching surface. Considering optimal fitting parameters, the three-dimensional model in [88] reproduced the ferroelectric and ferroelastic hysteresis curves. The resulting plots were compared to the experimental data provided in [55, 100]. McMeeking and Landis [106] proposed a simplified formulation of the multi-axial model [88] by treating the remnant strain as a function of the remnant polarisation, as proposed in [74].

Schröder and Romanowski [126] formulated a coordinate-invariant macroscopic model for polycrystalline ceramics. Their macroscopic model was based on the previous work by Schröder and Gross [124] on the coordinate-invariant formulation for electrostrictive and piezoelectric materials. Following the modelling assumptions in [106], the model in [126] assumed a one-to-one relation between the remnant polarisation and strain. In view of the coordinate-invariant theory, the enthalpy function in [126] was formulated in terms of basic and mixed invariants of the total strain, electric field, remnant quantities, and a structural vector. The framework [126] included the update algorithm needed for the implementation of the invariant-based material model in a finite element environment. Representative numerical examples, both under homogeneous and inhomogeneous states of deformation, were presented. However, the model does not capture the polarisation rotation of ceramics due to the assumption of a constant structural vector. For a more detailed insight on the coordinate-invariant model formulation for ferroelectric ceramics, the reader is referred to the doctoral dissertation by Romanowski [118].

A rate-independent constitutive model to capture the ferroelectric and ferroelastic hystereses of a ceramic under uni-axial loading conditions was proposed by Klinkel [85]. In his model, the electric field was assumed to be additively split into a reversible and an irreversible part. The assumption of such a split of the electric field was made in view of a straightforward implementation of the model in a finite element framework, where the nodal unknowns are the displacements and scalar electric potential. The remnant strain along with the irreversible electric field quantities were treated as the two internal state variables. The remnant strain was further considered to be additively decomposed into two parts. One part was due to the mechanical depolarisation and the other resulted from the dielectric switching effect. The uni-axial model [85] was extended to a generalised three-dimensional setting in the subsequent work by Klinkel [84]. The ferroelectric and ferroelastic hysteresis curves reproduced with the three-dimensional model were in good agreement with the experimental curves.

A three-dimensional phenomenological model to capture the rate-dependent behaviour of ferroelectric ceramics was formulated by Miehe and Rosato [110]. The rate-dependent, incremental variational model was motivated from the experimental observations on PZT ceramics at varying loading frequencies reported by Zhou et al. [156] and by Viehland and Chen [146]. The macroscopic remnant polarisation was considered as the only internal state variable in their model. An energy storage function and a convex rate-dependent dissipation potential were introduced to define an incremental functional for finite time increments. Solving the evolution equation for the update of remnant polarisation at each time step, the incremental stress and consistent tangent modulus were obtained. The macroscopic remnant strain was computed as a deviatoric function of the updated remnant polarisation. The butterfly and dielectric displacement hysteresis curves for varying loading frequencies under homogeneous states of deformation were reproduced. The model was further implemented in a finite element environment, with displacements and electric potential as primary fields, in order to solve inhomogeneous two-dimensional boundary value problems. An extension of the variational model [110] to study the magneto-electro-mechanical coupling behaviour in multi-ferroic solids was postulated in the subsequent work by Miehe et al. [112].

A very recent work on the constitutive modelling of ferroelectric bulk and composite materials along with parameter identification based on experimental data was carried out by Maniprakash et al. [104]. In their work, a constitutive model for bulk PZT was introduced by formulating an electric enthalpy per unit volume and a rate-dependent dissipation equation. The developed model was extended in order to study the behaviour of a 1–3 PZT composite by a simple homogenisation approach. In the subsequent work by Maniprakash et al. [103], a multi-surface model for polycrystalline ferroelectric solids was proposed. The motivation for a multi-surface model was to capture the minor hysteresis loops and the asymmetric butterfly curves observed in the experiments. Apart from these two model frameworks, the doctoral dissertation by Maniprakash [102] includes two other macroscopic model formulations for ferroelectric solids. One of the models included an anisotropic switching surface to study the influence of compressive loads, applied along the direction of the cyclic electrical field. The other being a temperature-dependent model to predict the anti-hysteresis loop and to investigate the influence of temperature on the hysteresis curves.

3.2 Rate-dependent phenomenological framework

This section presents a rate-dependent phenomenological material model to study the overall macroscopic response in single crystal tetragonal ferroelectric materials. The presented model is based on the general ideas for phenomenological modelling of ferroelectric ceramics outlined in the works by Kamlah [71], Schröder and Romanowski [126] and Miehe and Rosato [110]. The modelling framework is restricted to the capturing of the macroscopic rate-dependent remnant polarisation switching behaviour evident in

single crystal ferroelectric solids. Several micromechanical aspects, such as the resolution in space of the spontaneous polarisation switching, are not taken into account.

Bulk ferroelectric single crystals are sub-divided into multiple regions of uniformly oriented unit cells called domains. Two arbitrary domains of different orientations are separated by an interface termed as a domain wall. Any particular domain in the crystal is characterised by the spontaneous polarisation value and by the spontaneous strain coefficient. In case of a tetragonal BaTiO_3 , there are six equally possible directions in which the domains are aligned. The non-uniform distribution of the domains results in a macroscopic unpoled configuration of the crystal devoid of an overall polarisation and strain. A more detailed insight on the different types of domain configurations can be found in the monographs [35, 66, 96].

The spontaneous or microscopic ferroelectric polarisation switching is initiated in the crystal under the application of a sufficiently strong external electric field along a particular direction. This switching aligns the individual domains along the direction of the applied field. Consequently, the crystal reaches a poled state characterised by an elongation along the loading direction. This poled configuration is preserved even after the removal of external loads. The macroscopic remnant state of the crystal can be described by the remnant polarisation \mathbf{P}^r and the remnant strain $\boldsymbol{\varepsilon}^r$. Assuming the single crystal to be transversely-isotropic in both the poled and remnant states, we define two structural quantities in order to characterise the piezoelectric behaviour, namely the first-order structural tensor or polarisation director \mathbf{a} and the second-order structural tensor \mathbf{m} . The structural vector is defined as

$$\mathbf{a} := \frac{\mathbf{P}^r}{\|\mathbf{P}^r\|} \quad \text{with} \quad \|\mathbf{a}\| = 1, \quad (3.1)$$

and the second-order structural tensor is specified as

$$\mathbf{m} := \mathbf{a} \otimes \mathbf{a} \quad \text{with} \quad \text{tr}(\mathbf{m}) = 1. \quad (3.2)$$

The total strain $\boldsymbol{\varepsilon}$ and the dielectric displacement \mathbf{D} of the bulk ferroelectric crystal are considered to be additively decomposed into an elastic and a remnant part as

$$\boldsymbol{\varepsilon} = \boldsymbol{\varepsilon}^e + \boldsymbol{\varepsilon}^r \quad \text{and} \quad \mathbf{D} = \mathbf{D}^e + \mathbf{P}^r. \quad (3.3)$$

Here, $\boldsymbol{\varepsilon}^e$ denotes the reversible strain tensor and \mathbf{D}^e refers to the reversible dielectric displacement vector of the crystal. The macroscopic remnant polarisation \mathbf{P}^r is a result of the net microscopic polarisation of individual domains. Loading the crystal along a direction, aligns the microscopic polarisation such that a net macroscopic remnant polarisation is obtained along the loading direction. As a consequence, the macroscopic remnant strain $\boldsymbol{\varepsilon}^r$ also evolves along the direction of \mathbf{P}^r , see e.g. [74, 106]. Moreover, experimental findings in [24] show that the changes in strains are volume preserving in nature. Based on these findings and following the assumptions made in [74], a deviatoric

form of the remnant strain is considered for the single crystal response. Thus, the specific form of remnant strain tensor written as a function of the macroscopic polarisation is introduced as

$$\boldsymbol{\varepsilon}^r(\mathbf{P}^r) = \frac{3}{2} \frac{\varepsilon^{\text{sat}}}{P^{\text{sat}}} \|\mathbf{P}^r\| \left[\mathbf{m} - \frac{1}{3} \text{tr}(\mathbf{m}) \mathbf{I} \right] = \frac{3}{2} \frac{\varepsilon^{\text{sat}}}{P^{\text{sat}}} \|\mathbf{P}^r\| \left[\mathbf{m} - \frac{1}{3} \mathbf{I} \right], \quad (3.4)$$

cf. [110]. Here, P^{sat} denotes the saturation polarisation and ε^{sat} refers to the saturation strain value, both defined for the ferroelectric single crystal.

The electric Gibbs energy for the phenomenological model formulation to describe the dissipative response of ferroelectric crystal takes the form $H(\boldsymbol{\varepsilon}, \mathbf{E}, \mathbf{P}^r)$, wherein the macroscopic remnant polarisation vector \mathbf{P}^r is the only internal state variable driving the dissipative ferroelectric behaviour. The electric Gibbs energy is further additively decomposed as

$$H(\boldsymbol{\varepsilon}, \mathbf{E}, \mathbf{P}^r) = H^{\text{piezo}}(\boldsymbol{\varepsilon}^e, \mathbf{E}, \mathbf{P}^r) + H^{\text{rem}}(\mathbf{P}^r). \quad (3.5)$$

The piezoelectric part of the electric Gibbs energy reads

$$\begin{aligned} H^{\text{piezo}}(\boldsymbol{\varepsilon}^e, \mathbf{E}, \mathbf{P}^r) &= \frac{1}{2} [\boldsymbol{\varepsilon} - \boldsymbol{\varepsilon}^r(\mathbf{P}^r)] : \mathbf{E} : [\boldsymbol{\varepsilon} - \boldsymbol{\varepsilon}^r(\mathbf{P}^r)] - \frac{1}{2} \mathbf{E} \cdot \boldsymbol{\varepsilon} \cdot \mathbf{E} \\ &\quad - \frac{\|\mathbf{P}^r\|}{P^{\text{sat}}} \mathbf{E} \cdot \mathbf{e}(\mathbf{a}) : [\boldsymbol{\varepsilon} - \boldsymbol{\varepsilon}^r(\mathbf{P}^r)] - \mathbf{P}^r \cdot \mathbf{E}. \end{aligned} \quad (3.6)$$

This part of the total electric Gibbs energy takes an additive form comprising of mechanical, piezoelectric coupling and electrical terms. With respect to the piezoelectric energy (3.6), both the fourth-order elasticity modulus \mathbf{E} and the second-order dielectric tensor $\boldsymbol{\varepsilon}$ are considered to be isotropic. This assumption neglects the influence of loading history on the material moduli, cf. [71]. The third-order piezoelectric tensor $\mathbf{e}(\mathbf{a})$ in the reversible energy function (3.6) is considered to be transversely-isotropic dependent on the polarisation director. Referring to the model in [71], the piezoelectric modulus is scaled by a factor $\|\mathbf{P}^r\|/P^{\text{sat}}$ to consider the history dependence of anisotropy. The scaling factor ensures that the piezoelectric effect vanishes in an unpoled crystal. On the other hand, the piezoelectric response and the anisotropy becomes evident once the remnant polarisation evolves at stronger electric fields along the direction of the polarisation director \mathbf{a} . The closed form representation of the elasticity, piezoelectric and dielectric material moduli reads

$$\mathbf{E} := \lambda^{\text{E}} \mathbf{I} \otimes \mathbf{I} + 2\mu^{\text{E}} \mathbf{I}^{\text{sym}}, \quad (3.7)$$

$$\mathbf{e}(\mathbf{a}) := -\beta_1^{\text{e}} \mathbf{a} \otimes \mathbf{I} - \beta_2^{\text{e}} \mathbf{m} \otimes \mathbf{a} - \frac{\beta_3^{\text{e}}}{2} [\mathbf{I} \otimes \mathbf{a} + \mathbf{I} \overline{\otimes} \mathbf{a}] \quad \text{and} \quad (3.8)$$

$$\boldsymbol{\varepsilon} := -2\gamma^{\text{e}} \mathbf{I}. \quad (3.9)$$

3 Phenomenological modelling of ferroelectric materials

In Equations (3.7) to (3.9), λ^E and μ^E refer to the Lamé parameters, β_1^e , β_2^e and β_3^e are the piezoelectric constants and γ^e is the dielectric parameter. These coordinate-invariant material parameters can be identified from the single crystal BaTiO₃, referring to an orthonormal base system including the easy axis \mathbf{a} , as

$$\lambda^E = E_{1122}, \quad \mu^E = \frac{1}{2}[E_{1111} - E_{1122}], \quad (3.10)$$

$$\beta_1^e = -e_{311}, \quad \beta_2^e = -e_{333} + e_{311} + 2e_{131}, \quad \beta_3^e = -2e_{131}, \quad (3.11)$$

$$\gamma^e = -\frac{1}{2}\epsilon_{11}. \quad (3.12)$$

The remnant part of the total electric Gibbs energy, dependent on the macroscopic remnant polarisation, is formulated based on the saturation-type functions. These functions are postulated in order to capture the monotonically increasing remnant polarisation from zero to the saturation level P^{sat} . A detailed insight on the saturation-type functions can be found in [55, 88, 106, 137]. For the presented macroscopic model, the remnant contribution of the total electric Gibbs energy reads

$$H^{\text{rem}}(\mathbf{P}^r) = \frac{1}{c} \left[\frac{1}{2} P^{\text{sat}} \ln \left(1 - \left[\frac{\|\mathbf{P}^r\|}{P^{\text{sat}}} \right]^2 \right) + \|\mathbf{P}^r\| \operatorname{arctanh} \left(\frac{\|\mathbf{P}^r\|}{P^{\text{sat}}} \right) \right], \quad (3.13)$$

wherein scalar c is a model or fitting parameter that influences the shape of the hysteresis curves. The specific form of the tangent hyperbolic remnant function (3.13) is taken from the coordinate-invariant macroscopic ferroelectric model postulated by Schröder and Romanowski [126].

With reference to the essential equations introduced in Chapter 2, the local form of the Clausius–Duhem inequality for the electromechanical process, considering isothermal conditions, takes the form

$$-\dot{H}(\boldsymbol{\varepsilon}, \mathbf{E}, \mathbf{P}^r) + \boldsymbol{\sigma} : \dot{\boldsymbol{\varepsilon}} - \mathbf{D} \cdot \dot{\mathbf{E}} \geq 0. \quad (3.14)$$

Following the Coleman–Noll procedure of rational thermodynamics, the constitutive quantities, namely the stresses and dielectric displacements read

$$\boldsymbol{\sigma} = \frac{\partial H(\boldsymbol{\varepsilon}, \mathbf{E}, \mathbf{P}^r)}{\partial \boldsymbol{\varepsilon}} \quad \text{and} \quad \mathbf{D} = -\frac{\partial H(\boldsymbol{\varepsilon}, \mathbf{E}, \mathbf{P}^r)}{\partial \mathbf{E}}, \quad (3.15)$$

respectively. Furthermore, the procedure yields a reduced dissipation inequality of the form $\mathcal{D}_{\text{red}} = \mathbf{f}(\mathbf{P}^r) \cdot \dot{\mathbf{P}}^r \geq 0$, wherein $\mathbf{f}(\mathbf{P}^r)$ is the driving force vector conjugate to $\dot{\mathbf{P}}^r$ identified as

$$\mathbf{f}(\mathbf{P}^r) = -\frac{\partial H(\boldsymbol{\varepsilon}, \mathbf{E}, \mathbf{P}^r)}{\partial \mathbf{P}^r}. \quad (3.16)$$

Explicit expressions for the stress tensor, dielectric displacement vector and the driving force vector are derived respectively as

$$\boldsymbol{\sigma} = \mathbf{E} : [\boldsymbol{\varepsilon} - \boldsymbol{\varepsilon}^r(\mathbf{P}^r)] - \frac{\|\mathbf{P}^r\|}{P_{\text{sat}}} \mathbf{e}^t(\mathbf{a}) \cdot \mathbf{E}, \quad (3.17)$$

$$\mathbf{D} = \frac{\|\mathbf{P}^r\|}{P_{\text{sat}}} \mathbf{e}(\mathbf{a}) : [\boldsymbol{\varepsilon} - \boldsymbol{\varepsilon}^r(\mathbf{P}^r)] + \boldsymbol{\varepsilon} \cdot \mathbf{E} + \mathbf{P}^r \quad \text{and} \quad (3.18)$$

$$\begin{aligned} \mathbf{f}(\mathbf{P}^r) = & [\boldsymbol{\varepsilon} - \boldsymbol{\varepsilon}^r(\mathbf{P}^r)] : \mathbf{E} : \frac{\partial \boldsymbol{\varepsilon}^r(\mathbf{P}^r)}{\partial \mathbf{P}^r} + \frac{1}{P_{\text{sat}}} [\mathbf{E} \cdot \mathbf{e}(\mathbf{a}) : [\boldsymbol{\varepsilon} - \boldsymbol{\varepsilon}^r(\mathbf{P}^r)]] \mathbf{a} \\ & + \frac{\|\mathbf{P}^r\|}{P_{\text{sat}}} \mathbf{E} \cdot \frac{\partial \mathbf{e}(\mathbf{a})}{\partial \mathbf{P}^r} : [\boldsymbol{\varepsilon} - \boldsymbol{\varepsilon}^r(\mathbf{P}^r)] - \frac{\|\mathbf{P}^r\|}{P_{\text{sat}}} \mathbf{E} \cdot \mathbf{e}(\mathbf{a}) : \frac{\partial \boldsymbol{\varepsilon}^r(\mathbf{P}^r)}{\partial \mathbf{P}^r} \\ & + \mathbf{E} - \mathbf{E}^b(\mathbf{P}^r), \end{aligned} \quad (3.19)$$

wherein $\mathbf{E}^b(\mathbf{P}^r)$ denotes the back electric field defined as

$$\mathbf{E}^b(\mathbf{P}^r) := \frac{\partial H^{\text{rem}}(\mathbf{P}^r)}{\partial \mathbf{P}^r} = \frac{1}{c} \operatorname{arctanh}\left(\frac{\|\mathbf{P}^r\|}{P_{\text{sat}}}\right) \mathbf{a}. \quad (3.20)$$

In contrast to the macroscopic material model presented by Miehe and Rosato [110], wherein the driving force defining the macroscopic remnant polarisation evolution was approximated by $\mathbf{f}(\mathbf{P}^r) \approx \mathbf{E} - \mathbf{E}^b(\mathbf{P}^r)$, the presented numerical model is implemented by considering the full driving force expression (3.19).

With respect to kinetics, a suitable dissipation equation to capture the evolution of macroscopic remnant polarisation is formulated in terms of a convex and non-negative function. To this end, the rate-dependent form of the dissipation equation proposed by Miehe and Rosato [110] is considered. The scalar dissipation equation reads

$$\zeta(\dot{\mathbf{P}}^r) = \sup_{\mathbf{f}} \left\{ \mathbf{f}(\mathbf{P}^r) \cdot \dot{\mathbf{P}}^r - \frac{E^c}{\eta^p [m+1]} \left\langle \frac{\|\mathbf{f}(\mathbf{P}^r)\|}{E^c} - 1 \right\rangle^{m+1} \right\}, \quad (3.21)$$

wherein the Macaulay bracket, $\langle \bullet \rangle = \max\{\bullet, 0\}$, is used. The model parameters $\eta^p > 0$ and $m > 0$ influence the rate-dependent evolution of macroscopic remnant polarisation. Solving the necessary condition (3.21) particularises the rate-type evolution equation as

$$\dot{\mathbf{P}}^r = \frac{1}{\eta^p} \left\langle \frac{\|\mathbf{f}(\mathbf{P}^r)\|}{E^c} - 1 \right\rangle^m \frac{\mathbf{f}(\mathbf{P}^r)}{\|\mathbf{f}(\mathbf{P}^r)\|}. \quad (3.22)$$

Once the norm of driving force exceeds the coercive electric field E^c , the macroscopic remnant polarisation evolves along the direction of the driving force. The necessary relations for both the rate-dependent and rate-independent forms of the dissipation

equation are discussed in detail by Miehe and Rosato [110]. For the partial derivations of the quantities used in the phenomenological model formulation, the reader is referred to Appendix A.

3.3 Algorithmic treatment of the evolution equation

The rate-dependent equation defining the remnant polarisation evolution (3.22) is highly non-linear. To this end, we consider a straightforward discretisation of the evolution equation (3.22) within the finite time interval $[t_n, t_{n+1}]$. Let the time increment or the step size be defined as $\Delta t_{n+1} := t_{n+1} - t_n > 0$. Within this finite time increment, the rate of macroscopic polarisation is considered to be constant so that approximation

$$\dot{\mathbf{P}}^r_{n+1} \approx \frac{\mathbf{P}^r(t_{n+1}) - \mathbf{P}^r(t_n)}{\Delta t} = \frac{\mathbf{P}^r_{n+1} - \mathbf{P}^r_n}{\Delta t}, \quad (3.23)$$

holds. Henceforth, we denote the quantities evaluated at time t_{n+1} without subscript for the sake of brevity. The macroscopic remnant polarisation \mathbf{P}^r_n at time t_n is assumed to be known. Following the implicit Euler integration method, the current value of macroscopic polarisation \mathbf{P}^r at time t_{n+1} is obtained as

$$\mathbf{P}^r = \mathbf{P}^r_n + \Delta t \dot{\mathbf{P}}^r. \quad (3.24)$$

The solution of Equation (3.24) is determined by iteratively solving the residual

$$\mathbf{R}(\mathbf{P}^r) = \mathbf{P}^r - \mathbf{P}^r_n - \frac{\Delta t}{\eta^p} \left\langle \frac{\|\mathbf{f}(\mathbf{P}^r)\|}{E^c} - 1 \right\rangle^m \frac{\mathbf{f}(\mathbf{P}^r)}{\|\mathbf{f}(\mathbf{P}^r)\|} = \mathbf{0}, \quad (3.25)$$

by means of a suitable scheme such as the Newton–Raphson method. The residual vector is solved in each time increment for \mathbf{P}^r . The particular form of Newton-type update

$$\mathbf{P}^r|_{k+1} = \mathbf{P}^r|_k - \mathbf{J}^{-1}|_k \cdot \mathbf{R}(\mathbf{P}^r)|_k, \quad (3.26)$$

is fulfilled until $\|\mathbf{R}(\mathbf{P}^r)\| < \text{tol}$, wherein k denotes the iteration counter. The tangent matrix \mathbf{J} , related to the residual function (3.25) used in the update relation (3.26), is derived as

$$\begin{aligned} \mathbf{J} := \frac{d\mathbf{R}(\mathbf{P}^r)}{d\mathbf{P}^r} &= \mathbf{I} - \frac{m \Delta t}{\eta^p E^c} \left\langle \frac{\|\mathbf{f}(\mathbf{P}^r)\|}{E^c} - 1 \right\rangle^{m-1} \frac{\mathbf{f}(\mathbf{P}^r)}{\|\mathbf{f}(\mathbf{P}^r)\|} \frac{\partial \|\mathbf{f}(\mathbf{P}^r)\|}{\partial \mathbf{P}^r} \\ &\quad - \frac{\Delta t}{\eta^p} \left\langle \frac{\|\mathbf{f}(\mathbf{P}^r)\|}{E^c} - 1 \right\rangle^m \frac{\partial}{\partial \mathbf{P}^r} \left[\frac{\mathbf{f}(\mathbf{P}^r)}{\|\mathbf{f}(\mathbf{P}^r)\|} \right]. \end{aligned} \quad (3.27)$$

Table 3.1: Single crystal tetragonal BaTiO₃ material parameters used for the numerical computations with the phenomenological model. The material parameters are taken from [152] with the elasticity and dielectric constants fitted by means of a least-squares method, cf. [125].

| Denomination | Parameter | Value | Unit | Reference |
|------------------------------------|-------------------------|-------------------------|--------------------|-----------|
| Elastic stiffness | E_{1111} | 213.303×10^3 | MPa | – |
| Elastic stiffness | E_{1122} | 102.515×10^3 | MPa | – |
| Lateral piezoelectric coefficient | e_{311} | – 0.7 | C/m ² | [152] |
| Axial piezoelectric coefficient | e_{333} | 6.7 | C/m ² | [152] |
| Piezoelectric shearing coefficient | e_{131} | 34.2 | C/m ² | [152] |
| Vacuum permittivity | ϵ_0 | 8.854×10^{-12} | F/m | [152] |
| Dielectric permittivity | ϵ_{11} | $1485.33 \epsilon_0$ | F/m | – |
| Saturation polarisation | P^{sat} | 0.26 | C/m ² | – |
| Saturation strain | ϵ^{sat} | 0.001 | – | – |
| Coercive electric field | E^c | 1.0 | kV/mm | – |
| Viscosity-type parameter | η^p | 0.1 | m ² /Cs | – |

3.4 Numerical examples

In this section, numerical capabilities of the derived phenomenological model are shown with the help of representative examples. The butterfly and dielectric hysteresis loops for single crystal tetragonal BaTiO₃ are reproduced by tests under homogeneous states of deformation. These tests are performed on a three-dimensional specimen subjected to a cyclic electrical load at varying loading frequencies. Inhomogeneous boundary value problems are solved with respect to a plate with centred hole example. The strain and dielectric displacement distributions in the inhomogeneous specimen are studied for cyclic electrical loading.

The single crystal BaTiO₃ material constants such as elastic stiffness, piezoelectric and dielectric tensor components are taken from Zgonik et al. [152]. The elasticity and dielectric permittivity constants reported in [152] are fitted, respectively, to obtain isotropic elastic and dielectric permittivity constants by means of a least-squares method, cf. Schröder and Keip [125]. The parameter fitting procedure is briefly explained in Appendix A. The fitted elastic and dielectric constants along with the piezoelectric and other parameters needed for the computations are listed in Table 3.1.

3.4.1 Tests under homogeneous states of deformation

The schematic sketch of the three-dimensional specimen of interest along with the loading curve and boundary conditions is depicted in Figure 3.1. The crystallographic axes of

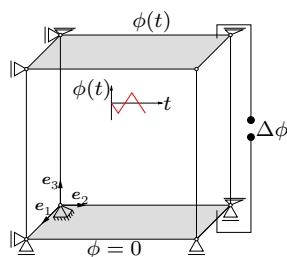


Figure 3.1: Schematic representation of the three-dimensional specimen along with load curve and boundary conditions considered for the tests under homogeneous states of deformation.

this initially unpoled specimen are assumed to coincide with the reference Cartesian axes $\mathbf{e}_{1,2,3}$. Cyclic electrical loading is applied along the \mathbf{e}_3 -axis. The potential difference across the specimen is generated by keeping the lower electrode grounded at all times, while its upper counterpart is surcharged with an alternating scalar electric potential $\phi(t)$ with $\phi^{\max} = \pm 10$ kV. Due to the applied cyclic loading and due to the prescribed displacement boundary conditions, the specimen under study elongates and contracts along the \mathbf{e}_3 -axis while experiencing corresponding contraction and elongation along both the \mathbf{e}_1 and \mathbf{e}_2 -axes. The strains and dielectric displacements resulting from this rate-dependent and non-linear deformation are computed iteratively. By plotting the obtained total strains against the applied electric field we arrive at the strain hysteretic response. Analogously, the dielectric hysteresis loop is obtained by plotting the resulting D_3 values against E_3 .

With the above described test set-up, a first set of computations is carried out by surcharging the specimen with an alternating electrical load at 0.05 Hz. The hysteretic responses of the specimen are plotted in Figure 3.2 for parameters $c = 3.0$ and $m = 2.0$. The initial unpoled configuration of the specimen is reflected with zero values of strain and dielectric displacement along the loading direction. Figure 3.2 shows the total strain and dielectric displacement values $\{\varepsilon_{33}, D_3\}|_{t_0} = 0$ at electric field $E_3|_{t_0} = 0$ kV/mm. Starting from this point, the potential difference across the specimen is decreased in steps of Δt . This is continued until the induced electric field reaches the coercive field $E^c = 1$ kV/mm. During this loading phase the specimen of interest does not undergo any deformation in shape. This can be verified by the butterfly curves in Figure 3.2, wherein for electrical loading $E_3 < E^c$ we obtain a total strain $\varepsilon_{33} = 0$. However, this initial loading results in a linear increase of dielectric displacement along the loading direction with respect to the applied electric field, see Figure 3.2. The linear relation $D_3 = \epsilon_{11} E_3$ holds for $E_3 < E^c$. Moreover, both the macroscopic remnant strain and polarisation do not evolve from their zero values, i.e. $\{\varepsilon_{33}^r, P_3^r\} = 0$, until the applied field reaches the coercive limit, see Figure 3.3. This is a further indication that no ferroelectric domain switching has occurred in the specimen during the loading phase $E_3 < E^c$.

Once the specimen is loaded beyond the coercive limit, domain switching is initiated followed by non-linear evolution of macroscopic polarisation. The remnant polarisation P_3^r evolves until it asymptotically approaches the saturation polarisation value P_3^{sat} . The

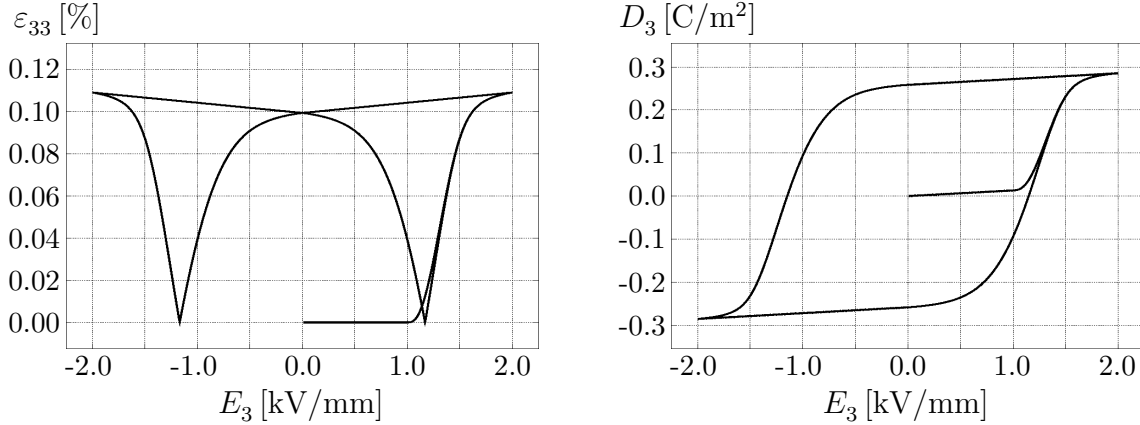


Figure 3.2: Hysteresis curves simulated with the phenomenological model under homogeneous states of deformation for $c = 3.0$, $m = 2.0$. Butterfly curve (left) and dielectric hysteresis loop (right) obtained for a single crystal BaTiO_3 specimen subjected to a cyclic electrical loading at 0.05 Hz.

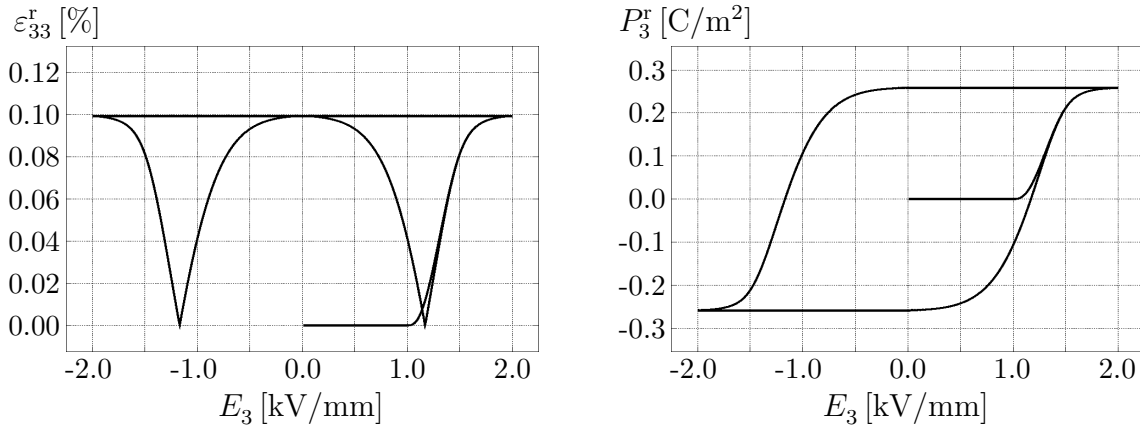


Figure 3.3: Macroscopic remnant strain response (left) and macroscopic remnant polarisation response (right) corresponding to the butterfly and dielectric hysteresis curves plotted in Figure 3.2.

evolution of macroscopic polarisation is accompanied by a non-linear elongation along the positive \mathbf{e}_3 -direction. The non-linear increase of the total strain ε_{33} can be observed in the strain hysteresis loop in Figure 3.2. With respect to dielectric hysteresis, the non-linear increase of D_3 beyond the coercive limit is also directly related to the evolution of macroscopic polarisation. One can observe the non-linear increase and subsequent saturation of D_3 , around $E_3 = 2$ kV/mm, in Figure 3.2. The specimen is now poled along the positive \mathbf{e}_3 -axis at this maximum loading point.

As the electric load is reduced from this point, the specimen contracts linearly along the \mathbf{e}_3 -axis and reaches a remnant state at $E_3 = 0$ kV/mm. This state is characterised by an irreversible remnant strain and a non-vanishing macroscopic remnant polarisation in the specimen, see Figures 3.2 and 3.3. The macroscopic remnant polarisation along the loading direction attained with the removal of electrical load is equal to saturation value P^{sat} . Analogously the macroscopic remnant strain ε_{33}^r equals the saturation value

of strain ε^{sat} . The relations $D_3 = P_3^r = P^{\text{sat}}$ and $\varepsilon_{33} = \varepsilon_{33}^r = \varepsilon^{\text{sat}}$ hold at remnant state for the considered perfect crystal specimen. Due to the unchanged P_3^r value during this unloading phase to zero electric field, the poled configuration of the specimen along the positive \mathbf{e}_3 -axis is still preserved in the remnant state.

Next, the specimen is loaded beyond the coercive limit in the negative regime. During this phase, the remnant polarisation P_3^r first decreases in magnitude and then switches by 180° . After its reversal, P_3^r evolves non-linearly along the negative \mathbf{e}_3 -direction. The evolution of polarisation continues until it asymptotically saturates around point $E_3 = -2 \text{ kV/mm}$, see Figure 3.3. Due to 180° macroscopic polarisation switching, the specimen is now poled along the negative \mathbf{e}_3 -axis. In view of deformation, the specimen initially contracts non-linearly as the electric field decreases in the negative direction. Once the coercive limit is exceeded, the specimen elongates along the positive \mathbf{e}_3 -direction. Note, that the resulting ε_{33} values at $E_3 = \pm 2 \text{ kV/mm}$ are identical even though the specimen under study is poled in opposite directions. This is due to the total strains being symmetric.

Subsequent increase in electrical loading to 2 kV/mm re-orientates the domains and macroscopic polarisation back along the positive \mathbf{e}_3 -axis. Consequently, the specimen is now re-poled along the loading direction. The remnant state is recovered once the electric field is completely reduced to zero. The characteristic butterfly and dielectric hysteresis loops are thus numerically reproduced. The influence of the viscous-like parameter and the dependence of loading frequency on the hysteretic response are studied in the following computations.

After setting slope parameter c to a constant value, the tests under homogeneous states of deformation are performed for two different positive values of the viscous-like parameter. The influence of this viscous-like model parameter m on the polarisation evolution can be observed in both the strain and dielectric hysteresis curves. With an electrical loading rate of 0.2 Hz and with slope parameter $c = 1.0$, the butterfly curves and dielectric hysteresis for two different values of m are shown in Figure 3.4. As the applied electric field exceeds the coercive limit, the evolution of macroscopic remnant polarisation differs for $m = 2.0$ and $m = 3.0$. This leads to a difference in shape of both the butterfly and dielectric hysteresis loops, see Figure 3.4. In view of the butterfly curves, the value of strain ε_{33} obtained at remnant state is of lower magnitude with $m = 3.0$ compared to the remnant strain value obtained for $m = 2.0$. Similarly, the values of total strain ε_{33} at $E_3 = \pm 2 \text{ kV/mm}$ are lower for $m = 3.0$ in comparison to the values obtained for $m = 2.0$. With respect to dielectric hysteresis, in addition to the decrease in absolute value of dielectric displacement $|D_3|$ at both remnant and poled states, the dielectric hysteresis curves widens for $m = 3.0$.

In order to study the rate-dependent behaviour, the last set of computations under homogeneous states of deformation are performed under varying electrical loading rates. By setting $c = 1.0$ and $m = 2.0$, the specimen is electrically loaded with three different frequencies of 1 Hz , 0.1 Hz and 0.01 Hz . The resulting butterfly and dielectric displacement hysteresis curves are plotted in Figure 3.5. From the butterfly curves, one observes

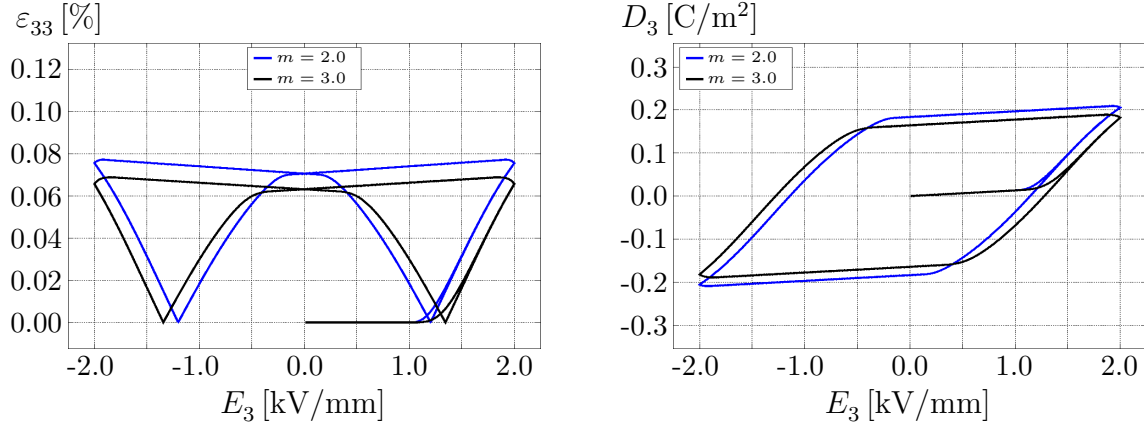


Figure 3.4: Influence of viscous-like parameter m on the hysteresis curves simulated with the phenomenological model for slope parameter $c = 1.0$. Butterfly curves (left) and dielectric hysteresis loops (right) obtained for a single crystal BaTiO_3 specimen subjected to a cyclic electrical loading at 0.2 Hz.

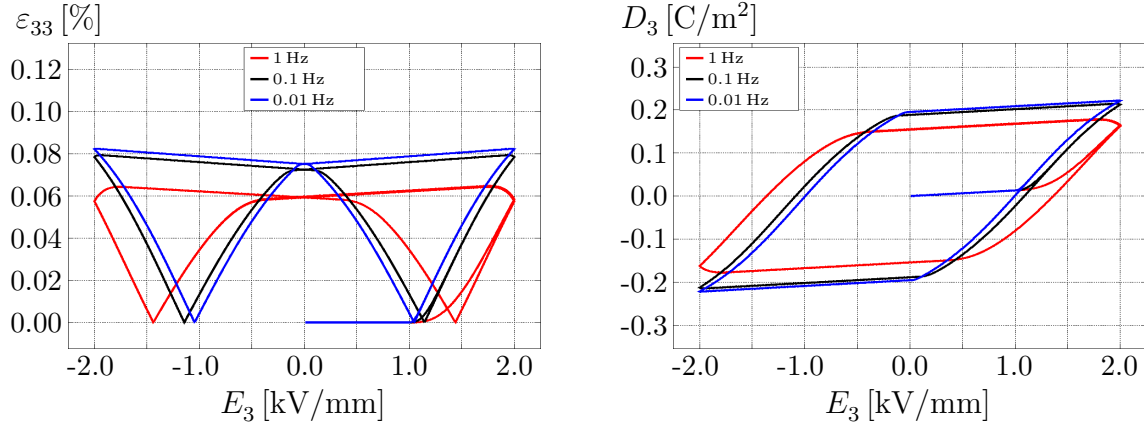


Figure 3.5: Rate-dependent hysteresis curves simulated with the phenomenological model for $c = 1.0$, $m = 2.0$. Butterfly curves (left) and dielectric hysteresis loops (right) obtained for a single crystal BaTiO_3 specimen subjected to a cyclic electrical loading at varying frequencies.

that the magnitude of ε_{33} at the remnant state reduces with increasing electrical loading rates. Furthermore, the shape of the butterfly curves computed at 1 Hz around $E_3 = \pm 2 \text{ kV/mm}$ differs from the responses obtained at lower frequency levels. The total strain does not saturate around these maximum loading points when loaded at higher frequencies of 1 Hz. This may be due to the incomplete switching of the domains which is typical for ferroelectric materials at higher rates of loading. With respect to dielectric hysteresis, the curves widen with increasing loading rates. The absolute value of dielectric displacement $|D_3|$ obtained at the remnant state decreases as the specimen is loaded at higher frequencies. Similar to the strain response, the dielectric displacement D_3 does not saturate around point $E_3 = \pm 2 \text{ kV/mm}$ at higher frequencies compared to the related values obtained at lower rates of loading.

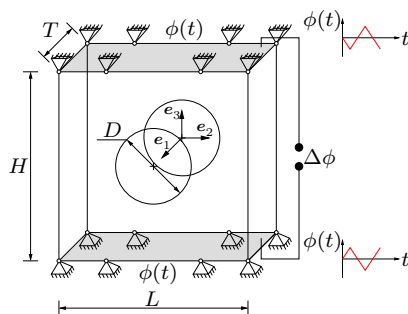


Figure 3.6: Schematic representation of a three-dimensional plate with a centred hole specimen along with the loading curves and boundary conditions subjected to a cyclic electrical load. The two loading curves refers, respectively, to the time-dependent electric potential applied at the top and bottom electrodes of the specimen.

3.4.2 Test under inhomogeneous states of deformation

In this subsection, the versatility of the phenomenological model is demonstrated by solving an inhomogeneous boundary value problem. The specimen of interest is a three-dimensional plate of planar dimensions $L \times H = 10 \text{ mm} \times 10 \text{ mm}$ and with a thickness $T = 1 \text{ mm}$. The plate has a centred hole of diameter $D = 3 \text{ mm}$. Both the top and bottom surfaces of the plate are prescribed with zero values of displacements along all the three Cartesian directions. The specimen is surcharged with alternating electric potential with $\phi^{\max} = \pm 10 \text{ kV}$ at both the top and bottom surfaces. The schematic sketch of the specimen along with boundary and loading conditions are depicted in Figure 3.6. The plate is discretised by 800 tri-linear brick elements. Both the resulting strain and dielectric displacement distribution in the specimen are studied for specific model parameters at different time intervals.

The considered inhomogeneous capacitor is subjected to an alternating electric field at 0.2 Hz. The viscosity and slope parameters for this test are set to $m = 2.0$ and $c = 3.0$, respectively. For the defined boundary and loading conditions, the total strains and the dielectric displacements are computed iteratively. Figure 3.7 shows the distribution of the electric potential, total strain and dielectric displacement at different time intervals along the loading direction across the specimen.

Starting from a virgin unpoled configuration, the electric potential is incrementally applied in steps of Δt . Domain switching and subsequent evolution of macroscopic polarisation along the loading direction is initiated once the applied electric field exceeds the coercive limit. Due to the inhomogeneity of the problem under study, the evolution of macroscopic polarisation in the specimen is not uniform. At $t = 1.25 \text{ sec}$, the potential difference across the specimen reaches its negative maximum value of $\Delta\phi = -20 \text{ kV}$. The generated field aligns the macroscopic polarisation and the specimen attains a poled configuration along the positive e_3 -direction at this point of maximum loading. Due to the imposed zero displacements at both the top and bottom surfaces, the deformation obtained across the specimen is highly non-uniform. This can be observed in Figure 3.7

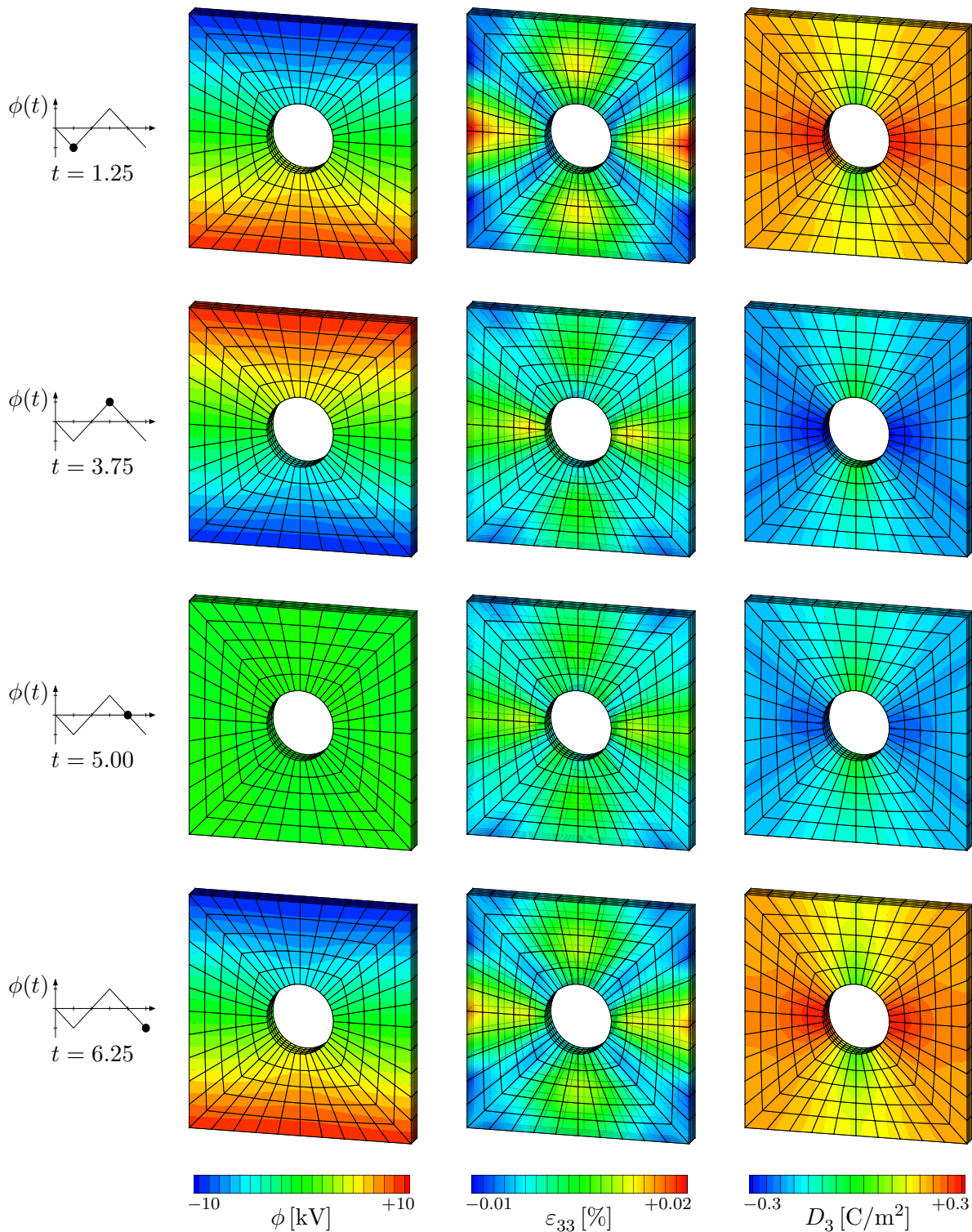


Figure 3.7: Contour plots of the scalar electric potential ϕ , total strain ε_{33} and dielectric displacement D_3 at different time intervals simulated with the phenomenological model. The load curve on the left-most side depicts the time-dependent electric potential loading at the top electrode.

with respect to the contour plot of the total strain ε_{33} at $t = 1.25$ sec. From this negative maximum loading point, the electrical load is decreased to zero and further loaded along the negative \mathbf{e}_3 -direction until $\Delta\phi = 20$ kV at $t = 3.75$ sec. The load reversal switches the macroscopic polarisation by 180° and the specimen attains a new poled configuration along the negative \mathbf{e}_3 -direction at this point. The remnant state is recovered at $t = 5$ sec when the specimen is electrically unloaded. As expected, the poled configuration along the negative \mathbf{e}_3 -direction is retained in this remnant state. Subsequent increase in loading until it reaches $\Delta\phi = -20$ kV at $t = 6.25$ sec re-orientes the specimen back along the positive \mathbf{e}_3 -direction. However, it can be observed that the distribution of both the total strain and dielectric displacement is slightly different for the poled states at $t = 1.25$ and 6.25 secs. This explains that the behaviour of ferroelectric material is different when loaded from an unpoled configuration compared to the re-poling of a specimen from its remnant state.

4 Laminate-based modelling of single crystalline ferroelectric materials

The present chapter deals with the development of laminate-based models to study the rate and external stress-dependent domain evolution, and hence the macroscopic hysteretic response, in single crystal tetragonal ferroelectric materials. Laminate-based models are micromechanically motivated and consider the volume fraction of the distinct ferroelectric variants or states directly in their formulation. These constitutive models are based on a mixture theory ansatz and aim to study the domain patterns, and their evolution, within the ferroelectric single crystal under external electrical and mechanical loading. By considering different mixture formulations and averaging principles, four laminate-based models are postulated in this chapter. The formulations are developed considering the average strain and polarisation compatibility conditions, as introduced for ferroelectric materials by Shu and Bhattacharya [134]. The four individual laminate models are verified by means of representative boundary value solutions under various loading scenarios. The individual formulations as well as the general algorithmic scheme considered to solve the evolution equations are largely based on the works by Dusthakar et al. [41–44, 46].

The chapter is structured as follows. Section 4.1 provides a brief overview of the micromechanical models established for the modelling of the single and polycrystalline ferroelectric solids. A general laminate-based approach for the numerical modelling of single crystal tetragonal ferroelectric solids is presented in Section 4.2. In particular, the necessary equations needed for the development of the four individual laminate-based models are outlined. Section 4.3 elaborates on the general algorithmic formulation for solving the update of the rate-dependent evolution equations. The Fischer–Burmeister-type algorithm in combination with a Newton–Raphson scheme is adopted in order to solve the rate-dependent evolution equations so as to arrive at the update of the inequality constrained multi-rank laminate volume fractions.

Following the general framework and the algorithmic formulation, Sections 4.4 to 4.7 are devoted to the detailed description of the individual laminate-based material models. The four distinct models are denoted as laminate-based Models 1, 2, 3 and 4 respectively. Each of the laminate models formulates an average electric Gibbs energy to describe the dissipative ferroelectric material behaviour. The average energy is written as a

Table 4.1: A short summary of Sections 4.4 to 4.8.

| Section | Description |
|-------------|---|
| Section 4.4 | Laminate-based Model 1 <ul style="list-style-type: none"> – Average electric Gibbs energy of the crystal is formulated by considering only the polarisation compatibility condition. – Numerical examples include tests under both homogeneous and inhomogeneous states of deformation. – Comparison of laminate-based Model 1 and the phenomenological model is shown with respect to simulated butterfly and dielectric hysteresis curves. |
| Section 4.5 | Laminate-based Model 2 <ul style="list-style-type: none"> – Electric Gibbs energy is postulated for each of the ferroelectric variants and weighted by the volume fractions to obtain the average energy of the crystal. – Numerical examples under homogeneous states of deformation are presented. |
| Section 4.6 | Laminate-based Model 3 <ul style="list-style-type: none"> – Average electric Gibbs energy formulated for the crystal based on both the average remnant quantities and on the averaged material moduli. – Numerical examples under homogeneous states of deformation are provided. |
| Section 4.7 | Laminate-based Model 4 <ul style="list-style-type: none"> – Extension of the average electric Gibbs energy introduced in Model 3 by postulating an additional average remnant energy contribution. – Numerical tests under homogeneous states of deformation are discussed. |
| Section 4.8 | Comparison of laminate-based Models 2, 3 and 4 <ul style="list-style-type: none"> – Comparison of the specific laminate Models 2, 3 and 4 in context of numerical tests under homogeneous states of deformation. |

function of the total linear strain tensor, the electric field vector, and the scalar-valued laminate volume fractions, treated as internal state variables. The precise form of the electric Gibbs energy for the individual laminate-based models is constructed based on the different mixture theory assumptions and averaging formulations. Table 4.1 provides a quick overview of Sections 4.4 to 4.8.

Section 4.4 focusses on the description of laminate-based Model 1. The particular form of the electric Gibbs energy and the explicit relations for the constitutive quantities and for the driving forces are introduced. Representative numerical examples based on tests under both homogeneous and inhomogeneous states of deformation are studied. Furthermore, a comparison of laminate-based Model 1 and the phenomenological model, established in Chapter 3, is provided. The comparison is accomplished in the context of numerical simulations under both homogeneous and inhomogeneous states of deformation. Section 4.5 is dedicated to laminate-based Model 2 formulation. With an electric Gibbs energy defined for each of the six tetragonal ferroelectric variants, the average

state of the crystal is obtained by weighting the individual energies over their respective variant volume fractions. Numerical simulations under homogeneous states of deformation considering electrical and combined electromechanical loading are presented. In Section 4.6, an alternate formulation for the overall electric Gibbs energy of the crystal is given, which forms the basis for laminate-based Model 3. The average electric Gibbs energy of the crystal is formulated based on the averaged remnant quantities and material moduli. Numerical examples based on tests under homogeneous states of deformation for three different loading scenarios are investigated. Section 4.7 outlines the average electric Gibbs energy along with the constitutive and the driving force relations corresponding to laminate-based Model 4. The average total electric Gibbs energy postulated for laminate-based Model 4 is decomposed into a piezoelectric and a saturation-type remnant energy part. Tests under homogeneous states of deformation are presented in order to demonstrate the versatility of the derived laminate-based Model 4.

Section 4.8 provides a comparison of laminate-based Models 2, 3 and 4 with respect to the simulated butterfly and dielectric hysteresis curves, obtained from the numerical tests under homogeneous states of deformation. The tests under homogeneous states of deformation are performed on a three-dimensional specimen under electrical, mechanical and under combined electromechanical loading scenarios. The comparison also highlights the difference in the hysteresis curves obtained with two different values of the viscosity-type parameter.

4.1 Overview of micromechanical models

This section provides an overview in the form of a literature survey of the existing micromechanical material models for ferroelectric solids. Micromechanical models are reliable means of studying the microscopic domain evolution and the polarisation switching giving rise to the macroscopic hysteretic behaviour in ferroelectric materials. A detailed review of the micromechanical modelling practices devised for the study of the overall ferroelectric material response is provided by Kamlah [71], Landis [89] and Huber [54].

The underlying micromechanical model formulations are classified into two categories. On the one hand, suitable energy arguments are postulated as switching criteria in order to determine the response of the individual single crystal unit cells. Considering appropriate homogenisation procedures, the individual response of the randomly oriented unit cells are averaged to obtain the macroscopic response of the overall ferroelectric ceramic. Alternate formulations are based on treating the volume fractions of the distinct variants of the individual single crystal unit cells as internal state variables in the constitutive model framework. The evolution of these volume fractions under applied external loads influences the domain switching, and hence the overall remnant strain and polarisation changes or evolves in the crystal.

Hwang et al. [63] proposed a hysteresis model for ferroelectric ceramics by postulating a switching criterion based on a combined mechanical and electrical energy argument. They assumed each grain in the ferroelectric ceramic as a single domain, characterised by values of both the spontaneous strain and polarisation. The spontaneous polarisation switching of an individual grain along the direction of the applied load was assumed to occur once the sum of the electrical and mechanical works exceeded a critical value. The work per unit volume in switching between any two polarisation states was considered as the critical value in their switching criterion. Averaging the obtained response of the randomly oriented individual grains, and along with the linear constitutive relations, the overall material behaviour of the ceramic was computed. Their averaging procedure neglected the interactions between the neighbouring grains and assumed a Reuss type approximation, wherein both the applied stress and electric field are uniform throughout the ceramic.

McMeeking and Hwang [105] developed a formulation by considering a piezoelectric inclusion in an isotropic matrix. The inclusion and the matrix were assumed to possess the same elastic and dielectric moduli. The potential energy of the inclusion, derived following the standard Eshelby method, was considered in the switching criterion to compute the increments of remnant polarisation and strain under applied electrical and mechanical loads. Following [105], Hwang et al. [64] simulated the response of a spherical piezoelectric inclusion in an infinite homogeneous matrix. Hwang and McMeeking [61] implemented the microscopic material model developed in [63] within a finite element framework. They studied the polarisation switching of the ferroelectric ceramic subject to pure electrical loading. For the simulations, each finite element was assumed to be a single domain grain, and 1000 such elements of random orientation were considered. The homogenised remnant polarisation of the ceramic was computed by averaging the response of the individual finite elements. They reproduced the macroscopic dielectric hysteresis to fit the experimental loop for a PLZT ceramic. In an analogous formulation, Hwang and McMeeking [62] considered only the stress-based switching criterion of [63] to reproduce the ferroelastic hysteresis loop by implementing the model within a finite element framework.

Chen and Lynch [32] developed a micromechanical model for ferroelectric ceramics based on a single crystal constitutive model formulation. Their framework included a modified ferroelectric/ferroelastic switching criterion in order to take the strain and polarisation discontinuities between two neighbouring single crystal grains into account. Their modified switching law was motivated from the assumptions considered in [105]. Defining random orientations for the individual grains, the macroscopic response of the polycrystalline ferroelectric was simulated and subsequently fitted to the experimental tetragonal and rhombohedral PLZT curves.

Arockiarajan et al. [4, 37] developed a three-dimensional micromechanical model for a ferroelectric ceramic. Based on the criterion for electric field switching, postulated in [63], their model investigated the rate-dependent polarisation switching behaviour in polycrystalline ferroelectric solids. A probability function was postulated to capture

the interactions between the adjacent grains. They computed the dielectric hysteresis curves at various electrical loading frequencies using the finite element method. Later, Arockiarajan et al. [5] extended the formulations [4, 37] by incorporating the combined electromechanical switching criterion postulated in [63]. In doing so, both the dielectric and strain hysteresis curves for a soft PZT ceramic under varying electrical loading amplitudes and frequencies were simulated, see [5]. In their subsequent work [6], the influence of an axial compressive stress applied along the direction of the external electrical field was presented with the help of finite element method. Further studies by Arockiarajan et al. [3, 7] aimed at incorporating the interaction between the neighbouring ferroelectric grains in their micromechanical model formulations. In [3], a Weibull-type probability function was adopted to handle the inter-granular effects. However, a gradient term at the boundary of the switching domain was considered in [7] to avoid the sharp change in the Gibbs energy between any two neighbouring grains.

Keip and Schröder [78] postulated a tetragonal model based on the microscopic energy switching criterion to study the single crystal ferroelectric material behaviour. Their model incorporated the underlying tetragonal structure of the ferroelectric unit cell by defining three perpendicular crystallographic axes, out of which one represented the normalised preferred direction. Suitable structural tensors were introduced to define the mechanical, piezoelectric and dielectric invariants. The electric enthalpy, governing the thermodynamic process, was written as an additive function of the introduced basic and mixed invariants. The microscopic ferroelectric switching criterion postulated in their model considered the difference of only the electrical energy causing the domain switching within a tetragonal unit cell. With the formulated energy enthalpy and switching criterion, strain and dielectric hystereses were presented for an ferroelectric single crystal specimen under homogeneous electrical loading conditions. An extension of the model to incorporate a unified ferroelectric and ferroelastic switching criterion was carried out in the subsequent works by Keip and Schröder [79, 80]. The microscopic switching criteria used in the three contributions [78–80] were comparable to those proposed in [63]. In the doctoral dissertation by Keip [77], the tetragonal model [79] was combined with a homogenisation procedure to simulate the macroscopic ferroelectric and ferroelastic hysteretic behaviour of a BaTiO_3 ceramic. Considering random orientations of the unit cells, the homogenised material moduli and constitutive quantities of the underlying ceramic were computed for both cyclic electrical and mechanical loading conditions.

Shilo et al. [133] proposed a model to capture the response of single crystal BaTiO_3 under combined electromechanical loading. The work was motivated from the measured data on BaTiO_3 reported in [21, 22]. Their one-dimensional model explicitly defined a Gibbs energy per unit volume for each of the in- and out-of-plane directions of the applied load. The total driving force defining the domain evolution was additively decomposed into two parts. One part of the driving force was due to the difference in the Gibbs energies obtained when switching from one state to another. The other part took the friction between the specimen and the loading fixture into account and was defined in terms of the frictional coefficient and of the specimen's geometry. The simulated

butterfly curves showed in [133] predicted an increase in the actuation strain response of the single crystal BaTiO_3 with decreasing values of the frictional coefficient.

A very recent contribution on formulating a switching criterion for single crystal tetragonal BaTiO_3 was presented by Li and Li [95]. Based on the energy-based switching criterion of [63], Li and Li [95] formulated an incremental criterion for 90° domain switching by considering the additional hardening effects. Their incremental switching criterion was motivated from the experimental findings reported in their previous works, on the hardening effects and on the large strain actuation observed in ferroelectric single crystals, see [93, 94]. Furthermore, the simulated ferroelectric and ferroelastic hystereses were compared to their experimental data, see [95].

In contrast to the above mentioned energy-based formulations for defining discrete switching criteria, a number of micromechanically motivated models were developed by taking the volume fraction of the distinct ferroelectric variants into account. The formulations by Huo and Jiang [59, 60] were based on the mixture theory to study the hysteretic behaviour of ferroelectric ceramics. Each grain in the polycrystal was assumed as a mixture of the distinct variants, characterised by their volume fractions. The average polarisation of an individual grain was assumed to be a linear function of the considered volume fractions. Under external loading, the change in volume fraction values of the corresponding domains was directly related to the domain switching in the grain. By considering interaction between the grains, the macroscopic dielectric hysteresis curves for a ceramic were reproduced. Kamlah and Jiang [73] presented a rate-dependent constitutive model by treating the volume fraction of the ferroelectric variants as internal state variables. Satisfying the Clausius–Duhem inequality, the driving forces were derived from the postulated Gibbs energy. Their generalised model was implemented to reproduce the rate-dependent hysteresis curves under uni-axial loading.

A micromechanical model based on the volume fraction concept was developed by Lu et al. [99] to investigate both the ferroelectric and ferroelastic hysteretic behaviour. Their work included the measured hysteresis curves of a soft PZT ceramic under electrical and mechanical loading scenarios. The theoretical framework considered the polycrystalline ferroelectric to be composed of multiple single crystal grains. An orientation distribution function was postulated to incorporate the random grain direction. Each single crystal tetragonal grain was modelled by postulating specific Gibbs energy for each variant state. The driving force responsible for the switching of domains was computed as the difference in the Gibbs energy between any two domain states. With the computed response of the individual crystals, the macroscopic behaviour of the ceramic was obtained by performing a Reuss approximation.

A constitutive model for polycrystalline ferroelectric was developed by Huber et al. [57]. Unlike the assumption of an instantaneous switching between the distinct variant states, their model incorporated the progressive polarisation switching and domain evolution. The progressive polarisation switching inside the individual grains was formulated analogously to the crystal plasticity approach. Considering the distinct variants in a tetragonal grain to be associated with their corresponding volume fractions, the

incremental transformation from one variant to another under external loading was defined similar to the incremental slip in crystal plasticity theory. The thermodynamic driving force determined the amount of energy dissipated in the transformation from one variant to another. Following a self-consistent scheme, the individual single crystal responses were used to compute the overall macroscopic properties of the ferroelectric ceramic. Based on the self-consistent estimates of the incremental response, representative numerical examples depicting the ferroelectric and ferroelastic hysteresis curves were presented. Huber and Fleck [55] discussed three material models to study the polarisation rotation evident in polycrystalline ferroelectric ceramics. Apart from their previous self-consistent model [57], both a simplified rate-dependent crystal plasticity model and a rate-independent phenomenological model were formulated in [55]. The change in dielectric displacement with respect to the applied electric field was computed for all the three models and compared with the experimental data of a PZT-5H ceramic. In their subsequent work, Huber and Fleck [56] calibrated and studied the influence of model parameters used in the self-consistent approach [57].

Kamlah et al. [75] implemented the micromechanical model developed in [57] within a finite element environment to obtain the macroscopic ferroelectric hysteresis curves. The model implementation was performed in the finite element framework proposed by Landis [87], wherein the dielectric displacement vector was treated as the primary field variable instead of the standard scalar electric potential. Contribution [75] presented the strain and dielectric hysteresis curves, as well as the volume fraction evolution of a ferroelectric single crystal grain. The obtained individual grain responses were embedded in the finite element framework of [87] by applying an orientation distribution to the crystallographic axes of the individual grains. Assuming plane-strain conditions, both strain and dielectric response of a bulk ferroelectric ceramic were numerically computed.

Kim and Seelecke [83] came up with a micromechanical model to study the behaviour of single crystal BaTiO_3 under combined electromechanical loading. Their three-dimensional model was based on the framework presented in [129, 138]. In their model, each of the six distinct tetragonal ferroelectric variants was associated with a volume fraction and with a specific Gibbs energy. The change in Gibbs energy between any two variants due to the applied external load defined the driving force associated with the domain evolution. Considering a probability factor, the evolution equations for the six volume fractions were formulated based on the computed changes in Gibbs energies. Numerical examples under homogeneous states of deformation were presented and compared with the experimental data provided in [21]. Their model reproduced both the rate-dependent and external stress-dependent response of the BaTiO_3 crystal.

Menzel et al. [107] proposed two micromechanical formulations in order to study the rate-dependent ferroelastic switching under mechanical loading. The first model was formulated by considering the volume fractions of the individual unit cells. By assigning a limit-time scalar parameter, the number of unit cells switched under external compressive loads was determined. The second model was based on a reorientation approach, whereby the introduced orientation tensor is dependent on the limit-time parameter.

Both the models were based on a Gibbs energy written as a function of the stress, electric field, and of a structural vector. The numerical ferroelastic hysteresis curves were compared to the experimental data provided in [99].

Laminate-based models are of particular interest among the micromechanically motivated formulations taking the distinct laminate volume fractions into account. The framework is based on a mixture theory ansatz and aims to study the domain patterns, and their evolution, under external electrical and mechanical loading. A review of the laminate-based methods to predict the evolving microstructures in general phase transforming materials is given by Li et al. [92]. With respect to ferroelectric materials, Shu and Bhattacharya [134] presented a theoretical work on the different types of domain patterns and explained the high actuation strain response of single crystal BaTiO_3 under combined electromechanical loading. Their study was based on the energy minimisation principles derived in [9, 18, 39] for phase transforming solids. In [134], the total energy of the ferroelectric crystal was constructed as an additive function of the Helmholtz energy, the domain wall energy, the free space energy, and of the energetic contribution due to the applied electrical and mechanical loads. The current state of a material point, namely the strain and polarisation, was obtained by minimising the total energy subject to the given loading conditions. Assuming an undistorted and a charge-free state at the domain interface, the formation of banded and crossed domain patterns as well as the magnitude of the actuation strains were derived for tetragonal, rhombohedral and orthorhombic ferroelectric phases. The theory presented in [134] formed the basis for the laminate-based models developed to predict the high magnitude of actuation strains obtained from single crystal ferroelectric solids. Subsequently, a concise theory on understanding the domain patterns of both the single and polycrystalline ferroelectrics was provided by Bhattacharya and Li [19].

Domain engineering and the construction of energy minimising multi-rank laminates for ferroelectric single crystals were introduced by Li and Liu [91, 97, 98]. Their works were largely based on the theoretical formulation of multi-rank laminates proposed in [18, 40]. Considering the average polarisation and strain compatibility conditions at the domain interfaces [134], Li and Liu [91] related the distinct tetragonal variant volume fractions to the multi-rank laminate volume fractions. The energy minimising domain configuration of a ferroelectric crystal was obtained with the help of these compatible laminate structures. Using the multi-rank construction, the effective properties of linear piezoelectric materials, such as tetragonal BaTiO_3 and rhombohedral PMN-PT, were computed and compared to the experimental values.

Yen et al. [135, 151] developed a two-dimensional laminate-based model, taking the effect of depolarisation into account, in order to explain the high actuation strain response of single crystal tetragonal BaTiO_3 under combined electromechanical loading. A rank-3 laminated domain structure was constructed in [135, 151], based on the multi-rank laminate domain pattern introduced in [91]. Both the average remnant polarisation and strains were postulated based on the multi-rank laminate volume fractions. The total energy of the crystal, formulated in [134], was taken as the reference and reduced to a

simplified form consisting of only the applied load terms and the depolarisation energy. The negative sensitivity of the simplified total energy with respect to the multi-rank laminate volume fractions defined the driving forces of the individual laminates. Suitable resistance forces, written in terms of the laminate volume fractions, were postulated such that the domain evolution was assumed to occur once the driving forces exceeded the resistance values. The influence of the depolarisation energy on the obtained strains was investigated and the computed ferroelectric butterfly curves were compared to their experimental data for different external compressive stress magnitudes. Shu et al. [136] extended the formulation [135] to study the domain patterns in rhombohedral single crystal ferroelectric materials by using a diffusive laminate-based formulation. In their formulations, the gradient of the laminate volume fractions was considered as an order parameter analogous to the gradient of polarisation postulated in the phase-field models, e.g. [122, 153, 154]. The total energy postulated in [136] was comprised of an additional domain wall and anisotropic energies. Under external electrical loads, the minimisation of the total energy lead to the herringbone-like domain structure.

Tsou and Huber [142, 143] postulated sequential laminate-based models considering exact compatibility between the distinct domain orientations. They studied the domain arrangements and, furthermore, investigated the poling behaviour of tetragonal and rhombohedral single crystal BaTiO_3 . Their formulations stood in contrast to the average jump conditions for polarisation and strain between the domain orientations proposed in [91, 131, 151]. In [143], a detailed summary of the domain patterns generated by considering both the average and exact compatibility conditions was provided. Furthermore, an algorithm was postulated in order to obtain the optimal domain configuration possessing the minimum energy during the poling process. Tsou et al. [144] extended the exact compatible domain patterns to arrive at the complete set of distinct domain combinations for tetragonal and rhombohedral systems with the help of a search algorithm. In doing so, they identified the particular set of domain configurations that formed exact compatible laminates. A variational model to study the domain evolution and the hysteretic response of a single crystal tetragonal BaTiO_3 was developed by Tsou et al. [145]. A Gibbs energy, consisting of the sum of potential and external loads, and a rate potential, consisting of a domain mobility function, was formulated in order to simulate the hysteresis curves and the shape of the domain patterns.

4.2 Rate-dependent laminate-based framework

Following the literature review of the micromechanically motivated models, we proceed to the general rate-dependent laminate-based model formulation for tetragonal single crystal ferroelectric solids. In particular, the important relations needed for developing the four distinct laminate-based models are outlined in this section.

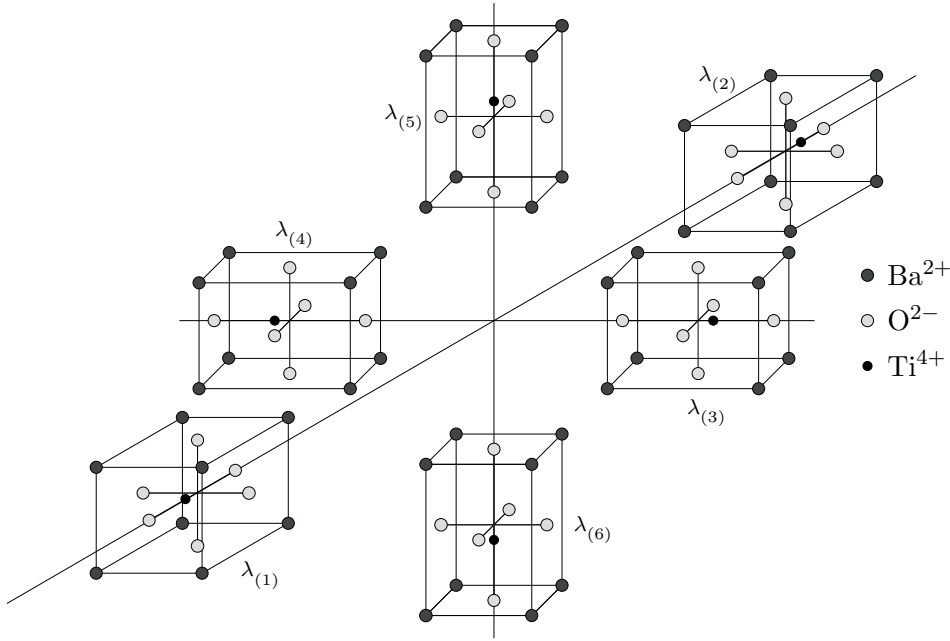


Figure 4.1: Schematic representation depicting the six equivalent orientation states, along with their respective variant volume fractions $\lambda_{(\alpha)}$, of a tetragonal BaTiO₃ unit cell below the Curie temperature.

4.2.1 Symmetry and material properties of ferroelectric variants

Considering BaTiO₃ at room temperature, the spontaneously polarised tetragonal unit cell exhibits six equally possible variants, see Figure 4.1 for a graphical representation. The individual variants are characterised by the spontaneous strain $\boldsymbol{\varepsilon}_{(\alpha)}$ and by the spontaneous polarisation $\mathbf{P}_{(\alpha)}$, wherein $\alpha \in \{1, \dots, nv = 6\}$. Depending on their specific crystallographic axis, the spontaneous quantities corresponding to the six tetragonal ferroelectric variants are represented by

$$\boldsymbol{\varepsilon}_{(1)} = \boldsymbol{\varepsilon}_{(2)} = [\eta_1^s - \eta_2^s] \mathbf{e}_1 \otimes \mathbf{e}_1 + \eta_2^s \mathbf{I}, \quad \mathbf{P}_{(1)} = -\mathbf{P}_{(2)} = P^s \mathbf{e}_1, \quad (4.1)$$

$$\boldsymbol{\varepsilon}_{(3)} = \boldsymbol{\varepsilon}_{(4)} = [\eta_1^s - \eta_2^s] \mathbf{e}_2 \otimes \mathbf{e}_2 + \eta_2^s \mathbf{I}, \quad \mathbf{P}_{(3)} = -\mathbf{P}_{(4)} = P^s \mathbf{e}_2, \quad (4.2)$$

$$\boldsymbol{\varepsilon}_{(5)} = \boldsymbol{\varepsilon}_{(6)} = [\eta_1^s - \eta_2^s] \mathbf{e}_3 \otimes \mathbf{e}_3 + \eta_2^s \mathbf{I}, \quad \mathbf{P}_{(5)} = -\mathbf{P}_{(6)} = P^s \mathbf{e}_3, \quad (4.3)$$

cf. [151]. Here, η_1^s and η_2^s are the measured spontaneous strain coefficients and P^s characterises the magnitude of the spontaneous polarisation, all referring to the BaTiO₃ crystal. The unit vectors $\mathbf{e}_{1,2,3}$ denote the crystallographic axes of the parent cubic unit cell.

With respect to the material properties, i.e. the characterisation of the individual variants, we assume the spontaneously polarised unit cell to be transversely-isotropic. Following this assumption, two structural quantities are introduced in order to charac-

terise the piezoelectric behaviour; one being the polarisation director or structural vector $\mathbf{a}_{(\alpha)}$ and the other, a second-order structural tensor $\mathbf{m}_{(\alpha)}$. For the particular variant α , the structural vector $\mathbf{a}_{(\alpha)}$ is defined as

$$\mathbf{a}_{(\alpha)} := \frac{\mathbf{P}_{(\alpha)}}{\|\mathbf{P}_{(\alpha)}\|} \quad \text{with} \quad \|\mathbf{a}_{(\alpha)}\| = 1, \quad (4.4)$$

and the second-order structural tensor $\mathbf{m}_{(\alpha)}$ is specified as

$$\mathbf{m}_{(\alpha)} := \mathbf{a}_{(\alpha)} \otimes \mathbf{a}_{(\alpha)} \quad \text{with} \quad \text{tr}(\mathbf{m}_{(\alpha)}) = 1. \quad (4.5)$$

The fourth-order elasticity tensor $\mathbf{E}_{(\alpha)}(\mathbf{a}_{(\alpha)})$, the third-order piezoelectric tensor $\mathbf{e}_{(\alpha)}(\mathbf{a}_{(\alpha)})$ and the second-order dielectric tensor $\boldsymbol{\epsilon}_{(\alpha)}(\mathbf{a}_{(\alpha)})$ defining the transverse isotropic material response of the individual ferroelectric variants are introduced based on the definition of the structural quantities in Equations (4.4) and (4.5). These transversely-isotropic material moduli for the individual variants read

$$\begin{aligned} \mathbf{E}_{(\alpha)}(\mathbf{a}_{(\alpha)}) &= \lambda^{\text{E}} \mathbf{I} \otimes \mathbf{I} + 2\mu^{\text{E}} \mathbf{I}^{\text{sym}} + \alpha_1^{\text{E}} [\mathbf{m}_{(\alpha)} \underline{\otimes} \mathbf{I} + \mathbf{I} \underline{\otimes} \mathbf{m}_{(\alpha)}] \\ &\quad + 2\alpha_2^{\text{E}} \mathbf{m}_{(\alpha)} \otimes \mathbf{m}_{(\alpha)} + \alpha_3^{\text{E}} [\mathbf{m}_{(\alpha)} \otimes \mathbf{I} + \mathbf{I} \otimes \mathbf{m}_{(\alpha)}], \end{aligned} \quad (4.6)$$

$$\begin{aligned} \mathbf{e}_{(\alpha)}(\mathbf{a}_{(\alpha)}) &= -\beta_1^{\text{e}} \mathbf{a}_{(\alpha)} \otimes \mathbf{I} - \beta_2^{\text{e}} \mathbf{m}_{(\alpha)} \otimes \mathbf{a}_{(\alpha)} \\ &\quad - \frac{\beta_3^{\text{e}}}{2} [\mathbf{I} \otimes \mathbf{a}_{(\alpha)} + \mathbf{I} \overline{\otimes} \mathbf{a}_{(\alpha)}] \quad \text{and} \end{aligned} \quad (4.7)$$

$$\boldsymbol{\epsilon}_{(\alpha)}(\mathbf{a}_{(\alpha)}) = -2\gamma_1^{\text{e}} \mathbf{I} - 2\gamma_2^{\text{e}} \mathbf{m}_{(\alpha)}, \quad (4.8)$$

cf. [125, 126]. In (4.6), λ^{E} , μ^{E} , α_1^{E} , α_2^{E} and α_3^{E} refer to the mechanical parameters. The piezoelectric coupling parameters in (4.7) are denoted by β_1^{e} , β_2^{e} and β_3^{e} . The dielectric parameters in (4.8) are represented by γ_1^{e} and γ_2^{e} . The relation between material parameters and coefficients of tensors when referring to an orthonormal base system, which includes the easy axis $\mathbf{a}_{(\alpha)}$, is given as

$$\begin{aligned} \lambda^{\text{E}} &= \mathbf{E}_{1122}, \quad \mu^{\text{E}} = \frac{1}{2} [\mathbf{E}_{1111} - \mathbf{E}_{1122}], \quad \alpha_1^{\text{E}} = \mathbf{E}_{1122} + 2\mathbf{E}_{1313} - \mathbf{E}_{1111}, \\ \alpha_2^{\text{E}} &= \frac{1}{2} [\mathbf{E}_{1111} + \mathbf{E}_{3333}] - 2\mathbf{E}_{1313} - \mathbf{E}_{1133}, \quad \alpha_3^{\text{E}} = \mathbf{E}_{1133} - \mathbf{E}_{1122}, \end{aligned} \quad (4.9)$$

$$\beta_1^{\text{e}} = -\mathbf{e}_{311}, \quad \beta_2^{\text{e}} = -\mathbf{e}_{333} + \mathbf{e}_{311} + 2\mathbf{e}_{131}, \quad \beta_3^{\text{e}} = -2\mathbf{e}_{131}, \quad (4.10)$$

$$\gamma_1^{\text{e}} = -\frac{1}{2} \epsilon_{11}, \quad \gamma_2^{\text{e}} = -\frac{1}{2} [\epsilon_{33} - \epsilon_{11}]. \quad (4.11)$$

4.2.2 Compatibility conditions and averaging principles

Under external loading, the ferroelectric crystal forms compatible domain configurations in order to minimise the total energy, see [35, 134]. For any two adjacent variants α and β existing in a crystal, separated by an interface, the average kinematic and polarisation compatibility conditions read

$$\boldsymbol{\varepsilon}_{(\alpha)} - \boldsymbol{\varepsilon}_{(\beta)} = [\mathbf{a}_{\alpha\beta} \otimes \mathbf{n}_{\alpha\beta}]^{\text{sym}} \quad \text{and} \quad [\mathbf{P}_{(\alpha)} - \mathbf{P}_{(\beta)}] \cdot \mathbf{n}_{\alpha\beta} = 0, \quad (4.12)$$

cf. [134], wherein $\mathbf{n}_{\alpha\beta}$ denotes the normal of the domain interface and where $\mathbf{a}_{\alpha\beta}$ represents an arbitrary vector. These compatibility conditions ensure that the interfaces separating the individual domains are undistorted and uncharged.

Considering any material point in a single crystal, a mixture of ferroelectric domains or variants separated by compatible domain walls is highly possible [91, 134]. Associating the distinct individual variants with their respective volume fraction $\lambda_{(\alpha)}$, wherein the restrictions $\sum_{\alpha=1}^{nv} \lambda_{(\alpha)} = 1$ and $\lambda_{(\alpha)} \geq 0$ hold, the volume average of any particular domain quantity in a material point is obtained by weighting the individual domain component by their corresponding volume fraction. In this context, the general form of any averaged quantity in a material point is represented as

$$[\bullet]^{\text{M}}(\boldsymbol{\lambda}) = \sum_{\alpha=1}^{nv} \lambda_{(\alpha)} [\bullet]_{(\alpha)} \quad \text{with} \quad \boldsymbol{\lambda} = [\lambda_{(1)}, \dots, \lambda_{(nv)}] \in \mathbb{R}^{nv}, \quad (4.13)$$

wherein $[\bullet]_{(\alpha)}$ refers to an arbitrary domain quantity and where $[\bullet]^{\text{M}}$ denotes the corresponding volume average of the particular domain quantity. Following the general expression (4.13), the average remnant quantities, namely the average remnant strain $\boldsymbol{\varepsilon}^{\text{M}}$ and the average remnant polarisation \mathbf{P}^{M} , of the crystal read

$$\boldsymbol{\varepsilon}^{\text{M}}(\boldsymbol{\lambda}) = \sum_{\alpha=1}^{nv} \lambda_{(\alpha)} \boldsymbol{\varepsilon}_{(\alpha)} \quad \text{and} \quad \mathbf{P}^{\text{M}}(\boldsymbol{\lambda}) = \sum_{\alpha=1}^{nv} \lambda_{(\alpha)} \mathbf{P}_{(\alpha)}. \quad (4.14)$$

Analogously, the volume averaged material moduli, i.e. the average elasticity tensor $\mathbf{E}^{\text{M}}(\boldsymbol{\lambda})$, the average third-order piezoelectric tensor $\mathbf{e}^{\text{M}}(\boldsymbol{\lambda})$ and the average second-order dielectric tensor $\boldsymbol{\varepsilon}^{\text{M}}(\boldsymbol{\lambda})$ are expressed as

$$\{\mathbf{E}^{\text{M}}(\boldsymbol{\lambda}), \mathbf{e}^{\text{M}}(\boldsymbol{\lambda}), \boldsymbol{\varepsilon}^{\text{M}}(\boldsymbol{\lambda})\} = \sum_{\alpha=1}^{nv} \lambda_{(\alpha)} \{\mathbf{E}_{(\alpha)}, \mathbf{e}_{(\alpha)}, \boldsymbol{\varepsilon}_{(\alpha)}\}. \quad (4.15)$$

Instead of weighting the individual domain quantities by the α -th variant volume fraction, a representation based on the multi-rank laminate volume fraction μ^j of the j -th rank laminate, wherein $j = 1, \dots, nv - 1$, can be introduced such that

$$\mu^j = \begin{cases} 0 & \text{for } \sum_{\alpha=1}^{j-1} \lambda_{(\alpha)} = 1, \\ \frac{\lambda_{(j)}}{1 - \sum_{\alpha=1}^{j-1} \lambda_{(\alpha)}} & \text{otherwise,} \end{cases} \quad (4.16)$$

holds, along with the inequality constraint $1 \geq \mu^j \geq 0$ for the individual j -th rank laminates, cf. [18, 91]. The distinct multi-rank laminate volume fractions are arranged in the form of an array $\boldsymbol{\mu} = [\mu^1, \dots, \mu^{nv-1}] \in \mathbb{R}^{nv-1}$. Considering such a multi-rank laminate volume fraction representation ensures that the interfaces remain compatible during the domain evolution, see [91, 151]. Following this $\boldsymbol{\mu}$ -based representation, the volume average of the remnant strains and polarisation, introduced in Equation (4.14), can be reformulated in terms of the multi-rank laminate volume fractions. The averaged remnant strain and polarisation at a material point in the crystal read

$$\begin{aligned} \boldsymbol{\varepsilon}^M(\boldsymbol{\mu}; \boldsymbol{\varepsilon}_{(1,3,5)}) &= [\mu^1 + \mu^2 [1 - \mu^1]] \boldsymbol{\varepsilon}_{(1)} \\ &+ [1 - \mu^1] [1 - \mu^2] [\mu^3 + \mu^4 [1 - \mu^3]] \boldsymbol{\varepsilon}_{(3)} \\ &+ [1 - \mu^1] [1 - \mu^2] [1 - \mu^3] [1 - \mu^4] \boldsymbol{\varepsilon}_{(5)} \quad \text{and} \end{aligned} \quad (4.17)$$

$$\begin{aligned} \mathbf{P}^M(\boldsymbol{\mu}; \mathbf{P}_{(1,3,5)}) &= [\mu^1 - \mu^2 [1 - \mu^1]] \mathbf{P}_{(1)} \\ &+ [1 - \mu^1] [1 - \mu^2] [\mu^3 - \mu^4 [1 - \mu^3]] \mathbf{P}_{(3)} \\ &+ [1 - \mu^1] [1 - \mu^2] [1 - \mu^3] [1 - \mu^4] [2\mu^5 - 1] \mathbf{P}_{(5)}. \end{aligned} \quad (4.18)$$

Similarly, the $\boldsymbol{\mu}$ -based representation can be extended so as to arrive at the volume average of the material moduli at any point within the crystal. Starting from the individual variant material moduli, introduced in Equations (4.6) to (4.8), the averaged fourth-order elasticity tensor $\mathbf{E}^M(\boldsymbol{\mu}; \mathbf{E}_{(1,3,5)})$, the averaged third-order piezoelectric tensor $\mathbf{e}^M(\boldsymbol{\mu}; \mathbf{e}_{(1,3,5)})$ and the averaged dielectric tensor $\boldsymbol{\varepsilon}^M(\boldsymbol{\mu}; \boldsymbol{\varepsilon}_{(1,3,5)})$ are re-formulated in terms of the multi-rank laminate volume fractions as

$$\begin{aligned} \mathbf{E}^M(\boldsymbol{\mu}; \mathbf{E}_{(1,3,5)}) &= [\mu^1 + \mu^2 [1 - \mu^1]] \mathbf{E}_{(1)} \\ &+ [1 - \mu^1] [1 - \mu^2] [\mu^3 + \mu^4 [1 - \mu^3]] \mathbf{E}_{(3)} \\ &+ [1 - \mu^1] [1 - \mu^2] [1 - \mu^3] [1 - \mu^4] \mathbf{E}_{(5)}, \end{aligned} \quad (4.19)$$

$$\begin{aligned} \mathbf{e}^M(\boldsymbol{\mu}; \mathbf{e}_{(1,3,5)}) &= [\mu^1 - \mu^2 [1 - \mu^1]] \mathbf{e}_{(1)} \\ &+ [1 - \mu^1] [1 - \mu^2] [\mu^3 - \mu^4 [1 - \mu^3]] \mathbf{e}_{(3)} \\ &+ [1 - \mu^1] [1 - \mu^2] [1 - \mu^3] [1 - \mu^4] [2\mu^5 - 1] \mathbf{e}_{(5)} \quad \text{and} \end{aligned} \quad (4.20)$$

$$\begin{aligned} \boldsymbol{\varepsilon}^M(\boldsymbol{\mu}; \boldsymbol{\varepsilon}_{(1,3,5)}) &= [\mu^1 + \mu^2 [1 - \mu^1]] \boldsymbol{\varepsilon}_{(1)} \\ &+ [1 - \mu^1] [1 - \mu^2] [\mu^3 + \mu^4 [1 - \mu^3]] \boldsymbol{\varepsilon}_{(3)} \\ &+ [1 - \mu^1] [1 - \mu^2] [1 - \mu^3] [1 - \mu^4] \boldsymbol{\varepsilon}_{(5)}. \end{aligned} \quad (4.21)$$

4.2.3 Thermodynamic model formulation

With the symmetry considerations and material properties governing the tetragonal ferroelectric variants as well as the averaging principles introduced, we proceed to the general thermodynamic laminate-based model formulation. The electric Gibbs energy is a function of the second-order strain tensor, the electric field vector, and of the internal state variables, determining the dissipative process. For the considered laminate-based models, domain evolution in the crystal occurs as one ferroelectric variant expands at the expense of the adjacent variant. In other words, domains in the crystal evolve as the volume fraction of one laminate increases with respect to its adjacent counterpart. This gives rise to the introduction of multi-rank laminate volume fractions $\boldsymbol{\mu}$ as the internal state variables. Both evolution and reduction of the multi-rank laminate volume fractions correlate to the rate-dependent switching of the domains in the ferroelectric single crystal. Thus, the general form of the electric Gibbs energy for the laminate-based model reads $H(\boldsymbol{\varepsilon}, \mathbf{E}, \boldsymbol{\mu})$, whereby the multi-rank laminate volume fractions $\boldsymbol{\mu}$ are considered as internal state variables. The specific form of the thermodynamic potential is defined for the four laminate models with respect to the different mixture ansatz assumptions and averaging formulations. The individual energy formulations are detailed in the subsequent sections.

Following the standard Coleman–Noll procedure, the constitutive equations for the second-order stress tensor and the dielectric displacement vector of the single crystal are obtained as

$$\boldsymbol{\sigma} = \frac{\partial H(\boldsymbol{\varepsilon}, \mathbf{E}, \boldsymbol{\mu})}{\partial \boldsymbol{\varepsilon}} \quad \text{and} \quad \mathbf{D} = - \frac{\partial H(\boldsymbol{\varepsilon}, \mathbf{E}, \boldsymbol{\mu})}{\partial \mathbf{E}}, \quad (4.22)$$

and the reduced dissipation inequality reads

$$\mathcal{D}_{\text{red}} = \sum_{j=1}^{nv-1} f^j(\boldsymbol{\mu}) \dot{\mu}^j \geq 0. \quad (4.23)$$

Herein, $f^j(\boldsymbol{\mu})$ is the thermodynamic driving force corresponding to the particular j -th rank laminate. The individual driving forces, defined as the work conjugate to the rate of change of the corresponding multi-rank volume fraction $\dot{\mu}^j$, are identified as

$$f^j(\boldsymbol{\mu}) = - \frac{\partial H(\boldsymbol{\varepsilon}, \mathbf{E}, \boldsymbol{\mu})}{\partial \mu^j} \quad \text{for } j = 1, \dots, nv - 1. \quad (4.24)$$

The definite form of the formulated electric Gibbs energy results in distinct driving forces for the respective laminate models. Thus, the material response predicted by the models, in terms of the laminate volume fraction evolution and hence the macroscopic hysteresis curves, is distinct for each of the four laminate-based models.

The individual driving forces $f^j(\boldsymbol{\mu})$ defining the domain evolution are resisted by the dissipative motion of the domain walls, cf. [57, 151]. The critical resistance force or the

threshold value corresponding to the j -th rank laminate is denoted by $g^{c,j}(\boldsymbol{\mu}) \geq 0$. An elastic domain, analogous to the classic plasticity and viscoplasticity theory, is postulated in the space of the individual driving forces $f^j(\boldsymbol{\mu})$ as

$$\mathbb{E} := \{ f^j(\boldsymbol{\mu}) \mid \Phi^j(f^j) := |f^j(\boldsymbol{\mu})| - g^{c,j}(\boldsymbol{\mu}) \leq 0; j = 1, \dots, nv - 1 \} . \quad (4.25)$$

Once the driving force of a particular j -th rank laminate exceeds the critical resistance force $g^{c,j}(\boldsymbol{\mu})$, domain evolution of the particular laminate occurs. The explicit form of the individual threshold quantities $g^{c,j}(\boldsymbol{\mu})$ can be written in terms of the experimentally determined values of the coercive fields required for 90° and 180° domain switching, as explained in the work by Yen et al. [151]. For a three-dimensional system with $nv = 6$, the critical resistance expressions based on the distinct domain wall movements read

$$g^{c,1}(\boldsymbol{\mu}) = 2 E_{180^\circ}^c P^s \mu^2 + E_{90^\circ}^c P^s [1 - \mu^2] , \quad (4.26)$$

$$g^{c,2}(\boldsymbol{\mu}) = E_{90^\circ}^c P^s [1 - \mu^1] , \quad (4.27)$$

$$g^{c,3}(\boldsymbol{\mu}) = [2 E_{180^\circ}^c P^s \mu^4 + E_{90^\circ}^c P^s [1 - \mu^4]] [1 - \mu^1] [1 - \mu^2] , \quad (4.28)$$

$$g^{c,4}(\boldsymbol{\mu}) = E_{90^\circ}^c P^s [1 - \mu^1] [1 - \mu^2] [1 - \mu^3] \quad \text{and} \quad (4.29)$$

$$g^{c,5}(\boldsymbol{\mu}) = 2 E_{180^\circ}^c P^s [1 - \mu^1] [1 - \mu^2] [1 - \mu^3] [1 - \mu^4] , \quad (4.30)$$

cf. [151]. In contrast to the constant resistance force values considered in many micromechanical models, the individual critical threshold force expressions (4.26) to (4.30) are functions of the evolving multi-rank laminate volume fractions $\boldsymbol{\mu}$. For more details on the resistance forces for a tetragonal system, the reader is referred to Yen et al. [151].

Based on the postulate of maximum dissipation, suitable evolution equations for the internal state variables need to be formulated. To this end, a non-negative rate-dependent dissipation equation $\zeta(\dot{\boldsymbol{\mu}})$ is postulated in terms of the rate of the multi-rank laminate volume fractions. The general form of the rate-dependent dissipation equation reads

$$\zeta(\dot{\boldsymbol{\mu}}) = \sum_{j=1}^{nv-1} \sup_{f^j} \left\{ f^j(\boldsymbol{\mu}) \dot{\mu}^j - \frac{1}{\eta^p [m+1]} \langle \Phi^j(f^j) \rangle^{m+1} \right\} , \quad (4.31)$$

cf. [110], wherein the Macaulay bracket $\langle \bullet \rangle = \max \{ \bullet, 0 \}$ is used, and where the model parameters $\eta^p > 0$ and $m > 0$ influence the time-dependent evolution of the laminate volume fractions. After solving the necessary condition of Equation (4.31), we arrive at the set of the rate-type evolution equations

$$\dot{\mu}^j = \frac{1}{\eta^p} \langle |f^j(\boldsymbol{\mu})| - g^{c,j}(\boldsymbol{\mu}) \rangle^m \frac{f^j(\boldsymbol{\mu})}{|f^j(\boldsymbol{\mu})|} \quad \text{for } j = 1, \dots, nv - 1 , \quad (4.32)$$

wherein the inequality constraint $1 \geq \mu^j \geq 0$ holds for the individual j -th rank laminates.

4.3 Algorithmic treatment of the evolution equations

An efficient numerical scheme is required in order to solve the set of non-linear rate-dependent evolution equations for the update of the inequality constrained multi-rank laminate volume fractions. To this end, the Fischer–Burmeister-type algorithm in combination with a standard Newton–Raphson method is considered. The particular algorithmic procedure has proved its efficiency in solving the inequality constrained volume fraction evolution equations in general phase transformation material models.

Fischer [50] introduced the algorithm to transform inequality constraints into equality relations. Schmidt-Baldassari [120] replaced the set of Kuhn–Tucker conditions with the Fischer–Burmeister complementarity functions in the context of a rate-independent crystal plasticity model. With respect to the micromechanical model formulations developed by Bartel et al. [10–12], the Fischer–Burmeister complementarity functions were employed to study the constrained volume fraction evolution describing the austenitic to martensitic phase transformations. Kiefer et al. [81] compared the standard predictor-corrector return-mapping scheme to the Fischer–Burmeister-based integration algorithm for the constitutive model predicting the martensitic variant reorientation in magnetic shape memory alloys. In a subsequent work, Kiefer et al. [82] detailed on the robustness and on the efficiency of the Fischer–Burmeister algorithm in comparison to two other solution schemes, namely the active set strategy and the staggered solution method. The Fischer–Burmeister complementarity functions were considered in their non-local gradient-enhanced formulation to solve the inequality constrained damage evolution. Based on the above-mentioned works, the Fischer–Burmeister algorithm in combination with a Newton–Raphson scheme is applied to all the distinct laminate-based models. By doing so, the non-linear rate-dependent evolution equations are solved with respect to the underlying inequality constraints of the laminate volume fractions.

As a starting point, let the electromechanical loading process be sub-divided into finite time intervals $[t_n, t_{n+1}]$ with the time increment defined as $\Delta t := t_{n+1} - t_n > 0$. The quantities computed at time t_{n+1} shall be denoted without the subscript $n + 1$ for the sake of brevity. The rate of the individual laminate volume fractions is considered to be constant within the defined finite time increment. In this context, the approximation

$$\dot{\mu}^j \approx \frac{\mu^j(t_{n+1}) - \mu^j(t_n)}{\Delta t} = \frac{\mu^j - \mu_n^j}{\Delta t}, \quad (4.33)$$

holds. Assuming that the value of the multi-rank laminate volume fractions μ_n^j at the previous time step t_n are known, the current values μ^j at time t_{n+1} are computed following the implicit Euler integration scheme as

$$\mu^j = \mu_n^j + \Delta t \dot{\mu}^j \quad \text{for } j = 1, \dots, nv - 1. \quad (4.34)$$

The update of the individual laminate volume fractions is obtained by iteratively solving the set of residual functions

$$R^j(\boldsymbol{\mu}) := \mu^j - \mu_n^j - \frac{\Delta t}{\eta^p} \langle |f^j(\boldsymbol{\mu})| - g^{c,j}(\boldsymbol{\mu}) \rangle^m \frac{f^j(\boldsymbol{\mu})}{|f^j(\boldsymbol{\mu})|} = 0, \quad (4.35)$$

within each time increment using the standard Newton–Raphson scheme.

In view of the Fischer–Burmeister approach, the inequality constrained multi-rank laminate volume fractions are reformulated into a set of additional constraints

$$r_I^j := -\mu^j \leq 0 \quad \text{and} \quad r_{II}^j := \mu^j - 1 \leq 0. \quad (4.36)$$

These additional constraints are assembled in the form of two arrays $\mathbf{r}_i = [r_i^1, \dots, r_i^{nv-1}]$ with $i = I, II$. In order to restrict the additional constraints within the bounds as defined in (4.36), Lagrange multipliers $\boldsymbol{\Gamma}_i = [\Gamma_i^1, \dots, \Gamma_i^{nv-1}]$ with $i = I, II$, dual to the additional constraints \mathbf{r}_i , are introduced. These Lagrange multipliers $\boldsymbol{\Gamma}_I$ and $\boldsymbol{\Gamma}_{II}$ take arbitrary values during external loading so as to restrict the multi-rank laminate volume fractions within their limits. The list of dependent variables governing the electric Gibbs energy $H(\boldsymbol{\varepsilon}, \mathbf{E}, \boldsymbol{\mu})$ is extended with the Lagrange multipliers as additional arguments, such that an enhanced electric Gibbs energy of the form $H_{\text{enh}}(\boldsymbol{\varepsilon}, \mathbf{E}, \boldsymbol{\mu}, \boldsymbol{\Gamma}_I, \boldsymbol{\Gamma}_{II})$ is devised in order to describe the governing electromechanical response. Considering the additional constraints and Lagrange multipliers, the enhanced form of the electric Gibbs energy is formulated as

$$H_{\text{enh}}(\boldsymbol{\varepsilon}, \mathbf{E}, \mathbf{v}) = H(\boldsymbol{\varepsilon}, \mathbf{E}, \boldsymbol{\mu}) + \sum_{j=1}^{nv-1} r_I^j \Gamma_I^j + \sum_{j=1}^{nv-1} r_{II}^j \Gamma_{II}^j, \quad (4.37)$$

cf. [81], wherein \mathbf{v} denotes the solution array

$$\mathbf{v} = [\mathbf{v}^1, \dots, \mathbf{v}^{nv-1}]^t = [\boldsymbol{\mu}, \boldsymbol{\Gamma}_I, \boldsymbol{\Gamma}_{II}]^t \in \mathbb{R}^{15 \times 1}, \quad (4.38)$$

for a tetragonal system with $nv = 6$. Here, $\mathbf{v}^j = [\mu^j, \Gamma_I^j, \Gamma_{II}^j]^t$, for $j = 1, \dots, nv - 1$, is the solution array for the individual laminate system. Considering the definitions of the additional constraints (4.36), the enhanced electric Gibbs energy (4.37) is reformulated as

$$H_{\text{enh}}(\boldsymbol{\varepsilon}, \mathbf{E}, \mathbf{v}) = H(\boldsymbol{\varepsilon}, \mathbf{E}, \boldsymbol{\mu}) - \sum_{j=1}^{nv-1} \mu^j \Gamma_I^j + \sum_{j=1}^{nv-1} [\mu^j - 1] \Gamma_{II}^j. \quad (4.39)$$

From the reduced dissipation inequality, the individual enhanced driving forces corresponding to the j -th rank laminate read

$$f_{\text{enh}}^j(\boldsymbol{\mu}, \Gamma_I^j, \Gamma_{II}^j) = -\frac{\partial H_{\text{enh}}(\boldsymbol{\varepsilon}, \mathbf{E}, \mathbf{v})}{\partial \mu^j} = -\frac{\partial H(\boldsymbol{\varepsilon}, \mathbf{E}, \boldsymbol{\mu})}{\partial \mu^j} + \Gamma_I^j - \Gamma_{II}^j. \quad (4.40)$$

The set of residual functions (4.35) are reformulated considering the enhanced driving forces and the Fischer–Burmeister functions, which read

$$\xi_i^j = \sqrt{[r_i^j]^2 + [\Gamma_i^j]^2} + r_i^j - \Gamma_i^j \quad \text{for } i = I, II. \quad (4.41)$$

With these complementarity functions, the residual vector for an individual j -th rank laminate system takes the form

$$\mathbf{R}^j(\boldsymbol{\mu}, \Gamma_I^j, \Gamma_{II}^j) = \begin{bmatrix} R_{\text{enh}}^j \\ \xi_I^j \\ \xi_{II}^j \end{bmatrix} = \begin{bmatrix} \mu^j - \mu_n^j - \frac{\Delta t}{\eta^p} \langle |f_{\text{enh}}^j| - g^{c,j} \rangle^m \frac{f_{\text{enh}}^j}{|f_{\text{enh}}^j|} \\ \sqrt{[\Gamma_I^j]^2 + [r_I^j]^2} + r_I^j - \Gamma_I^j \\ \sqrt{[\Gamma_{II}^j]^2 + [r_{II}^j]^2} + r_{II}^j - \Gamma_{II}^j \end{bmatrix} = \mathbf{0}, \quad (4.42)$$

for $j = 1, \dots, nv-1$. The overall residual for a tetragonal ferroelectric system is obtained as an array of the individual residual functions (4.42) as $\mathbf{R}(\mathbf{v}) = [\mathbf{R}^1, \dots, \mathbf{R}^{nv-1}]^t \in \mathbb{R}^{15 \times 1}$. The non-linear residual $\mathbf{R}(\mathbf{v})$ is solved by means of the Newton–Raphson method in each time increment for the current update of the solution vector $\mathbf{v} = [\mathbf{v}^1, \dots, \mathbf{v}^{nv-1}]^t$. The particular form of the Newton-type update

$$\mathbf{v}|_{k+1} = \mathbf{v}|_k - \mathbf{J}^{-1}|_k \cdot \mathbf{R}(\mathbf{v})|_k, \quad (4.43)$$

is fulfilled until $\|\mathbf{R}(\mathbf{v})\| < \text{tol}$, wherein k denotes the iteration counter. The computed volume fractions are automatically constrained within the limits $[0, 1]$. The overall tangent matrix $\mathbf{J} \in \mathbb{R}^{15 \times 15}$, related to the residual $\mathbf{R}(\mathbf{v})$ used in the update relation (4.43), consists of the individual laminate tangent matrices arranged diagonally. The corresponding tangent matrix \mathbf{J}^j for the individual laminate system related to the residual $\mathbf{R}^j(\boldsymbol{\mu}, \Gamma_I^j, \Gamma_{II}^j)$ reads

$$\mathbf{J}^j := \frac{d\mathbf{R}^j}{d\mathbf{v}^j} = \begin{bmatrix} \mathbf{J}_{\mu\mu}^j & \mathbf{J}_{\mu\Gamma_I}^j & \mathbf{J}_{\mu\Gamma_{II}}^j \\ \mathbf{J}_{\xi_I\mu}^j & \mathbf{J}_{\xi_I\Gamma_I}^j & \mathbf{J}_{\xi_I\Gamma_{II}}^j \\ \mathbf{J}_{\xi_{II}\mu}^j & \mathbf{J}_{\xi_{II}\Gamma_I}^j & \mathbf{J}_{\xi_{II}\Gamma_{II}}^j \end{bmatrix} = \begin{bmatrix} \frac{dR_{\text{enh}}^j}{d\mu^j} & \frac{dR_{\text{enh}}^j}{d\Gamma_I^j} & \frac{dR_{\text{enh}}^j}{d\Gamma_{II}^j} \\ \frac{d\xi_I^j}{d\mu^j} & \frac{d\xi_I^j}{d\Gamma_I^j} & \frac{d\xi_I^j}{d\Gamma_{II}^j} \\ \frac{d\xi_{II}^j}{d\mu^j} & \frac{d\xi_{II}^j}{d\Gamma_I^j} & \frac{d\xi_{II}^j}{d\Gamma_{II}^j} \end{bmatrix}. \quad (4.44)$$

With respect to the implementation, the total derivatives $\mathbf{J}_{\mu\mu}^j$, $\mathbf{J}_{\mu\Gamma_I}^j$ and $\mathbf{J}_{\mu\Gamma_{II}}^j$ are numerically approximated due to the algebraic complexity involved. For a detailed insight on the numerical approximation of tangent moduli, the reader is referred to [38, 109]. The

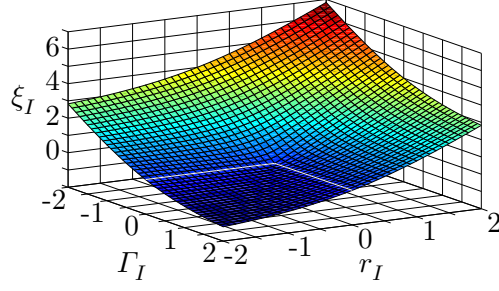


Figure 4.2: Graphical representation of the Fischer–Burmeister function $\xi_I = \sqrt{[r_I]^2 + [\Gamma_I]^2} + r_I - \Gamma_I$.

remaining total derivative entries, $\mathbf{J}_{\xi_i^j \mu}$, $\mathbf{J}_{\xi_i^j \Gamma_I^j}$ and $\mathbf{J}_{\xi_i^j \Gamma_{II}^j}$, of the tangent matrix (4.44) are analytically computed, see Appendix B.

The Fischer–Burmeister complementarity functions are numerically sensitive since their derivatives are non-smooth, see e.g. [10, 12, 81]. In particular, the functions (4.41) are not differentiable at $r_i^j = 0$ and $\Gamma_i^j = 0$, see Figure 4.2 for a graphical representation of the Fischer–Burmeister functions (4.41) for the case $i = I$. In order to overcome this numerical instability, a regularisation parameter $1 \gg \delta > 0$ is introduced such that the functions (4.41) takes a regularised form

$$\xi_i^j = \sqrt{[r_i^j]^2 + [\Gamma_i^j]^2 + 2\delta^2} + r_i^j - \Gamma_i^j \quad \text{for } i = I, II, \quad j = 1, \dots, nv - 1. \quad (4.45)$$

The regularised set of equations (4.45) are considered in the residual (4.42) in order to obtain the solution update. Moreover, the individual Lagrange multipliers are initialised to $\Gamma_I^j = \Gamma_{II}^j = 10^{-6}$ at the start of numerical simulations as compared to the theoretical initial zero values. This ensures further numerical stability of the algorithmic scheme. For more details on the different regularised forms, the reader is referred to [8, 38, 76, 82].

4.4 Laminate-based Model 1

This section provides details on laminate-based Model 1 to study the domain evolution and the subsequent polarisation switching in ferroelectric single crystals. For comparison purposes, the particular laminate-based Model 1 is developed analogously to the phenomenological model presented in Section 3.2.

With regards to laminate-based Model 1, the microscopic evolution of domains under external electromechanical loading considers the average polarisation compatibility condition (4.12)₂. The macroscopic remnant polarisation of the crystal $\mathbf{P}^M(\boldsymbol{\mu})$ is computed following the relation (4.18). The average kinematic compatibility (4.12)₁ and the subsequent volume averaged remnant strain relation (4.17) are not considered for laminate-based Model 1. Instead, the average remnant strain of the crystal is postulated as a function of $\mathbf{P}^M(\boldsymbol{\mu})$.

As a starting point, we define two structural quantities, namely the structural vector $\mathbf{a}(\mathbf{P}^M)$ and the second-order structural tensor $\mathbf{m}(\mathbf{P}^M)$, both similar to the assumptions followed in the phenomenological model. The particular structural vector for laminate-based Model 1 is defined as

$$\mathbf{a}(\mathbf{P}^M) := \frac{\mathbf{P}^M}{\|\mathbf{P}^M\|} \quad \text{with} \quad \|\mathbf{a}(\mathbf{P}^M)\| = 1, \quad (4.46)$$

whereas the second-order structural tensor reads

$$\mathbf{m}(\mathbf{P}^M) := \mathbf{a}(\mathbf{P}^M) \otimes \mathbf{a}(\mathbf{P}^M) \quad \text{with} \quad \text{tr}(\mathbf{m}(\mathbf{P}^M)) = 1, \quad (4.47)$$

cf. Equations (3.1) and (3.2). The two structural quantities characterise the transversely-isotropic behaviour of the crystal in both the poled and remnant states. Moreover, these structural quantities $\mathbf{a}(\mathbf{P}^M)$ and $\mathbf{m}(\mathbf{P}^M)$ are introduced as a function of the average remnant polarisation which is, in turn, dependent on the inequality constrained multi-rank laminate volume fractions $\boldsymbol{\mu} = [\mu^1, \dots, \mu^{nv-1}]$.

The second-order linear strain tensor $\boldsymbol{\varepsilon}$ and the dielectric displacement vector \mathbf{D}_{M1} of the ferroelectric single crystal for laminate-based Model 1 are additively decomposed into an elastic and a remnant part as

$$\boldsymbol{\varepsilon} = \boldsymbol{\varepsilon}^e + \boldsymbol{\varepsilon}^r(\mathbf{P}^M) \quad \text{and} \quad \mathbf{D}_{M1} = \mathbf{D}^e + \mathbf{P}^M, \quad (4.48)$$

wherein $\boldsymbol{\varepsilon}^e$ and \mathbf{D}^e denote the elastic strain tensor and dielectric displacement vector, respectively. The remnant polarisation $\mathbf{P}^M(\boldsymbol{\mu})$, as introduced in Equation (4.18), is the volume average of the distinct microscopic polarisations of the tetragonal ferroelectric crystal. For comparison purposes with the phenomenological model, the average remnant strain of the crystal for laminate-based Model 1 is written as a function of the averaged remnant polarisation $\mathbf{P}^M(\boldsymbol{\mu})$. The average remnant strain tensor takes the specific form

$$\boldsymbol{\varepsilon}^r(\mathbf{P}^M) = \frac{3}{2} \frac{\varepsilon^{\text{sat}}}{P^{\text{sat}}} \|\mathbf{P}^M\| \left[\mathbf{m}(\mathbf{P}^M) - \frac{1}{3} \mathbf{I} \right], \quad (4.49)$$

cf. the phenomenological remnant strain relation (3.4). Here, P^{sat} and ε^{sat} denote the saturation polarisation and strain of the crystal, respectively.

A suitable thermodynamic potential for laminate-based Model 1 needs to be constructed. The average electric Gibbs energy of the crystal is postulated in terms of the linear strain tensor, electric field vector, and the multi-rank laminate volume fractions as the internal state variables, i.e. $H_{M1}(\boldsymbol{\varepsilon}, \mathbf{E}, \boldsymbol{\mu})$. Analogous to the phenomenological model, the electric Gibbs energy for laminate-based Model 1 is additively decomposed into a reversible or piezoelectric and into a remnant part as

$$H_{M1}(\boldsymbol{\varepsilon}, \mathbf{E}, \boldsymbol{\mu}) = H_{M1}^{\text{piezo}}(\boldsymbol{\varepsilon}^e, \mathbf{E}, \mathbf{P}^M) + H_{M1}^{\text{rem}}(\mathbf{P}^M). \quad (4.50)$$

The particular form of the piezoelectric energy for laminate-based Model 1 reads

$$H_{M1}^{\text{piezo}}(\boldsymbol{\varepsilon}^e, \mathbf{E}, \mathbf{P}^M) = \frac{1}{2} [\boldsymbol{\varepsilon} - \boldsymbol{\varepsilon}^r(\mathbf{P}^M)] : \mathbf{E} : [\boldsymbol{\varepsilon} - \boldsymbol{\varepsilon}^r(\mathbf{P}^M)] - \frac{1}{2} \mathbf{E} \cdot \boldsymbol{\varepsilon} \cdot \mathbf{E} - \frac{\|\mathbf{P}^M\|}{P_{\text{sat}}} \mathbf{E} \cdot \mathbf{e}(\mathbf{a}(\mathbf{P}^M)) : [\boldsymbol{\varepsilon} - \boldsymbol{\varepsilon}^r(\mathbf{P}^M)] - \mathbf{P}^M \cdot \mathbf{E}, \quad (4.51)$$

wherein \mathbf{E} and $\boldsymbol{\varepsilon}$ refer to the isotropic elasticity and dielectric moduli, respectively, and where $\mathbf{e}(\mathbf{a}(\mathbf{P}^M))$ denotes the transversely-isotropic piezoelectric modulus. The closed form representation of the elasticity and the dielectric material moduli are provided in Equations (3.7) and (3.9). The third-order piezoelectric modulus $\mathbf{e}(\mathbf{a}(\mathbf{P}^M))$ takes the form as given in Equation (3.8), wherein the definitions for the structural quantities $\mathbf{a}(\mathbf{P}^M)$ and $\mathbf{m}(\mathbf{P}^M)$ are introduced in Equations (4.46) and (4.47). The remnant energy contribution of the thermodynamic potential (4.50) is constructed based on a saturation-type function dependent on the average remnant polarisation $\mathbf{P}^M(\boldsymbol{\mu})$. The considered form of the remnant energy for laminate-based Model 1 reads

$$H_{M1}^{\text{rem}}(\mathbf{P}^M) = \frac{1}{c} \left[\frac{1}{2} P_{\text{sat}} \ln \left(1 - \left[\frac{\|\mathbf{P}^M\|}{P_{\text{sat}}} \right]^2 \right) + \|\mathbf{P}^M\| \operatorname{arctanh} \left(\frac{\|\mathbf{P}^M\|}{P_{\text{sat}}} \right) \right], \quad (4.52)$$

cf. Equation (3.13), wherein c denotes a model parameter influencing the shape of the hysteresis curves. The piezoelectric and remnant energy contributions for laminate-based Model 1 are postulated analogous to the phenomenological model.

Based on the Coleman–Noll procedure, the explicit relations of the constitutive equations for the average stress tensor and for the average dielectric displacement vector for the particular laminate-based Model 1 are derived as

$$\boldsymbol{\sigma}_{M1} = \frac{\partial H_{M1}}{\partial \boldsymbol{\varepsilon}} = \mathbf{E} : [\boldsymbol{\varepsilon} - \boldsymbol{\varepsilon}^r(\mathbf{P}^M)] - \frac{\|\mathbf{P}^M\|}{P_{\text{sat}}} \mathbf{e}^t(\mathbf{a}(\mathbf{P}^M)) \cdot \mathbf{E} \quad \text{and} \quad (4.53)$$

$$\mathbf{D}_{M1} = - \frac{\partial H_{M1}}{\partial \mathbf{E}} = \frac{\|\mathbf{P}^M\|}{P_{\text{sat}}} \mathbf{e}(\mathbf{a}(\mathbf{P}^M)) : [\boldsymbol{\varepsilon} - \boldsymbol{\varepsilon}^r(\mathbf{P}^M)] + \boldsymbol{\varepsilon} \cdot \mathbf{E} + \mathbf{P}^M. \quad (4.54)$$

Following Equation (4.24), the driving force responsible for the domain evolution of the j -th rank laminate is derived as

$$f_{M1}^j(\boldsymbol{\mu}) = \boldsymbol{\sigma}_{M1} : \frac{\partial \boldsymbol{\varepsilon}^r(\mathbf{P}^M)}{\partial \mu^j} + \frac{\|\mathbf{P}^M\|}{P_{\text{sat}}} \mathbf{E} \cdot \frac{\partial \mathbf{e}(\mathbf{a}(\mathbf{P}^M))}{\partial \mu^j} : [\boldsymbol{\varepsilon} - \boldsymbol{\varepsilon}^r(\mathbf{P}^M)] + \frac{1}{P_{\text{sat}}} \left[\mathbf{E} \cdot \mathbf{e}(\mathbf{a}(\mathbf{P}^M)) : [\boldsymbol{\varepsilon} - \boldsymbol{\varepsilon}^r(\mathbf{P}^M)] \right] \left[\mathbf{a}(\mathbf{P}^M) \cdot \frac{\partial \mathbf{P}^M}{\partial \mu^j} \right] + \frac{\partial \mathbf{P}^M}{\partial \mu^j} \cdot \mathbf{E} - E_{M1}^{b,j}(\mathbf{P}^M). \quad (4.55)$$

The term $E_{M1}^{b,j}(\mathbf{P}^M)$ represents the back electric field contribution of the individual j -th rank laminates and is derived as

$$E_{M1}^{b,j}(\mathbf{P}^M) := \frac{\partial H_{M1}^{\text{rem}}(\mathbf{P}^M)}{\partial \mu^j} = \frac{1}{c} \operatorname{arctanh}\left(\frac{\|\mathbf{P}^M\|}{P_{\text{sat}}}\right) \left[\boldsymbol{\alpha}(\mathbf{P}^M) \cdot \frac{\partial \mathbf{P}^M}{\partial \mu^j} \right]. \quad (4.56)$$

With respect to the Fischer–Burmeister complementarity function-based algorithm, the enhanced driving forces for laminate-based Model 1 considering the derived driving force of the individual laminates (4.55) are given as

$$f_{\text{enh}}^j(\boldsymbol{\mu}, \Gamma_I^j, \Gamma_{II}^j) = f_{M1}^j(\boldsymbol{\mu}) + \Gamma_I^j - \Gamma_{II}^j, \quad (4.57)$$

cf. Equation (4.40). The domain evolution does not occur until the enhanced driving force within each laminate exceeds the critical resistance force of the particular laminate system. Equation (4.25) is reformulated in terms of the enhanced driving forces and is considered as the modified elastic range of the laminates. Once the driving force in each laminate exceeds the corresponding threshold limit, domain evolution of the particular laminate occurs, responsible for the macroscopic hysteretic response. The dissipation and the evolution equations defining the rate-dependent domain switching are introduced in Equations (4.31) and (4.32), respectively. The inequality constraints are satisfied automatically and efficiently by the considered Fischer–Burmeister approach. The overall residual $\mathbf{R}(\mathbf{v})$ is iteratively solved with the Newton–Raphson update (4.43) for the current value of the solution vector $\mathbf{v} = [\boldsymbol{\mu}, \boldsymbol{\Gamma}_I, \boldsymbol{\Gamma}_{II}]^t \in \mathbb{R}^{15 \times 1}$. The algorithmic scheme to arrive at the update of the multi-rank laminate volume fractions is explained in Section 4.3.

4.4.1 Numerical examples

This section presents the numerical capabilities of laminate-based Model 1. Several representative tests under both homogeneous and inhomogeneous states of deformation are performed considering single crystal tetragonal BaTiO₃ material parameters. The butterfly and dielectric displacement hysteresis curves for an initially poled three-dimensional specimen, subjected to a cyclic electrical load at varying frequencies, are reproduced by tests under homogeneous states of deformation. Furthermore, the influence of the viscous-like parameter on the hysteretic behaviour is discussed for the tests under homogeneous states of deformation. The derived model is implemented in a standard finite element environment with displacements and electric potential as primary field variables in order to solve an inhomogeneous boundary value problem. A three-dimensional quarter hole plate is considered for the tests under inhomogeneous states of deformation. The total strain and dielectric displacement distributions in the inhomogeneous specimen are investigated for cyclic electrical loading.

Table 4.2: Single crystal tetragonal BaTiO₃ material parameters considered for numerical computations with laminate-based Model 1.

| Denomination | Parameter | Value | Unit | Reference |
|--|----------------------------|-------------------------|--------------------|-----------|
| Elastic stiffness | E_{1111} | 213.303×10^3 | MPa | – |
| Elastic stiffness | E_{1122} | 102.515×10^3 | MPa | – |
| Lateral piezoelectric coefficient | e_{311} | – 0.7 | C/m ² | [152] |
| Axial piezoelectric coefficient | e_{333} | 6.7 | C/m ² | [152] |
| Piezoelectric shearing coefficient | e_{131} | 34.2 | C/m ² | [152] |
| Vacuum permittivity | ϵ_0 | 8.854×10^{-12} | F/m | [152] |
| Dielectric permittivity | ϵ_{11} | $1485.33 \epsilon_0$ | F/m | [152] |
| Saturation polarisation | P^{sat} | 0.26 | C/m ² | – |
| Saturation strain | ϵ^{sat} | 0.001 | – | – |
| Spontaneous polarisation | P^{s} | 0.26 | C/m ² | [151] |
| Coercive electric field for 90° switching | $E_{90^\circ}^{\text{c}}$ | 0.26 | kV/mm | [151] |
| Coercive electric field for 180° switching | $E_{180^\circ}^{\text{c}}$ | 0.23 | kV/mm | [151] |
| Viscosity-type parameter | η^{p} | 0.1 | m ² /Cs | – |

The single crystal BaTiO₃ material constants such as elastic stiffness, piezoelectric and dielectric tensor components are exactly the same as considered for the numerical simulations with the phenomenological model. The spontaneous polarisation, and the coercive electric field limits for 90° and 180° domain switching, respectively, are the additional material parameters. These three constants referring to the single crystal tetragonal BaTiO₃ are taken from the data published by Yen et al. [151]. The parameter defining the rate-dependency of the polarisation evolution is set to $\eta^{\text{p}} = 0.1 \text{ m}^2/\text{Cs}$, whereas different values for viscous-like parameter m and for slope parameter c are chosen. Table 4.2 summarises the input material parameters used in the simulations pertaining to laminate-based Model 1.

4.4.1.1 Tests under homogeneous states of deformation

The schematic sketch of the three-dimensional specimen under study along with the loading curve and boundary conditions is depicted in Figure 4.3. An initially poled specimen is considered for the following tests under homogeneous states of deformation. The crystallographic axes of this initially poled specimen are assumed to coincide with the reference Cartesian axes $e_{1,2,3}$.

For the considered specimen, the initial variant volume fraction values are set to $\lambda_{(6)}|_{t_0} = 1$ and $\lambda_{(1,2,3,4,5)}|_{t_0} = 0$. Using Equation (4.16), the initial variant volume frac-

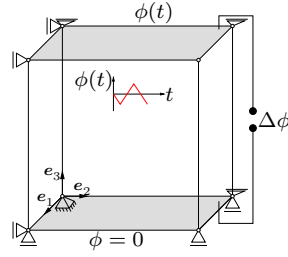


Figure 4.3: Schematic representation of an initially poled three-dimensional specimen subjected to a cyclic electrical load along with the loading curve and boundary conditions. The poled state along the e_3 -axis is obtained by setting the multi-rank laminate volume fractions $\mu^{1,2,3,4,5}|_{t_0} = 0$.

tion values correspond directly to the zero value of the multi-rank laminate volume fractions, i.e. $\mu^{1,2,3,4,5}|_{t_0} = 0$. Inserting the distinct laminate volume fraction values in Equation (4.18), the average remnant polarisation results in $P_3^M|_{t_0} = -P^s$. Following Equation (4.49), the magnitude of the average remnant strain along the e_3 -axis, $\varepsilon_{33}^M|_{t_0}$, equals the saturation strain value ε^{sat} . The non-vanishing values of the average remnant strain and polarisation result in the initial poled configuration of the specimen along the negative e_3 -axis.

Analogous to the tests performed under homogeneous states of deformation with the phenomenological model, a cyclic electrical load is applied along the e_3 -axis. The electric potential difference across the specimen is generated by keeping the lower electrode grounded at all times, while its upper counterpart is surcharged with a time-dependent cyclic scalar electric potential $\phi(t)$ with $\phi^{\text{max}} = \pm 10$ kV. The dielectric displacements and the total strains resulting from this rate-dependent and non-linear homogeneous deformation are iteratively computed. The obtained total strains ε_{33} and dielectric displacements D_3 of the specimen are plotted, respectively, against the applied cyclic electric field E_3 , see Figure 4.4. The average remnant polarisation \mathbf{P}^M and the average remnant strain $\varepsilon^r(\mathbf{P}^M)$ are computed using Equations (4.18) and (4.49), respectively. Figure 4.5 shows $\varepsilon_{33}^r(\mathbf{P}^M)$ versus E_3 plot as well as P_3^M versus E_3 plot. The corresponding laminate and variant volume fraction evolution in the specimen with respect to the cyclic electric field E_3 for the considered loading are plotted in Figure 4.6. All the plotted curves, Figures 4.4 to 4.6, are obtained for an electrical loading frequency of 0.05 Hz and for model parameters $c = 3.0$ and $m = 2.0$.

Starting from the initial poled configuration along the negative e_3 -axis, the potential difference across the specimen is reduced from $\Delta\phi|_{t_0} = 0$ kV in steps of Δt . During this loading phase, laminate-based Model 1 predicts a non-linear evolution of only the laminate volume fraction μ^5 in the specimen, see Figure 4.6. The value of μ^5 evolves from its initial zero value and reaches its maximum limit $\mu^5 = 1$ at $E_3 \approx 1$ kV/mm. This non-linear evolution of laminate volume fraction μ^5 is directly related to the change in remnant polarisation P_3^M from its initial value $-P^s$ to a magnitude of $P_3^M = P^s$ at $E_3 \approx 1$ kV/mm. The reversal of P_3^M corresponds to the switching of the specimen from its initial negative e_3 -direction to along the positive e_3 -axis. Upon further loading of

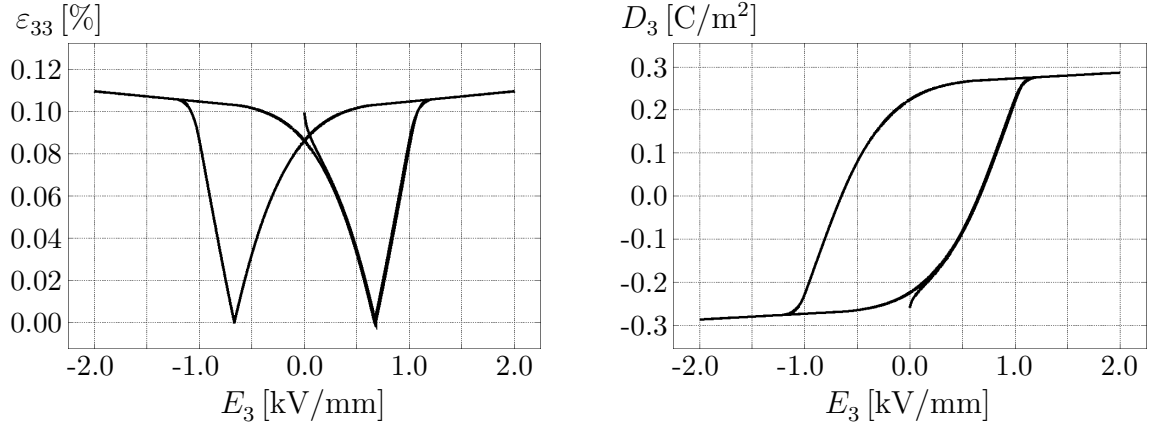


Figure 4.4: Hysteresis curves simulated with laminate-based Model 1 under homogeneous states of deformation for $c = 3.0$, $m = 2.0$. Butterfly curve (left) and dielectric hysteresis loop (right) obtained for a single crystal BaTiO₃ specimen subjected to a cyclic electrical loading at 0.05 Hz.

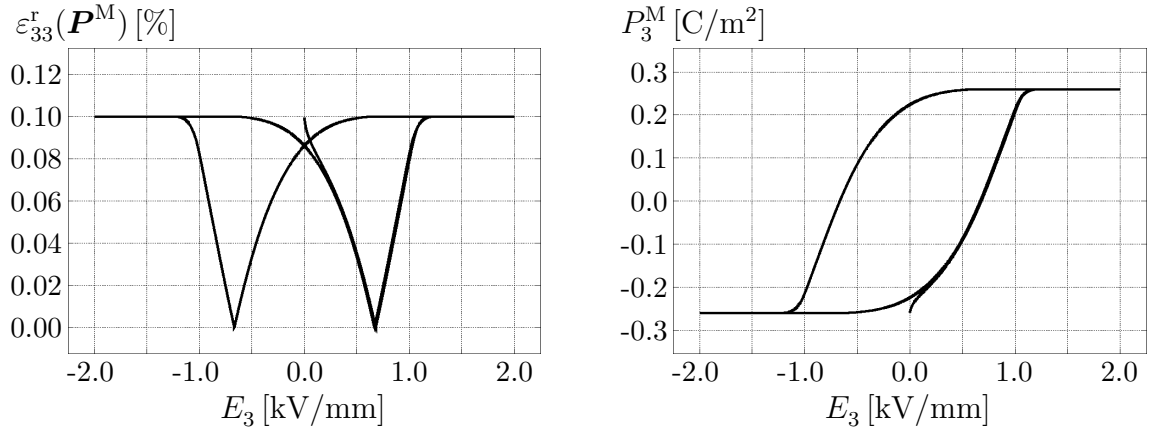


Figure 4.5: Remnant strain response (left) and average remnant polarisation response (right) corresponding to the butterfly and dielectric hysteresis curves plotted in Figure 4.4.

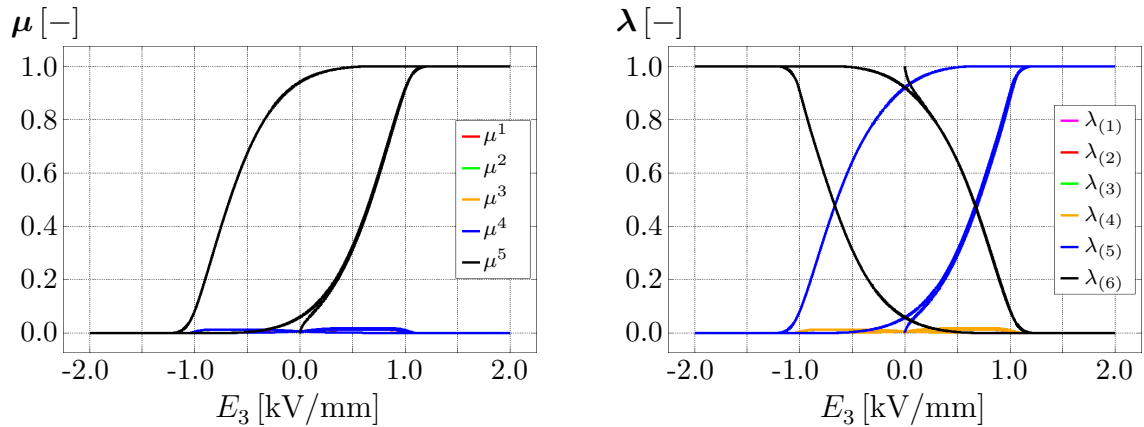


Figure 4.6: Evolution of the laminate volume fractions (left) and of the variant volume fractions (right) corresponding to the butterfly and dielectric hysteresis curves plotted in Figure 4.4.

the specimen, until the applied electric field reaches $E_3 = 2 \text{ kV/mm}$, the considered Fischer–Burmeister algorithm ensures that the maximum limit $\mu^5 = 1$ is not exceeded. At the maximum positive electrical loading of $E_3 = 2 \text{ kV/mm}$, the specimen remains poled along the positive \mathbf{e}_3 -axis.

From this maximum positive electrical load, the applied electric field is gradually reduced to $E_3 = 0 \text{ kV/mm}$ in steps of Δt . During this unloading phase, the specimen contracts linearly at first and then non-linearly before reaching the remnant state at $E_3 = 0 \text{ kV/mm}$. As predicted, the remnant state is characterised by an irreversible remnant strain $\varepsilon_{33}^r = \varepsilon^{\text{sat}} = \varepsilon_{33}$ and a non-vanishing remnant polarisation $P_3^M = P^{\text{sat}} = D_3$ for the perfect single crystal under study. Moreover, the poled configuration of the specimen along the positive \mathbf{e}_3 -axis is still preserved in the remnant state even after the removal of the external electrical loads.

Next, the specimen is loaded from $E_3 = 0 \text{ kV/mm}$ until the applied electrical load reaches $E_3 = -2 \text{ kV/mm}$. During this phase, the laminate volume fraction μ^5 decreases non-linearly from $\mu^5 \approx 0.95$ at $E_3 = 0 \text{ kV/mm}$ to $\mu^5 \approx 0$ at $E_3 = -2 \text{ kV/mm}$. The reduction in the magnitude of μ^5 corresponds directly to the decrease in the value of P_3^M followed by the reversal of P_3^M by 180° . At $E_3 = -2 \text{ kV/mm}$ the magnitude of remnant polarisation equals $-P^s$. Due to 180° remnant polarisation switching, the specimen is now poled along the negative \mathbf{e}_3 -axis. Note, that the resulting ε_{33} values at $E_3 = \pm 2 \text{ kV/mm}$ are identical even though the specimen is poled in opposite directions. This is due to the total strains being symmetric.

Subsequent increase in electrical loading to 2 kV/mm re-orientates the particular laminate volume fraction μ^5 , and hence the remnant polarisation P_3^M , back along the positive \mathbf{e}_3 -axis. Consequently, the specimen is now re-poled along the loading direction. The remnant state is recovered once the electric field is completely reduced to zero. The characteristic butterfly and dielectric hysteresis loops are thus numerically reproduced, see Figure 4.4. During the entire electrical loading and unloading of the specimen, only the laminate volume fraction μ^5 showed a predominant evolution and reduction in its values between 0 and 1. The other laminate volume fractions $\mu^{1,2,3,4}$ did not show a significant change from their initialised almost zero values highlighting the absence of 90° domain switching within the specimen, see Figure 4.6.

The influence of the viscous-like parameter and the dependence of loading frequency on the hysteretic response are studied in the following computations. After setting the slope parameter c to a constant value, the tests under homogeneous states of deformation are performed for two different positive values of viscous-like parameter m . With an electrical loading rate of 0.2 Hz and with slope parameter $c = 1.0$, the butterfly curves and dielectric hysteresis loops for two different values of viscous-like parameter m are plotted in Figure 4.7. The shape of both the strain and dielectric hysteresis curves differs for $m = 2.0$ and $m = 3.0$. In context of the strain response of the specimen for the two different viscous-like parameters, the total strains ε_{33} obtained at the remnant configuration is of a lower magnitude with $m = 3.0$ in comparison to the remnant strain obtained with $m = 2.0$. The magnitudes of ε_{33} at $E_3 = \pm 2 \text{ kV/mm}$ are lower for $m = 3.0$

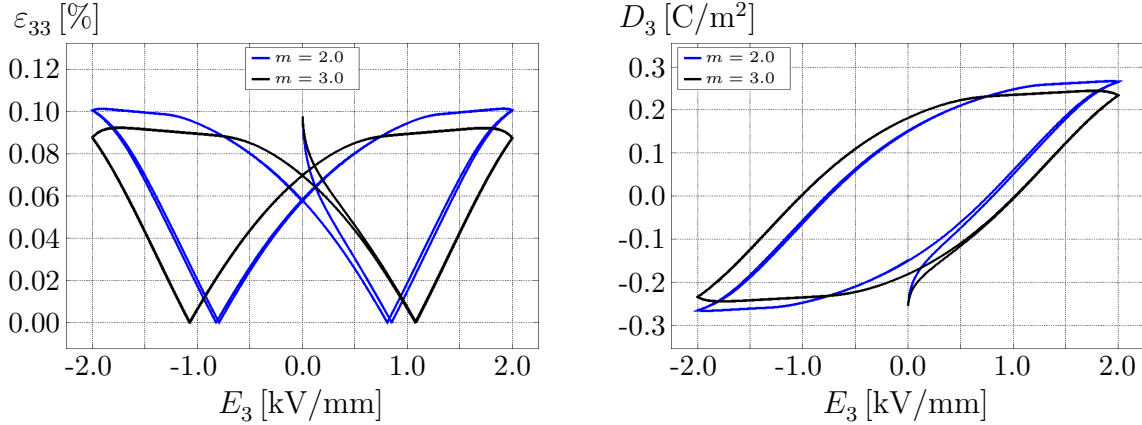


Figure 4.7: Influence of viscous-like parameter m on the hysteresis curves simulated with laminate-based Model 1 for slope parameter $c = 1$. Butterfly curves (left) and dielectric hysteresis loops (right) obtained for a single crystal BaTiO_3 specimen subjected to a cyclic electrical loading at 0.2 Hz.

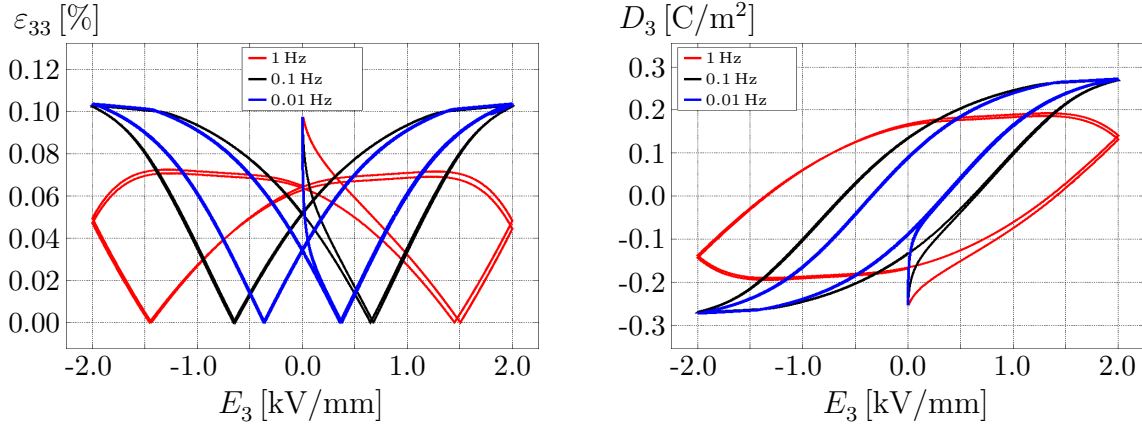


Figure 4.8: Rate-dependent hysteresis curves simulated with laminate-based Model 1 for $c = 1.0$ and for $m = 2.0$. Butterfly curves (left) and dielectric hysteresis loops (right) obtained for a single crystal BaTiO_3 specimen subjected to a cyclic electrical loading at varying frequencies of 1, 0.1 and 0.01 Hz.

compared to those obtained for $m = 2.0$. Moreover, with an increasing magnitude of the viscous-like parameter from $m = 2.0$ to 3.0, the dielectric hysteresis loops widen in shape during the entire loading and unloading process.

In order to study the rate-dependent behaviour, the last set of computations under homogeneous states of deformation are performed under varying electrical loading rates. By setting $c = 1.0$ and $m = 2.0$, the specimen is electrically loaded with three different frequencies of 1 Hz, 0.1 Hz and 0.01 Hz. The resulting butterfly curves and dielectric hysteresis loops are plotted in Figure 4.8. Both the total strain ε_{33} and dielectric displacement D_3 do not saturate around $E_3 = \pm 2 \text{ kV/mm}$ when loaded at higher frequencies of 1 Hz in comparison to the values obtained considering the other two loading frequencies. The incomplete switching of the ferroelectric domains within the specimen at higher loading rates is well predicted by laminate-based Model 1. At such high elec-

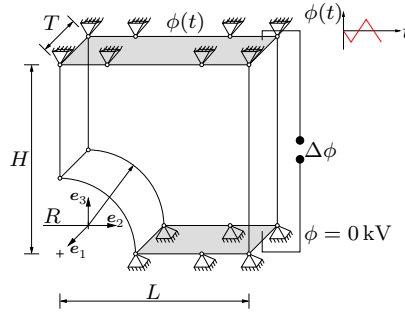


Figure 4.9: Schematic representation of the three-dimensional specimen along with loading curves and boundary conditions considered for the test under inhomogeneous states of deformation. The loading curve refers to the time-dependent electric potential applied at the top electrode of the specimen. The bottom electrode is grounded by setting $\phi = 0$ kV.

trical loading frequencies, laminate-based Model 1 also predicts the widening in shape of both the butterfly and dielectric displacement hysteresis curves.

4.4.1.2 Test under inhomogeneous states of deformation

In this subsection, the versatility of laminate-based Model 1 is demonstrated by solving an inhomogeneous boundary value problem. The specimen is a three-dimensional plate of planar dimensions $L \times H = 5 \text{ mm} \times 5 \text{ mm}$ and with a thickness $T = 1 \text{ mm}$. The plate has a radial cut measuring $R = 1.5 \text{ mm}$. Both the top and bottom surfaces of the plate are prescribed with zero values of displacements along all the three Cartesian directions. With respect to the electrical boundary conditions, both the top and bottom are prescribed with electric potential values. At the top surface, an alternating time-dependent electric potential $\phi(t)$ with $\phi^{\max} = \pm 10 \text{ kV}$ is applied to all the nodes, whereas the nodes at the bottom surface are grounded by prescribing $\phi = 0 \text{ kV}$. The schematic sketch of the specimen along with boundary and loading conditions are depicted in Figure 4.9. The plate is discretised by 200 tri-linear brick elements. Both the resulting strain and dielectric displacements are studied for an applied electrical frequency of 0.2 Hz and for model parameters $m = 2.0$ and $c = 3.0$.

The initial variant volume fractions are set to $\lambda_{(6)}|_{t_0} = 1$ and $\lambda_{(1,2,3,4,5)}|_{t_0} = 0$ at all integration points within the individual finite elements rendering an initial poled configuration of the specimen along the negative e_3 -axis. These initial variant volume fractions correspond directly to zero value of the multi-rank laminate volume fractions, i.e. $\mu^{1,2,3,4,5}|_{t_0} = 0$. For the defined boundary and loading conditions, the total strains and the dielectric displacements within the specimen are computed iteratively under external electrical loading. Figure 4.10 shows the distribution of electric potential ϕ , total strain ε_{33} and of dielectric displacement D_3 at different time intervals across the specimen.

Starting from the initial poled configuration, the applied electric potential difference is decreased in steps of Δt from $\Delta\phi|_{t_0} = 0 \text{ kV}$ until $\Delta\phi|_{t_{1.25}} = -10 \text{ kV}$. During this

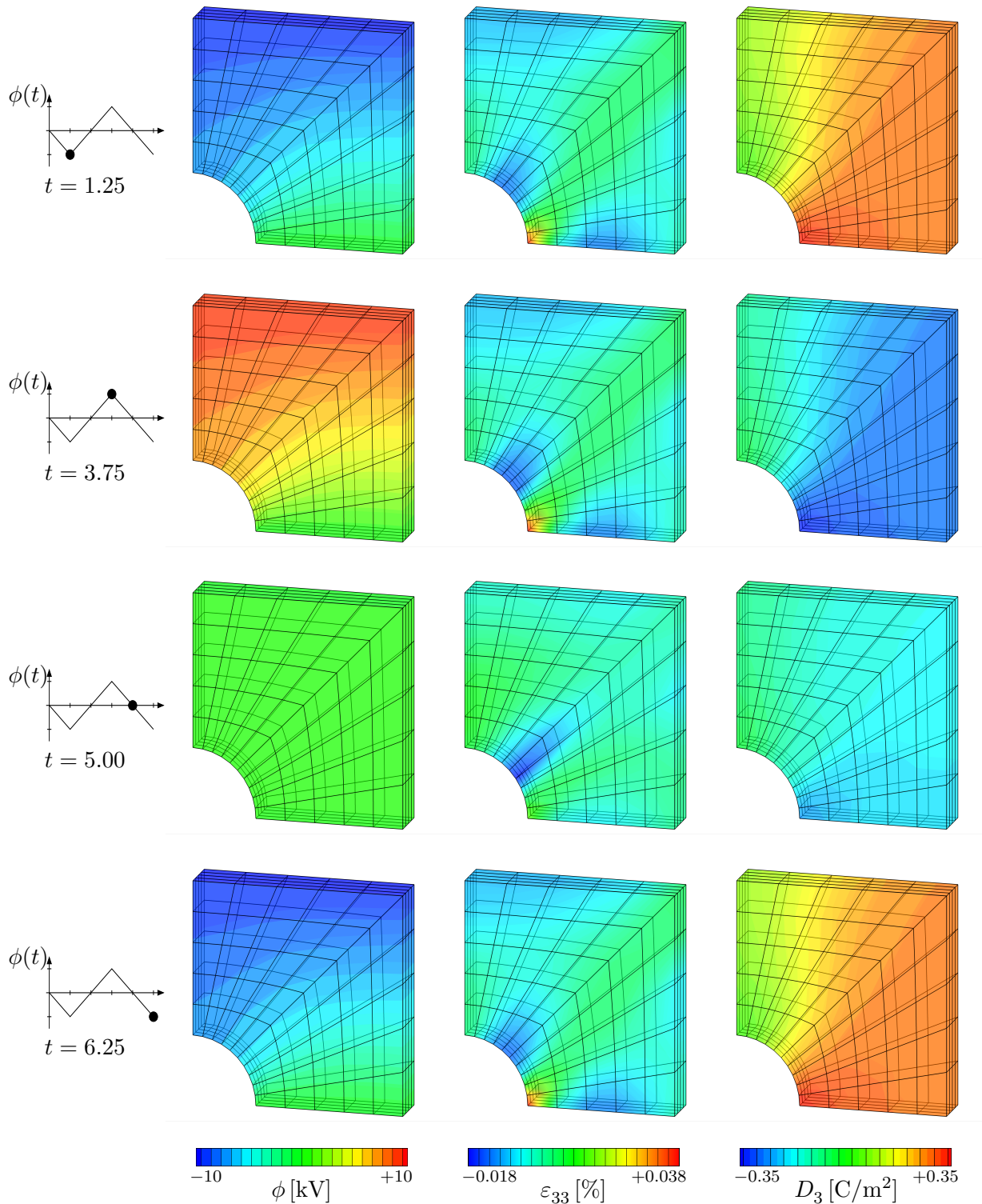


Figure 4.10: Contour plots of the scalar electric potential ϕ , total strain ε_{33} and dielectric displacement D_3 at different time intervals simulated with laminate-based Model 1. The load curve on the left-most side depicts the time-dependent electric potential loading at the top electrode.

loading phase, evolution of the multi-rank laminate volume fractions is initiated once the driving force corresponding to the particular laminates within the specimen exceeds the critical resistance force value. In context of the problem under study, the inhomogeneous loading and boundary conditions result in a non-uniform evolution of the laminate volume fractions within the specimen. This corresponds to the non-uniform distribution of the total strains and dielectric displacements within the specimen along the loading direction. At $t = 1.25$ sec, the generated negative maximum potential difference aligns the remnant polarisation along the positive \mathbf{e}_3 -direction, and the specimen attains a poled configuration along that direction. This is observed in Figure 4.10 with respect to the contour plots of ε_{33} and D_3 at $t = 1.25$ sec. From this negative maximum loading, the potential difference is increased until it reaches $\Delta\phi = 10$ kV at $t = 3.75$ sec. The load reversal initiates the evolution of the corresponding laminate volume fractions along the loading direction and hence switches the remnant polarisation by 180° . The specimen attains a poled configuration along the negative \mathbf{e}_3 -direction at $t = 3.75$ sec. The remnant state of the specimen is recovered at $t = 5$ sec. The specimen retains its poled configuration along the negative \mathbf{e}_3 -axis in its remnant state. Subsequent increase in loading until it reaches $\Delta\phi = -10$ kV at $t = 6.25$ sec re-orientes the specimen back along the positive \mathbf{e}_3 -direction.

4.4.2 Comparison of laminate-based Model 1 and phenomenological model

This section highlights the differences in the single crystal BaTiO_3 material responses obtained when considering the phenomenological model and laminate-based Model 1. With respect to the phenomenological model, the polarisation vector is treated as the only internal state variable. The evolution of the polarisation determines the remnant strain; dependence of energy storage on its direction results in generally transversely-isotropic material behaviour. In contrast, laminate-based Model 1 treats the volume fractions of the distinct ferroelectric as internal state variables. The evolution of these multi-rank laminate volume fractions determines, in turn, the remnant polarisation as volume averages of corresponding ferroelectric variant quantities. The respective model formulations, detailed in Sections 3.2 and 4.4 respectively, are compared in the context of numerical simulation examples considering three-dimensional specimens based on tests under both homogeneous and inhomogeneous states of deformation. The considered material parameters for the phenomenological and laminate-based Model 1 are listed in Tables 3.1 and 4.2 respectively. The influence of viscous-like parameter m and slope parameter c with respect to both the butterfly and dielectric hysteresis curves will be studied in the subsequent simulations.

With reference to the tests under homogeneous states of deformation, the boundary value problem depicted in Figure 4.3 is considered. In view of laminate-based Model 1, the initial multi-rank laminate volume fractions are set to zero values, i.e. $\mu^{1,2,3,4,5}|_{t_0} = 0$. Note, that this results in an initially poled specimen along the negative \mathbf{e}_3 -direction. In

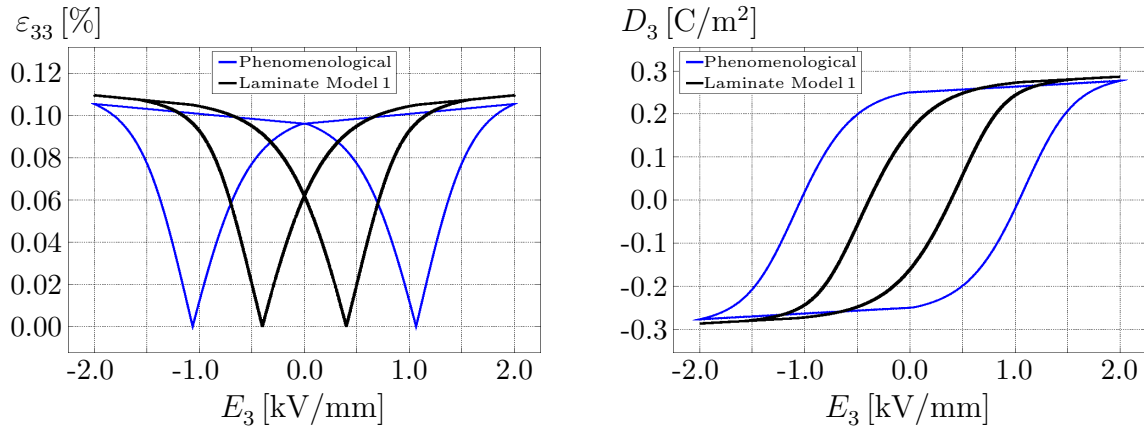


Figure 4.11: Comparison of the phenomenological model and laminate-based Model1 with respect to the butterfly curves (left) and dielectric displacement hysteresis loops (right) for a cyclic electrical load at 0.01 Hz and for $m = 2.0$, $c = 2.0$.

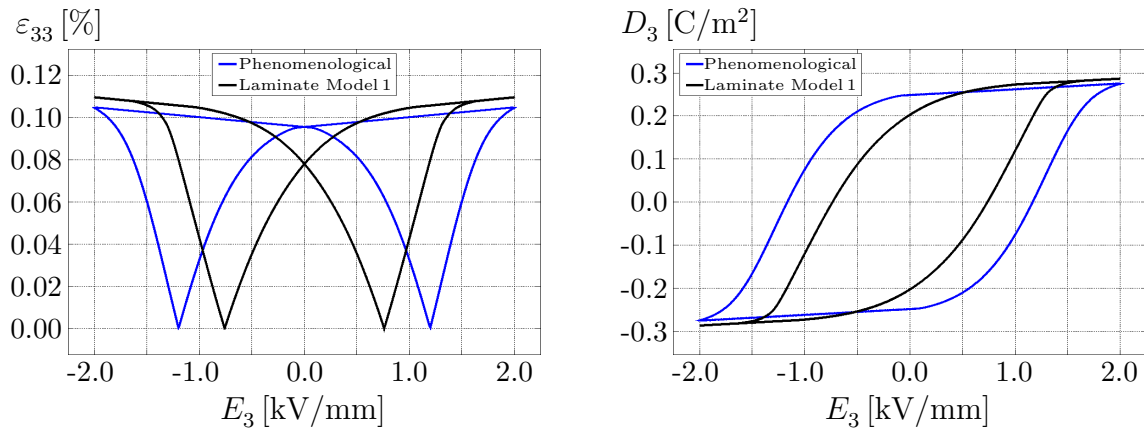


Figure 4.12: Comparison of the phenomenological model and laminate-based Model1 with respect to the butterfly curves (left) and dielectric displacement hysteresis loops (right) for a cyclic electrical load at 0.1 Hz and for $m = 2.0$, $c = 2.0$.

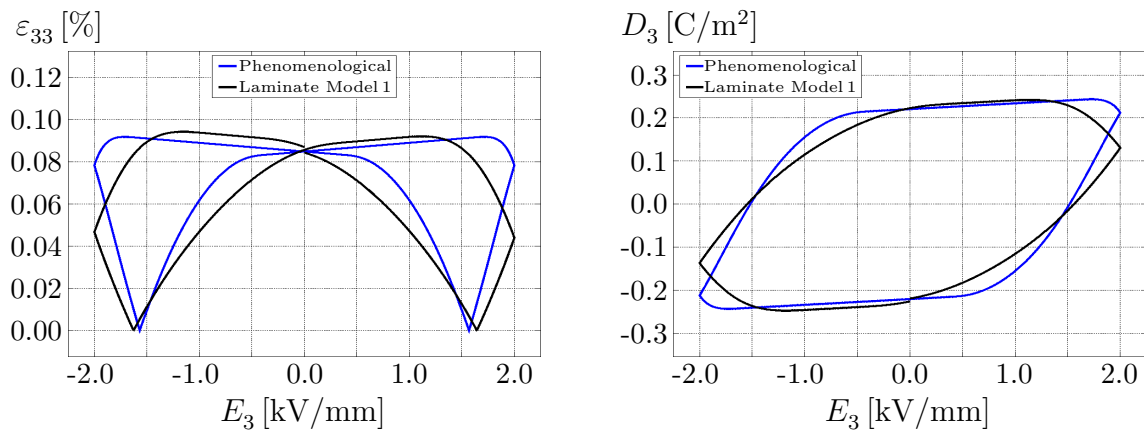


Figure 4.13: Comparison of the phenomenological model and laminate-based Model1 with respect to the butterfly curves (left) and dielectric displacement hysteresis loops (right) for a cyclic electrical load at 1 Hz and for $m = 2.0$, $c = 2.0$.

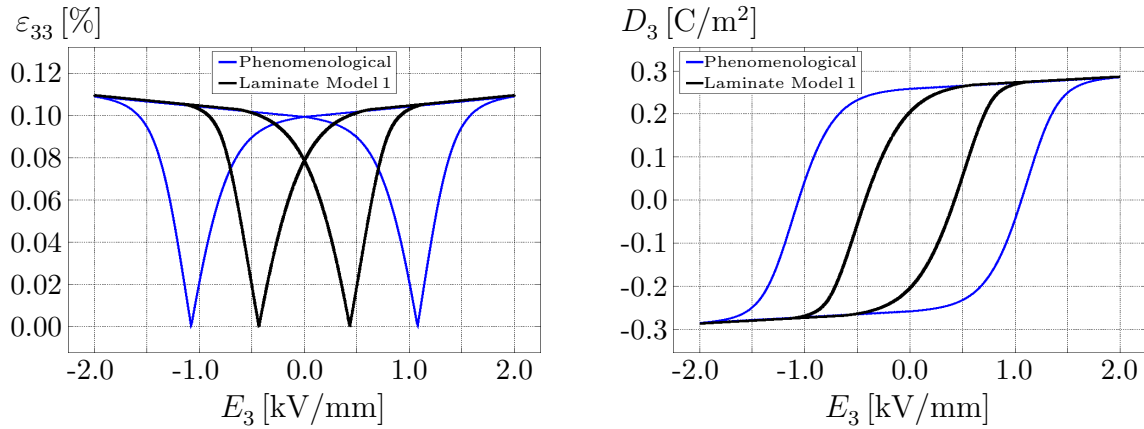


Figure 4.14: Comparison of the phenomenological model and laminate-based Model1 with respect to the butterfly curves (left) and dielectric displacement hysteresis loops (right) for a cyclic electrical load at 0.01 Hz and for $m = 2.0$, $c = 3.0$.

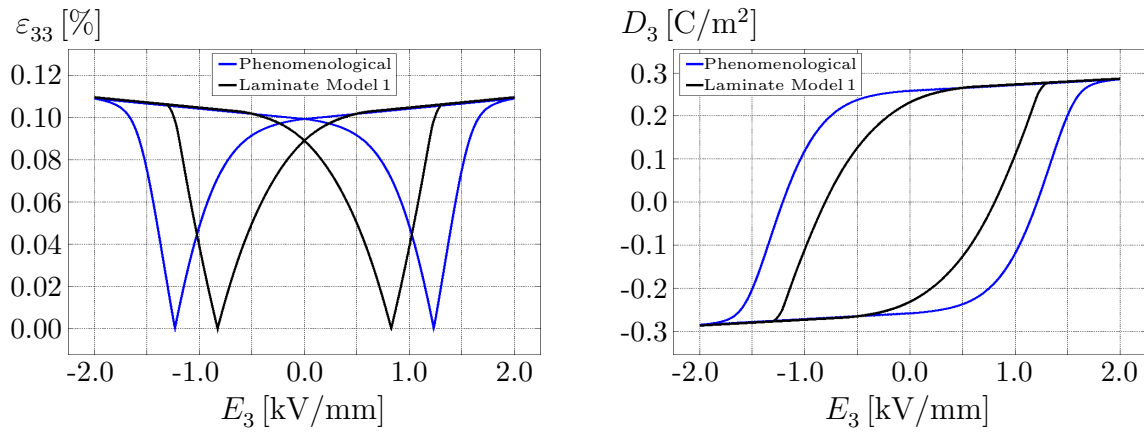


Figure 4.15: Comparison of the phenomenological model and laminate-based Model1 with respect to the butterfly curves (left) and dielectric displacement hysteresis loops (right) for a cyclic electrical load at 0.1 Hz and for $m = 2.0$, $c = 3.0$.

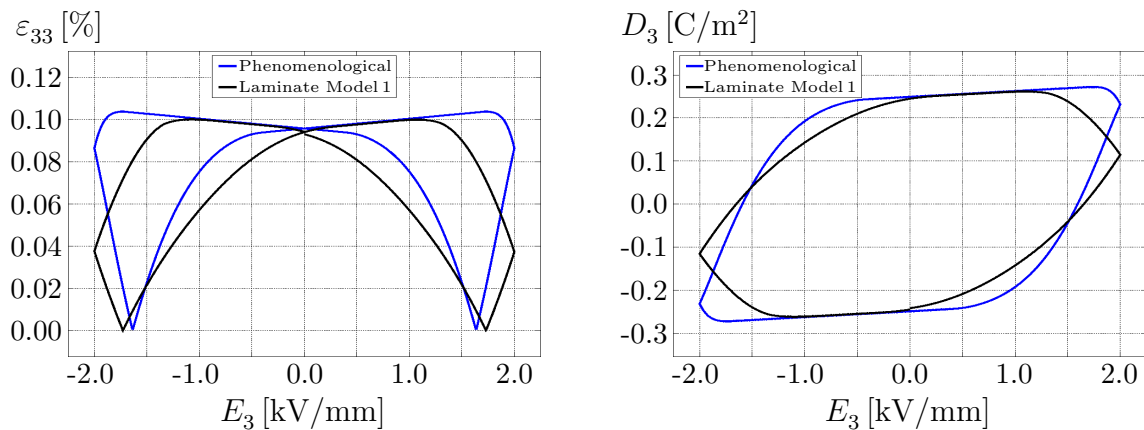


Figure 4.16: Comparison of the phenomenological model and laminate-based Model1 with respect to the butterfly curves (left) and dielectric displacement hysteresis loops (right) for a cyclic electrical load at 1 Hz and for $m = 2.0$, $c = 3.0$.

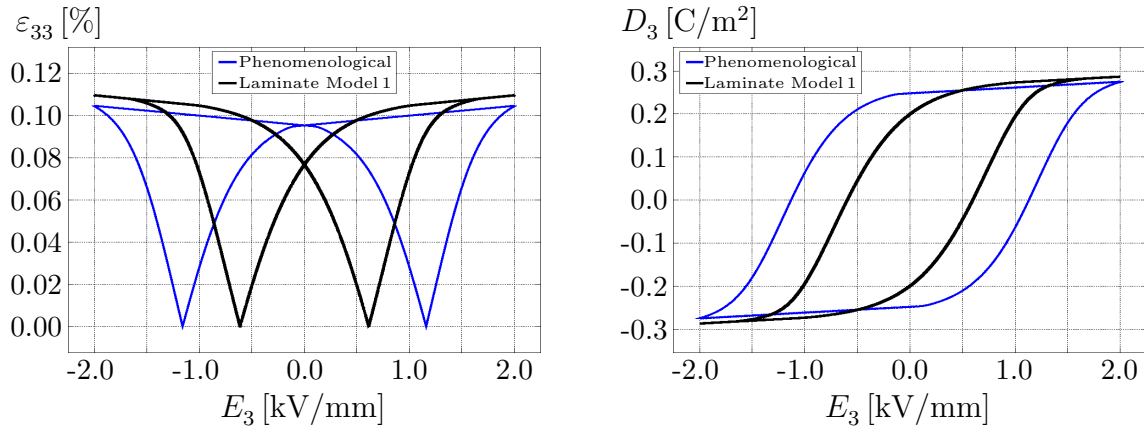


Figure 4.17: Comparison of the phenomenological model and laminate-based Model1 with respect to the butterfly curves (left) and dielectric displacement hysteresis loops (right) for a cyclic electrical load at 0.01 Hz and for $m = 3.0$, $c = 2.0$.

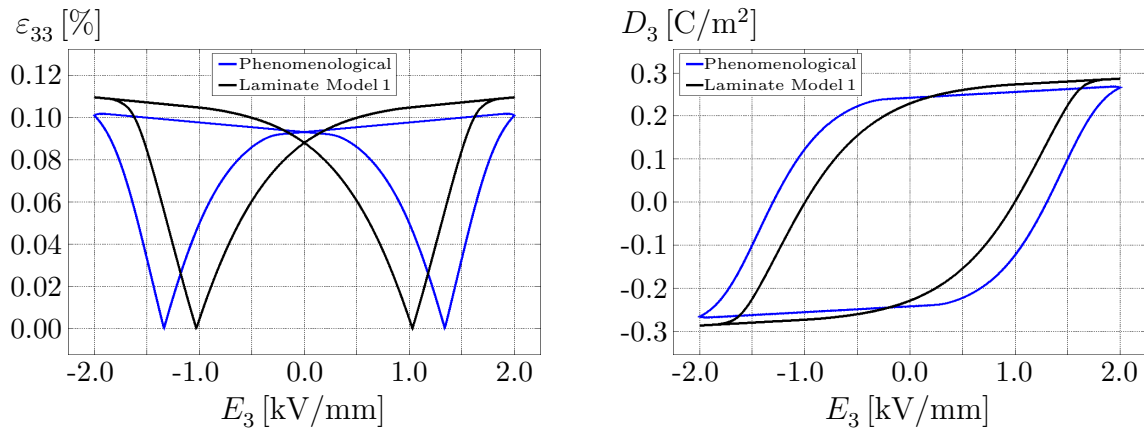


Figure 4.18: Comparison of the phenomenological model and laminate-based Model1 with respect to the butterfly curves (left) and dielectric displacement hysteresis loops (right) for a cyclic electrical load at 0.1 Hz and for $m = 3.0$, $c = 2.0$.

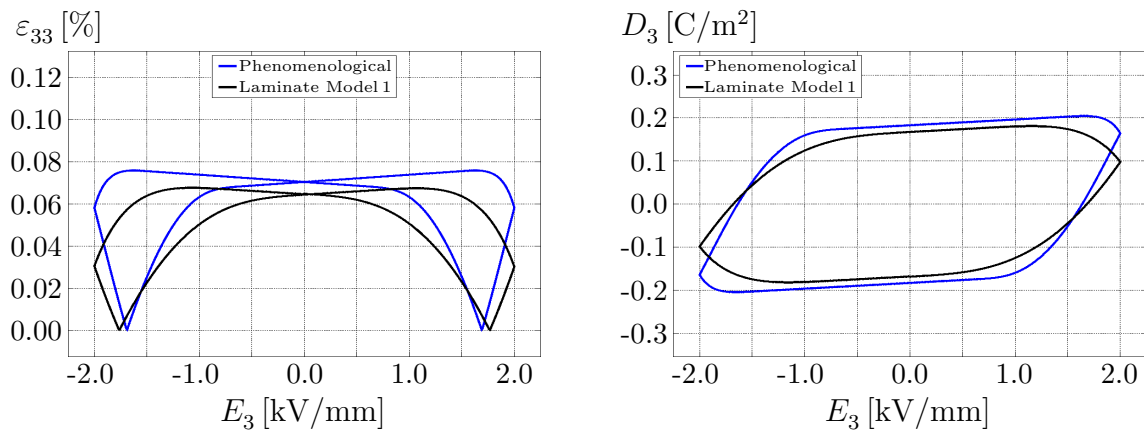


Figure 4.19: Comparison of the phenomenological model and laminate-based Model1 with respect to the butterfly curves (left) and dielectric displacement hysteresis loops (right) for a cyclic electrical load at 1 Hz and for $m = 3.0$, $c = 2.0$.

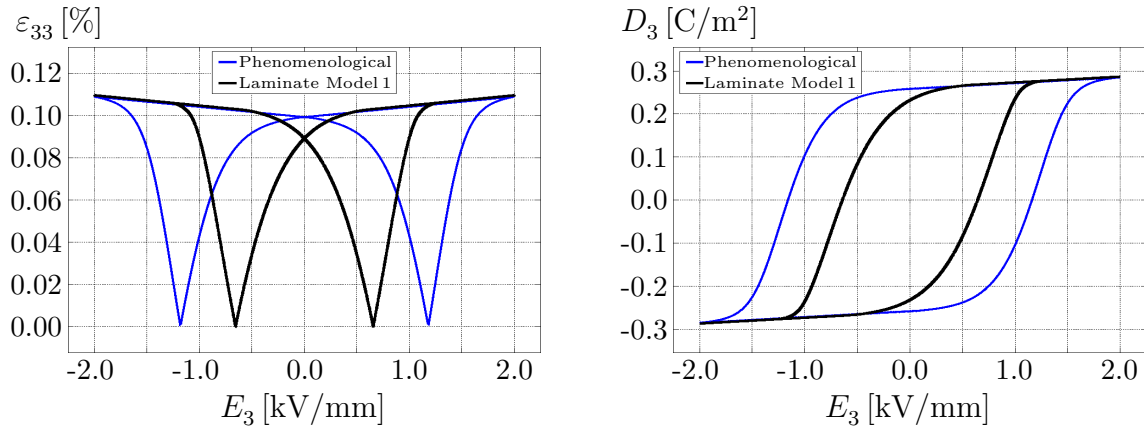


Figure 4.20: Comparison of the phenomenological model and laminate-based Model1 with respect to the butterfly curves (left) and dielectric displacement hysteresis loops (right) for a cyclic electrical load at 0.01 Hz and for $m = 3.0$, $c = 3.0$.

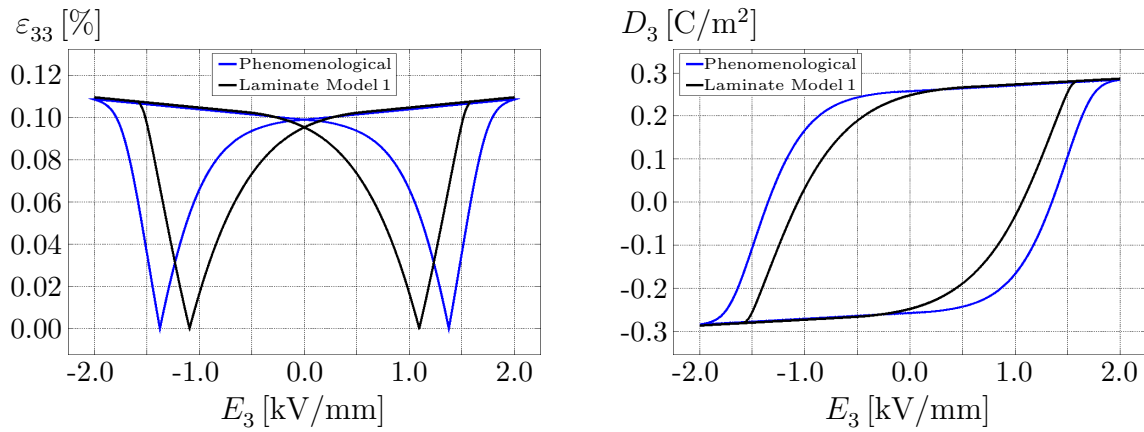


Figure 4.21: Comparison of the phenomenological model and laminate-based Model1 with respect to the butterfly curves (left) and dielectric displacement hysteresis loops (right) for a cyclic electrical load at 0.1 Hz and for $m = 3.0$, $c = 3.0$.

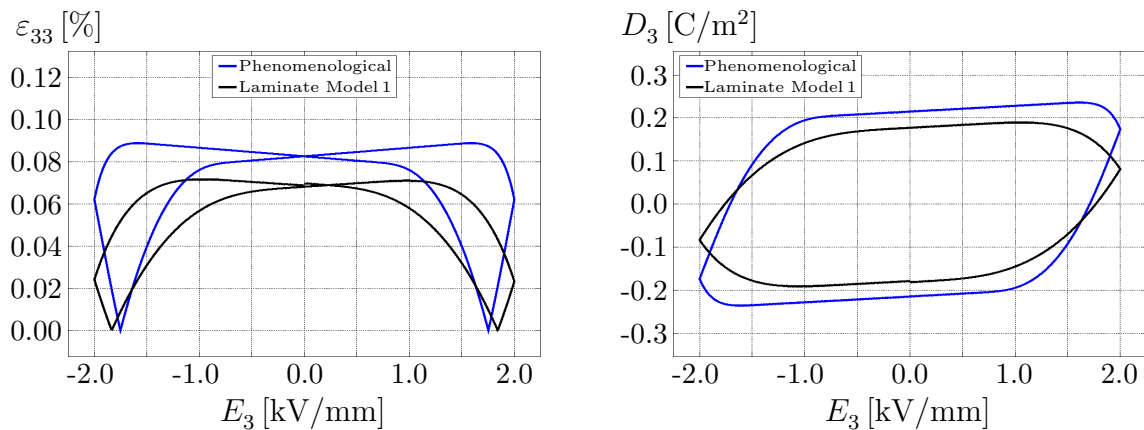


Figure 4.22: Comparison of the phenomenological model and laminate-based Model1 with respect to the butterfly curves (left) and dielectric displacement hysteresis loops (right) for a cyclic electrical load at 1 Hz and for $m = 3.0$, $c = 3.0$.

contrast, the initial state of the specimen is unpoled for the tests considering the phenomenological model. Due to the differences in the initial configurations, the butterfly and dielectric displacement hysteresis curves plotted in Figures 4.11 to 4.22 correspond to the second loading cycle.

Cyclic electrical loading under homogeneous deformations is considered. Under the action of a cyclic electric field, along the \mathbf{e}_3 -axis, the total strains and dielectric displacements are computed iteratively. In view of the phenomenological model, switching is initiated as the applied electric field E_3 reaches the coercive limit value E^c , such that the macroscopic remnant quantities, namely the remnant polarisation \mathbf{P}^r and the remnant strains $\boldsymbol{\varepsilon}^r(\mathbf{P}^r)$, evolve. With reference to laminate-based Model 1, evolution of the multi-rank laminate volume fractions $\boldsymbol{\mu}$ occurs as the driving forces exceed the critical threshold values which, in turn, are used to compute the average remnant polarisation \mathbf{P}^M . The simulated butterfly and dielectric hysteresis curves comparing the phenomenological model and laminate-based Model 1 for slope parameter $c = 2$ and for viscous-like parameter $m = 2$, for different electrical loading frequencies, are shown in Figures 4.11 to 4.13. The tests are repeated by setting different model parameter values. The hysteresis curves simulated with both the models for other sets of model parameter values are plotted, see Figures 4.14 to 4.22. The important features of the strain and dielectric hysteresis curves are recaptured by both models for all the considered loading rates and for the different model parameters. In particular, laminate-based Model 1 predicts a more pronounced rate-dependent response at higher loading frequencies, say at 1 Hz, in comparison to the phenomenological model, see Figures 4.13, 4.16, 4.19 and 4.22. The incomplete domain switching evident in the ferroelectric crystals at higher frequencies is well reciprocated by laminate-based Model 1 for all sets of model parameter values. The region of switching initiation observed in the strain and dielectric hysteresis plots differs for both models. This difference is due to the fact that the coercive electric field E^c , defining the macroscopic polarisation evolution, is a direct input parameter for the phenomenological model. In view of laminate-based Model 1, the domain wall motion is initiated once the driving force exceeds the corresponding threshold value for the particular laminate, and hence the switching initialisation is not based on an input parameter. Both the modelling frameworks nicely recapture the underlying dissipative and rate-dependent effects, represented by means of simulated butterfly and dielectric hysteresis loops. The differences in the hysteresis curves between the two models also reflect that the phenomenological model is motivated from the modelling of polycrystalline ferroelectric solids, whereas laminate-based Model 1 is designed specifically to capture the response of the single crystalline ferroelectric materials.

The boundary value problem sketched in Figure 4.9 is chosen for the comparison of the phenomenological model and laminate-based Model 1 in context of the tests under inhomogeneous states of deformation. The planar dimensions of the specimen are $L \times H = 5 \text{ mm} \times 5 \text{ mm}$ and thickness $T = 1 \text{ mm}$. The radial cut in the plate measures $R = 1.5 \text{ mm}$. The plate is discretised by 200 tri-linear brick elements. Both the top and bottom surfaces of the plate are prescribed with zero values of displacements along all

4 Laminate-based modelling of single crystalline ferroelectric materials

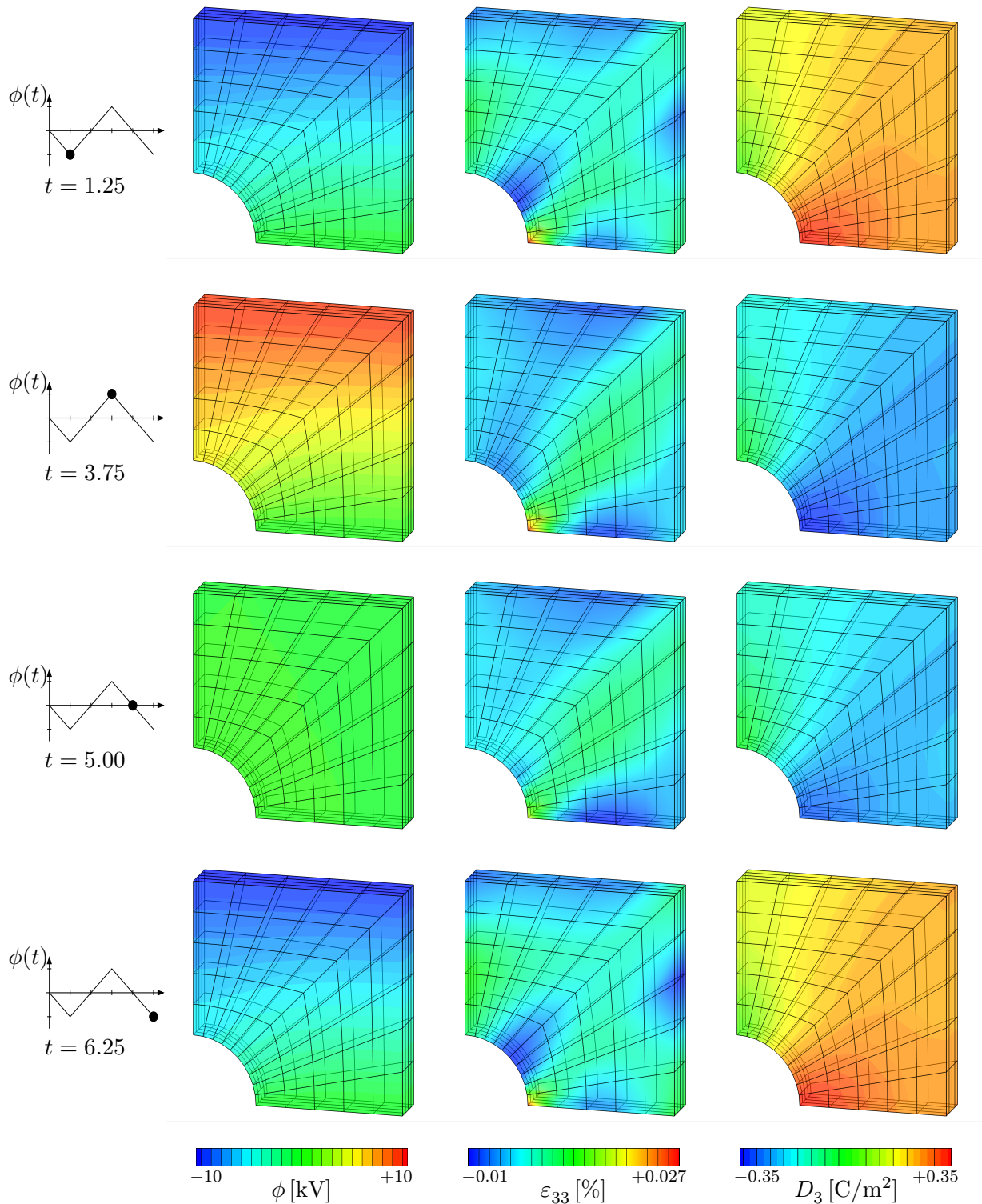


Figure 4.23: Phenomenological model: contour plots of the scalar electric potential ϕ , total strain ε_{33} and dielectric displacement D_3 at different time intervals for model parameters $m = 1.5$, $c = 3.5$. The load curve on the left-most side depicts the time-dependent electric potential loading at the top electrode.

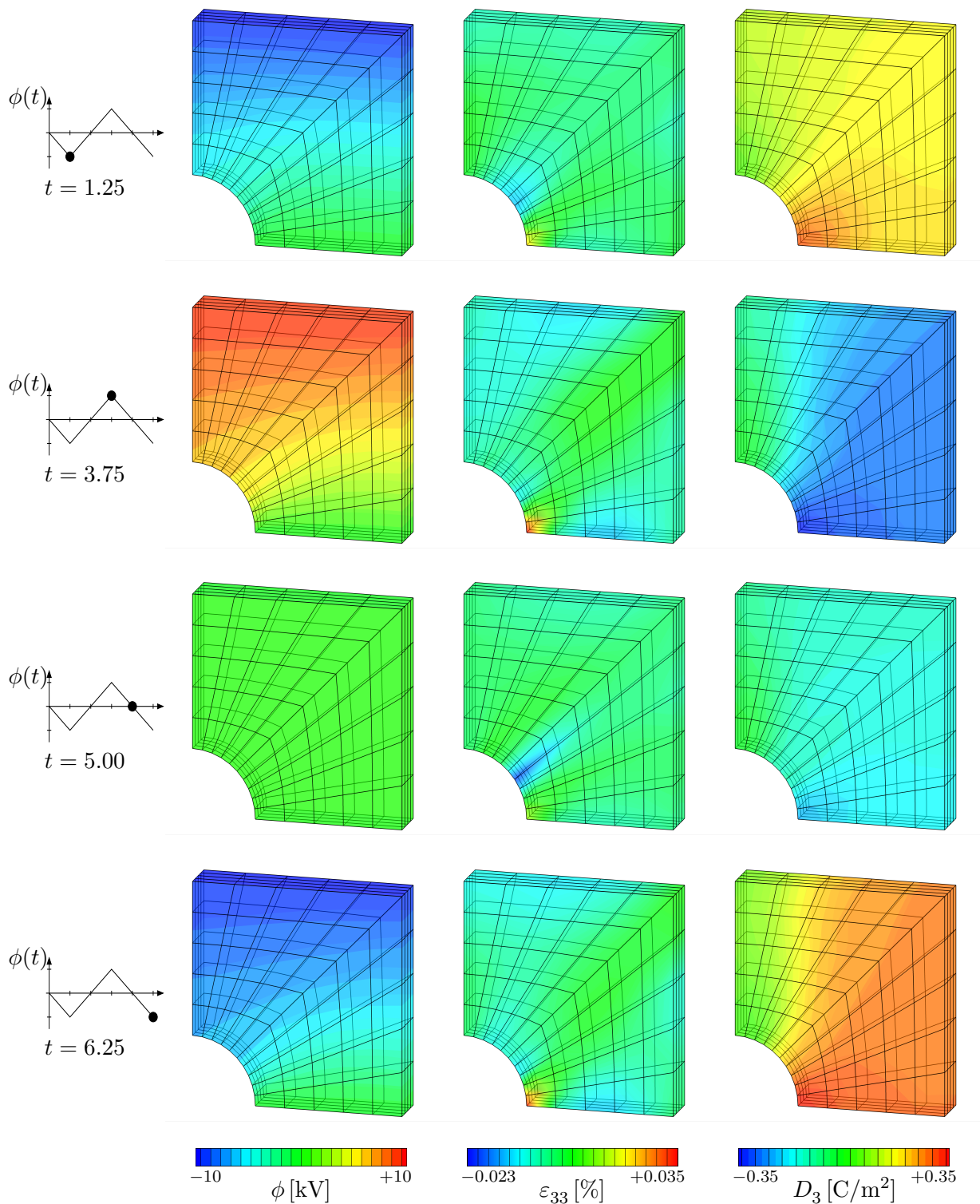


Figure 4.24: Laminate-based Model 1: contour plots of the scalar electric potential ϕ , total strain ε_{33} and dielectric displacement D_3 at different time intervals for model parameters $m = 1.5$, $c = 3.5$. The load curve on the left-most side depicts the time-dependent electric potential loading at the top electrode.

the three Cartesian directions. With respect to the electrical boundary conditions, an alternating time-dependent electric potential with $\phi^{\max} = \pm 10$ kV is applied to all the nodes at the top surface. All the nodes at the bottom surface are grounded by prescribing $\phi = 0$ kV. The comparison of the phenomenological model and laminate-based Model 1 with respect to the obtained strain and dielectric displacement distributions within the specimen is studied for an applied cyclic electrical frequency of 0.2 Hz and for model parameters $m = 1.5$ and $c = 3.5$.

Analogous to the initial configuration of the specimen considered for the tests under homogeneous states of deformation, the initial multi-rank laminate volume fractions are set to $\mu^{1,2,3,4,5}|_{t_0} = 0$ for laminate-based Model 1 rendering an initially poled state of the inhomogeneous specimen along the negative \mathbf{e}_3 -direction. With respect to the phenomenological model, the initial state of the specimen is considered to be in an unpoled state. The distribution of the scalar electric potential ϕ , total strain ε_{33} and dielectric displacement D_3 at different time intervals along the loading direction across the specimen simulate with laminate-based Model 1 and the phenomenological models is shown in Figures 4.23 and 4.24. Due to the considered inhomogeneous boundary value problem, the distribution of the total strains and dielectric displacements within the specimen, for both the models, are non-uniform. The differences in the total strain distribution within the specimen between the two models are due to the different assumptions postulated for the remnant strain evolution. In the case of the phenomenological model, the macroscopic remnant strain is computed directly based on the evolution of remnant polarisation \mathbf{P}^r . With reference to laminate-based Model 1, the remnant strains are obtained based on remnant polarisation \mathbf{P}^M which are, in turn, dependent on the evolution of the multi-rank laminate volume fractions μ . Nevertheless, both the modelling frameworks nicely recapture the underlying polarisation switching effects evident in single crystal ferroelectric solids based on finite element simulations.

4.5 Laminate-based Model 2

This section focusses on the development of laminate-based Model 2. Based on the spontaneous strain and polarisation as well as on the material moduli introduced for each of the distinct tetragonal ferroelectric variants, an electric Gibbs energy $H_{(\alpha)}$ corresponding to the individual tetragonal ferroelectric variants α is postulated for the particular model formulation. Thus, each of the distinct states of the tetragonal single crystal BaTiO₃ is characterised by the energy level of the particular state. The variant specific electric Gibbs energy is formulated as a function of the elastic strains $\varepsilon_{(\alpha)}^e$, the electric field \mathbf{E} and of the structural vector $\mathbf{a}_{(\alpha)}$, defining the transversely-isotropic tetragonal ferroelectric unit cell. The elastic strains corresponding to the individual ferroelectric variants α is defined as

$$\varepsilon_{(\alpha)}^e = \boldsymbol{\varepsilon} - \boldsymbol{\varepsilon}_{(\alpha)}. \quad (4.58)$$

The particular form of the electric Gibbs energy for the distinct ferroelectric variant α is postulated as

$$H_{(\alpha)}(\boldsymbol{\varepsilon}, \mathbf{E}, \mathbf{a}_{(\alpha)}) = \frac{1}{2} [\boldsymbol{\varepsilon} - \boldsymbol{\varepsilon}_{(\alpha)}] : \mathbf{E}_{(\alpha)}(\mathbf{a}_{(\alpha)}) : [\boldsymbol{\varepsilon} - \boldsymbol{\varepsilon}_{(\alpha)}] - \frac{1}{2} \mathbf{E} \cdot \boldsymbol{\varepsilon}_{(\alpha)}(\mathbf{a}_{(\alpha)}) \cdot \mathbf{E} - \mathbf{E} \cdot \mathbf{e}_{(\alpha)}(\mathbf{a}_{(\alpha)}) : [\boldsymbol{\varepsilon} - \boldsymbol{\varepsilon}_{(\alpha)}] - \mathbf{P}_{(\alpha)} \cdot \mathbf{E}. \quad (4.59)$$

The variant specific quantities, namely the spontaneous strains and polarisation, $\boldsymbol{\varepsilon}_{(\alpha)}$ and $\mathbf{P}_{(\alpha)}$, the structural vector $\mathbf{a}_{(\alpha)}$ and the transversely-isotropic material moduli, $\mathbf{E}_{(\alpha)}(\mathbf{a}_{(\alpha)})$, $\boldsymbol{\varepsilon}_{(\alpha)}(\mathbf{a}_{(\alpha)})$ and $\mathbf{e}_{(\alpha)}(\mathbf{a}_{(\alpha)})$, are introduced in Equations (4.1) to (4.8). The individual electric Gibbs energies are weighted by the volume fraction of the respective variants in order to arrive at an average electric Gibbs energy for the single crystal. For a three-dimensional setting with $nv = 6$, the average electric Gibbs energy $H_{M2}(\boldsymbol{\varepsilon}, \mathbf{E}, \boldsymbol{\lambda})$ for laminate-based Model 2 is specified following the general relation (4.13) as

$$H_{M2}(\boldsymbol{\varepsilon}, \mathbf{E}, \boldsymbol{\lambda}) = \sum_{\alpha=1}^{nv} \lambda_{(\alpha)} H_{(\alpha)}(\boldsymbol{\varepsilon}, \mathbf{E}, \mathbf{a}_{(\alpha)}). \quad (4.60)$$

Considering the $\boldsymbol{\mu}$ -based representation, as introduced in Equation (4.16), wherein the domain quantities corresponding to the α -th variant volume fraction are related to the j -th rank multi-rank laminate volume fraction μ^j , the average electric Gibbs energy (4.60) is reformulated based on the multi-rank laminate volume fractions $\boldsymbol{\mu}$ as

$$\begin{aligned} H_{M2}(\boldsymbol{\varepsilon}, \mathbf{E}, \boldsymbol{\mu}) &= \mu^1 H_{(1)} + \mu^2 [1 - \mu^1] H_{(2)} \\ &+ [1 - \mu^1] [1 - \mu^2] [\mu^3 H_{(3)} + \mu^4 [1 - \mu^3] H_{(4)}] \\ &+ [1 - \mu^1] [1 - \mu^2] [1 - \mu^3] [1 - \mu^4] [\mu^5 H_{(5)} + [1 - \mu^5] H_{(6)}]. \end{aligned} \quad (4.61)$$

With the average electric Gibbs energy governing the coupled electromechanical response of the ferroelectric single crystal postulated, the constitutive equations for the stress tensor and the dielectric displacement vector of the single crystal for laminate-based Model 2 are obtained following the standard Coleman–Noll procedure as

$$\boldsymbol{\sigma}_{M2} = \frac{\partial H_{M2}(\boldsymbol{\varepsilon}, \mathbf{E}, \boldsymbol{\mu})}{\partial \boldsymbol{\varepsilon}} \quad \text{and} \quad (4.62)$$

$$\mathbf{D}_{M2} = - \frac{\partial H_{M2}(\boldsymbol{\varepsilon}, \mathbf{E}, \boldsymbol{\mu})}{\partial \mathbf{E}}. \quad (4.63)$$

The explicit relations of the average stress tensor and the average dielectric displacement vector read

$$\begin{aligned} \boldsymbol{\sigma}_{M2} = & \mu^1 \boldsymbol{\sigma}_{(1)} + \mu^2 [1 - \mu^1] \boldsymbol{\sigma}_{(2)} + [1 - \mu^1] [1 - \mu^2] \left[\mu^3 \boldsymbol{\sigma}_{(3)} + \mu^4 [1 - \mu^3] \boldsymbol{\sigma}_{(4)} \right] \\ & + [1 - \mu^1] [1 - \mu^2] [1 - \mu^3] [1 - \mu^4] \left[\mu^5 \boldsymbol{\sigma}_{(5)} + [1 - \mu^5] \boldsymbol{\sigma}_{(6)} \right] \quad \text{and} \quad (4.64) \end{aligned}$$

$$\begin{aligned} \mathbf{D}_{M2} = & \mu^1 \mathbf{D}_{(1)} + \mu^2 [1 - \mu^1] \mathbf{D}_{(2)} + [1 - \mu^1] [1 - \mu^2] \left[\mu^3 \mathbf{D}_{(3)} + \mu^4 [1 - \mu^3] \mathbf{D}_{(4)} \right] \\ & + [1 - \mu^1] [1 - \mu^2] [1 - \mu^3] [1 - \mu^4] \left[\mu^5 \mathbf{D}_{(5)} + [1 - \mu^5] \mathbf{D}_{(6)} \right], \quad (4.65) \end{aligned}$$

wherein the second-order stress tensor $\boldsymbol{\sigma}_{(\alpha)}$ and dielectric displacement vector $\mathbf{D}_{(\alpha)}$ of the specific variant α are identified as

$$\boldsymbol{\sigma}_{(\alpha)} = \frac{\partial H_{(\alpha)}}{\partial \boldsymbol{\varepsilon}} = \mathbf{E}_{(\alpha)} : \boldsymbol{\varepsilon}_{(\alpha)}^e - \mathbf{e}_{(\alpha)}^t \cdot \mathbf{E} \quad \text{and} \quad (4.66)$$

$$\mathbf{D}_{(\alpha)} = - \frac{\partial H_{(\alpha)}}{\partial \mathbf{E}} = \mathbf{e}_{(\alpha)} : \boldsymbol{\varepsilon}_{(\alpha)}^e + \boldsymbol{\varepsilon}_{(\alpha)} \cdot \mathbf{E} + \mathbf{P}_{(\alpha)}. \quad (4.67)$$

The thermodynamic driving force responsible for the domain evolution and polarisation switching within the particular j -th rank laminate in the single crystal is identified as

$$f_{M2}^j(\boldsymbol{\mu}) = - \frac{\partial H_{M2}(\boldsymbol{\varepsilon}, \mathbf{E}, \boldsymbol{\mu})}{\partial \mu^j} \quad \text{for } j = 1, \dots, nv - 1, \quad (4.68)$$

wherein the derived relations for the individual driving forces read

$$\begin{aligned} f_{M2}^1(\boldsymbol{\mu}) = & - H_{(1)} + \mu^2 H_{(2)} + [1 - \mu^2] \left[\mu^3 H_{(3)} + \mu^4 [1 - \mu^3] H_{(4)} \right] \\ & + [1 - \mu^2] [1 - \mu^3] [1 - \mu^4] \left[\mu^5 H_{(5)} + [1 - \mu^5] H_{(6)} \right], \quad (4.69) \end{aligned}$$

$$\begin{aligned} f_{M2}^2(\boldsymbol{\mu}) = & - [1 - \mu^1] H_{(2)} + [1 - \mu^1] \left[\mu^3 H_{(3)} + \mu^4 [1 - \mu^3] H_{(4)} \right] \\ & + [1 - \mu^1] [1 - \mu^3] [1 - \mu^4] \left[\mu^5 H_{(5)} + [1 - \mu^5] H_{(6)} \right], \quad (4.70) \end{aligned}$$

$$\begin{aligned} f_{M2}^3(\boldsymbol{\mu}) = & [1 - \mu^1] [1 - \mu^2] \left[- H_{(3)} + \mu^4 H_{(4)} \right] \\ & + [1 - \mu^1] [1 - \mu^2] [1 - \mu^4] \left[\mu^5 H_{(5)} + [1 - \mu^5] H_{(6)} \right], \quad (4.71) \end{aligned}$$

$$f_{M2}^4(\boldsymbol{\mu}) = [1 - \mu^1] [1 - \mu^2] [1 - \mu^3] \left[- H_{(4)} + \mu^5 H_{(5)} + [1 - \mu^5] H_{(6)} \right] \quad \text{and} \quad (4.72)$$

$$f_{M2}^5(\boldsymbol{\mu}) = [1 - \mu^1] [1 - \mu^2] [1 - \mu^3] [1 - \mu^4] \left[- H_{(5)} + H_{(6)} \right]. \quad (4.73)$$

The derived driving forces corresponding to the individual laminates, Equations (4.69) to (4.73), are considered for the computation of the enhanced driving force expressions

$$f_{\text{enh}}^j(\boldsymbol{\mu}, \Gamma_I^j, \Gamma_{II}^j) = f_{\text{M2}}^j(\boldsymbol{\mu}) + \Gamma_I^j - \Gamma_{II}^j, \quad (4.74)$$

in context with the Fischer–Burmeister algorithm. The enhanced driving forces are considered in the modified Fischer–Burmeister residual (4.42) in order to arrive at the update of the multi-rank laminate volume fractions defining the hysteretic response for laminate-based Model 2.

4.5.1 Numerical examples

In order to verify the proposed laminate-based Model 2, representative numerical simulations under homogeneous states of deformation are performed and are presented in this section. The butterfly curves and the dielectric displacement hysteresis loops at varying frequencies are reproduced by the tests under homogeneous states of deformation. The domain considered is a three-dimensional poled specimen, the crystallographic axes of which are assumed to coincide with reference Cartesian axes $\mathbf{e}_{1,2,3}$. Based on the single crystal tetragonal BaTiO₃ material parameters, the poled specimen under study is subjected to purely cyclic electrical loading and to a combined electromechanical loading.

The single crystal tetragonal BaTiO₃ material constants, such as the piezoelectric coupling coefficients and the dielectric permittivity parameters are taken from Zgonik et al. [152]. The transversely-isotropic elasticity components of the single crystal are chosen from the values computed by Schröder and Keip [125]. The spontaneous polarisation and strain coefficients as well as the coercive electric field limits for 90° and 180° domain switching, all referring to single crystal tetragonal BaTiO₃, are taken from the data reported by Yen et al. [151]. The magnitude of the saturation polarisation is considered to be the same as its spontaneous polarisation value, with the assumption of a perfect single crystal devoid of any impurities. Apart from these material parameters, the model or fitting parameters such as viscosity-type parameter η^p , viscous-like parameter m and slope parameter c are initialised to non-zero positive values. Table 4.3 summarises the material parameters used in all of the subsequent numerical simulations. Note, that the single crystal material parameters in Table 4.3 refer to coefficients of tensors and, accordingly, to a particular base system, see Equations (4.9) to (4.11). Moreover, the listed material parameters in Table 4.3 are considered for all the simulations pertaining to the present laminate-based Model 2 as well as for all the numerical simulations considering laminate-based Models 3 and 4, to be dealt in Sections 4.6 and 4.7 respectively.

Table 4.3: Single crystal tetragonal BaTiO₃ material parameters used for the numerical computations with laminate-based Models 2, 3 and 4, taken from [125, 151, 152].

| Denomination | Parameter | Value | Unit | Reference |
|--|-------------------|-------------------------|---------------------|-----------|
| Lateral piezoelectric coefficient | e_{311} | -0.7 | C/m ² | [152] |
| Axial piezoelectric coefficient | e_{333} | 6.7 | C/m ² | [152] |
| Piezoelectric shearing coefficient | e_{131} | 34.2 | C/m ² | [152] |
| Vacuum permittivity | ϵ_0 | 8.854×10^{-12} | F/m | [152] |
| Dielectric permittivity | ϵ_{11} | $2200 \epsilon_0$ | F/m | [152] |
| Dielectric permittivity | ϵ_{33} | $56 \epsilon_0$ | F/m | [152] |
| Elastic stiffness | E_{1111} | 237.4×10^3 | MPa | [125] |
| Elastic stiffness | E_{1122} | 92.6×10^3 | MPa | [125] |
| Elastic stiffness | E_{1133} | 111×10^3 | MPa | [125] |
| Elastic stiffness | E_{3333} | 151×10^3 | MPa | [125] |
| Elastic stiffness | E_{1313} | 61×10^3 | MPa | [125] |
| Spontaneous polarisation | P^s | 0.26 | C/m ² | [151] |
| Spontaneous strain coefficient | η_1^s | 0.67 | % | [151] |
| Spontaneous strain coefficient | η_2^s | -0.42 | % | [151] |
| Coercive electric field for 90° switching | $E_{90^\circ}^c$ | 0.26 | kV/mm | [151] |
| Coercive electric field for 180° switching | $E_{180^\circ}^c$ | 0.23 | kV/mm | [151] |
| Saturation polarisation | P^{sat} | 0.26 | C/m ² | - |
| Viscosity-type parameter | η^p | 0.01 | m ² /C s | - |
| Viscous-like parameter | m | 1.5 | - | - |
| Slope parameter | c | 3.5 | - | - |

4.5.1.1 Tests under homogeneous states of deformation

The butterfly and dielectric hysteresis curves for single crystal tetragonal BaTiO₃ simulated with laminate-based Model 2 are reproduced by tests under homogeneous states of deformation. The representative single finite element is subjected to two different loading scenarios for varying electrical loading frequencies, namely cyclic electrical and combined electromechanical loading. The schematic sketches of the boundary value problems are depicted in Figure 4.25. The crystallographic axes of the specimen for the two homogeneous loading scenarios are assumed to coincide with reference Cartesian axes $e_{1,2,3}$.

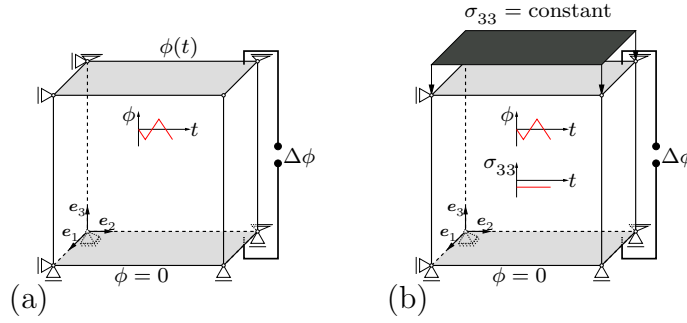


Figure 4.25: Schematic representation of three-dimensional specimens along with the load curves and boundary conditions considered for tests under homogeneous deformation with laminate-based Model 2. The specimens are subjected, respectively, to (a) cyclic electrical and (b) combined electromechanical load. For the two loading scenarios, the specimens are initially poled along the positive e_3 -axis.

By initialising the initial variant volume fraction values to $\lambda_{(1,2,3,4,6)}|_{t_0} = 0$ and $\lambda_{(5)}|_{t_0} = 1$ we arrive at the initial multi-rank laminate volume fractions $\mu^{1,2,3,4}|_{t_0} = 0$ and $\mu^5|_{t_0} = 1$. These starting values of the laminate volume fractions result in the initial poled configuration of the specimen along the positive e_3 -axis. For the first loading scenario, the poled specimen is subjected to a cyclic electric field applied along the Cartesian e_3 -axis as shown in Figure 4.25 (a). Starting from the poled configuration, the specimen deforms linearly with respect to the applied positive electric field and attains the maximum value of strain and dielectric displacement as the loading level approaches $E_3 = 2 \text{ kV/mm}$. This linear relationship between the electric field and strains as well as between the electric field and dielectric displacements for the initial loading path can be observed in the hysteresis plots, see Figures 4.26 and 4.28. Furthermore, with reference to Figure 4.27, it is observed that the laminate volume fraction μ^5 as well as the variant volume fraction $\lambda_{(5)}$ during this entire linear deformation does not change from its initial value, i.e. $\mu^5 = \lambda_{(5)} = 1$, indicating the piezoelectric response without any domain evolution in the specimen under study.

After decreasing the electric field from $E_3 = 2 \text{ kV/mm}$, the specimen undergoes a linear contraction along the e_3 -axis and reaches a remnant state at $E_3 = 0 \text{ kV/mm}$. The values of the remnant strain and polarisation of the specimen is identical to the starting values of total strains and dielectric displacements for laminate-based Model 2. As the applied electric field decreases further from 0 kV/mm , a 180° polarisation reversal of the specimen is initiated once the driving forces responsible for the domain evolution exceed the threshold values. The specimen is now switched along the negative e_3 -axis and attains the maximum value of deformation and the minimum value of dielectric displacement at $E_3 = -2 \text{ kV/mm}$. This can be further verified with the decrease of the variant volume fraction $\lambda_{(5)}$ from 1 to 0 and subsequently with the increase of $\lambda_{(6)}$ from 0 to 1, indicating poling along the negative e_3 -direction, see Figure 4.27. This 180° switching results in a hysteretic response as predicted by laminate-based Model 2, see Figure 4.26. Note, that the value of strains ϵ_{33} obtained at $E_3 = \pm 2 \text{ kV/mm}$ are identical due to the symmetric total strains. Further loading with positive electric fields

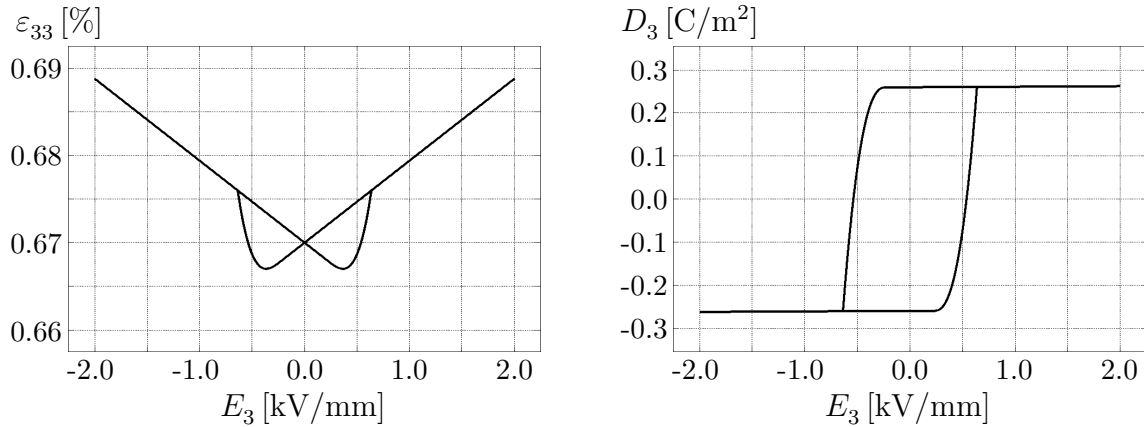


Figure 4.26: Hysteresis curves simulated with laminate-based Model 2 under homogeneous states of deformation. Butterfly curve (left) and dielectric hysteresis loop (right) obtained for a single crystal BaTiO₃ specimen subjected to a cyclic electrical loading at 0.2 Hz.

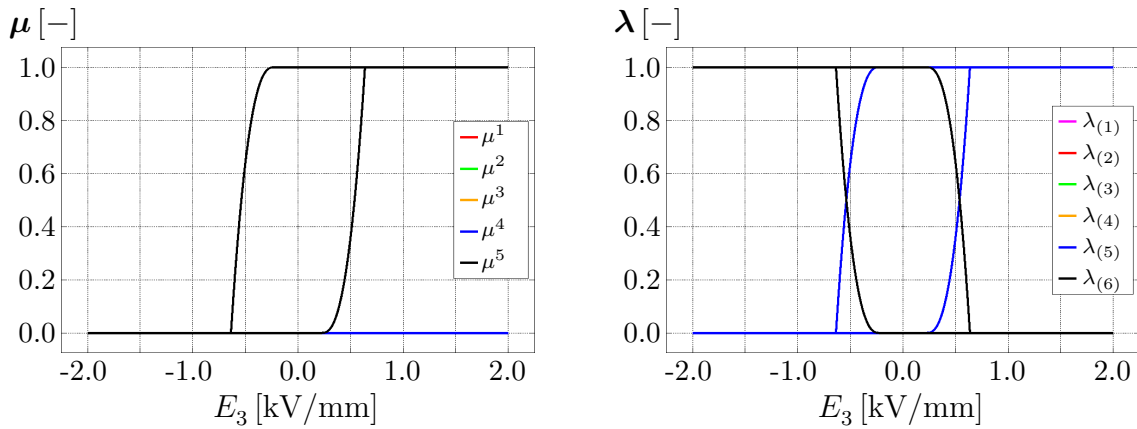


Figure 4.27: Evolution of the laminate volume fractions (left) and of the variant volume fractions (right) corresponding to the butterfly and dielectric hysteresis curves plotted in Figure 4.26.

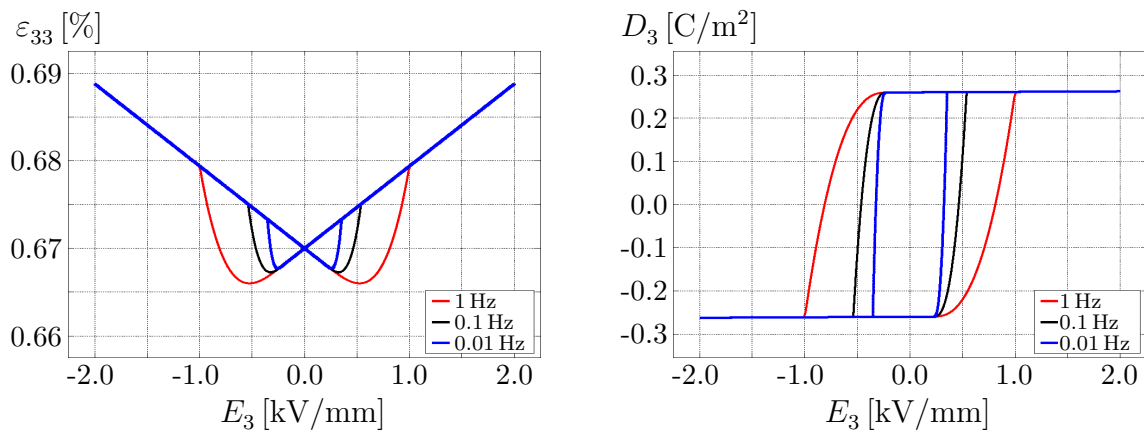


Figure 4.28: Rate-dependent hysteresis curves simulated with laminate-based Model 2. Butterfly curves (left) and dielectric hysteresis loops (right) obtained for a single crystal BaTiO₃ specimen subjected to a cyclic electrical loading at varying frequencies of 1, 0.1 and 0.01 Hz.

switches the specimen back to the positively-poled state, and the remnant state of the specimen is recovered once the electrical field is reduced to zero. In order to study the influence of loading rates, the specimen is electrically loaded with frequencies of 1 Hz, 0.1 Hz and 0.01 Hz. The rate-dependent hysteretic response of laminate-based Model 2 is shown in Figure 4.28. At 1 Hz, the magnitude of total strains ε_{33} increases along with the broadening of both strain and dielectric displacement hysteresis loops.

Starting from its poled configuration, the specimen is subjected to a combined electromechanical load, i.e. a constant compressive stress and a cyclic electric field, along the \mathbf{e}_3 -axis. The schematic sketch of the boundary value problem is depicted in Figure 4.25 (b). Such combined electromechanical loading of single crystal BaTiO_3 results in high actuation strains, mainly due to the enhancement of the stress-driven 90° ferroelastic switching, cf. [22, 131, 134, 151]. Furthermore, experimental studies show a significant increase in obtained actuation strains with an increase in magnitudes of the applied compressive stresses, cf. [95, 131, 151]. In context with the simulations carried out under combined electromechanical loading, laminate-based Model 2 did not predict an increase in magnitude of the actuation stress levels with an increase in the magnitude of the external compressive stresses along the electrical loading direction. The stress-activated 90° switching evident in single crystal tetragonal BaTiO_3 is not observed in both the strain and dielectric hysteresis curves with the particular laminate-based Model 2, see Figure 4.29. Only a shift in the butterfly curves with increasing mechanical loads is observed, without a notable difference in the shape of the strain response. The dielectric displacement D_3 for laminate-based Model 2 results in the same set of values for different stress levels. Thus, the dielectric hysteresis did not predict any change in shape with increasing stress magnitudes. The averaging principle used for laminate-based Model 2 does not appropriately predict the stress-driven 90° switching responsible for increased strain magnitudes under combined electromechanical loading. The response of the variant volume fractions against the applied electric load at a constant stress level of 2.7 MPa shows the evolution of only the volume fractions $\lambda_{(5)}$ and $\lambda_{(6)}$, both responsible for 180° domain switching in the specimen, see Figure 4.30. The other variant volume fractions $\lambda_{(1,2,3,4)}$ do not evolve from their initial zero values, augmenting the absence of 90° domain switching in the specimen during the entire cyclic loading process. The rate-dependent behaviour of the specimen with respect to laminate Model 2 is shown in Figure 4.31.

From the evolution of both the variant and laminate volume fractions and from the hysteresis curves under combined electromechanical loading, it is observed that the stress-driven response is not predicted by laminate-based Model 2. One reason may be that the magnitude of the driving forces, obtained as the negative sensitivity of the average electric Gibbs energy with respect to the corresponding laminate volume fractions, does not exceed the critical threshold values under combined electromechanical loading. This corresponds to the fact that the energy level corresponding to the variant specific electric Gibbs energy $H_{(\alpha)}$ is not influenced explicitly by the applied external stress magnitudes. In order to overcome this, an average Gibbs energy based on the stress and electric

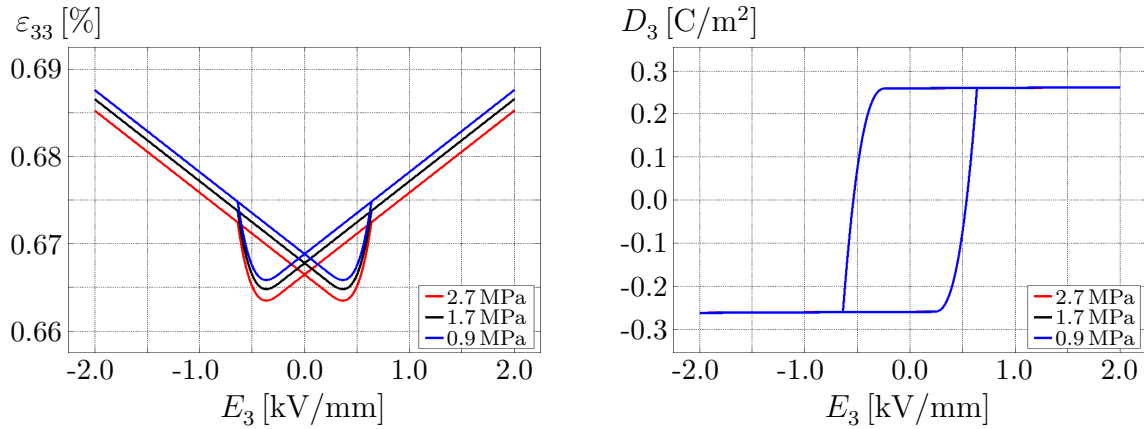


Figure 4.29: External-stress dependent hysteresis curves simulated with laminate-based Model 2 under homogeneous states of deformation for combined electromechanical loading. Butterfly curves (left) and dielectric hysteresis loops (right) obtained for a single crystal BaTiO₃ specimen subjected to a cyclic electrical loading at 0.2 Hz along with a constant compressive stress of varying magnitudes.

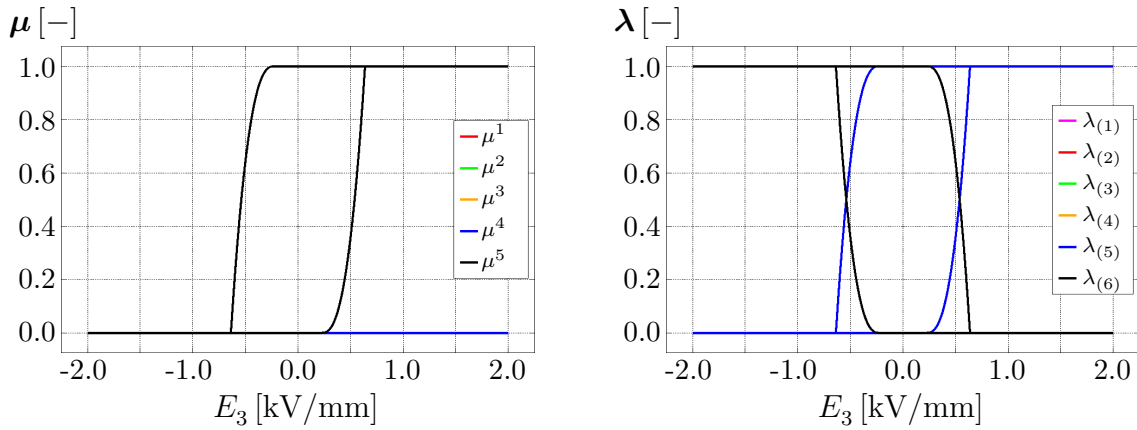


Figure 4.30: Evolution of the laminate volume fractions (left) and of the variant volume fractions (right) simulated with laminate-based Model 2 under homogeneous states of deformation for an applied electrical loading at 0.2 Hz along with a constant compressive stress of 2.7 MPa.

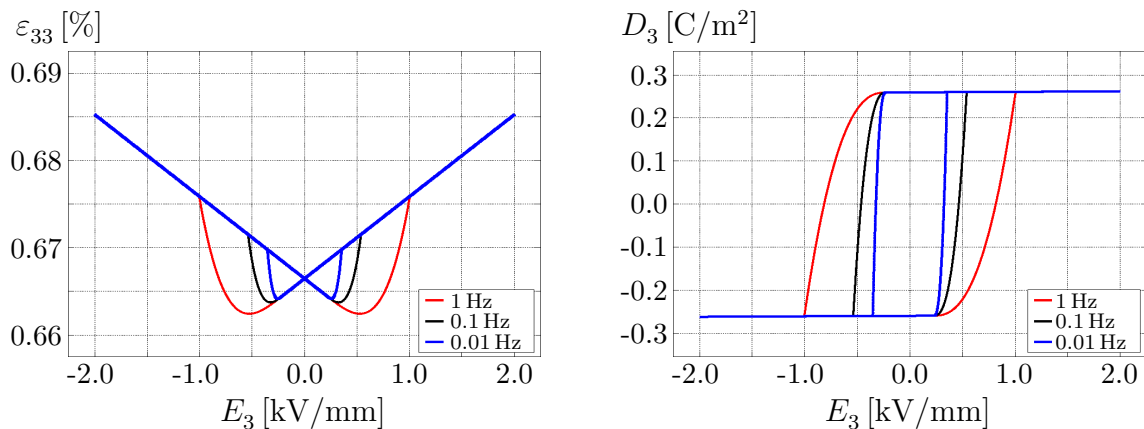


Figure 4.31: Rate-dependent hysteresis curves simulated with laminate-based Model 2 under homogeneous states of deformation for combined electromechanical loading. Butterfly curves (left) and dielectric hysteresis loops (right) obtained for a single crystal BaTiO₃ specimen subjected to a constant compressive stress of 2.7 MPa along with a cyclic electrical loading at varying frequencies.

field as independent variables is postulated for the crystal. On this basis, a Legendre transformation of the average electric Gibbs energy (4.60) with respect to the variable $\boldsymbol{\varepsilon}$ is performed resulting in the average Gibbs energy $G_{\text{M2}}(\partial H_{\text{M2}}/\partial \boldsymbol{\varepsilon}, \mathbf{E}, \boldsymbol{\lambda})$, namely

$$\begin{aligned} G_{\text{M2}}(\partial H/\partial \boldsymbol{\varepsilon}, \mathbf{E}, \boldsymbol{\lambda}) &= H_{\text{M2}}(\boldsymbol{\varepsilon}, \mathbf{E}, \boldsymbol{\lambda}) - \left. \frac{\partial H_{\text{M2}}}{\partial \boldsymbol{\varepsilon}} \right|_{\mathbf{E}} : \boldsymbol{\varepsilon} \\ &= \sum_{\alpha=1}^{nv} \lambda_{(\alpha)} H_{(\alpha)}(\boldsymbol{\varepsilon}, \mathbf{E}, \mathbf{a}_{(\alpha)}) - \boldsymbol{\sigma}_{\text{M2}} : \boldsymbol{\varepsilon}. \end{aligned} \quad (4.75)$$

For a three-dimensional setting with $nv = 6$, the average Gibbs energy is reformulated based on the multi-rank laminate volume fractions as

$$\begin{aligned} G_{\text{M2}}(\boldsymbol{\sigma}, \mathbf{E}, \boldsymbol{\mu}) &= \mu^1 H_{(1)} + \mu^2 [1 - \mu^1] H_{(2)} \\ &\quad + [1 - \mu^1] [1 - \mu^2] [\mu^3 H_{(3)} + \mu^4 [1 - \mu^3] H_{(4)}] \\ &\quad + [1 - \mu^1] [1 - \mu^2] [1 - \mu^3] [1 - \mu^4] [\mu^5 H_{(5)} + [1 - \mu^5] H_{(6)}] \\ &\quad - \boldsymbol{\sigma}_{\text{M2}} : \boldsymbol{\varepsilon}. \end{aligned} \quad (4.76)$$

The driving force defining the domain evolution within the j -th rank laminate is now introduced as

$$f_{\text{M2}}^j(\boldsymbol{\mu}) = - \frac{\partial G_{\text{M2}}(\boldsymbol{\sigma}, \mathbf{E}, \boldsymbol{\mu})}{\partial \mu^j} = - \frac{\partial H_{\text{M2}}(\boldsymbol{\varepsilon}, \mathbf{E}, \boldsymbol{\mu})}{\partial \mu^j} + \boldsymbol{\sigma}_{\text{M2}} : \frac{\partial \boldsymbol{\varepsilon}^{\text{M}}(\boldsymbol{\mu})}{\partial \mu^j}. \quad (4.77)$$

The enhanced driving force, needed for the Fischer–Burmeister algorithm, for a given constant stress tensor reads

$$f_{\text{enh}}^j(\boldsymbol{\mu}, \Gamma_I^j, \Gamma_{II}^j) = - \frac{\partial H_{\text{M2}}(\boldsymbol{\varepsilon}, \mathbf{E}, \boldsymbol{\mu})}{\partial \mu^j} + \boldsymbol{\sigma}_{\text{M2}} : \frac{\partial \boldsymbol{\varepsilon}^{\text{M}}(\boldsymbol{\mu})}{\partial \mu^j} + \Gamma_I^j - \Gamma_{II}^j. \quad (4.78)$$

Laminate-based Model 2 was implemented considering the enhanced driving force (4.78) and the numerical tests under homogeneous states of deformation under combined electromechanical loading were repeated. However, no significant difference is noted in the hysteresis loops as well as in the laminate volume fraction evolution curves with the average Gibbs energy formulation (4.76) in comparison to the response obtained by considering the average electric Gibbs energy (4.61). It can be concluded that laminate-based Model 2 is not suitable to predict the external stress-dependent hysteresis response in single crystal ferroelectric solids under combined electromechanical loading.

4.6 Laminate-based Model 3

On the basis of the general relations defining the symmetry and material properties of the distinct ferroelectric variants and by considering the general averaging principles, this section is devoted to the development of laminate-based Model 3. The particular model formulation is considered to study the external stress and rate-dependent domain evolution and the subsequent polarisation switching in tetragonal BaTiO₃ single crystals under external applied loads. In the context of laminate-based Model 3, both the average strain and polarisation compatibility conditions (4.12) are taken into account in defining the compatible evolution of the domains. Following Equations (4.17) and (4.18), the macroscopic remnant strain and polarisation for the single crystal are computed directly based on the evolution of the multi-rank volume fractions under suitable loading conditions.

Both total linear strain $\boldsymbol{\varepsilon}$ and the dielectric displacement \boldsymbol{D}_{M3} of the ferroelectric crystal for the laminate-based Model 3 are considered to be additively decomposed into an elastic and a remnant part as

$$\boldsymbol{\varepsilon} = \boldsymbol{\varepsilon}^e + \boldsymbol{\varepsilon}^M \quad \text{and} \quad \boldsymbol{D}_{M3} = \boldsymbol{D}^e + \boldsymbol{P}^M. \quad (4.79)$$

Here, $\boldsymbol{\varepsilon}^e$ denotes the reversible or elastic strain tensor and \boldsymbol{D}^e refers to the reversible dielectric displacement vector of the crystal. The remnant quantities $\boldsymbol{\varepsilon}^M(\boldsymbol{\mu}; \boldsymbol{\varepsilon}_{(1,3,5)})$ and $\boldsymbol{P}^M(\boldsymbol{\mu}; \boldsymbol{P}_{(1,3,5)})$ are defined in Equations (4.17) and (4.18) respectively.

An average electric Gibbs energy is specified, written as a function of the total linear strains, the electric field and of the multi-rank laminate volume fractions. The specific form of the average electric Gibbs energy defining the coupled electromechanical response of the crystal for the specific laminate-based Model 3 reads

$$\begin{aligned} H_{M3}(\boldsymbol{\varepsilon}, \boldsymbol{E}, \boldsymbol{\mu}) = & \frac{1}{2} [\boldsymbol{\varepsilon} - \boldsymbol{\varepsilon}^M] : \boldsymbol{E}^M : [\boldsymbol{\varepsilon} - \boldsymbol{\varepsilon}^M] - \frac{1}{2} \boldsymbol{E} \cdot \boldsymbol{\epsilon}^M \cdot \boldsymbol{E} \\ & - \boldsymbol{E} \cdot \boldsymbol{e}^M : [\boldsymbol{\varepsilon} - \boldsymbol{\varepsilon}^M] - \boldsymbol{P}^M \cdot \boldsymbol{E}. \end{aligned} \quad (4.80)$$

The average electric Gibbs energy takes an additive form comprising of mechanical, piezoelectric coupling and electrical terms. The volume averaged transversely-isotropic material moduli, namely the averaged fourth-order elasticity tensor $\boldsymbol{E}^M(\boldsymbol{\mu}; \boldsymbol{E}_{(1,3,5)})$, the averaged third-order piezoelectric tensor $\boldsymbol{e}^M(\boldsymbol{\mu}; \boldsymbol{e}_{(1,3,5)})$ and the averaged dielectric tensor $\boldsymbol{\epsilon}^M(\boldsymbol{\mu}; \boldsymbol{\epsilon}_{(1,3,5)})$ appearing in (4.80) are introduced in Equations (4.19) to (4.21). The specific form of the average electric Gibbs energy (4.80), considering the averaged anisotropic material moduli, differs from the laminate-based formulations presented in [41–43].

Following the standard Coleman–Noll procedure, the constitutive equations for the stress tensor and for the dielectric displacement vector of the crystal for laminate-based Model 3 are obtained as

$$\boldsymbol{\sigma}_{\text{M3}} = \frac{\partial H_{\text{M3}}(\boldsymbol{\varepsilon}, \mathbf{E}, \boldsymbol{\mu})}{\partial \boldsymbol{\varepsilon}} = \mathbf{E}^{\text{M}} : [\boldsymbol{\varepsilon} - \boldsymbol{\varepsilon}^{\text{M}}] - [\mathbf{e}^{\text{M}}]^{\text{t}} \cdot \mathbf{E} \quad \text{and} \quad (4.81)$$

$$\mathbf{D}_{\text{M3}} = - \frac{\partial H_{\text{M3}}(\boldsymbol{\varepsilon}, \mathbf{E}, \boldsymbol{\mu})}{\partial \mathbf{E}} = \mathbf{e}^{\text{M}} : [\boldsymbol{\varepsilon} - \boldsymbol{\varepsilon}^{\text{M}}] + \boldsymbol{\varepsilon}^{\text{M}} \cdot \mathbf{E} + \mathbf{P}^{\text{M}}, \quad (4.82)$$

and the reduced dissipation inequality is given by

$$\mathcal{D}_{\text{red}} = \sum_{j=1}^{nv-1} f_{\text{M3}}^j(\boldsymbol{\mu}) \dot{\mu}^j \geq 0. \quad (4.83)$$

Herein, $f_{\text{M3}}^j(\boldsymbol{\mu})$ is the thermodynamic driving force corresponding to the particular j -th rank laminate for laminate-based Model 3. The individual driving forces, defined as the work conjugate to the rate of change of the corresponding multi-rank volume fraction $\dot{\mu}^j$, are identified as

$$\begin{aligned} f_{\text{M3}}^j(\boldsymbol{\mu}) &= - \frac{\partial H_{\text{M3}}(\boldsymbol{\varepsilon}, \mathbf{E}, \boldsymbol{\mu})}{\partial \mu^j} \\ &= \frac{\partial \boldsymbol{\varepsilon}^{\text{M}}}{\partial \mu^j} : \boldsymbol{\sigma}_{\text{M3}} - \frac{1}{2} [\boldsymbol{\varepsilon} - \boldsymbol{\varepsilon}^{\text{M}}] : \frac{\partial \mathbf{E}^{\text{M}}}{\partial \mu^j} : [\boldsymbol{\varepsilon} - \boldsymbol{\varepsilon}^{\text{M}}] + \frac{1}{2} \mathbf{E} \cdot \frac{\partial \boldsymbol{\varepsilon}^{\text{M}}}{\partial \mu^j} \cdot \mathbf{E} \\ &\quad + \mathbf{E} \cdot \frac{\partial \mathbf{e}^{\text{M}}}{\partial \mu^j} : [\boldsymbol{\varepsilon} - \boldsymbol{\varepsilon}^{\text{M}}] + \frac{\partial \mathbf{P}^{\text{M}}}{\partial \mu^j} \cdot \mathbf{E}. \end{aligned} \quad (4.84)$$

The driving forces $f_{\text{M3}}^j(\boldsymbol{\mu})$ defining the domain evolution are resisted by the dissipative motion of the domain walls, cf. [57, 151]. The critical resistance forces or threshold values corresponding to the j -th rank laminate are denoted by $g^{c,j}(\boldsymbol{\mu}) \geq 0$, see Equations (4.26) to (4.30) for the explicit forms.

In view of the Fischer–Burmeister algorithm, the obtained set of driving forces (4.84) are reformulated into an enhanced form by considering the additional Lagrange multipliers

$$f_{\text{enh}}^j(\boldsymbol{\mu}, \Gamma_I^j, \Gamma_{II}^j) = f_{\text{M3}}^j(\boldsymbol{\mu}) + \Gamma_I^j - \Gamma_{II}^j, \quad (4.85)$$

cf. Equation (4.40). The enhanced driving force for the j -th rank laminate system is considered in the elastic range definition (4.25) and in the subsequent rate-dependent evolution equation (4.32) as well as in the modified Fischer–Burmeister residual (4.42) in order to arrive at the update of the multi-rank laminate volume fractions defining the hysteretic response. With respect to the algorithmic scheme, the reader is referred to Section 4.3.

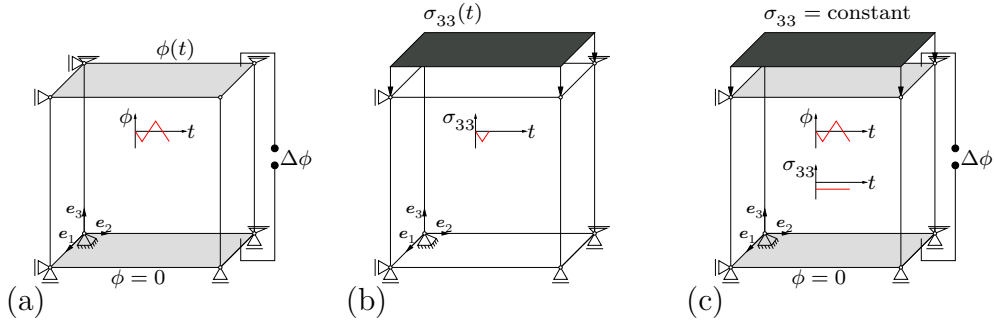


Figure 4.32: Schematic representation of the three-dimensional specimens along with the boundary conditions and load curves considered for the tests under homogeneous states of deformation. The specimens are subjected respectively to (a) cyclic electrical loading, (b) compressive mechanical loading and to (c) combined electromechanical loading. For the three individual loading scenarios, the specimens are initially poled along the positive e_3 -axis.

4.6.1 Numerical examples

In this section, the single crystal tetragonal BaTiO_3 material response under homogeneous states of deformation is presented for the particular laminate-based Model 3 formulation. The strain and dielectric displacement hysteresis loops depicting the external stress and loading rate-dependent response are reproduced by the tests under homogeneous states of deformation. For the simulations, the domain of interest is a three-dimensional poled specimen, the crystallographic axes of which are assumed to coincide with reference Cartesian axes $e_{1,2,3}$. The poled specimen is subjected to three different loading scenarios. These include a cyclic time-dependent electrical loading, a time-dependent compressive mechanical loading and finally a combined electromechanical loading of the three-dimensional specimen. The material and the model parameters considered for the simulations with the present laminate-based Model 3 are the same as the ones chosen for laminate-based Model 2, see Table 4.3.

4.6.1.1 Tests under homogeneous states of deformation

The external stress and rate-dependent butterfly and dielectric hysteresis loops corresponding to laminate-based Model 3 are reproduced by tests under homogeneous states of deformation. The schematic sketches of the boundary value problems are depicted in Figure 4.32. The crystallographic axes of the specimen under study for all the three loading scenarios are assumed to coincide with reference Cartesian axes $e_{1,2,3}$. Before the start of the simulations, the multi-rank laminate volume fractions are initialised to $\mu^{1,2,3,4}|_{t_0} = 0$ and $\mu^5|_{t_0} = 1$. These starting values of the laminate volume fractions result in the initial poled configuration of the specimen along the positive e_3 -axis, characterised by average remnant polarisation $P_3^M|_{t_0} = P^s$ and by average remnant strain $\varepsilon_{33}^M|_{t_0} = \eta_1^s$.

For the first loading scenario, i.e. pure cyclic electrical loading of the poled specimen, a time-dependent potential difference is applied along the Cartesian e_3 -axis as depicted in Figure 4.32 (a). The electric potential difference across the specimen is generated by

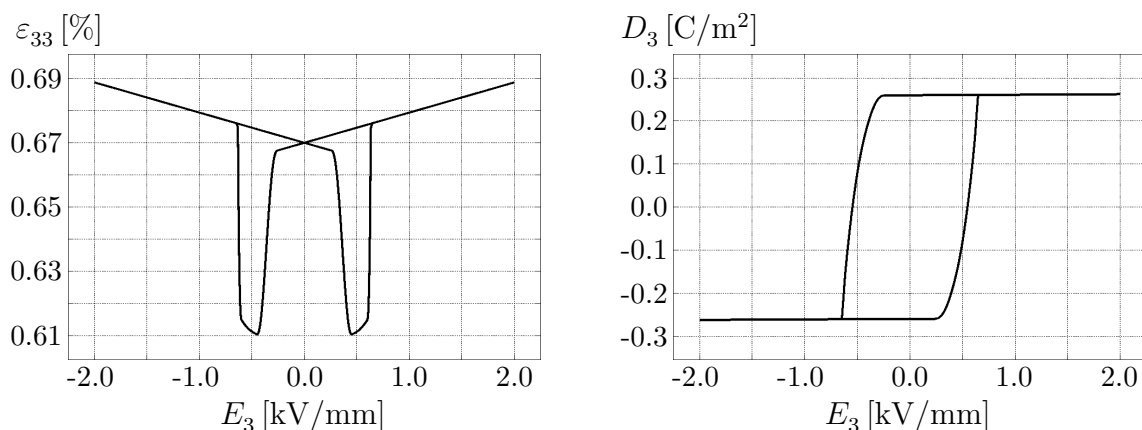


Figure 4.33: Ferroelectric hysteresis curves simulated with laminate-based Model 3 under homogeneous states of deformation. Butterfly curve (left) and dielectric hysteresis loop (right) obtained for a single crystal BaTiO₃ specimen subjected to a cyclic electrical loading at 0.2 Hz.

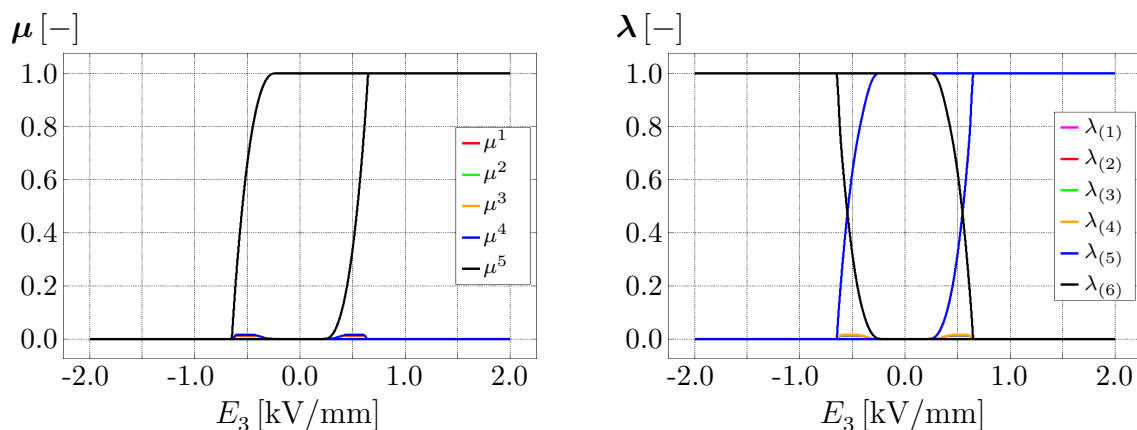


Figure 4.34: Evolution of the laminate volume fractions (left) and of the variant volume fractions (right) corresponding to the butterfly and dielectric hysteresis curves plotted in Figure 4.33.

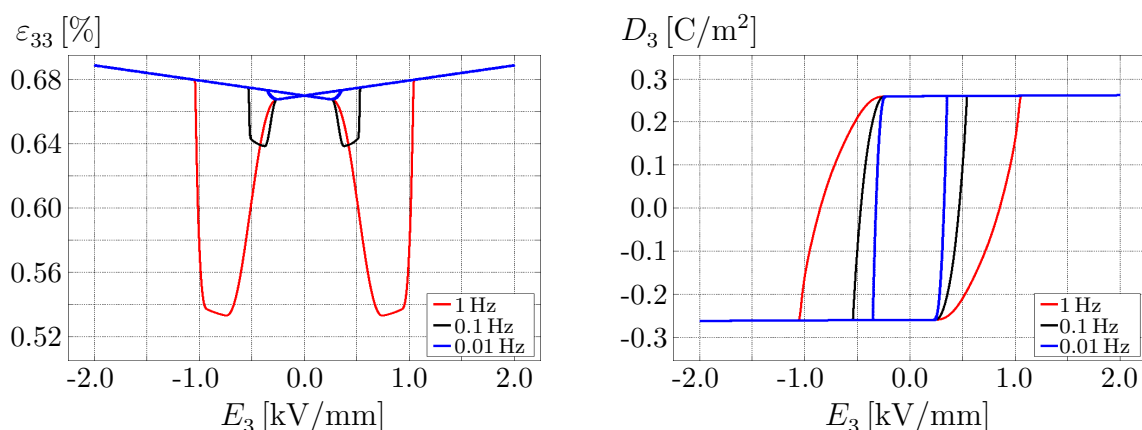


Figure 4.35: Rate-dependent ferroelectric hysteresis curves simulated with laminate-based Model 3 under homogeneous states of deformation. Butterfly curves (left) and dielectric hysteresis loops (right) obtained for a single crystal BaTiO₃ specimen subjected to a cyclic electrical loading at varying frequencies of 1, 0.1 and 0.01 Hz.

keeping the lower electrode grounded at all times while its upper counterpart is subjected to a time-dependent cyclic scalar electric potential $\phi(t)$ with $\phi^{\max} = \pm 10$ kV. The dielectric displacements and the total strains resulting from this rate-dependent and non-linear homogeneous deformation are iteratively computed. The obtained total strains ε_{33} and dielectric displacements D_3 are plotted, respectively, against the applied cyclic electric field E_3 at 0.2 Hz. These plots correspond to the butterfly and dielectric hysteresis loop of the specimen simulated with laminate-based Model 3, see Figure 4.33. The corresponding multi-rank laminate as well as the variant volume fraction evolution in the specimen with respect to the cyclic electric field E_3 at 0.2 Hz are plotted in Figure 4.34. It is observed that, even though the evolution of the laminate volume fraction μ^5 is predominant, laminate-based Model 3 predicts a small deviation in the volume fractions $\mu^{1,2,3,4}$ from their initialised zero values. This may be due to the particular formulation of the average electric Gibbs energy, based on the averaged remnant quantities and on the averaged material moduli. Due to the small increase in the multi-rank laminate volume fraction values $\mu^{1,2,3,4}$, the specimen undergoes a small amount of 90° domain switching during electrical loading at 0.2 Hz. The butterfly curves and the dielectric displacement hysteresis loops obtained under cyclic electrical loading for three different frequencies of 1 Hz, 0.1 Hz and 0.01 Hz are shown in Figure 4.35. The butterfly curve corresponding to loading rate 1 Hz predicts a higher magnitude of the total strain ε_{33} in comparison to the strains obtained at 0.1 Hz and 0.01 Hz. As the loading rate increases, more and more domains within the specimen undergo the stress-activated 90° switching resulting in the increase of the total strain ε_{33} values. Moreover, laminate-based Model 3 predicts widening of both the butterfly and dielectric displacement hysteresis curves at higher electrical rates, say at 1 Hz.

In the second loading scenario, the poled specimen is loaded with a compressive mechanical stress along the e_3 -axis as illustrated in Figure 4.32 (b). The top surface of the specimen is loaded and unloaded by a time-dependent compressive mechanical stress. From a theoretical point of view, such a compressive loading of the poled BaTiO₃ crystal initiates pure 90° switching of the domains. Once the applied mechanical stress exceeds the coercive stress values or once the driving forces needed for the 90° domain evolution exceed the threshold values, the specimen switches along any of the four directions perpendicularly to the loading direction. This leads to mechanical depolarisation of the specimen along with a change in strain values along the loading direction. Both the numerically obtained depolarisation curve and ferroelastic hysteresis curve corresponding to a mechanical loading and unloading at 0.2 Hz are plotted in Figure 4.36. In the context of the depolarisation and ferroelastic hysteresis curves, the 90° switching is initiated and further enhanced during the compressive loading as observed by the non-linear change in dielectric displacement values D_3 and by the decrease of the total strains ε_{33} along the e_3 -axis. The specimen then reaches the minimum value of D_3 and ε_{33} at $\sigma_{33}^{\max} = -15$ MPa. At this maximum value of the compressive stress, not all the domains are switched along the e_1 and e_2 -directions, since $\{D_3, \varepsilon_{33}\}|_{\sigma_{33}^{\max}}$ did not reach the theoretical values of 0 C/m² and -0.42% , see Figure 4.36. During unloading, laminate-

based Model 3 predicts an initial non-linear decrease in both the dielectric displacement D_3 and total strain ε_{33} values. This may result from the non-linear response in back switching of the domains along the stable \mathbf{e}_1 and \mathbf{e}_2 -directions. At $\sigma_{33} \approx -8.5$ MPa, the specimen depolarises completely and remains in the depolarised state. The evolution of both the variant and laminate volume fractions for the mechanical loading and unloading of the poled specimen at 0.2 Hz simulated with laminate-based Model 3 are plotted in Figure 4.37. During the loading phase of the specimen, wherein the applied compressive mechanical load is increased from $\sigma_{33}^{\min} = 0$ MPa to $\sigma_{33}^{\max} = -15$ MPa, the variant volume fraction $\lambda_{(5)}$ decreases non-linearly from its initial value, whereas $\lambda_{(1,2,3,4)}$ show an increase from their initialised zero values indicating 90° domain switching along the \mathbf{e}_1 and \mathbf{e}_2 -directions. Both the laminate volume fraction μ^5 and the variant volume fraction $\lambda_{(6)}$ did not show a deviation from their initialised value during the entire loading-unloading cycle, indicating that the 180° domain switching has not occurred in the specimen, see Figure 4.37. The rate-dependent depolarisation and ferroelastic curves simulated with laminate-based Model 3 are plotted in Figure 4.38.

The schematic sketch of the poled specimen subjected to a combined electromechanical loading, i.e. a constant compressive stress and a cyclic electric field, both along the \mathbf{e}_3 -axis is depicted in Figure 4.32 (c). Such combined electromechanical loading results in high magnitudes of actuation strain along the loading direction, mainly due to the enhancement of the stress-driven 90° ferroelastic switching, cf. [22, 131, 134, 151]. Furthermore, experimental studies show a significant increase in the obtained actuation strains with an increase in the applied compressive stress magnitudes in addition to the cyclic electrical loading. The butterfly curves and dielectric hysteresis loops under cyclic electrical loading at 0.2 Hz along with varying magnitudes of the constant compressive stresses simulated with laminate-based Model 3 are plotted in Figure 4.39. The increase in total strain values ε_{33} , without a significant difference in dielectric displacements D_3 , for increase in the applied compressive stress magnitudes is well predicted with laminate-based Model 3. The evolution of the laminate and variant volume fractions simulated with laminate-based Model 3 for an electrical loading frequency of 0.2 Hz along with a constant mechanical stress magnitude of 2.7 MPa is shown in Figure 4.40. At an applied compressive stress of 2.7 MPa, the evolution of the variant volume fractions $\lambda_{(1,2,3,4)}$ along both the \mathbf{e}_1 and \mathbf{e}_2 -directions, indicates that some of the domains initially switch to 90° due to the mechanical load and then complete a 180° switching. The enhancement of the stress-activated 90° domain switching at higher magnitudes of the compressive load is responsible for the increase in the actuation strains obtained. In the context of rate-dependent response, the butterfly curves and the dielectric displacement hysteresis loops simulated with laminate-based Model 3 for a constant compressive stress $\sigma_{33} = 2.7$ MPa and for varying electrical loading frequencies are plotted in Figure 4.41. As the electrical load is applied at a frequency of 0.01 Hz, the total strains ε_{33} obtained are quite high compared to the ε_{33} values computed at 1 Hz. At lower loading rates the stress-activated 90° switching is probably more pronounced, leading to increased total strain values ε_{33} along the loading direction.

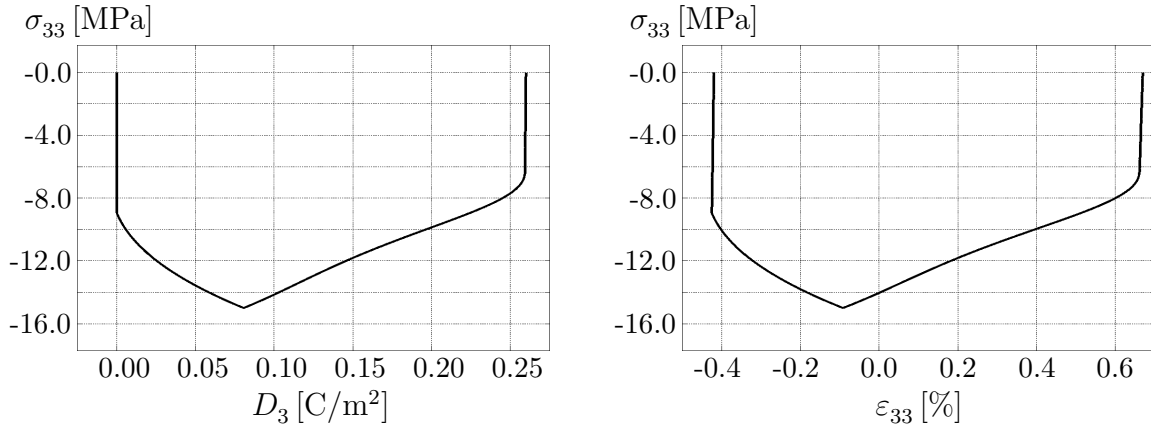


Figure 4.36: Ferroelastic hysteresis curves simulated with laminate-based Model 3 under homogeneous states of deformation. Mechanical depolarisation curve (left) and ferroelastic hysteresis curve (right) obtained for a single crystal BaTiO₃ specimen subjected to a compressive mechanical loading and unloading at 0.2 Hz.

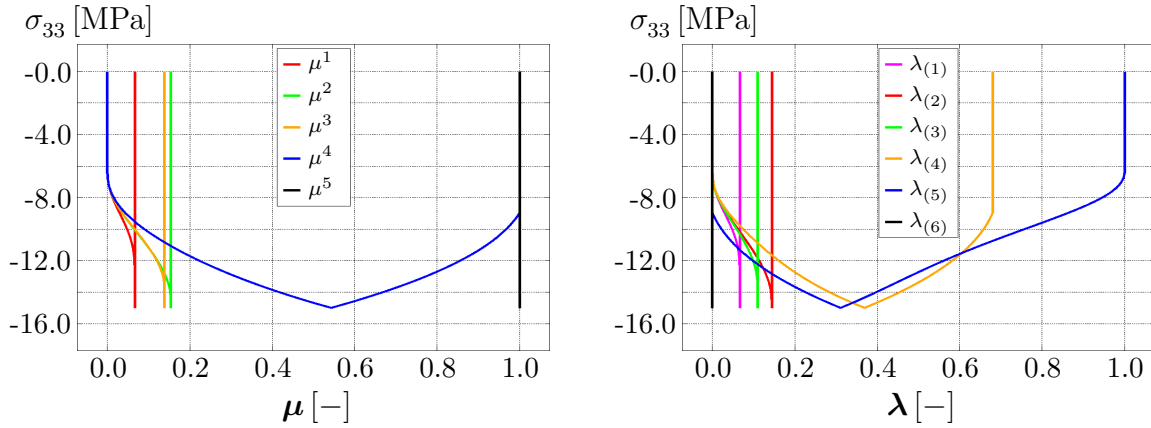


Figure 4.37: Evolution of the laminate volume fractions (left) and of the variant volume fractions (right) corresponding to the depolarisation and ferroelastic hysteresis curves plotted in Figure 4.36.

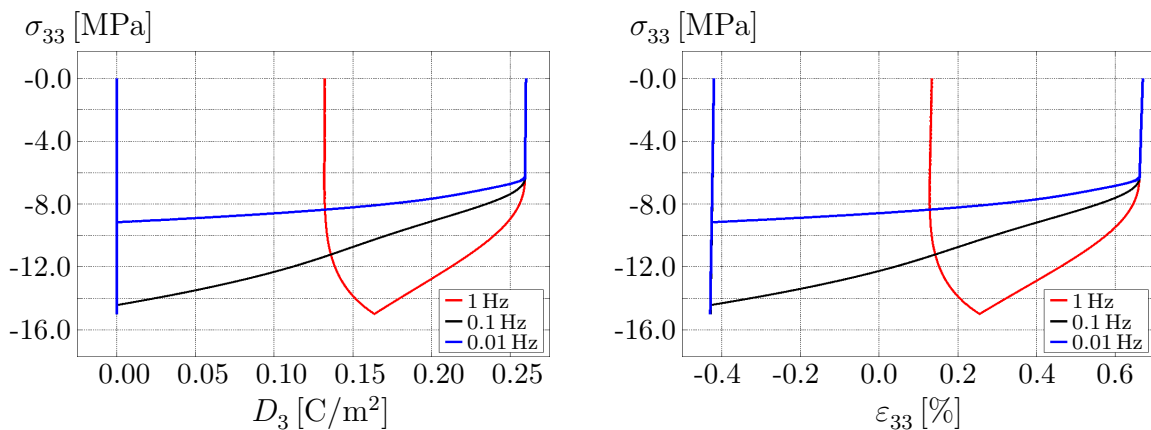


Figure 4.38: Rate-dependent ferroelastic hysteresis curves simulated with laminate-based Model 3 under homogeneous states of deformation. Mechanical depolarisation curves (left) and ferroelastic hysteresis curves (right) obtained for a single crystal BaTiO₃ specimen subjected to a compressive mechanical loading and unloading at varying frequencies of 1, 0.1 and 0.01 Hz.

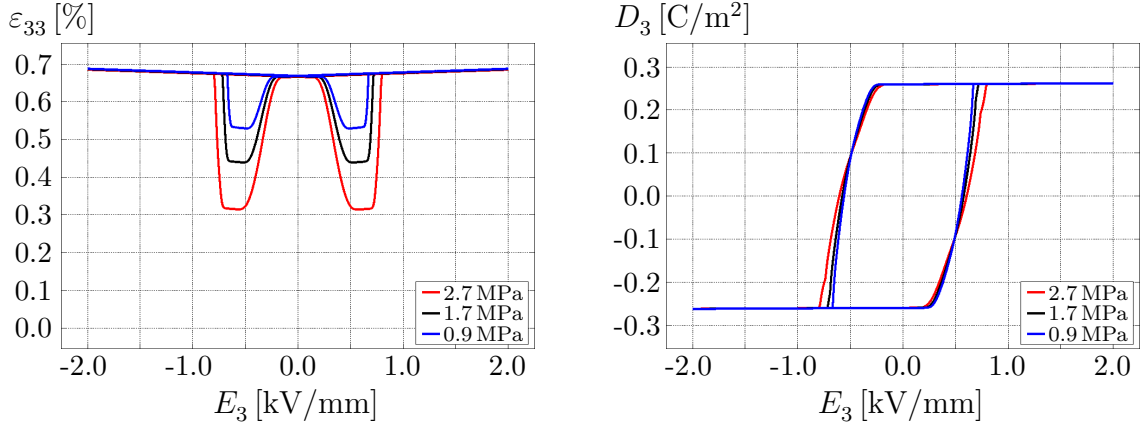


Figure 4.39: External-stress dependent ferroelectric hysteresis curves simulated with laminate-based Model3 under homogeneous states of deformation for combined electromechanical loading. Butterfly curves (left) and dielectric hysteresis loops (right) obtained for a single crystal BaTiO₃ specimen subjected to a cyclic electrical loading at 0.2 Hz along with constant compressive stresses.

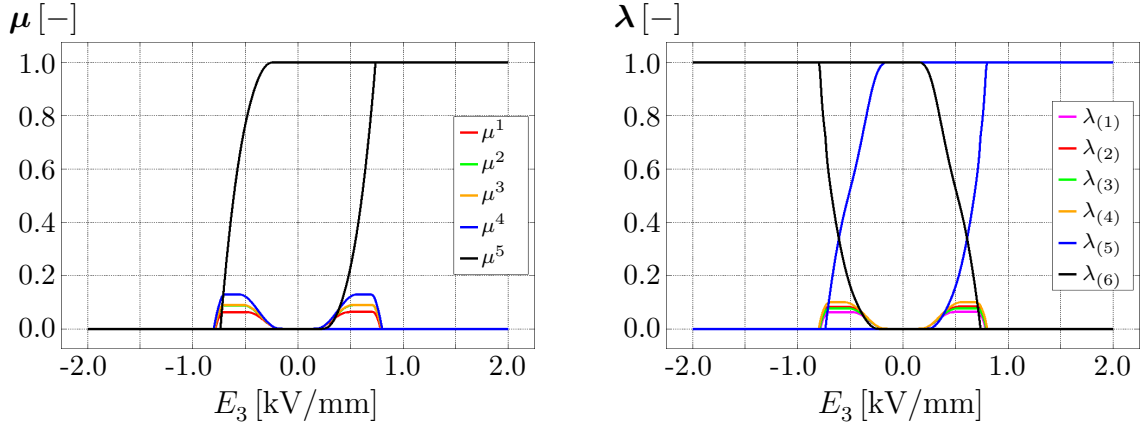


Figure 4.40: Evolution of the laminate volume fractions (left) and of the variant volume fractions (right) simulated with laminate-based Model3 under homogeneous states of deformation for an electrical loading frequency of 0.2 Hz along with a constant compressive stress of 2.7 MPa.

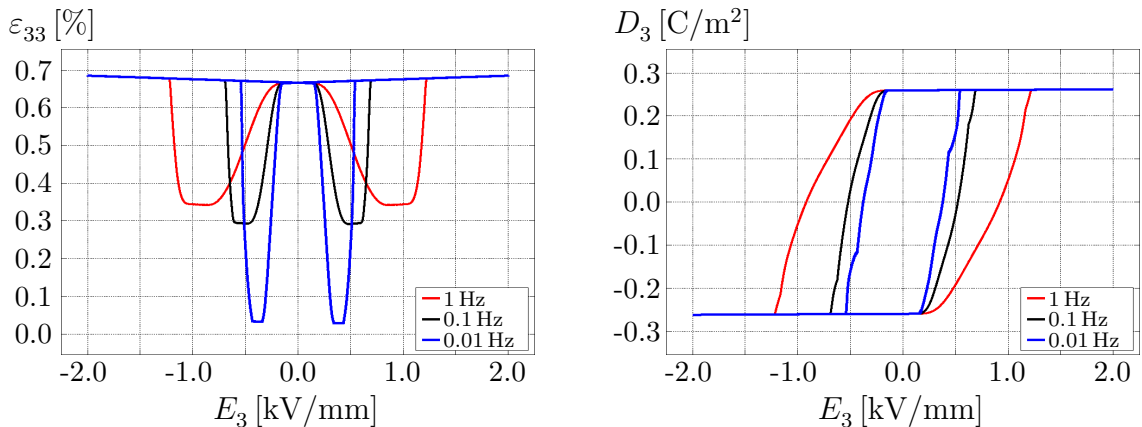


Figure 4.41: Rate-dependent hysteresis curves simulated with laminate-based Model3 under homogeneous states of deformation for combined electromechanical loading. Butterfly curves (left) and dielectric hysteresis loops (right) obtained for a single crystal BaTiO₃ specimen subjected to a constant compressive stress of 2.7 MPa along with a cyclic electrical loading at frequencies of 1, 0.1 and 0.01 Hz.

4.7 Laminate-based Model 4

Based on the underlying equations outlined in Section 4.2, the present section elaborates on the particular laminate-based Model 4. Analogous to laminate-based Model 3, both the total linear strains $\boldsymbol{\varepsilon}$ and the dielectric displacement \mathbf{D}_{M4} of the ferroelectric single crystal for the present laminate-based Model 4 formulation are considered to be additively decomposed into an elastic and a remnant part as

$$\boldsymbol{\varepsilon} = \boldsymbol{\varepsilon}^e + \boldsymbol{\varepsilon}^M \quad \text{and} \quad \mathbf{D}_{M4} = \mathbf{D}^e + \mathbf{P}^M. \quad (4.86)$$

Here, $\boldsymbol{\varepsilon}^e$ denotes the reversible strain tensor and \mathbf{D}^e refers to the reversible dielectric displacement vector of the crystal. The remnant quantities $\boldsymbol{\varepsilon}^M(\boldsymbol{\mu}; \boldsymbol{\varepsilon}_{(1,3,5)})$ and $\mathbf{P}^M(\boldsymbol{\mu}; \mathbf{P}_{(1,3,5)})$ are defined in Equations (4.17) and (4.18) respectively. Similar to the phenomenological model and to the previously introduced laminate-based models, the total linear strains and electric field enter the specific laminate-based Model 4 as the independent constitutive variables defining the average electric Gibbs energy.

In context of the model formulation, the average electric Gibbs energy defining the coupled electromechanical response of the single crystal is additively decomposed into a reversible piezoelectric and a remnant part as

$$H_{M4}(\boldsymbol{\varepsilon}, \mathbf{E}, \boldsymbol{\mu}) = H_{M4}^{\text{piezo}}(\boldsymbol{\varepsilon}^e, \mathbf{E}, \boldsymbol{\mu}) + H_{M4}^{\text{rem}}(\boldsymbol{\mu}). \quad (4.87)$$

The average electric Gibbs energy $H_{M3}(\boldsymbol{\varepsilon}, \mathbf{E}, \boldsymbol{\mu})$ postulated for laminate-based Model 3 is chosen for the piezoelectric part of the average electric Gibbs energy for the present laminate-based Model 4. The piezoelectric part of the average electric Gibbs energy (4.87) reads

$$H_{M4}^{\text{piezo}}(\boldsymbol{\varepsilon}^e, \mathbf{E}, \boldsymbol{\mu}) = \frac{1}{2} \boldsymbol{\varepsilon}^e : \mathbf{E}^M : \boldsymbol{\varepsilon}^e - \frac{1}{2} \mathbf{E} \cdot \boldsymbol{\varepsilon}^M \cdot \mathbf{E} - \mathbf{E} \cdot \mathbf{e}^M : \boldsymbol{\varepsilon}^e - \mathbf{P}^M \cdot \mathbf{E}. \quad (4.88)$$

As postulated in laminate-based Model 3, the piezoelectric electric Gibbs energy (4.88) comprises of the transversely-isotropic material moduli, i.e. $\mathbf{E}^M(\boldsymbol{\mu}; \mathbf{E}_{(1,3,5)})$, $\mathbf{e}^M(\boldsymbol{\mu}; \mathbf{e}_{(1,3,5)})$ and $\boldsymbol{\varepsilon}^M(\boldsymbol{\mu}; \boldsymbol{\varepsilon}_{(1,3,5)})$, all defined in Equations (4.19) to (4.21).

The remnant part of the total electric Gibbs energy (4.87), dependent on the multi-rank laminate volume fractions, is formulated as a saturation-type energy function. The considered remnant energy contribution reads

$$H_{M4}^{\text{rem}}(\boldsymbol{\mu}) = \frac{1}{c} \left[\frac{1}{2} P^{\text{sat}} \ln \left(1 - [P^N(\boldsymbol{\mu})]^2 \right) + \|\mathbf{P}^M\| \operatorname{arctanh}(P^N(\boldsymbol{\mu})) \right], \quad (4.89)$$

cf. [126, 137]. Here, scalar c is a model or fitting parameter that influences the shape of the hysteresis curves. Saturation scalar $P^N(\boldsymbol{\mu}) := \|\mathbf{P}^M\|/P^{\text{sat}}$ introduced in Equations

tion (4.89) captures the monotonically increasing remnant polarisation up to the saturation level P^{sat} .

Following the standard Coleman–Noll procedure, the constitutive equations for the stress tensor and the dielectric displacement vector of the crystal are obtained as

$$\boldsymbol{\sigma}_{\text{M4}} = \frac{\partial H_{\text{M4}}(\boldsymbol{\varepsilon}, \mathbf{E}, \boldsymbol{\mu})}{\partial \boldsymbol{\varepsilon}} = \mathbf{E}^{\text{M}} : \boldsymbol{\varepsilon}^e - [\mathbf{e}^{\text{M}}]^{\text{t}} \cdot \mathbf{E} \quad \text{and} \quad (4.90)$$

$$\mathbf{D}_{\text{M4}} = - \frac{\partial H_{\text{M4}}(\boldsymbol{\varepsilon}, \mathbf{E}, \boldsymbol{\mu})}{\partial \mathbf{E}} = \mathbf{e}^{\text{M}} : \boldsymbol{\varepsilon}^e + \boldsymbol{\varepsilon}^{\text{M}} \cdot \mathbf{E} + \mathbf{P}^{\text{M}}, \quad (4.91)$$

and the reduced dissipation inequality reads

$$\mathcal{D}_{\text{red}} = \sum_{j=1}^{nv-1} f_{\text{M4}}^j(\boldsymbol{\mu}) \dot{\mu}^j \geq 0. \quad (4.92)$$

Herein, $f_{\text{M4}}^j(\boldsymbol{\mu})$ is the thermodynamic driving force of the specific j -th rank laminate identified as

$$\begin{aligned} f_{\text{M4}}^j(\boldsymbol{\mu}) &= - \frac{\partial H_{\text{M4}}(\boldsymbol{\varepsilon}, \mathbf{E}, \boldsymbol{\mu})}{\partial \mu^j} \\ &= \frac{\partial \boldsymbol{\varepsilon}^{\text{M}}}{\partial \mu^j} : \boldsymbol{\sigma}_{\text{M4}} - \frac{1}{2} \boldsymbol{\varepsilon}^e : \frac{\partial \mathbf{E}^{\text{M}}}{\partial \mu^j} : \boldsymbol{\varepsilon}^e + \frac{1}{2} \mathbf{E} \cdot \frac{\partial \boldsymbol{\varepsilon}^{\text{M}}}{\partial \mu^j} \cdot \mathbf{E} + \mathbf{E} \cdot \frac{\partial \mathbf{e}^{\text{M}}}{\partial \mu^j} : \boldsymbol{\varepsilon}^e \\ &\quad + \frac{\partial \mathbf{P}^{\text{M}}}{\partial \mu^j} \cdot \mathbf{E} - E^{\text{b},j}(\boldsymbol{\mu}), \end{aligned} \quad (4.93)$$

wherein the back electric field $E^{\text{b},j}(\boldsymbol{\mu})$ for the j -th rank laminate is defined as

$$E^{\text{b},j}(\boldsymbol{\mu}) := \frac{\partial H_{\text{M4}}^{\text{rem}}(\boldsymbol{\mu})}{\partial \mu^j} = \frac{1}{c} \operatorname{arctanh}(P^{\text{N}}(\boldsymbol{\mu})) \left[\frac{\mathbf{P}^{\text{M}}}{\|\mathbf{P}^{\text{M}}\|} \cdot \frac{\partial \mathbf{P}^{\text{M}}}{\partial \mu^j} \right]. \quad (4.94)$$

The thermodynamic driving force $f_{\text{M4}}^j(\boldsymbol{\mu})$ responsible for the domain evolution in the corresponding j -th rank laminate for the specific laminate-based Model 4 is influenced by the additional back electric field $E^{\text{b},j}(\boldsymbol{\mu})$ defined for the individual laminates. Once the driving force $f_{\text{M4}}^j(\boldsymbol{\mu})$ exceeds the critical threshold value $g^{c,j}(\boldsymbol{\mu}) \geq 0$, the evolution of the laminate volume fraction μ^j is computed by solving the rate-dependent evolution equation (4.32) for the j -th rank laminate. The evolution of the multi-rank laminate volume fractions under the applied external loads is constrained within their range due to the considered Fischer–Burmeister-type algorithm. The reader is referred to Section 4.3, for further details on the algorithmic scheme.

4.7.1 Numerical examples

This section demonstrates the numerical capabilities of the formulated laminate-based Model 4. With respect to the application of the particular material model in order to study the single crystal behaviour, tests under homogeneous states of deformation are performed. The hysteresis curves and the volume fraction evolution of the single crystal are obtained by tests under homogeneous states of deformation. The material parameters corresponding to the single crystal tetragonal BaTiO₃ as well as the model parameters chosen for laminate-based Model 4 are listed in Table 4.3.

4.7.1.1 Tests under homogeneous states of deformation

The butterfly and dielectric hysteresis curves as well as the mechanical depolarisation and ferroelastic hysteresis loops for single crystal tetragonal BaTiO₃ are reproduced with tests under homogeneous states of deformation. The representative single finite element is subjected to three different loading scenarios, namely cyclic electrical, compressive mechanical and combined electromechanical loading. The schematic sketches of the boundary value problems are depicted in Figure 4.32. The crystallographic axes of the specimen corresponding to the individual loading conditions are assumed to coincide with reference Cartesian axes $\mathbf{e}_{1,2,3}$.

The specimen is initially poled along the positive \mathbf{e}_3 -axis. The initial variant volume fraction values are set to $\lambda_{(1,2,3,4,6)}|_{t_0} = 0$ and $\lambda_{(5)}|_{t_0} = 1$. These initial values correspond to the multi-rank laminate volume fractions $\mu^{1,2,3,4}|_{t_0} = 0$ and $\mu^5|_{t_0} = 1$. With these starting values of the laminate volume fractions, the initial average remnant polarisation results in $P_3^M|_{t_0} = P^s$, refer to Equation (4.18). Following Equation (4.17), the magnitude of the average remnant strain along the \mathbf{e}_3 -axis for the initial state, $\varepsilon_{33}^M|_{t_0}$, equals the strain value coefficient η_1^s . These non-vanishing magnitudes of the average remnant strain and polarisation result in the initial poled configuration of the specimen along the positive \mathbf{e}_3 -axis.

For the first loading scenario, as depicted in Figure 4.32 (a), the specimen is loaded by a cyclic electrical field at varying frequencies. The potential difference across the specimen is generated by keeping the lower electrode grounded at all times, while its upper counterpart is surcharged with an alternating scalar electric potential $\phi(t)$ with $\phi^{\max} = \pm 10$ kV. Due to the prescribed homogeneous displacement boundary conditions and due to the applied cyclic electrical loading, the specimen elongates and contracts along the \mathbf{e}_3 -direction while experiencing a corresponding contraction and expansion along both the \mathbf{e}_1 and \mathbf{e}_2 -axes. The strains and dielectric displacements resulting from this rate-dependent and non-linear deformation are computed iteratively. The butterfly curve is obtained by plotting the total strains ε_{33} against the applied electric field E_3 . Analogously, the dielectric displacement hysteresis loop is obtained by plotting the resulting D_3 values against E_3 . The strain and dielectric hysteresis curves obtained by surcharging the specimen with an alternating electrical load at 0.2 Hz are plotted in

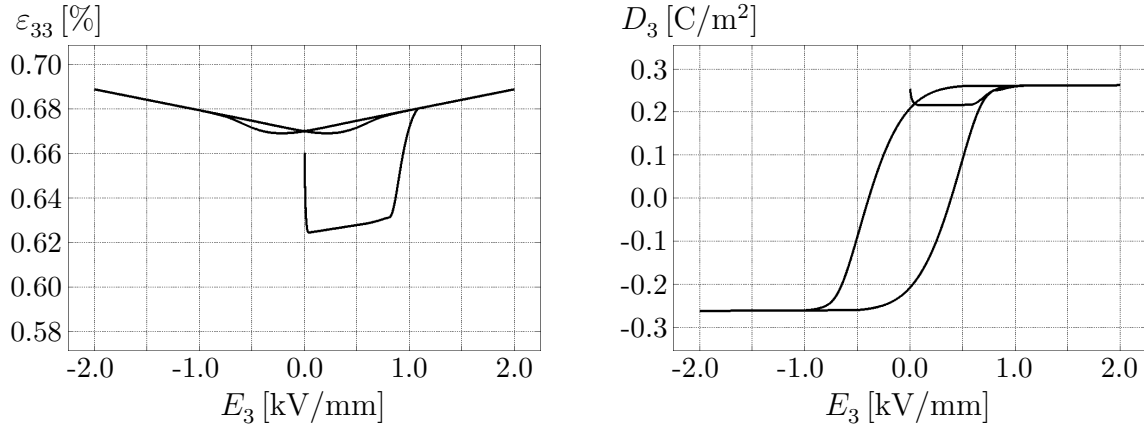


Figure 4.42: Ferroelectric hysteresis curves simulated with laminate-based Model 4 under homogeneous states of deformation. Butterfly curve (left) and dielectric hysteresis loop (right) obtained for a single crystal BaTiO_3 specimen subjected to a cyclic electrical loading at 0.2 Hz.

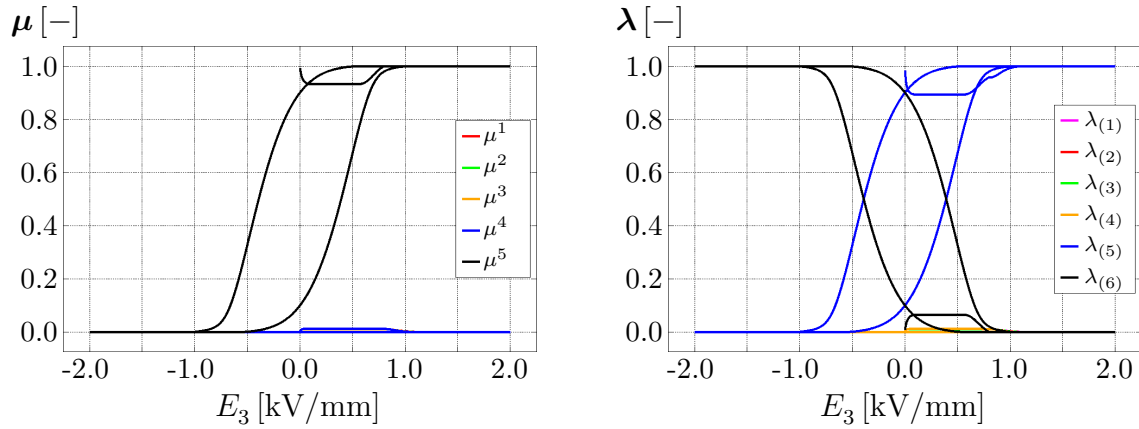


Figure 4.43: Evolution of the laminate volume fractions (left) and of the variant volume fractions (right) in the specimen corresponding to the butterfly and dielectric hysteresis curves plotted in Figure 4.42.

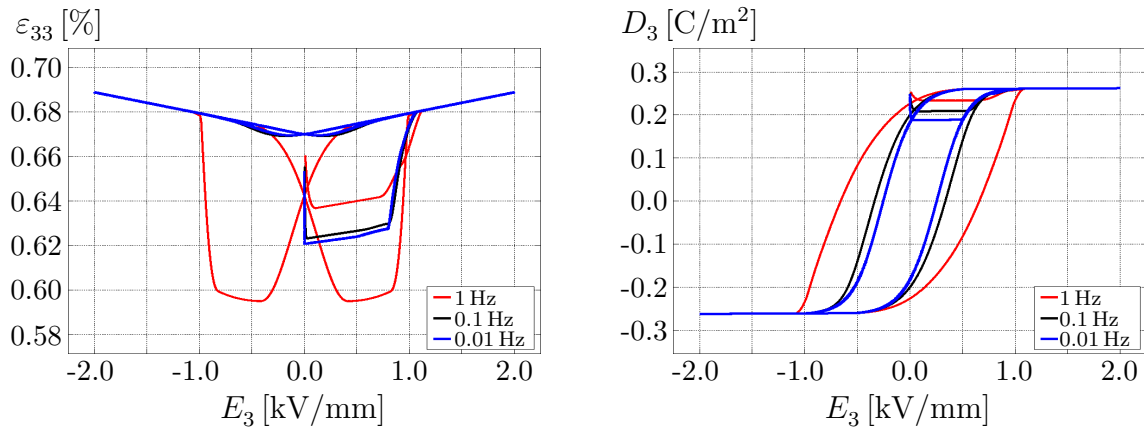


Figure 4.44: Rate-dependent ferroelectric hysteresis curves simulated with laminate-based Model 4 under homogeneous states of deformation. Butterfly curves (left) and dielectric hysteresis loops (right) obtained for a single crystal BaTiO_3 specimen subjected to a cyclic electrical loading at varying frequencies of 1, 0.1 and 0.01 Hz.

4 Laminate-based modelling of single crystalline ferroelectric materials

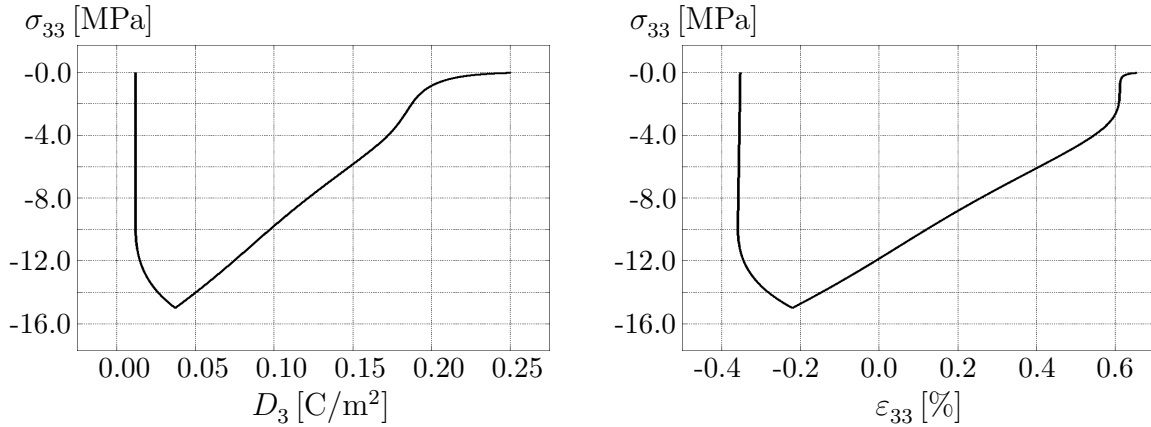


Figure 4.45: Ferroelastic hysteresis curves simulated with laminate-based Model 4 under homogeneous states of deformation. Mechanical depolarisation curve (left) and ferroelastic hysteresis loop (right) obtained for a single crystal BaTiO₃ specimen subjected to a compressive mechanical loading and unloading at 0.2 Hz.

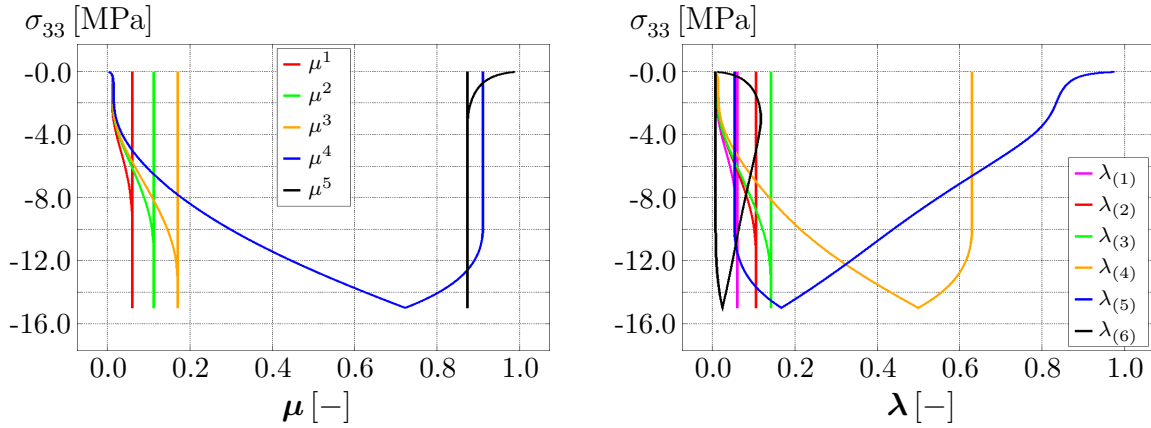


Figure 4.46: Evolution of the laminate volume fractions (left) and of the variant volume fractions (right) in the specimen corresponding to the depolarisation and ferroelastic hysteresis curves plotted in Figure 4.45.

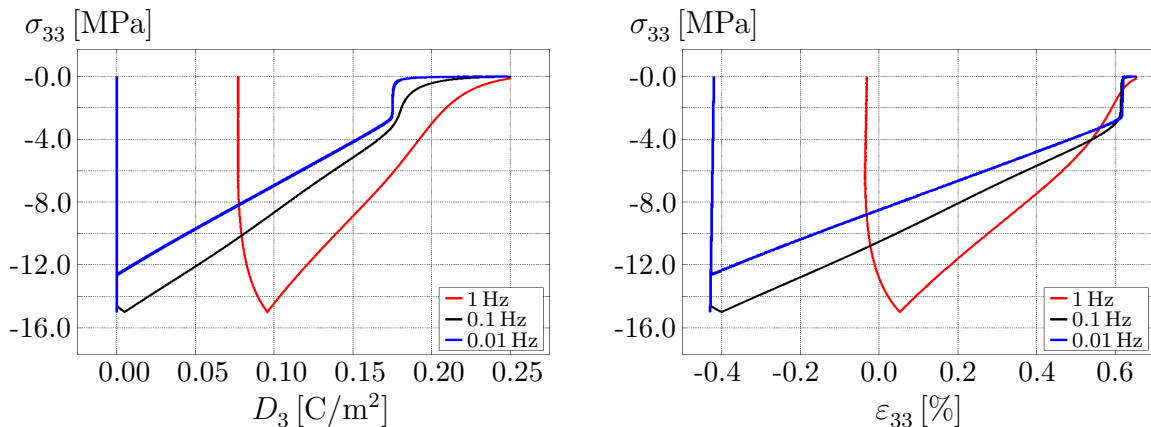


Figure 4.47: Rate-dependent ferroelastic hysteresis curves simulated with laminate-based Model 4 under homogeneous states of deformation. Mechanical depolarisation curves (left) and ferroelastic hysteresis curves (right) obtained for a single crystal BaTiO₃ specimen subjected to a compressive mechanical loading and unloading at varying frequencies of 1, 0.1 and 0.01 Hz.

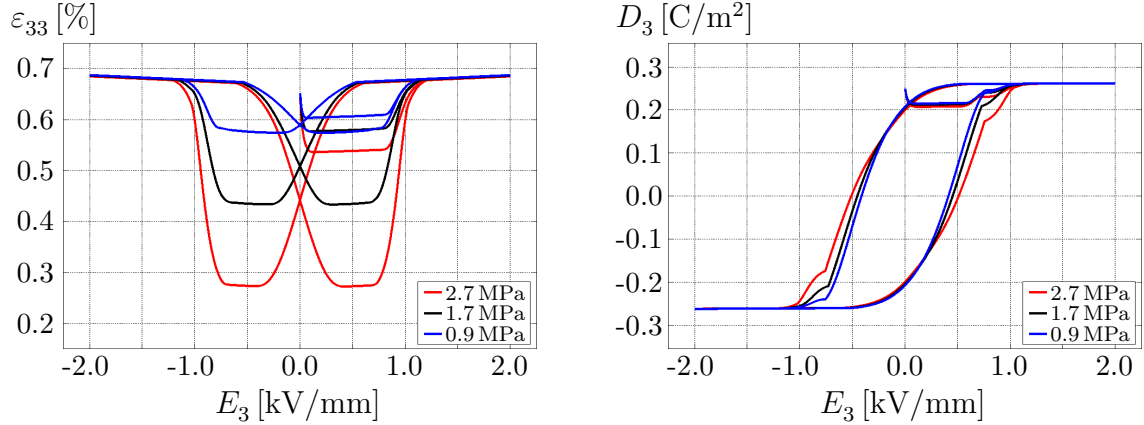


Figure 4.48: External-stress dependent ferroelectric hysteresis curves simulated with laminate-based Model 4 under homogeneous states of deformation for combined electromechanical loading. Butterfly curves (left) and dielectric hysteresis loops (right) obtained for a single crystal BaTiO₃ specimen subjected to a cyclic electrical loading at 0.2 Hz along with constant compressive stresses.

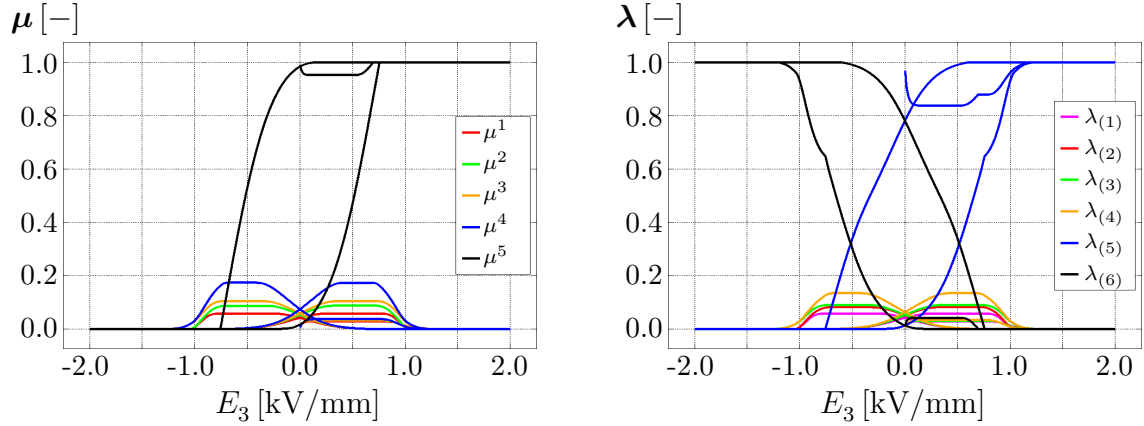


Figure 4.49: Evolution of the laminate volume fractions (left) and of the variant volume fractions (right) simulated with laminate-based Model 4 under homogeneous states of deformation for an electrical loading frequency of 0.2 Hz along with a constant compressive stress of 2.7 MPa.

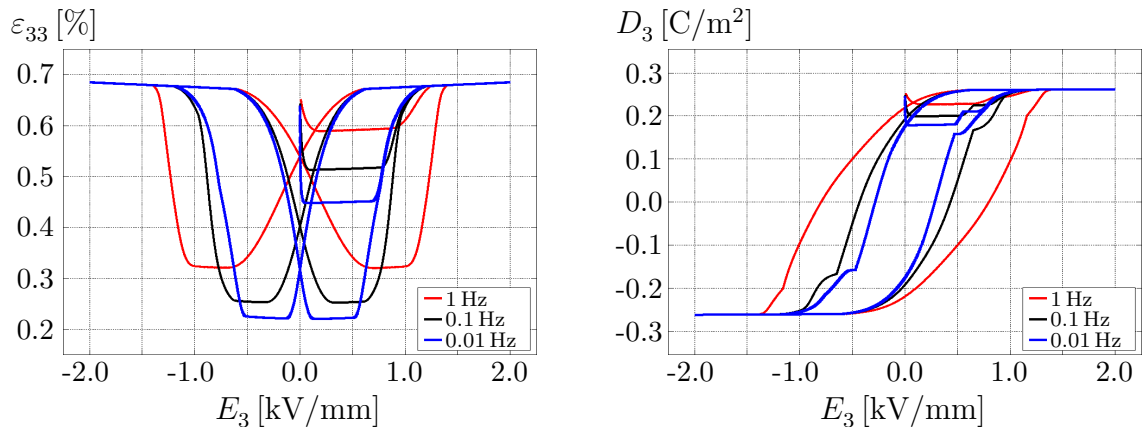


Figure 4.50: Rate-dependent hysteresis curves simulated with laminate-based Model 4 under homogeneous states of deformation for combined electromechanical loading. Butterfly curves (left) and dielectric hysteresis loops (right) obtained for a single crystal BaTiO₃ specimen subjected to a constant compressive stress of 2.7 MPa along with a cyclic electrical loading at frequencies of 1, 0.1 and 0.01 Hz.

Figure 4.42. Looking at the simulated hysteresis curves, it can be predicted that only 180° domain switching occurs within the specimen. The small variations of the total strains in the butterfly curves augment, so that no stress induced 90° domain switching ensues in the specimen. The corresponding evolution of the multi-rank laminate and variant volume fractions in the specimen with respect to the cyclic electric field E_3 at 0.2 Hz is plotted in Figure 4.43. The multi-rank laminate volume fraction values are restricted within the limits 0 and 1 highlighting the efficiency of the implemented Fischer–Burmeister algorithm. The evolution of the variant volume fractions $\lambda_{(5)}$ and $\lambda_{(6)}$ further confirm that the specimen undergoes only 180° domain switching for cyclic electric loading at 0.2 Hz. With respect to the rate-dependent response, the hysteresis loops obtained for varying electrical loading frequencies are shown in Figure 4.44. The widening of the butterfly and dielectric hysteresis loops at an electrical loading frequency of 1 Hz indicates the incomplete switching of the domains at higher loading rates. The increased magnitudes of strains along the e_3 -direction at 1 Hz in comparison to the values obtained for 0.1 and 0.01 Hz may be due to the presence of some 90° domain switching within the specimen at higher electrical loading rates.

In the second loading test, the poled specimen is loaded with a compressive mechanical load along the e_3 -direction as depicted in Figure 4.32 (b). The compressive mechanical loading initiates the stress-activated 90° domain switching in the specimen. As a consequence, the spontaneous polarisation, initially oriented along the positive e_3 -axis, will be switched along any one of the energetically favourable e_1 and e_2 -directions. The rate-dependent mechanical loading and unloading of the poled specimen during this stress-driven process results in mechanical depolarisation and ferroelastic hysteresis curves. The numerically obtained depolarisation and ferroelastic hysteresis for a loading and unloading rate of 0.2 Hz is shown in Figure 4.45. The stress-induced 90° switching of the domains initiates at lower magnitudes of compressive loads and advances with increasing stress levels. This becomes evident from the decreasing values of the dielectric displacement and total strains with increasing compressive loading. Furthermore, from the 0.2 Hz hysteresis plots, one may observe that the specimen does not depolarise completely at the maximum compressive load of $\sigma_{33} = -15$ MPa. The simulated stress-induced ferroelastic response with laminate-based Model 4 is comparable with the experimental data reported by Li and Li [95]. The evolution of the laminate and variant volume fractions for the mechanical loading scenario at 0.2 Hz are plotted in Figure 4.46. The rate-dependent hysteretic response of the specimen with respect to varying mechanical loading and unloading frequencies is plotted in Figure 4.47.

With respect to the high actuation strain response of the tetragonal single crystal BaTiO_3 , the final homogeneous test comprises a combined electromechanical loading of the poled specimen. In this test, a constant compressive mechanical load of varying magnitudes is applied parallelly to the cyclic electrical field along the e_3 -axis of the poled specimen. Figure 4.32 (c) depicts the schematic sketch of the particular boundary value problem. Setting $\phi = 0$ kV at the lower electrode, a time-dependent cyclic scalar potential is applied at the top surface of the specimen with $\phi^{\max} = \pm 10$ kV at 0.2 Hz.

A constant compressive stress is applied in addition to the electrical load at the top surface. The response of the specimen is studied for different magnitudes of compressive stress levels ranging from 0 to 2.7 MPa. The applied combined electromechanical load enhances the stress-driven 90° domain switching in the specimen, resulting in high actuation strains along the loading direction, cf. [22, 131, 134, 151]. The numerically obtained butterfly and dielectric displacement hysteresis curves for the combined electromechanical loading are plotted in Figure 4.48. The increase in the obtained actuation strains with moderate increase in the applied stress levels, without significant difference in the dielectric displacement values, is well captured by laminate-based Model 4. The evolution of the multi-rank laminate and the variant volume fractions in the specimen subjected to a cyclic electrical load at 0.2 Hz and a constant compressive stress of 2.7 MPa are plotted in Figure 4.49. The variant volume fractions $\lambda_{(1,2,3,4)}$, along the \mathbf{e}_1 and \mathbf{e}_2 -directions, evolve in addition to the evolution of $\lambda_{(5)}$ and $\lambda_{(6)}$. This indicates that some of the domains initially undergo a 90° switching, due to the compressive mechanical stress, and then complete the 180° switching which explains the enhanced actuation strains obtained during combined electromechanical loading. The hysteretic response of the specimen under a compressive load of 2.7 MPa along with varying electrical loading frequencies is plotted in Figure 4.50. As expected, at higher electrical loading frequencies of 1 Hz, both the butterfly and dielectric displacement curves widen due to the incomplete switching of the domains within the specimen at high electrical loading rates.

4.8 Comparison of laminate-based Models 2, 3 and 4

This section highlights the differences in the single crystal BaTiO_3 hysteretic responses simulated with laminate-based Models 2, 3 and 4. The respective model formulations, detailed in Sections 4.5 to 4.7, are compared in the context of tests under homogeneous states of deformation. The representative single finite element is subjected to three different loading scenarios, namely cyclic electrical, compressive mechanical and combined electromechanical loading, see Figure 4.32. The considered material parameters are listed in Table 4.3. Different values for viscous-like parameter m are considered for the subsequent simulations and their influence is studied. The poled configuration along the positive \mathbf{e}_3 -axis for all the simulations are obtained by setting $\mu^{1,2,3,4}|_{t_0} = 0$ and $\mu^5|_{t_0} = 1$. The plotted butterfly and dielectric hysteresis curves, Figures 4.51 to 4.56, correspond to the second loading cycle.

A comparison of laminate-based material Models 2, 3 and 4 with respect to the simulated butterfly curves and dielectric displacement hysteresis loops for an electrical loading frequency of 0.05 Hz and for two different values of viscous-like parameter m is plotted in Figures 4.51 and 4.52. With respect to the butterfly curves, the obtained minimum total strain value ε_{33}^{\min} of the individual models is considered as reference point to which the individual curves are shifted. One may observe the high magnitude of remnant and

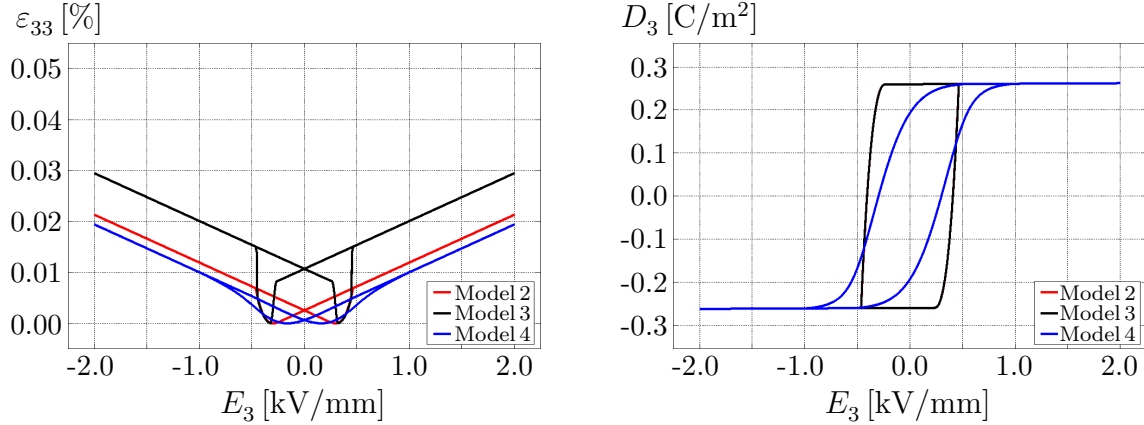


Figure 4.51: Comparison of laminate-based Models 2, 3 and 4 with respect to butterfly curves (left) and dielectric hysteresis loops (right) under homogeneous states of deformation for a cyclic electrical loading at 0.05 Hz and for model parameters $m = 1.5$, $c = 3.5$.

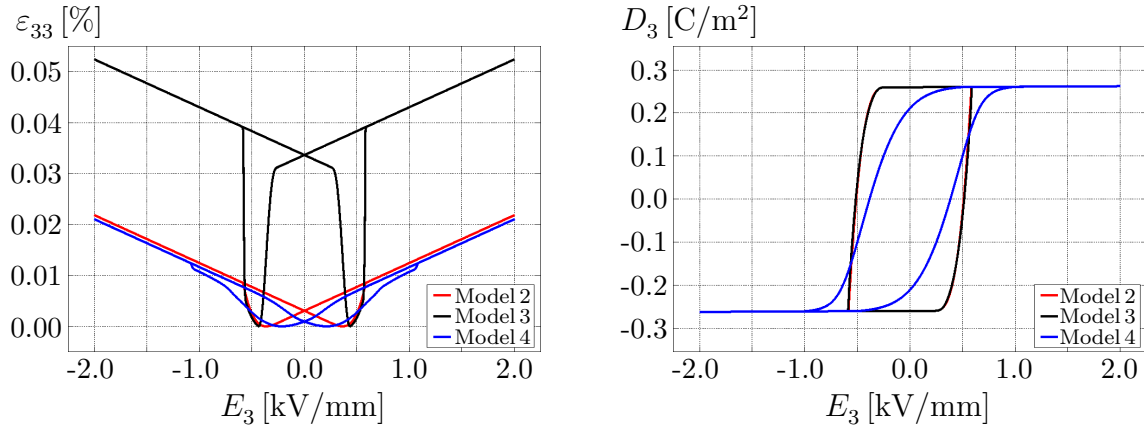


Figure 4.52: Comparison of laminate-based Models 2, 3 and 4 with respect to butterfly curves (left) and dielectric hysteresis loops (right) under homogeneous states of deformation for a cyclic electrical loading at 0.05 Hz and for model parameters $m = 2.0$, $c = 3.5$.

maximum strains obtained when considering laminate-based Model 3 in comparison to the values obtained with laminate-based Models 2 and 4 for both $m = 1.5$ and $m = 2.0$. This may result from the fact that with laminate-based Model 3 some domains within the specimen prefer to initially switch to 90° and thereafter complete a 180° domain switching. In addition, laminate-based Model 3 predicts higher values of the remnant strains along the e_3 -axis for $m = 2.0$ in comparison to the remnant strain values obtained for $m = 1.5$. It can be inferred that laminate-based Model 3 predicts increased stress-activated 90° domain switching with increasing values of viscous-like parameter m . The comparison of laminate-based Models 2, 3 and 4 with respect to the dielectric response for two different values of viscous-like parameter m is shown in Figures 4.51 and 4.52. The dielectric hysteresis response simulated with laminate Models 2 and 3 is identical for $m = 1.5$, respectively for $m = 2.0$. The 90° domain evolution observed with laminate-based Model 3 did not influence the dielectric response of the specimen. The

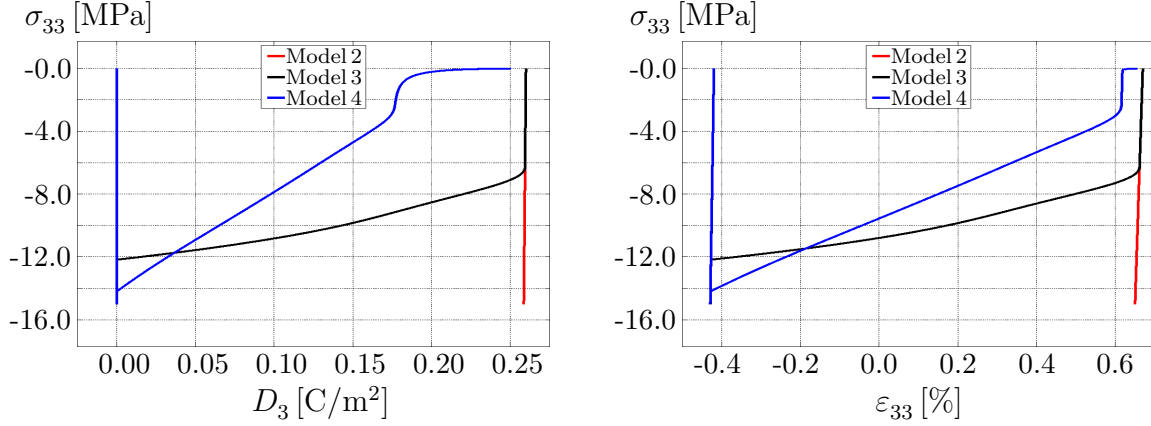


Figure 4.53: Comparison of laminate-based Models 2, 3 and 4 with respect to mechanical depolarisation curves (left) and ferroelastic hysteresis curves (right) under compressive mechanical loading and unloading at 0.05 Hz and for model parameters $m = 1.5$, $c = 3.5$.

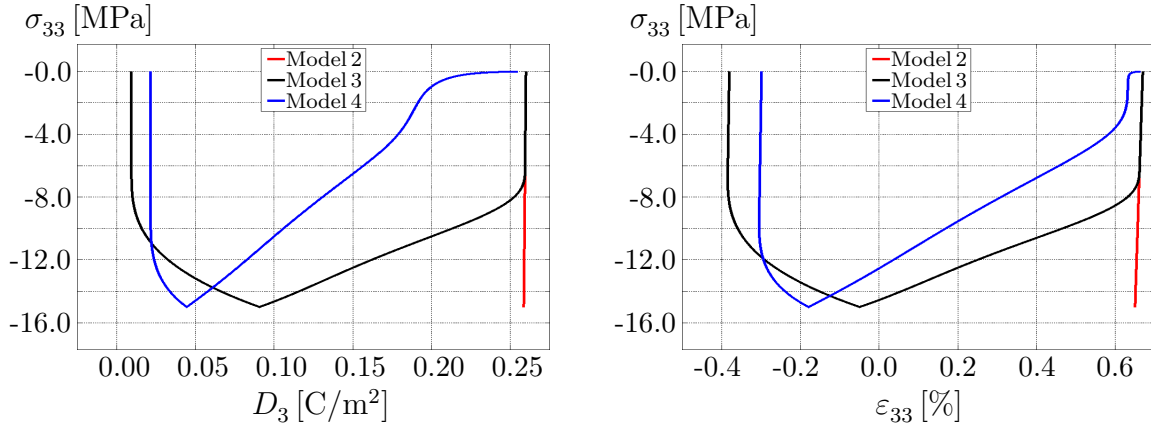


Figure 4.54: Comparison of laminate-based Models 2, 3 and 4 with respect to mechanical depolarisation curves (left) and ferroelastic hysteresis curves (right) under compressive mechanical loading and unloading at 0.05 Hz and for model parameters $m = 2.0$, $c = 3.5$.

additional remnant energy contribution of the average electric Gibbs energy postulated for laminate-based Model 4 leads to the difference in the obtained dielectric displacement values D_3 in comparison to D_3 values obtained with laminate-based Models 2 and 3. It is to be observed that all laminate-based Models 2, 3 and 4 predict a broader dielectric hysteresis curves for $m = 2.0$ than with $m = 1.5$.

A comparison of laminate-based material Models 2, 3 and 4 with respect to depolarisation and ferroelastic hysteresis curves for a mechanical loading-unloading loading frequency of 0.05 Hz and for two different values of viscous-like parameter m is shown in Figures 4.53 and 4.54. Note, that laminate-based Model 2 did not capture the mechanical depolarisation behaviour as predicted by laminate-based Models 3 and 4. Even at compressive loads of $\sigma_{33}^{\max} = -15$ MPa, laminate-based Model 2 did not predict the initialisation of the stress-activated 90° switching in the specimen. The entire loading-unloading path for laminate-based Model 2 results in a linear deformation of the specimen

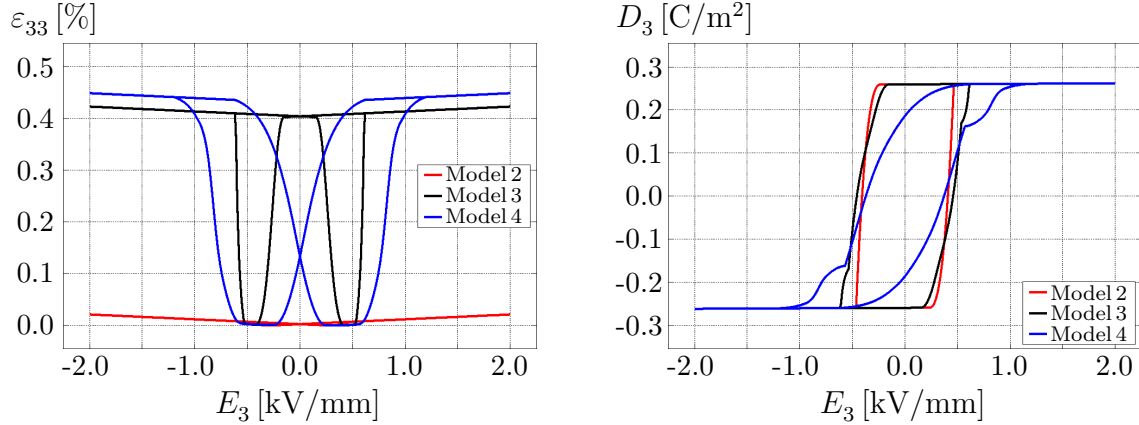


Figure 4.55: Comparison of laminate-based Models 2, 3 and 4 with respect to butterfly curves (left) and dielectric hysteresis loops (right) under homogeneous states of deformation for a cyclic electrical loading at 0.05 Hz along with a constant compressive stress of 2.7 MPa for model parameters $m = 1.5$, $c = 3.5$.

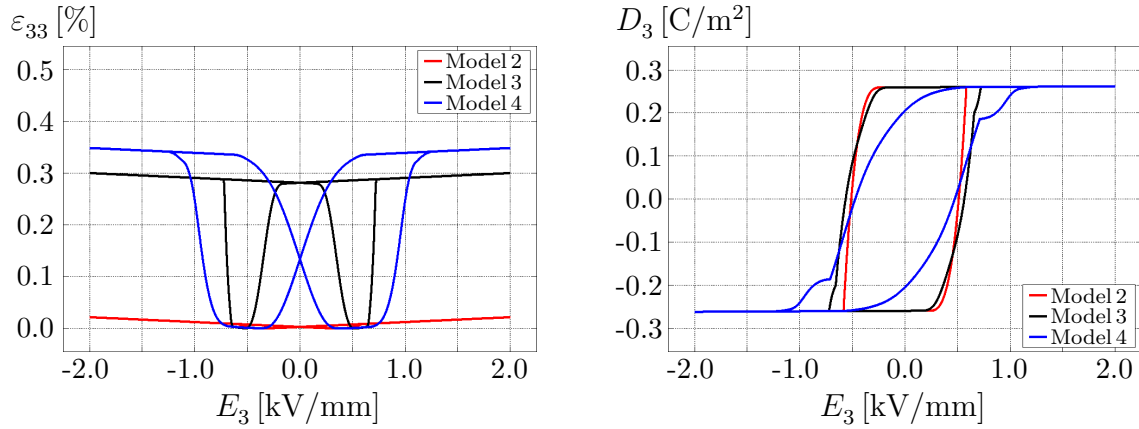


Figure 4.56: Comparison of laminate-based Models 2, 3 and 4 with respect to butterfly curves (left) and dielectric hysteresis loops (right) under homogeneous states of deformation for a cyclic electrical loading at 0.05 Hz along with a constant compressive stress of 2.7 MPa for model parameters $m = 2.0$, $c = 3.5$.

which is uncharacteristic for a single crystal tetragonal BaTiO₃ solid, see Figures 4.53 and 4.54. The particular averaging principle and the subsequent driving force derivation for laminate-based Model 2 did not predict the evolution of the variant volume fractions $\lambda_{(1,2,3,4)}$ responsible for the 90° domain switching in the specimen, refer Figure 4.30. The initialisation of the 90° domain switching and the subsequent non-linear depolarisation of the specimen with increasing compressive loading are different for laminate-based Models 3 and 4 for both the viscous-like parameter values. However, both laminate-based Models 3 and 4 predict complete depolarisation of the specimen before the maximum compressive load of $\sigma_{33}^{\max} = -15$ MPa for $m = 1.5$ in comparison to the curves obtained with $m = 2.0$.

The last part of the comparison study is performed on a three-dimensional specimen subjected to combined electromechanical loading. For this test, a constant compressive mechanical load of varying magnitudes is applied parallelly to the cyclic electrical

field at 0.05 Hz along the e_3 -axis of the poled specimen, as depicted in Figure 4.32 (c). The butterfly curves and dielectric hysteresis loops simulated with laminate-based Models 2, 3 and 4 for two different values of viscous-like parameter m are plotted in Figures 4.55 and 4.56. For viscous-like parameter $m = 1.5$, though both laminate Models 3 and 4 capture the high magnitude strain response of the poled BaTiO₃ specimen, the material response, in terms of the butterfly curves and dielectric hysteresis loops, obtained from laminate-based Model 4 is closest to the experimental observations. The difference between laminate-based Models 3 and 4 with respect to the remnant strain and polarisation values, obtained at $E_3 = 0$ kV/mm, for both $m = 1.5$ and $m = 2.0$ is due to the influence of the additional remnant energetic part considered in laminate-based Model 4. As the value of the viscous-like parameter is increased to $m = 2.0$ from $m = 1.5$, both the butterfly and dielectric hysteresis curves widen in shape for all laminate-based Models 2, 3 and 4. In the context of laminate-based Model 2, the high strain response of the butterfly curves is not as well pronounced as compared to the response obtained with laminate-based Models 3 and 4, since the ferroelastic 90° domain switching is not captured by the averaged electric Gibbs energy formulated for laminate-based Model 2. With reference to the dielectric hysteresis, however, laminate-based Model 2 predicts a response comparable to laminate-based Models 3 and 4 for both $m = 1.5$ and $m = 2.0$.

5 Laminate-based modelling of polycrystalline ferroelectric materials

Many technological and engineering applications involving ferroelectric devices are based on piezoceramics, i.e. polycrystalline ferroelectrics. In order to increase the design efficiency of these ferroelectric devices, the overall macroscopic response under external loads needs to be predicted well in advance. This chapter deals with the computational framework in order to simulate the polarisation switching behaviour and hence the macroscopic hysteretic response of a polycrystalline ferroelectric.

A polycrystalline ceramic is a compact aggregate of a number of single crystal grains of various shapes and orientations. Due to the, say randomly oriented grains, the virgin and unpoled polycrystalline ceramic may be considered isotropic on a macroscopic level. Upon application of a large external electrical field along a particular global axis, the randomly oriented domains within each grain gradually align along the loading direction. The alignment of the microscopic domains leads to the evolution of macroscopic remnant polarisation along the particular direction. A saturation point is reached, wherein an additional increase of the applied electric field does not induce any further deformation or polarisation evolution in the ceramic. At this saturated state, the polycrystalline ferroelectric is poled and possesses macroscopic anisotropic properties along the loading direction. The switching phenomenon encountered in the ferroelectric polycrystalline ceramics is dissipative in nature resulting in a macroscopic non-linear hysteretic material response.

In order to obtain a clear picture of the macroscopic behaviour of the polycrystalline ceramics from the polarisation switching response of the individual single crystal grains, several micromechanical models along with suitable homogenisation or averaging strategies exist in the literature. With the help of these homogenisation procedures, both the ferroelectric and ferroelastic behaviour of polycrystalline ceramics can be predicted well in advance. Reference is made to the works by Hwang et al. [63], Chen and Lynch [32], Hwang and McMeeking [61, 62], Huber et al. [57], Arokiarajan et al. [5–7] and to the references cited therein for a theoretical and numerical background. Kamlah et al. [75] implemented the micromechanical model developed in [57] within a finite element environment to obtain the macroscopic polycrystalline response. The model implementation was performed in the finite element framework proposed by Landis [87], wherein the electric displacement vector was treated as the primary field variable instead of the

standard scalar electric potential. Contribution [75] summarised the strain and dielectric hysteresis curves, as well as the volume fraction evolution of a ferroelectric single crystal grain first. The obtained individual grain responses were embedded in the finite element framework of [87] by applying an orientation distribution to the crystallographic axes of the individual grains. Assuming plane-strain conditions, both strain and dielectric response of a polycrystalline ferroelectric were numerically computed. In view of the study of the bulk polycrystalline behaviour, Jayabal et al. [68, 69] used the volume fraction-based approach within a polygonal finite element framework in order to predict the ferroelectric and ferroelastic hysteresis curves. Each Voronoi polygonal finite element was assumed to be a single crystal grain. The remnant polarisation and strain, as well as the material moduli of the individual grains were obtained by weighting the respective spontaneous values with their corresponding volume fractions. A micromechanical switching criterion based on both 90° and 180° domain switching effects was postulated for each Voronoi grain. Their polygonal model reproduced the hysteresis curves and the polarisation rotation test for a PZT specimen under combined electromechanical loading. Extending the formulation of [69], Jayabal and Menzel [67] demonstrated the applicability of the hybrid finite element method in studying the deformation of a three-dimensional polycrystalline ceramic under mechanical bending load. As in their previous formulations, the individual grains of the ferroelectric polycrystal were represented by means of a Voronoi cell to take the irregular grain shape into account.

Based on the ideas elaborated in the works by Chen and Lynch [32], Arokiarajan et al. [5] and Bhattacharya and Li [19], the present chapter details the computational framework in order to simulate the polarisation switching behaviour and the macroscopic hysteretic response of a polycrystalline ferroelectric. In particular, laminate-based Model 4, developed in Chapter 4 for single crystal tetragonal ferroelectrics, is used to predict the bulk polycrystalline tetragonal BaTiO_3 material response by performing a simple homogenisation procedure. At first, focus is set on the identification of the model parameters by minimising a least-square functional based on available experimental data. The identification of the model parameters, based on the single crystal BaTiO_3 experimental butterfly and dielectric hysteresis curves, is investigated in the first part of Section 5.1. The subsequent parts in Section 5.1 validate the single crystal laminate Model 4 based on tests under both homogeneous and inhomogeneous states of deformation considering the optimal model parameter values. Following the calibration procedure, a homogenisation-type strategy based on random orientation of the individual grains in a polycrystalline aggregate is explained in Section 5.2. The material properties and the polarisation switching response of the randomly oriented individual grains are averaged by using a finite element framework in order to study the macroscopic polycrystalline behaviour. In order to show the capabilities of the proposed computational framework, representative finite element simulations depicting the solution of the boundary value problems are presented in Section 5.3. These simulations include the study of the macroscopic hysteretic response of a three-dimensional block under cyclic electrical loading at varying frequencies. The obtained macroscopic butterfly curve and dielectric

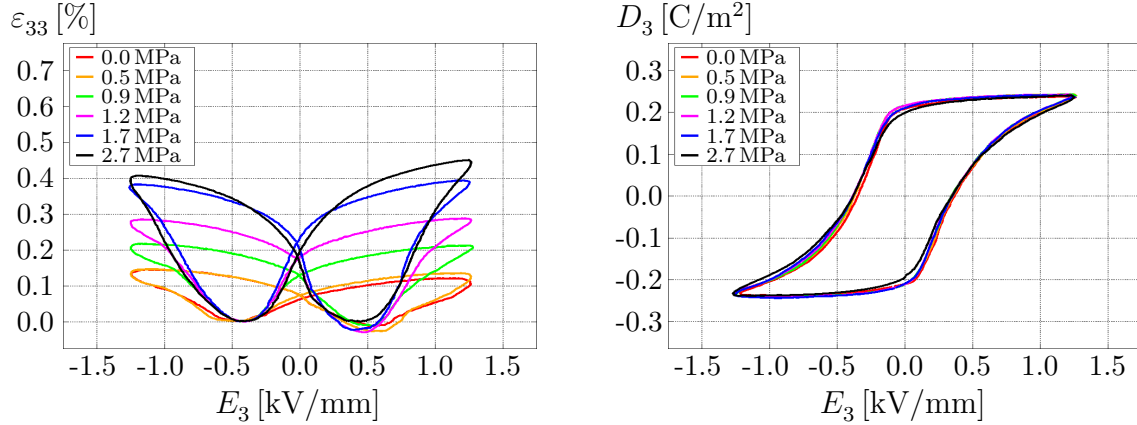


Figure 5.1: Experimental butterfly curves (left) and dielectric hysteresis loops (right) for a [001]-oriented single crystal tetragonal BaTiO₃ subjected to combined electromechanical loading. The plotted curves are extracted from the hysteresis data reported by Shieh et al. [131].

hysteresis loop for a particular electrical loading frequency are compared with newly generated experimental data for a bulk BaTiO₃ piezoceramic. Furthermore, the macroscopic ferroelastic hysteresis curves of the three-dimensional block specimen is predicted for different loading-unloading frequencies. Section 5.3 closes with the analysis of the non-linear poling behaviour of an inhomogeneous actuator specimen.

5.1 Calibration of model parameters

This section details the calibration procedure considered in order to identify the model parameters of the laminate-based formulations for single crystal tetragonal ferroelectric solids based on the available experimental butterfly and dielectric hysteresis curves. For the calibration process, laminate-based Model 4 is considered as the basis model which predicts the external stress and rate-dependent material response of the single crystal tetragonal BaTiO₃ closest to the experimental data.

The material parameters defining the linear piezoelectric response behaviour as well as the coercive electric field constants characterising the onset of polarisation switching of single crystal tetragonal BaTiO₃ are taken from the literature. The list of single crystal tetragonal BaTiO₃ material constants, adopted from [125, 151, 152], are summarised in Table 4.3. The derived laminate-based Model 4 includes parameters which influence the non-linear hysteretic behaviour in addition to the listed material constants. These model or fitting parameters include viscosity-type parameter η^p , viscous-like parameter m and slope parameter c . These additional fitting parameters need to be identified based on measured butterfly and dielectric hysteresis data for single crystal BaTiO₃ samples. The discrepancies between the experimental data and the simulated total strains and dielectric displacements are minimised in order to arrive at the optimal values following a least-square error minimisation technique.

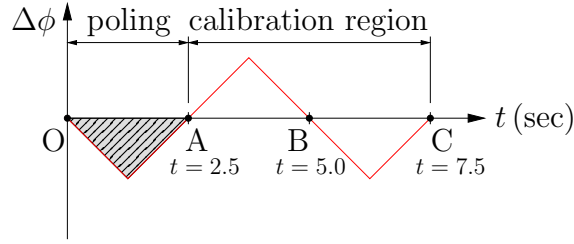


Figure 5.2: Loading curve considered for the simulation: applied potential difference vs time.

For reference values, we consider the butterfly and dielectric hysteresis curves measured by Shieh et al. [131], see Figure 5.1. Unpoled [001]-oriented single crystal tetragonal BaTiO_3 samples of dimensions $5 \text{ mm} \times 5 \text{ mm} \times 2 \text{ mm}$ were used in their study. In their experiments, the single crystal sample was subjected to a combined electromechanical loading, wherein a cyclic electrical load was applied at 0.2 Hz along with varying magnitudes of constant compressive mechanical stress between 0 and 2.7 MPa. With respect to the numerical simulations, a constitutive driver routine is used to iteratively compute the strains and the dielectric displacements for the prescribed electric field and compressive stress, cf. [81, 110, 111].

Since the considered experiments [131] were carried out at a fixed electrical loading frequency, viscosity-type parameter η^p is set to a constant value during the entire calibration process. By setting $\eta^p = 0.01 \text{ m}^2/\text{C s}$, viscous-like parameter $m > 0$, introduced in the rate-dependent dissipation equation (4.31), and slope parameter $c > 0$, influencing the remnant energy contribution (4.89) of laminate-based Model 4, are identified by minimising a least-square functional $f(\boldsymbol{\kappa})$. The specific non-linear constrained optimisation problem reads

$$\boldsymbol{\kappa} = \arg \min_{\boldsymbol{\kappa}} \{f(\boldsymbol{\kappa})\} \quad \text{such that} \quad \boldsymbol{\kappa} = \{m > 0, c > 0\}, \quad (5.1)$$

wherein the least-square functional depending on $\boldsymbol{\kappa} = \{m, c\}$ is formulated as

$$f(\boldsymbol{\kappa}) = \frac{1}{2} \sum_{k=1}^T \left[\sum_{i=1}^{N_1^k} w_1^{ki} \left| \varepsilon_{33}^{ki, \text{sim}}(\boldsymbol{\kappa}, E_3^{ki, \text{exp}}) - \varepsilon_{33}^{ki, \text{exp}}(E_3^{ki, \text{exp}}) \right|^2 + \sum_{j=1}^{N_2^k} w_2^{kj} \left| D_3^{kj, \text{sim}}(\boldsymbol{\kappa}, E_3^{kj, \text{exp}}) - D_3^{kj, \text{exp}}(E_3^{kj, \text{exp}}) \right|^2 \right]. \quad (5.2)$$

Here, index $T = 6$ represents the set of experimental hysteresis curves for the six different external stress levels, see Figure 5.1. Indices N_1^k and N_2^k denote the number of data points extracted from the butterfly and the dielectric hysteresis curves corresponding to the k^{th} -set of external stress levels. The extracted data points are arranged in the

form of an array, wherein N_1^k provides information on the experimental electrical field values $E_3^{ki, \text{exp}}$ and their equivalent total strain magnitudes $\varepsilon_{33}^{ki, \text{exp}}$. Analogously, N_2^k decodes the experimental electrical field values $E_3^{kj, \text{exp}}$ and their corresponding dielectric displacements $D_3^{kj, \text{exp}}$. Before starting the calibration process, the simulation results and the experimental data must be referred to identical events in time which, in general, requires appropriate interpolation techniques. The iteratively computed total strains under homogeneous states of deformation, for the electric fields $E_3^{ki, \text{exp}}$ and for varying compressive stress magnitudes σ_{33} as input values, are denoted by $\varepsilon_{33}^{ki, \text{sim}}(\boldsymbol{\kappa}, E_3^{ki, \text{exp}})$. Similarly, the simulated dielectric displacements also under homogeneous states of deformation using $E_3^{kj, \text{exp}}$ and σ_{33} as inputs are designated by $D_3^{kj, \text{sim}}(\boldsymbol{\kappa}, E_3^{kj, \text{exp}})$. Finally, the scalar and non-negative weighting factors considered in the least-square functional (5.2) are defined as

$$w_1^{ki} := \Delta t^{ki, \text{exp}} / \Delta t^{ki, \text{sim}} \quad \text{and} \quad (5.3)$$

$$w_2^{kj} := \Delta t^{kj, \text{exp}} / \Delta t^{kj, \text{sim}}, \quad (5.4)$$

wherein Δt is defined as the difference between any two successive time intervals within the considered loading curve. To be specific, $\Delta t^{ki, \text{sim}} = \Delta t^{kj, \text{sim}} = 0.002 \text{ sec}$ is the constant time increment considered during the simulations. The time increments

$$\Delta t^{ki, \text{exp}} = t_{n+1}^{ki, \text{exp}} - t_n^{ki, \text{exp}} \quad \text{and} \quad \Delta t^{kj, \text{exp}} = t_{n+1}^{kj, \text{exp}} - t_n^{kj, \text{exp}}, \quad (5.5)$$

vary with respect to the experimental hysteresis curves corresponding to the specific external stress level.

The experimental butterfly and dielectric displacement hysteresis plots for varying external stress magnitudes were reported by Shieh et al. [131] for one full triangular loading cycle. Information on the loops preceding the reported hysteresis curves was not provided in their work. Based on the available data, the points are extracted starting from the remnant configuration of the sample, see Figure 5.1. In order to be in line with the experimental results, the poled specimen considered for the simulations is loaded and unloaded once at 0.2 Hz such that the remnant state is reached, see the shaded region OA in Figure 5.2. Starting from this reference remnant state, point A in Figure 5.2, the identification process is commenced by minimising the least-square functional (5.2).

The error minimisation problem is first solved using the `ga` solver (genetic algorithm) within the Optimization Toolbox provided in MATLAB in order to find the suitable initial values for the two model parameters. By setting the lower and upper bounds to finite non-negative values, this initial procedure is carried out separately for the six individual external stress-dependent hysteresis loops. From the generated list of initial values, an appropriate starting value is selected for each of the two model parameters. Considering the new start values, the least-square functional (5.2) is minimised by using the `fmincon` solver (constrained nonlinear minimisation) powered by SQP-based algorithm considering all the reported hysteresis curves simultaneously in MATLAB. The

optimal viscous-like and slope parameters obtained considering all six sets of external stress level data read

$$m = 1.494 \quad \text{and} \quad c = 3.648. \quad (5.6)$$

Having identified the optimal fitting parameters and by considering the material parameters listed in Table 4.3, representative boundary value problems both under homogeneous and inhomogeneous states of deformation are solved with the help of the finite element method in order to validate the particular laminate-based Model 4.

In the context of the tests under homogeneous states of deformation, the specimen is subjected to a combined electromechanical loading, wherein varying magnitudes of compressive mechanical load is applied parallel to the cyclic electrical loading direction. The boundary conditions as well as the load curves are the same as depicted in Figure 4.32 (c). The strain and dielectric hysteresis loops under cyclic electrical loading at 0.2 Hz along with varying magnitudes of constant compressive stresses starting from 0 to 2.7 MPa simulated with laminate-based Model 4 for the calibrated model parameters are plotted in Figure 5.3. For comparison with the experimental data, see Figure 5.1, the simulated strain and dielectric hysteresis plots correspond to the second loading cycle. Moreover, for the individual applied stress levels, the minimum value of the obtained total strains is considered as the reference point to which the individual butterfly curves are shifted. The increase in the obtained actuation strains, with increase in the applied stress levels without significant differences in the dielectric displacement values, is well captured by laminate-based Model 4. The comparison of the experimental data to the simulated results, with the calibrated model parameters, with respect to the butterfly curves and dielectric displacement hysteresis loops for a cyclic electrical loading frequency of 0.2 Hz and for one specific mechanical load of $\sigma_{33} = -2.7$ MPa is shown in Figure 5.4. It is observed that the particular laminate-based Model 4 with the calibrated model parameters captures the external stress-dependent hysteretic response of the single crystal tetragonal BaTiO₃ in line with the experimentally obtained data.

The versatility of single crystal laminate-based Model 4 is further demonstrated by solving an inhomogeneous boundary value problem. This test under inhomogeneous states of deformation is performed on an initially poled three-dimensional plate with a centred hole. The boundary conditions along with the load curves for the specimen under study are the same as the ones considered for the inhomogeneous study with the phenomenological model, depicted in Figure 3.6. The crystallographic axes of the initially poled specimen are assumed to coincide with reference Cartesian axes $\mathbf{e}_{1,2,3}$. The specimen has the planar dimensions $L \times H = 10 \text{ mm} \times 10 \text{ mm}$ spanning along the \mathbf{e}_2 and \mathbf{e}_3 -directions. The thickness of the specimen along the \mathbf{e}_1 -axis is $T = 1 \text{ mm}$ and the diameter of the centred hole is $D = 3 \text{ mm}$. In view of the finite element method, the specimen under study is discretised by 400 tri-linear brick elements. With respect to the displacement boundary conditions, both the top and bottom surfaces of the plate are prescribed with zero values of displacements along all the three Cartesian directions.

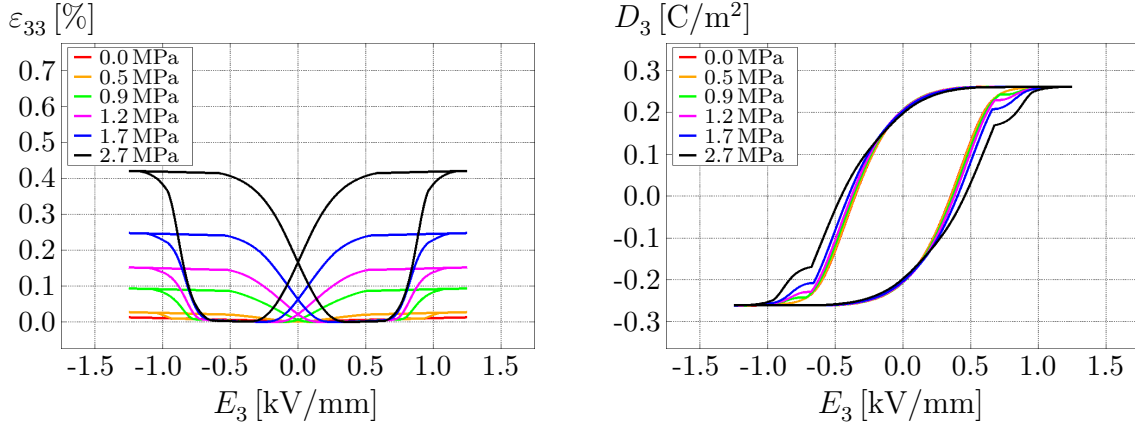


Figure 5.3: External stress-dependent hysteresis curves simulated with laminate-based Model4 for calibrated model parameters $m = 1.494$, $c = 3.648$. Butterfly curves (left) and dielectric hysteresis loops (right) for a cyclic electrical loading at 0.2Hz along with varying compressive stress levels.

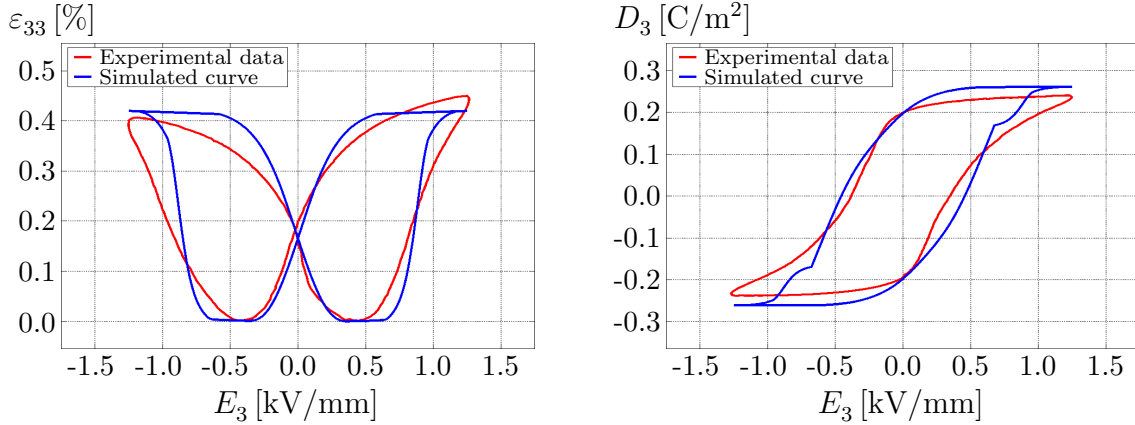


Figure 5.4: Comparison of experimental and simulated butterfly curves (left) and dielectric hysteresis loops (right) for a single crystal BaTiO_3 specimen subjected to a cyclic electrical loading at 0.2 Hz along with a compressive stress $\sigma_{33} = 2.7$ MPa. The experimental data is taken from [131] and the simulated hysteresis curves are obtained with laminate-based Model 4 for $m = 1.494$, $c = 3.648$.

A cyclic time-dependent electric field with a potential difference of $\Delta\phi^{\max} = \pm 20$ kV at a loading frequency of 1 Hz is applied across the top and bottom surfaces of the plate along the \mathbf{e}_3 -axis. For the defined boundary conditions, the total strains and the dielectric displacements are computed iteratively with respect to the applied external electrical field. Figure 5.5 shows the distribution of the electric potential, total strain and dielectric displacement at different time intervals along the loading direction across the specimen. Domain switching and subsequent evolution of the laminate volume fraction along the loading direction is initiated once the corresponding driving force exceeds the coercive limit. Due to the inhomogeneity of the problem under study, the evolution of the multi-rank laminate volume fractions in the specimen are not uniform. Moreover, due to the imposed zero displacements at both the top and bottom surfaces, the deformation

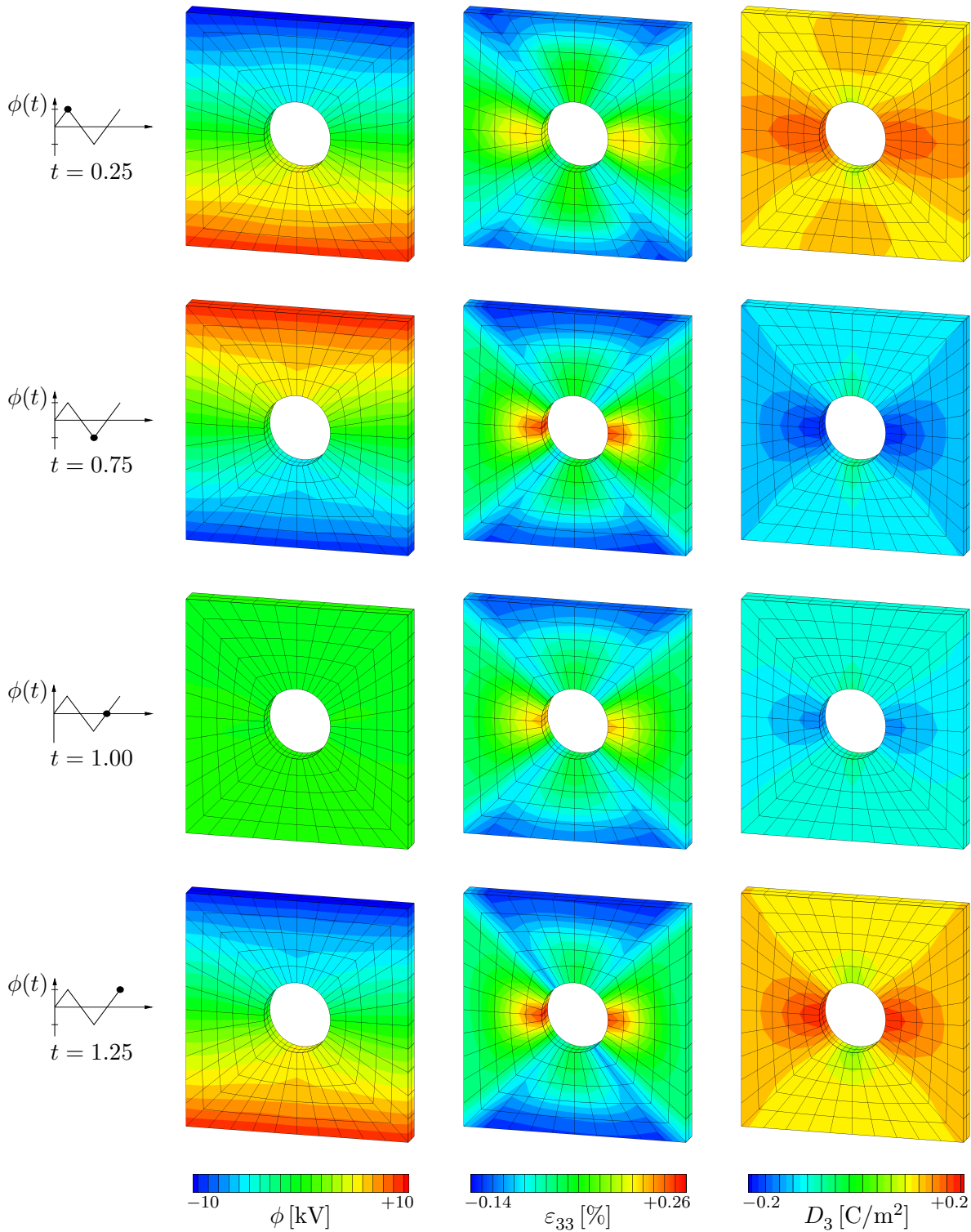


Figure 5.5: Contour plots of scalar electric potential ϕ , total strain ε_{33} and of dielectric displacement D_3 at different time intervals simulated with laminate-based Model 4 for the calibrated model parameters $m = 1.494$, $c = 3.648$. The specimen is subjected purely to a cyclic electrical field at 1 Hz. The load curve on the left-most side depicts the time-dependent electric potential loading at the top electrode. The schematic sketch of the corresponding boundary value problem is shown in Figure 3.6.

obtained across the specimen is highly non-uniform and mostly concentrated near the hole region. It can be observed that the distribution of both the total strain and dielectric displacement is slightly different for the poled states at $t = 0.25$ and 1.25 secs. This explains that the response of the ferroelectric specimen is different when loaded from an initially poled configuration compared to the re-poling from its remnant state.

5.2 Averaged response of polycrystalline ferroelectrics

The bulk polycrystalline ferroelectric is an aggregate of a number of single crystal grains of various shapes and orientations. Two neighbouring grains are separated from each other by a grain boundary. The properties of the crystal near the grain boundaries as well as the intergranular effects play an important role while studying the macroscopic response of the bulk ceramic under sufficiently large external electrical or mechanical loads. In our averaging procedure, the grain-to-grain interactions are not explicitly taken into account by postulating additional functions. However, the intergranular effects are established implicitly by solving the necessary finite element equations. In addition, the assumption of a perfect ceramic devoid of any defects or voids is considered in our formulation.

Based on these assumptions, the bulk polycrystalline ferroelectric is assigned to a global reference coordinate system coinciding with Cartesian axes $\mathbf{e}_{1,2,3}$. The single crystal grains in the bulk ceramic are assigned to a local coordinate system which is randomly oriented corresponding to the global reference coordinate system. The random orientation of the individual crystals is obtained by carrying out three successive proper Euler rotations of the individual default local coordinate axes, cf. [32, 63]. The three consecutive Euler angles of rotation are designated by $\boldsymbol{\theta} = (\Phi, \Theta, \Psi)$. The three Euler angles are initialised with random values for individual grains so that

$$\Phi, \Psi \in [0, 2\pi] \quad \text{and} \quad \sin(\Theta - \pi/2) \in [-1, 1], \quad (5.7)$$

hold. For further details on the Euler angles and their properties, the reader is referred to the textbook by Goldstein [51].

The sequence of rotations is as follows. Let an arbitrary single crystal grain be initially oriented along the default global crystallographic axes $\mathbf{e}_{1,2,3}$, as depicted in Figure 5.6 (a). The default orientation is rotated by an angle Φ in counter-clockwise direction around the \mathbf{e}_3 -axis to arrive at the orientation spanned by $\tilde{\mathbf{e}}_{1,2,3}$, as denoted in Figure 5.6 (b). During this first rotation, $\mathbf{e}_3 = \tilde{\mathbf{e}}_3$ holds. The oriented grain, Figure 5.6 (b), is rotated counter-clockwise around the $\tilde{\mathbf{e}}_1$ by an angle Θ to arrive at the grain orientation with base vectors $\hat{\mathbf{e}}_{1,2,3}$, see Figure 5.6 (c). During the transformation from the second to the third orientation, condition $\tilde{\mathbf{e}}_1 = \hat{\mathbf{e}}_1$ holds. Finally, the rotated configuration, Figure 5.6 (c), is subjected to a third rotation by an angle Ψ counter-clockwise around the $\hat{\mathbf{e}}_3$ -axis to arrive at the configuration depicted in Figure 5.6 (d) with unit bases $\mathbf{e}'_{1,2,3}$, with the condition

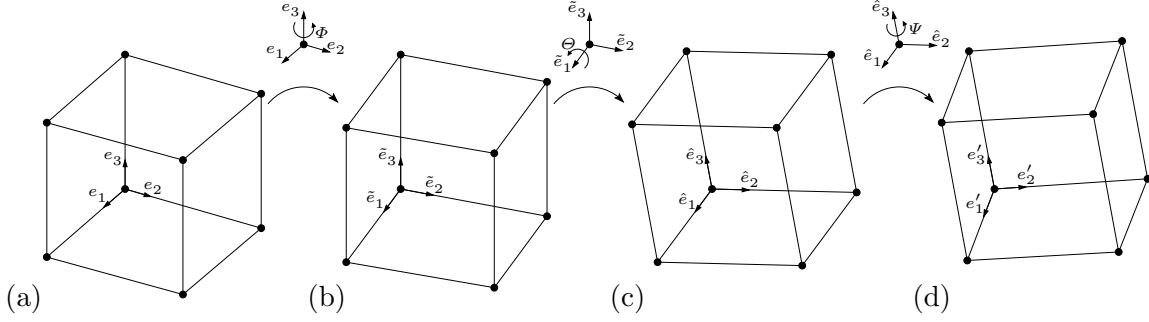


Figure 5.6: Schematic representation of the elemental rotation sequence defined by proper Euler angles Φ, Θ, Ψ starting from an initial configuration (a) to a final rotated configuration (d).

$\hat{e}_3 = e'_3$. The local coordinates of the rotated individual grains, spanned by the base vectors $e'_{1,2,3}$, are related to the global default coordinate system via the relation

$$e'_i = \mathbf{R}^\theta(\boldsymbol{\theta}) \cdot e_i \quad \text{for } i = 1, 2, 3, \quad (5.8)$$

wherein $\mathbf{R}^\theta(\boldsymbol{\theta})$ is the product of the three successive rotation tensors

$$\mathbf{R}^\theta(\boldsymbol{\theta}) = \mathbf{R}^\Psi(\Psi) \cdot \mathbf{R}^\Theta(\Theta) \cdot \mathbf{R}^\Phi(\Phi). \quad (5.9)$$

The individual rotation tensors for the three proper rotations are defined by the respective coefficients

$$[\mathbf{R}^\Phi]_{e_i} = \begin{bmatrix} \cos(\Phi) & \sin(\Phi) & 0 \\ -\sin(\Phi) & \cos(\Phi) & 0 \\ 0 & 0 & 1 \end{bmatrix}, \quad (5.10)$$

$$[\mathbf{R}^\Theta]_{\tilde{e}_i} = \begin{bmatrix} 1 & 0 & 0 \\ 0 & \cos(\Theta) & \sin(\Theta) \\ 0 & -\sin(\Theta) & \cos(\Theta) \end{bmatrix} \quad \text{and} \quad (5.11)$$

$$[\mathbf{R}^\Psi]_{\hat{e}_i} = \begin{bmatrix} \cos(\Psi) & \sin(\Psi) & 0 \\ -\sin(\Psi) & \cos(\Psi) & 0 \\ 0 & 0 & 1 \end{bmatrix}. \quad (5.12)$$

The reader is referred to the works, for instance [5, 32], for more details on the treatment of grain orientation effects in polycrystalline ferroelectric solids.

Due to the random Euler rotations of the single crystals, the spontaneous strain and polarisation as well as the material properties of the individual crystals are described based on the rotated local crystallographic axes $\mathbf{e}'_{1,2,3}$. The rotated spontaneous strain and polarisation of the six tetragonal ferroelectric variants of individual crystals are represented as

$$\boldsymbol{\varepsilon}_{(1)}^R = \boldsymbol{\varepsilon}_{(2)}^R = [\eta_1^s - \eta_2^s] \mathbf{e}'_1 \otimes \mathbf{e}'_1 + \eta_2^s \mathbf{I}, \quad \mathbf{P}_{(1)}^R = -\mathbf{P}_{(2)}^R = P^s \mathbf{e}'_1, \quad (5.13)$$

$$\boldsymbol{\varepsilon}_{(3)}^R = \boldsymbol{\varepsilon}_{(4)}^R = [\eta_1^s - \eta_2^s] \mathbf{e}'_2 \otimes \mathbf{e}'_2 + \eta_2^s \mathbf{I}, \quad \mathbf{P}_{(3)}^R = -\mathbf{P}_{(4)}^R = P^s \mathbf{e}'_2, \quad (5.14)$$

$$\boldsymbol{\varepsilon}_{(5)}^R = \boldsymbol{\varepsilon}_{(6)}^R = [\eta_1^s - \eta_2^s] \mathbf{e}'_3 \otimes \mathbf{e}'_3 + \eta_2^s \mathbf{I}, \quad \mathbf{P}_{(5)}^R = -\mathbf{P}_{(6)}^R = P^s \mathbf{e}'_3. \quad (5.15)$$

Based on the rotated spontaneous polarisation, the structural vector and the structural tensor of the tetragonal variants within the rotated single crystals read

$$\mathbf{a}_{(\alpha)}^R := \frac{\mathbf{P}_{(\alpha)}^R}{\|\mathbf{P}_{(\alpha)}^R\|} \quad \text{and} \quad \mathbf{m}_{(\alpha)}^R := \mathbf{a}_{(\alpha)}^R \otimes \mathbf{a}_{(\alpha)}^R, \quad (5.16)$$

for $\alpha = 1, \dots, nv = 6$. Following the definitions of the rotated spontaneous and structural quantities, the material moduli of the individual variants of the randomly oriented crystals are obtained considering the rotated structural quantities (5.16). The rotated fourth-order elasticity tensor $\mathbf{E}_{(\alpha)}^R(\mathbf{a}_{(\alpha)}^R)$, the rotated third-order piezoelectric tensor $\mathbf{e}_{(\alpha)}^R(\mathbf{a}_{(\alpha)}^R)$, and the rotated second-order dielectric tensor $\boldsymbol{\varepsilon}_{(\alpha)}^R(\mathbf{a}_{(\alpha)}^R)$ are arrived by reformulating Equations (4.6) to (4.8) considering the modified definitions for the rotated structural quantities $\mathbf{a}_{(\alpha)}^R$ and $\mathbf{m}_{(\alpha)}^R$.

The volume average of remnant strain $\boldsymbol{\varepsilon}^{M,R}(\boldsymbol{\mu}; \boldsymbol{\varepsilon}_{(1,3,5)}^R)$ and of remnant polarisation $\mathbf{P}^{M,R}(\boldsymbol{\mu}; \mathbf{P}_{(1,3,5)}^R)$ of the rotated single crystal grains is arrived at by reformulating the volume average expressions (4.17) and (4.18) considering the rotated spontaneous strain and polarisation defined in Equations (5.13) to (5.15). Analogously, the rotated volume averaged material moduli, namely elasticity tensor $\mathbf{E}^{M,R}(\boldsymbol{\mu}; \mathbf{E}_{(1,3,5)}^R)$, piezoelectric tensor $\mathbf{e}^{M,R}(\boldsymbol{\mu}; \mathbf{e}_{(1,3,5)}^R)$ and dielectric tensor $\boldsymbol{\varepsilon}^{M,R}(\boldsymbol{\mu}; \boldsymbol{\varepsilon}_{(1,3,5)}^R)$ are reformulated in terms of the rotated material moduli of the individual variants. The rotated structural and remnant quantities as well as the rotated material moduli enter the average electric Gibbs energy corresponding to laminate-based Model 4 to describe the coupled electromechanical process. The global governing constitutive equations are solved using the finite element method in order to arrive at the overall macroscopic response.

5.3 Numerical examples

This section is aimed at studying the average macroscopic response and the remnant polarisation switching behaviour of bulk ceramic BaTiO₃ by solving representative numerical examples. The first part of the simulation involves the investigation of both

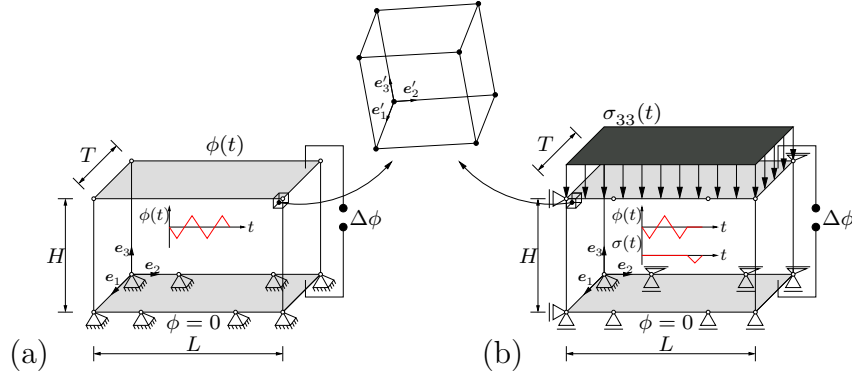


Figure 5.7: Schematic representation of three-dimensional specimen along with the boundary conditions and load curves subjected to (a) cyclic electrical and (b) electromechanical loading. The geometry of both the boundary value problems are discretised by 100 tri-linear brick elements, wherein the crystallographic axes e'_i within each element are randomly generated.

the average ferroelectric and ferroelastic hysteresis curves of a three-dimensional block under electrical and under electromechanical loading conditions. The numerically simulated macroscopic butterfly and dielectric hysteresis loops under pure electrical loading at 0.2 Hz are compared to the newly measured experimental data. The final part of the polycrystalline simulation deals with the analysis of an inhomogeneous boundary value problem in connection with its relevance to practical applications. A multilayer stack actuator example with necessary symmetry conditions is considered for the study. The simulated poling behaviour and the remnant polarisation switching response of the actuator specimen are examined under cyclic electrical loading.

For all the polycrystalline numerical simulations, the bulk specimen under study is described by a global coordinate frame assumed to coincide with the reference Cartesian axes $e_{1,2,3}$. With respect to the finite element method, the respective boundary value problems are discretised by a number of elements, wherein the crystallographic directions attached to each finite element are randomly generated. The orientation of the respective crystallographic axes are spanned by the rotated Cartesian axes $e'_{1,2,3}$ as defined by the three randomly initialised Euler angles $\theta = (\Phi, \Theta, \Psi)$, see Section 5.2. Note, that one set of Euler angles is generated for all integration points within each finite element.

5.3.1 Hysteretic response of a polycrystalline block

In order to predict the average macroscopic hysteretic response of a bulk polycrystalline BaTiO_3 with the computational framework based on laminate Model 4 formulation, the following numerical tests are performed on a block-type specimen separately under electrical and under electromechanical loading. The schematic representation of the boundary value problems considered for the numerical tests is shown in Figure 5.7. The three-dimensional specimen measures $L \times H = 5 \text{ mm} \times 2 \text{ mm}$ with a thickness of $T = 5 \text{ mm}$. The global coordinate system of the block specimen is assumed to coincide

with reference Cartesian axes $e_{1,2,3}$. With respect to the finite element discretisation, the specimen is subdivided into 100 tri-linear brick elements. The crystallographic axes of the individual finite elements, assigned to a local coordinate frame spanned by $e'_{1,2,3}$, are oriented in different directions due to the random initialisation of the three Euler angles. Moreover, initial poling along the (local) positive e'_3 -axis is considered by setting $\mu^{1,2,3,4}|_{t_0} = 0$ and $\mu^5|_{t_0} = 1$.

For the first of the two boundary value problems, the specimen is subjected to an alternating electrical field at varying loading frequencies. The potential difference across the specimen is generated by grounding the lower electrode and by applying a time-dependent scalar electrical potential $\phi(t)$ at the upper electrode with $\phi^{\max} = \pm 6$ kV. With respect to the displacement boundary conditions, all the nodes at the bottom surface of the specimen are prescribed to zero values along all the three global Cartesian axes. The particular boundary value problem along with the load curve is depicted in Figure 5.7 (a).

The average butterfly and dielectric displacement hysteresis curves obtained for an electrical loading frequency of 0.2 Hz are plotted in comparison to the experimentally measured hysteresis data in Figure 5.8. The experiments were carried out in collaboration with Prof. A. Arockiarajan at the Department of Applied Mechanics, Indian Institute of Technology Madras. The cylindrical sample used for the experimental study was a poled polycrystalline tetragonal BaTiO₃ with a diameter measuring 10 mm and with a thickness of 2 mm. For the purpose of comparison, the remnant strain values of both the measured and simulated data are considered as reference points to which the butterfly curves are shifted.

Due to the random initial orientations of the individual crystallographic directions, the ceramic specimen does not possess a macroscopic polarisation along any particular direction in its virgin state. The initial unpoled state is characterised by almost zero values of average dielectric displacements along the loading direction, $D_3|_{t_0} \approx 0$ C/m². As the applied macroscopic electrical field gradually increases, the driving force of the individual laminate systems within each grain exceeds the critical force value. This initiates the microscopic switching and aligns the domains along the electrical loading direction within the individual grains. On a macroscopic level, one may observe the non-linear increase in both the simulated average total strain and dielectric displacement from their initial zero values to their maximum positive values obtained at $E_3 = 3$ kV/mm. At this maximum positive electrical loading, the ceramic specimen is in an elongated poled state along the loading direction. Though differences in the strain values at $E_3 = 3$ kV/mm are visible between the experimental and the simulated butterfly curves, the magnitude of the numerically computed dielectric displacement D_3 at this maximum positive loading point correlates its experimentally measured counterpart. The specimen reaches a remnant state once the applied electric field is decreased from $E_3 = 3$ kV/mm to 0 kV/mm. During this unloading phase, the specimen behaves linearly exhibiting a linear piezoelectric response. Moreover, the simulated dielectric displacement values are comparable to the experimentally measured data during the piezoelectric response. Re-

versal of the electric field and loading of the specimen further with negative electrical fields orients the domains within the individual single crystals along the reversed loading direction. At the negative maximum load of $E_3 = -3 \text{ kV/mm}$, the dielectric displacement is almost saturated and the specimen acquires a new poled state along the global negative e_3 -axis. Subsequent loading of the specimen up to $E_3 = 3 \text{ kV/mm}$ re-orientes the domains, and hence the macroscopic remnant polarisation back along the loading direction. The closed butterfly and dielectric hysteresis loops are obtained after the completion of one full loading cycle. The simulation results predict wider butterfly and dielectric displacement hysteresis loops for 0.2 Hz in comparison to the measured curves. The experimental investigation on the ceramic shows that domain switching begins at much lower magnitudes of the electric field, at $E_3 \approx \pm 0.3 \text{ kV/mm}$, whereas in the simulations, macroscopic domain switching initiates at around $E_3 = \pm 1 \text{ kV/mm}$. The difference in the simulated and measured curves may be due to the fact that the averaging procedure carried out to arrive at the polycrystalline response from single crystal laminate-based Model 4 is a simple strategy and does not explicitly take into account the grain-to-grain interactions evident in the bulk ceramic. Moreover, the considered material parameters for the polycrystalline simulations are based on the single crystal data. These parameters may also be a source of error.

The simulated average strains and dielectric displacements of the ceramic specimen under cyclic electrical loading for varying frequencies are shown in Figure 5.9. The plotted strain and dielectric displacement curves correspond to the second loading cycle. Furthermore, the butterfly curves for different frequency levels are shifted, such that the corresponding remnant strains obtained in the simulations at $E_3 = 0 \text{ kV/mm}$ are set to zero and treated as the reference points. The following features are observed from the simulated rate-dependent hysteresis curves. With increasing electrical loading rates from 1 Hz to 10 Hz, the coercive electric limit of the bulk specimen shows an increase, and so consequently both the butterfly and dielectric hysteresis curves widen in shape. This is due to the delay in the initialisation of the domain switching within the individual crystals as the applied frequency increases. The magnitude of both the average strains and dielectric displacements obtained at $E_3 = \pm 3 \text{ kV/mm}$ decreases with increasing loading rates. At higher frequencies, due to the limited time available, not all domains are switched completely at the maximum electrical load. As a result, the strains and the dielectric displacements obtained at frequencies greater than 2 Hz do not saturate at the maximum load $E_3 = \pm 3 \text{ kV/mm}$.

In view of the second boundary value problem, the ceramic specimen is subjected first to an alternating electrical field and is then loaded by a time-dependent mechanical compressive stress. The boundary value problem along with the load curve for this electromechanical loading of the block specimen is depicted in Figure 5.7 (b). The potential difference across the ceramic is generated by grounding the lower electrode and by applying a time-dependent scalar electrical potential $\phi(t)$ at the top electrode with $\phi^{\max} = \pm 6 \text{ kV}$. With respect to the displacement boundary conditions, the ceramic is allowed to elongate and contract along the positive global e_3 -axis while experiencing a

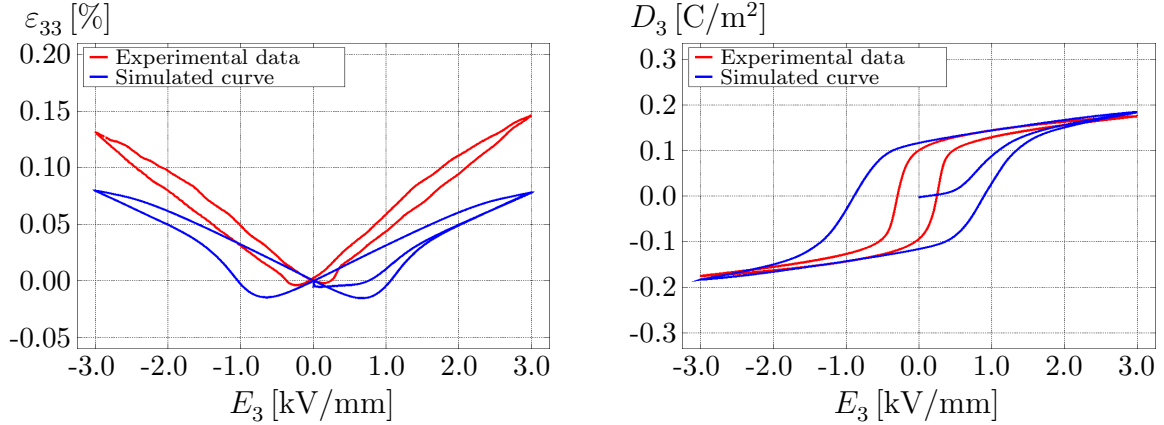


Figure 5.8: Comparison of the experimental and simulated butterfly curves (left) and dielectric hysteresis loops (right) for a polycrystalline tetragonal BaTiO_3 subjected to a cyclic electric loading at 0.2 Hz along the global \mathbf{e}_3 -axis. The experiments were performed in collaboration with Prof. A. Arockiarajan, Department of Applied Mechanics, Indian Institute of Technology Madras. The simulated curves are obtained for the boundary value problem depicted in Figure 5.7 (a).

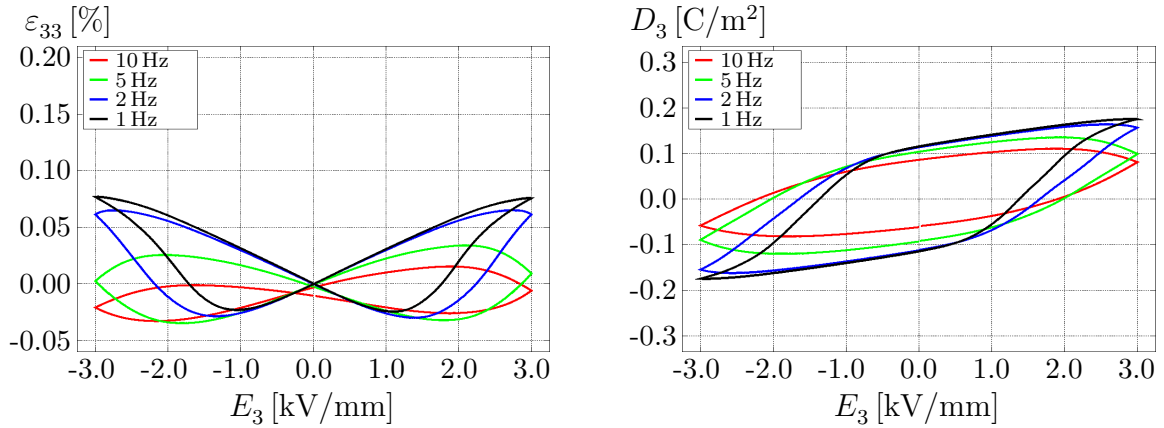


Figure 5.9: Simulated butterfly curves (left) and dielectric hysteresis loops (right) of a polycrystalline tetragonal BaTiO_3 subjected to varying frequencies of cyclic electrical loading along the global \mathbf{e}_3 -axis, with respect to the boundary value problem depicted in Figure 5.7 (a).

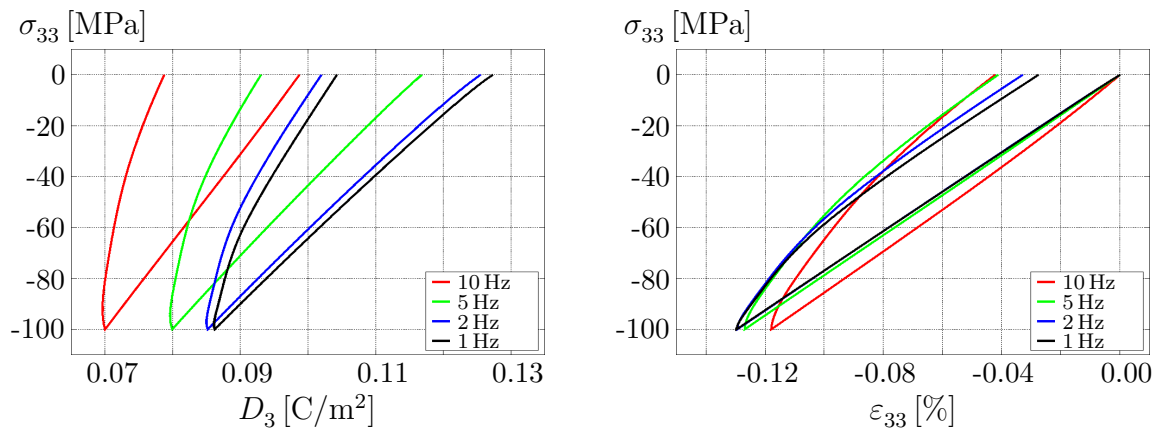


Figure 5.10: Simulated mechanical depolarisation curves (left) and ferroelastic hysteresis curves (right) of a bulk polycrystalline tetragonal BaTiO_3 . The specimen, from its remnant configuration, is subjected to varying frequencies of compressive mechanical loading and unloading along the global \mathbf{e}_3 -axis in accordance to the boundary and loading scenario as sketched in Figure 5.7 (b).

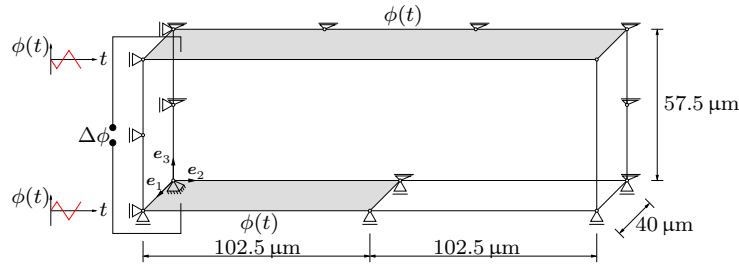


Figure 5.11: Schematic representation of three-dimensional stack actuator specimen along with the boundary conditions and load curves subjected to cyclic electrical loading at 0.2 Hz. The boundary value problem is discretised by 400 tri-linear brick finite elements, wherein the crystallographic axes within each element are randomly generated.

corresponding contraction and elongation along both the positive global e_1 and e_2 -axes. Cyclic electrical loading is applied until the ceramic specimen reaches a macroscopic remnant configuration. From this remnant state, a rate-dependent mechanical compressive stress $\sigma_{33}(t)$ is applied at the top surface of the ceramic specimen. Starting from the remnant state, the simulated average mechanical depolarisation curves and ferroelastic hysteresis curves resulting from the rate-dependent mechanical loading and unloading scenario are plotted in Figure 5.10. For the ferroelastic hysteretic response, the remnant state of the ceramic is set as the reference point to which the obtained average ferroelastic hysteresis curves are shifted, see the ferroelastic curves in Figure 5.10. From both the macroscopic ferroelastic and depolarisation hysteresis plots it becomes evident that, even as the applied stress reaches a magnitude of $\sigma_{33} = -100$ MPa, not all the domains in the bulk ceramic are switched perpendicularly to the loading direction. Moreover, as the frequency of the applied load increases, the incomplete domain switching in the ceramic results in an increased non-linear response which becomes visible from the average hysteresis plots.

5.3.2 Poling behaviour of a polycrystalline stack actuator

Following the investigation on the ferroelectric and the ferroelastic hysteretic response of a bulk polycrystalline BaTiO_3 , we proceed to analyse the non-linear response of an inhomogeneous actuator specimen under cyclic electrical loading. Kamlah and Böhle [72] have previously studied the response of a two-dimensional stack actuator specimen. Exploiting the symmetry conditions of the stack actuator boundary value problem as explained in their work, the dimensions of the actuator specimen along with the boundary conditions and load curves are shown in Figure 5.11. As assumed in the boundary value problems solved in the preceding subsection, the global coordinate system of the actuator specimen coincides with the reference Cartesian axes $e_{1,2,3}$. The boundary value problem is sub-divided into 400 tri-linear brick elements. Each finite element possesses randomly oriented crystallographic directions, such that the virgin state of the specimen corresponds to an unpoled configuration with a nullified overall macroscopic polarisa-

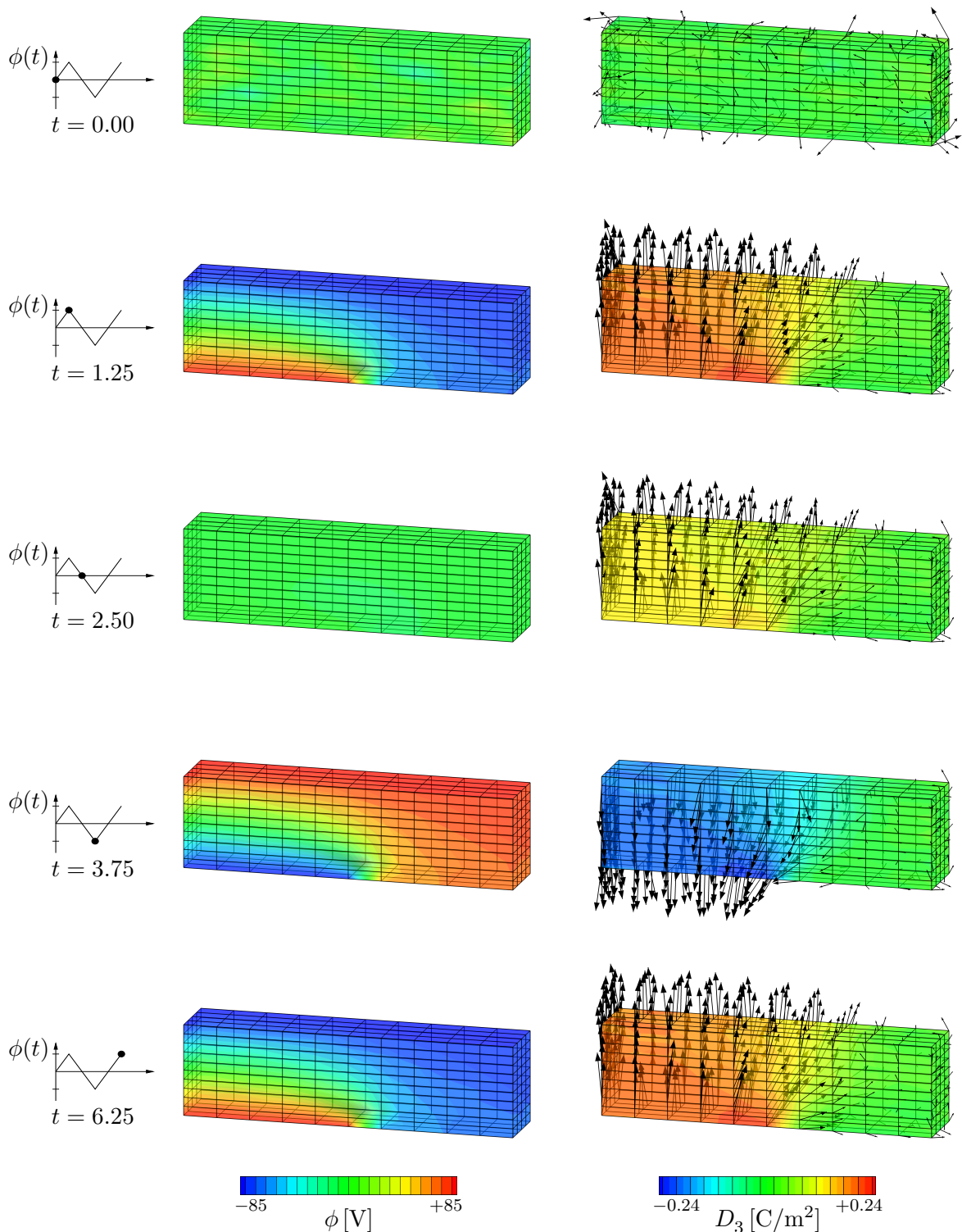


Figure 5.12: Contour plots depicting the scalar electric potential ϕ (left) and dielectric displacement D_3 (right), along with the remnant polarisation vectors, of the polycrystalline stack actuator specimen at different time intervals simulated with the help of the computational framework within the finite element environment. The load curves depicted on the left-most region correspond to the electric potential at specific time applied at the bottom electrode of the specimen.

tion. The initial poling direction is chosen along the respective (local) positive e'_3 -axis by initialising $\mu^{1,2,3,4}|_{t_0} = 0$ and $\mu^5|_{t_0} = 1$ within each finite element. In view of the electrical loading conditions, a time-dependent electric potential $\phi(t)$ is applied at both the top and bottom surfaces of the specimen at 0.2 Hz with $\phi^{\max} = \pm 85$ V. Due to the applied load, a potential difference of $\Delta\phi^{\max} = \pm 170$ V is generated between the electrodes at the maximum point of loading. The contour plots corresponding to the distribution of electric potential and to the distribution of macroscopic dielectric displacement, along with remnant polarisation vectors, at different time intervals are shown in Figure 5.12.

Due to the random initialisation of the single crystal orientations, the virgin state of bulk polycrystalline specimen corresponds to an unpoled configuration without a macroscopic remnant polarisation. We obtain almost zero values for the overall dielectric displacement along the loading direction at this initial state, that is $D_3|_{t_0} \approx 0$ C/m². Starting from this unpoled initial configuration, the potential difference across the specimen is decreased in steps of Δt . As the magnitude of the applied load increases with time, the driving force exceeds the critical resistance value defined for each laminate system. This results in the microscopic domain switching within each single crystal grain and, on a macroscopic level, the remnant polarisation of the bulk specimen evolves along the loading direction. At $t = 1.25$ sec, as the applied potential difference reaches a negative maximum of $\Delta\phi = -170$ V, the spontaneous polarisation of the individual grains between the two electrodes is aligned along the loading direction and the actuator reaches a poled state. From this poled state, as the applied electrical loading is linearly increased to zero value at $t = 2.5$ sec, the actuator reaches a remnant state. At this point the macroscopic remnant polarisation direction is still aligned along the global positive e_3 -direction. After further increasing the applied potential difference from zero to a positive maximum $\Delta\phi = 170$ V, the macroscopic remnant polarisation reverses its direction and evolves along the electrical loading direction. Due to the reorientation, the actuator reaches a poled state at $t = 3.75$ sec with the remnant polarisation vectors aligned along the global negative e_3 -axis. Finally the macroscopic remnant polarisation is reoriented along the global positive e_3 -direction as the potential difference is decreased to its positive maximum of $\Delta\phi = 170$ V at $t = 6.25$ sec.

From the simulations it can be observed that, at the fully poled and at the remnant states, the actuator acquires a high concentration of macroscopic remnant polarisation at the lower electrode tip, highlighting the inhomogeneity of the problem. Moreover, at the fully poled and remnant states, the actuator is only polarised in the region between the electrodes. The right-most part of the actuator is devoid of an effective macroscopic polarisation.

6 Summary and outlook

This dissertation deals with the development of thermodynamic consistent material models along with their numerical implementation in order to simulate the macroscopic non-linear hysteretic behaviour of both ferroelectric tetragonal single and polycrystalline solids.

Starting with a brief introduction to ferroelectric crystals and ceramics, the influence of both the loading frequency and the magnitude of the compressive mechanical stress, applied in parallel to the external electrical field, on the macroscopic hysteresis curves are highlighted in Chapter 1. The essential balance relations needed for the development of thermodynamically consistent material models in order to describe the coupled electromechanical behaviour in ferroelectric materials are summarised in Chapter 2. In particular, the basic equations of electrostatics and the considered strain and stress measures, assuming geometrically linear theory, governing the deformation of the material are introduced. Following the kinematic and stress measures, the balance equations for the coupled electromechanical response as well as the general thermodynamic framework for dissipative ferroelectric materials are provided. Thereafter, the weak formulation of the governing equilibrium equations and their approximations as well as the nodal residual equations needed for the finite element framework are outlined. The displacement vector and scalar electric potential are both treated as the primary field variables in the finite element formulation for solving the global boundary value problems.

A rate-dependent phenomenological material model to predict the macroscopic hysteretic response of tetragonal ferroelectric materials is discussed in Chapter 3. The model framework focusses on postulating a total electric Gibbs energy, with the macroscopic remnant polarisation as the only internal state variable, and a rate-dependent dissipation equation, written as a function of the rate of the macroscopic remnant polarisation. The evolution of the macroscopic remnant polarisation is obtained by solving the particular rate-dependent dissipation equation. In contrast to the incremental variational formulation [110], the full driving force expression defining the remnant polarisation evolution is considered for the numerical implementation of the presented phenomenological model. Considering single crystal tetragonal BaTiO_3 material parameters, the phenomenological model reproduces the characteristic rate-dependent butterfly curves and dielectric hysteresis loops for a three-dimensional specimen subjected to purely cyclic electrical loading under homogeneous states of deformation. Moreover, the influence of both the

loading frequency and the viscous-like parameter on the obtained strain and dielectric hysteresis curves is studied. The macroscopic material model is further implemented in a finite element environment to solve boundary value problems to study the total strain and dielectric displacement distribution under inhomogeneous states of deformation.

Based on the average strain and polarisation compatibility conditions between the distinct tetragonal ferroelectric variants, four laminate-based models are developed in Chapter 4 in order to study the rate and external stress-dependent response of ferroelectric single crystals. Starting with the introduction of the symmetry considerations and material properties of the tetragonal ferroelectric variants, four different formulations of the average electric Gibbs energy are suggested. The general form of the average electric Gibbs energy corresponding to the individual models is postulated in terms of the total strains, electric field and of the multi-rank laminate volume fractions, the latter playing the role of internal state variables. The update of the inequality constrained laminate volume fractions is solved by a Fischer–Burmeister-type algorithm in combination with a Newton–Raphson scheme. The specific algorithm is chosen in order to solve the evolution equations along with automatically constraining the laminate volume fractions within their allowed range. In context with the formulation of the average electric Gibbs energy for the individual laminate models, the four laminate-based models are developed based on different averaging principles. For laminate-based Model 1, the average electric Gibbs energy of the crystal is formulated analogous to the phenomenological model. Neglecting the average kinematic compatibility equation, the average remnant strain of the crystal is postulated as a function of the average remnant polarisation, computed by considering the polarisation compatibility condition. The material responses obtained with laminate Model 1 for tests under both homogeneous and inhomogeneous states of deformation are furthermore compared to those obtained with the phenomenological model. Laminate-based Model 2 postulates six distinct electric Gibbs energies corresponding to the individual tetragonal ferroelectric variants. The distinct electric Gibbs energies are weighted by their respective volume fractions so as to arrive at the average electric Gibbs energy of the single crystal. The rate-dependent hysteresis curves corresponding to an initially poled three-dimensional specimen subjected to a cyclic electrical load depicting pure 180° domain switching are reproduced by tests under homogeneous states of deformation. However, the high strain response of a single crystal specimen under combined electromechanical loads is not predicted by the averaging principle considered for laminate-based Model 2. In laminate-based Model 3, the averaged remnant quantities and material moduli of the six tetragonal variants are considered in order to define the average electric Gibbs energy. In view of laminate-based Model 4, the electric Gibbs energy introduced for laminate-based Model 3 is extended by a saturation-type remnant energy part based on the averaged remnant polarisation to capture the so-called back electric field effect observed during the hysteretic response. The differences in the material responses obtained with laminate-based Models 2, 3 and 4 are highlighted in the form of a comparison study. Out of the four laminate-based formulations, the butterfly curves and dielectric hysteresis loops as well as the mechanical depolarisation

and ferroelastic hysteresis curves predicted by laminate-based Model 4 is closest to the experimental observations.

Following the laminate-based formulations for tetragonal single crystal ferroelectric materials, Chapter 5 details the homogenisation procedure to predict the macroscopic rate-dependent hysteretic response of a ferroelectric ceramic under electromechanical loading. The first part of this chapter focusses on the identification of the single crystal model parameters by minimising a least-square functional based on available experimental hysteresis data. For the calibration process, laminate-based Model 4 is considered as the basis model. Considering the optimal model parameter values, laminate-based Model 4 is validated based on tests under both homogeneous and inhomogeneous states of deformation. The second part of this chapter gives details on a simple homogenisation-type strategy based on random orientations of the single crystal grains in a polycrystalline ferroelectric aggregate. The averaged polarisation switching response of the randomly oriented individual grains is obtained by means of the numerical implementation within a finite element framework. Both the simulated macroscopic butterfly curve and dielectric hysteresis loop for a particular electrical loading frequency are compared with newly generated experimental data for a barium titanate ceramic.

Outlook

The phenomenological and laminate-based model formulations developed in this work are verified by means of solving representative boundary value problems and the simulated macroscopic hysteretic responses well reproduced the characteristic ferroelectric and ferroelastic behaviour.

The phenomenological model offers a robust framework for the simulation of the rate-dependent macroscopic remnant polarisation evolution in ferroelectric materials. The macroscopic remnant strains within the constitutive model are assumed as a function of the remnant polarisation vector, thus simplifying the model formulation and its numerical implementation. As a further development, the ferroelectric yield function defining the polarisation evolution can be extended by considering the mechanical stress-induced factors in order to study the combined electromechanical response. With regard to numerics, the coupled global finite element tangent matrix is currently approximated for the simulations. An analytical exact form of the global tangent matrix is needed which may increase the computing efficiency.

In view of the laminate-based model formulations developed for single crystal ferroelectric solids, the average electric Gibbs energy is postulated by neglecting the domain wall energy contribution. Ab-initio and phase-field calculations as well as experimental observations confirm the influence of the domain wall energy barrier during the ferroelectric domain evolution under external loads. Future work should consider the contribution of the domain wall energy in order to study the microstructural polarisation evolution in detail within a single crystal grain. With such an enhanced average energy, the simulated material responses arrived with the laminate-based formulations can be

compared to those obtained from phase-field or other diffusive interface modelling approaches. Furthermore, the developed laminate-based models can be extended to study the behaviour of ferroelectric crystals with unit cells of rhombohedral symmetry, exhibiting eight equally possible variant orientations. The homogenisation procedure used in this work in order to compute the average polycrystalline ferroelectric response is a simple procedure based on random initialisation of the individual single crystal grains. As a future work, the grain-to-grain interactions evident in a polycrystalline aggregate needs to be explicitly taken into account in the formulation.

A Derivations and identification of parameters – phenomenological model

The derivations of some of the tensorial quantities with respect to the macroscopic remnant polarisation needed for the numerical implementation of the phenomenological model are provided in the first part of this appendix. The latter part gives details on the identification of the isotropic tensor coefficients based on the transversely isotropic elasticity modulus.

A.1 Useful derivations for the phenomenological model

The first and second-order derivatives of the structural quantities $\mathbf{a}(\mathbf{P}^r)$ and $\mathbf{m}(\mathbf{P}^r)$, introduced in Equations (3.1) and (3.2) respectively, with respect to \mathbf{P}^r are derived as

$$[\partial_{\mathbf{P}^r} \mathbf{a}]_{ij} = \frac{\partial a_i}{\partial P_j^r} = \frac{1}{\|\mathbf{P}^r\|} [\delta_{ij} - a_i a_j], \quad (\text{A.1})$$

$$[\partial_{\mathbf{P}^r} \mathbf{m}]_{ijk} = \frac{\partial m_{ij}}{\partial P_k^r} = \frac{\partial a_i}{\partial P_k^r} a_j + a_i \frac{\partial a_j}{\partial P_k^r}, \quad (\text{A.2})$$

$$\begin{aligned} [\partial_{\mathbf{P}^r \mathbf{P}^r}^2 \mathbf{a}]_{ijk} &= \frac{\partial}{\partial P_k^r} \left[\frac{\partial a_i}{\partial P_j^r} \right] \\ &= \frac{1}{\|\mathbf{P}^r\|} \left[-\frac{\partial a_i}{\partial P_k^r} a_j - a_i \frac{\partial a_j}{\partial P_k^r} \right] - \frac{1}{\|\mathbf{P}^r\|^2} [\delta_{ij} a_k - a_i a_j a_k] \quad \text{and} \quad (\text{A.3}) \end{aligned}$$

$$\begin{aligned} [\partial_{\mathbf{P}^r \mathbf{P}^r}^2 \mathbf{m}]_{ijkl} &= \frac{\partial}{\partial P_l^r} \left[\frac{\partial m_{ij}}{\partial P_k^r} \right] \\ &= \frac{\partial}{\partial P_l^r} \left[\frac{\partial a_i}{\partial P_k^r} \right] a_j + \frac{\partial a_i}{\partial P_k^r} \frac{\partial a_j}{\partial P_l^r} + \frac{\partial a_i}{\partial P_l^r} \frac{\partial a_j}{\partial P_k^r} + a_i \frac{\partial}{\partial P_l^r} \left[\frac{\partial a_j}{\partial P_k^r} \right], \quad (\text{A.4}) \end{aligned}$$

whereby the indices refer to a Cartesian frame $\{\mathbf{e}_1, \mathbf{e}_2, \mathbf{e}_3\}$.

The first and second-order partial derivatives of the third-order piezoelectric coupling tensor $\mathbf{e}(\mathbf{P}^r)$, introduced in Equation (3.8), with respect to \mathbf{P}^r are derived as

$$\begin{aligned} [\partial_{\mathbf{P}^r} \mathbf{e}]_{ijkl} &= \frac{\partial e_{ijk}}{\partial P_l^r} \\ &= -\beta_1^e \frac{\partial a_i}{\partial P_l^r} \delta_{jk} - \beta_2^e \left[\frac{\partial a_i}{\partial P_l^r} m_{jk} + a_i \frac{\partial m_{jk}}{\partial P_l^r} \right] \\ &\quad - \frac{\beta_3^e}{2} \left[\frac{\partial a_j}{\partial P_l^r} \delta_{ik} + \frac{\partial a_k}{\partial P_l^r} \delta_{ij} \right] \quad \text{and} \end{aligned} \quad (\text{A.5})$$

$$\begin{aligned} [\partial_{\mathbf{P}^r \mathbf{P}^r}^2 \mathbf{e}]_{ijklt} &= \frac{\partial}{\partial P_t^r} \left[\frac{\partial e_{ijk}}{\partial P_l^r} \right] \\ &= -\beta_1^e \frac{\partial}{\partial P_t^r} \left[\frac{\partial a_i}{\partial P_l^r} \right] \delta_{jk} - \beta_2^e \left[\frac{\partial}{\partial P_t^r} \left[\frac{\partial a_i}{\partial P_l^r} \right] m_{jk} + \frac{\partial a_i}{\partial P_l^r} \frac{\partial m_{jk}}{\partial P_t^r} \right] \\ &\quad - \beta_2^e \left[\frac{\partial a_i}{\partial P_t^r} \frac{\partial m_{jk}}{\partial P_l^r} + a_i \frac{\partial}{\partial P_t^r} \left[\frac{\partial m_{jk}}{\partial P_l^r} \right] \right] \\ &\quad - \frac{\beta_3^e}{2} \left[\frac{\partial}{\partial P_t^r} \left[\frac{\partial a_j}{\partial P_l^r} \right] \delta_{ik} + \frac{\partial}{\partial P_t^r} \left[\frac{\partial a_k}{\partial P_l^r} \right] \delta_{ij} \right]. \end{aligned} \quad (\text{A.6})$$

Analogously, the first and second-order partial sensitivities of remnant strain tensor $\boldsymbol{\varepsilon}^r(\mathbf{P}^r)$, see Equation (3.4), with respect to remnant polarisation \mathbf{P}^r are given as

$$[\partial_{\mathbf{P}^r} \boldsymbol{\varepsilon}^r]_{ijk} = \frac{\partial \varepsilon_{ij}^r}{\partial P_k^r} = \frac{3}{2} \frac{\varepsilon^{\text{sat}}}{P^{\text{sat}}} \left[m_{ij} a_k - \frac{1}{3} \delta_{ij} a_k + \|\mathbf{P}^r\| \frac{\partial m_{ij}}{\partial P_k^r} \right] \quad \text{and} \quad (\text{A.7})$$

$$\begin{aligned} [\partial_{\mathbf{P}^r \mathbf{P}^r}^2 \boldsymbol{\varepsilon}^r]_{ijkl} &= \frac{\partial}{\partial P_l^r} \left[\frac{\partial \varepsilon_{ij}^r}{\partial P_k^r} \right] \\ &= \frac{3}{2} \frac{\varepsilon^{\text{sat}}}{P^{\text{sat}}} \left[\frac{\partial m_{ij}}{\partial P_l^r} a_k + m_{ij} \frac{\partial a_k}{\partial P_l^r} + \|\mathbf{P}^r\| \frac{\partial}{\partial P_l^r} \left[\frac{\partial m_{ij}}{\partial P_k^r} \right] + \frac{\partial m_{ij}}{\partial P_k^r} a_l \right] \\ &\quad - \frac{1}{2} \frac{\varepsilon^{\text{sat}}}{P^{\text{sat}}} \delta_{ij} \frac{\partial a_k}{\partial P_l^r}. \end{aligned} \quad (\text{A.8})$$

The driving force vector (3.19) reads

$$\begin{aligned} [\mathbf{f}]_i &= \varepsilon_{mn}^e \mathbf{E}_{mnop} \frac{\partial \varepsilon_{op}^r}{\partial P_i^r} + \frac{1}{P^{\text{sat}}} E_m \mathbf{e}_{mno} \varepsilon_{no}^e a_i + \frac{\|\mathbf{P}^r\|}{P^{\text{sat}}} E_m \frac{\partial \mathbf{e}_{mno}}{\partial P_i^r} \varepsilon_{no}^e \\ &\quad - \frac{\|\mathbf{P}^r\|}{P^{\text{sat}}} E_m \mathbf{e}_{mno} \frac{\partial \varepsilon_{no}^r}{\partial P_i^r} + E_i - \frac{1}{c} \operatorname{arctanh} \left(\frac{\|\mathbf{P}^r\|}{P^{\text{sat}}} \right) a_i. \end{aligned} \quad (\text{A.9})$$

The first-order partial derivative of $\mathbf{f}(\mathbf{P}^r)$ with respect to \mathbf{P}^r is obtained as

$$\begin{aligned}
[\partial_{\mathbf{P}^r} \mathbf{f}]_{ij} = & -\frac{\partial \varepsilon_{mn}^r}{\partial P_j^r} \mathbf{E}_{mnop} \frac{\partial \varepsilon_{op}^r}{\partial P_i^r} + \varepsilon_{mn}^e \mathbf{E}_{mnop} \frac{\partial}{\partial P_j^r} \left[\frac{\partial \varepsilon_{op}^r}{\partial P_i^r} \right] \\
& + \frac{1}{P_{\text{sat}}} E_m \left[\frac{\partial \mathbf{e}_{mno}}{\partial P_j^r} \varepsilon_{no}^e a_i - \mathbf{e}_{mno} \frac{\partial \varepsilon_{no}^r}{\partial P_j^r} a_i + \mathbf{e}_{mno} \varepsilon_{no}^e \frac{\partial a_i}{\partial P_j^r} \right] \\
& + \frac{1}{P_{\text{sat}}} E_m \frac{\partial \mathbf{e}_{mno}}{\partial P_i^r} \varepsilon_{no}^e a_j + \frac{\|\mathbf{P}^r\|}{P_{\text{sat}}} E_m \left[\frac{\partial}{\partial P_j^r} \left[\frac{\partial \mathbf{e}_{mno}}{\partial P_i^r} \right] \varepsilon_{no}^e - \frac{\partial \mathbf{e}_{mno}}{\partial P_i^r} \frac{\partial \varepsilon_{no}^r}{\partial P_j^r} \right] \\
& - \frac{1}{P_{\text{sat}}} E_m \mathbf{e}_{mno} \frac{\partial \varepsilon_{no}^r}{\partial P_i^r} a_j - \frac{\|\mathbf{P}^r\|}{P_{\text{sat}}} E_m \left[\frac{\partial \mathbf{e}_{mno}}{\partial P_j^r} \frac{\partial \varepsilon_{no}^r}{\partial P_i^r} + \mathbf{e}_{mno} \frac{\partial}{\partial P_j^r} \left[\frac{\partial \varepsilon_{no}^r}{\partial P_i^r} \right] \right] \\
& - \frac{1}{c} \operatorname{arctanh} \left(\frac{\|\mathbf{P}^r\|}{P_{\text{sat}}} \right) \frac{\partial a_i}{\partial P_i^r} + \frac{1}{c} \frac{1}{P_{\text{sat}}} \frac{1}{[1 - (\|\mathbf{P}^r\|/P_{\text{sat}})^2]} a_i a_j. \quad (\text{A.10})
\end{aligned}$$

The tangent matrix \mathbf{J} , derived in Equation (3.27), used for the update of \mathbf{P}^r , reads

$$[\partial_{\mathbf{P}^r} \mathbf{R}]_{ij} = \delta_{ij} - \frac{\Delta t}{\eta^p} \left[\frac{m}{E^c} \left\langle \frac{\|\mathbf{f}\|}{E^c} - 1 \right\rangle^{m-1} \frac{f_i}{\|\mathbf{f}\|} \frac{\partial \|\mathbf{f}\|}{\partial P_j^r} + \left\langle \frac{\|\mathbf{f}\|}{E^c} - 1 \right\rangle^m \frac{\partial}{\partial P_j^r} \left[\frac{f_i}{\|\mathbf{f}\|} \right] \right], \quad (\text{A.11})$$

wherein $\frac{\partial \|\mathbf{f}\|}{\partial P_j^r} = \frac{f_k}{\|\mathbf{f}\|} \frac{\partial f_k}{\partial P_j^r}$ and (A.12)

$$\frac{\partial}{\partial P_j^r} \left[\frac{f_i}{\|\mathbf{f}\|} \right] = \frac{1}{\|\mathbf{f}\|} \left[\frac{\partial f_i}{\partial P_j^r} - \frac{f_i}{\|\mathbf{f}\|} \left[\frac{f_k}{\|\mathbf{f}\|} \frac{\partial f_k}{\partial P_j^r} \right] \right]. \quad (\text{A.13})$$

A.2 Identification of isotropic elastic tensor coefficients

The matrix form of the transversely isotropic elasticity modulus corresponding to the single crystal ferroelectric BaTiO₃ oriented along the crystallographic axis \mathbf{e}_3 reads

$$[\mathbf{E}^{e_3}]_{ij} = \begin{bmatrix} 237.4 & 92.6 & 111 & 0 & 0 & 0 \\ 92.6 & 237.4 & 111 & 0 & 0 & 0 \\ 111 & 111 & 151 & 0 & 0 & 0 \\ 0 & 0 & 0 & 72.4 & 0 & 0 \\ 0 & 0 & 0 & 0 & 61 & 0 \\ 0 & 0 & 0 & 0 & 0 & 61 \end{bmatrix} \times 10^3 \text{ MPa}, \quad (\text{A.14})$$

see Schröder and Keip [125]. Analogously, the matrix entries of the transversely isotropic elasticity moduli oriented along the crystallographic axes \mathbf{e}_1 and \mathbf{e}_2 are obtained by initialising the structural vector \mathbf{a} along the corresponding crystallographic directions.

The elasticity modulus referring to the cubic symmetry of a BaTiO₃ crystal is computed by averaging the individual elasticity moduli along \mathbf{e}_1 , \mathbf{e}_2 and \mathbf{e}_3 as

$$\mathbf{E}^{\text{cub}} = \frac{1}{3} [\mathbf{E}^{e_1} + \mathbf{E}^{e_2} + \mathbf{E}^{e_3}], \quad (\text{A.15})$$

wherein \mathbf{E}^{e_1} and \mathbf{E}^{e_2} denote the transversely isotropic elasticity moduli along \mathbf{e}_1 and \mathbf{e}_2 respectively. Following Equation (A.15), the matrix form of the averaged elasticity modulus \mathbf{E}^{cub} is computed as

$$[\mathbf{E}^{\text{cub}}]_{ij} = \begin{bmatrix} 208.60 & 104.87 & 104.87 & 0 & 0 & 0 \\ 104.87 & 208.60 & 104.87 & 0 & 0 & 0 \\ 104.87 & 104.87 & 208.60 & 0 & 0 & 0 \\ 0 & 0 & 0 & 64.8 & 0 & 0 \\ 0 & 0 & 0 & 0 & 64.8 & 0 \\ 0 & 0 & 0 & 0 & 0 & 64.8 \end{bmatrix} \times 10^3 \text{ MPa}. \quad (\text{A.16})$$

The matrix coefficients of \mathbf{E}^{cub} are taken as basis for the identification of the tensor coefficients appearing in the isotropic elasticity modulus of the ferroelectric crystal. The matrix form of the isotropic elasticity modulus \mathbf{E} , introduced in Equation (3.7) and by initialising $\lambda^{\text{E}} = E_{1122}$ and $\mu^{\text{E}} = \frac{1}{2} [E_{1111} - E_{1122}]$, reads

$$[\mathbf{E}]_{ij} = \begin{bmatrix} E_{1111} & E_{1122} & E_{1122} & 0 & 0 & 0 \\ E_{1122} & E_{1111} & E_{1122} & 0 & 0 & 0 \\ E_{1122} & E_{1122} & E_{1111} & 0 & 0 & 0 \\ 0 & 0 & 0 & \frac{1}{2} [E_{1111} - E_{1122}] & 0 & 0 \\ 0 & 0 & 0 & 0 & \frac{1}{2} [E_{1111} - E_{1122}] & 0 \\ 0 & 0 & 0 & 0 & 0 & \frac{1}{2} [E_{1111} - E_{1122}] \end{bmatrix}. \quad (\text{A.17})$$

By defining a least-square functional $f(\boldsymbol{\kappa} = \{E_{1111}, E_{1122}\})$ of the form

$$f(\boldsymbol{\kappa}) = \frac{1}{2} \left\| [\mathbf{E}^{\text{cub}}]_{ij} - [\mathbf{E}]_{ij} \right\|^2, \quad (\text{A.18})$$

the isotropic elasticity tensor coefficients E_{1111} and E_{1122} are computed by solving the system of equations $\partial f(\boldsymbol{\kappa}) / \partial \boldsymbol{\kappa} = \mathbf{0}$, cf. Schröder and Keip [125]. The identified isotropic elastic stiffness constants read

$$E_{1111} = 213.303 \text{ MPa} \quad \text{and} \quad E_{1122} = 102.515 \text{ MPa}. \quad (\text{A.19})$$

B Derivations – laminate-based formulation

The partial derivations of some of the first and second-order tensorial quantities with respect to the individual multi-rank laminate volume fractions needed for the numerical implementation of the laminate-based models are provided in this appendix.

B.1 Useful derivations for the laminate-based formulations

The first-order partial derivative of the averaged remnant strain $\boldsymbol{\varepsilon}^M(\boldsymbol{\mu})$, introduced in Equation (4.17), with respect to the individual laminate volume fractions $\mu^{1,2,3,4,5}$ is derived as

$$\begin{aligned} \frac{\partial \boldsymbol{\varepsilon}^M}{\partial \mu^1} &= [1 - \mu^2] \boldsymbol{\varepsilon}_{(1)} - [1 - \mu^2] [\mu^3 + \mu^4 [1 - \mu^3]] \boldsymbol{\varepsilon}_{(3)} \\ &\quad - [1 - \mu^2] [1 - \mu^3] [1 - \mu^4] \boldsymbol{\varepsilon}_{(5)}, \end{aligned} \quad (\text{B.1})$$

$$\begin{aligned} \frac{\partial \boldsymbol{\varepsilon}^M}{\partial \mu^2} &= [1 - \mu^1] \boldsymbol{\varepsilon}_{(1)} - [1 - \mu^1] [\mu^3 + \mu^4 [1 - \mu^3]] \boldsymbol{\varepsilon}_{(3)} \\ &\quad - [1 - \mu^1] [1 - \mu^3] [1 - \mu^4] \boldsymbol{\varepsilon}_{(5)}, \end{aligned} \quad (\text{B.2})$$

$$\frac{\partial \boldsymbol{\varepsilon}^M}{\partial \mu^3} = [1 - \mu^1] [1 - \mu^2] [1 - \mu^4] [\boldsymbol{\varepsilon}_{(3)} - \boldsymbol{\varepsilon}_{(5)}], \quad (\text{B.3})$$

$$\frac{\partial \boldsymbol{\varepsilon}^M}{\partial \mu^4} = [1 - \mu^1] [1 - \mu^2] [1 - \mu^3] [\boldsymbol{\varepsilon}_{(3)} - \boldsymbol{\varepsilon}_{(5)}] \quad \text{and} \quad (\text{B.4})$$

$$\frac{\partial \boldsymbol{\varepsilon}^M}{\partial \mu^5} = \mathbf{0}. \quad (\text{B.5})$$

Analogously, the first-order partial derivative of the average remnant polarisation $\mathbf{P}^{\text{M}}(\boldsymbol{\mu})$, see Equation (4.18), with respect to the individual laminate volume fractions $\mu^{1,2,3,4,5}$ is derived as

$$\begin{aligned} \frac{\partial \mathbf{P}^{\text{M}}}{\partial \mu^1} &= [1 + \mu^2] \mathbf{P}_{(1)} - [1 - \mu^2] [\mu^3 - \mu^4 [1 - \mu^3]] \mathbf{P}_{(3)} \\ &\quad - [1 - \mu^2] [1 - \mu^3] [1 - \mu^4] [2\mu^5 - 1] \mathbf{P}_{(5)}, \end{aligned} \quad (\text{B.6})$$

$$\begin{aligned} \frac{\partial \mathbf{P}^{\text{M}}}{\partial \mu^2} &= -[1 - \mu^1] \mathbf{P}_{(1)} - [1 - \mu^1] [\mu^3 - \mu^4 [1 - \mu^3]] \mathbf{P}_{(3)} \\ &\quad - [1 - \mu^1] [1 - \mu^3] [1 - \mu^4] [2\mu^5 - 1] \mathbf{P}_{(5)}, \end{aligned} \quad (\text{B.7})$$

$$\begin{aligned} \frac{\partial \mathbf{P}^{\text{M}}}{\partial \mu^3} &= [1 - \mu^1] [1 - \mu^2] [1 + \mu^4] \mathbf{P}_{(3)} \\ &\quad - [1 - \mu^1] [1 - \mu^2] [1 - \mu^4] [2\mu^5 - 1] \mathbf{P}_{(5)}, \end{aligned} \quad (\text{B.8})$$

$$\begin{aligned} \frac{\partial \mathbf{P}^{\text{M}}}{\partial \mu^4} &= -[1 - \mu^1] [1 - \mu^2] [1 - \mu^3] \mathbf{P}_{(3)} \\ &\quad - [1 - \mu^1] [1 - \mu^2] [1 - \mu^3] [2\mu^5 - 1] \mathbf{P}_{(5)} \quad \text{and} \end{aligned} \quad (\text{B.9})$$

$$\frac{\partial \mathbf{P}^{\text{M}}}{\partial \mu^5} = 2 [1 - \mu^1] [1 - \mu^2] [1 - \mu^3] [1 - \mu^4] \mathbf{P}_{(5)}. \quad (\text{B.10})$$

With respect to laminate-based Model 1, the sensitivity of structural vector $\mathbf{a}(\mathbf{P}^{\text{M}})$, defined in Equation (4.46), with respect to the multi-rank laminate volume fractions μ^j , for $j = 1, \dots, 5$, is given by

$$\frac{\partial \mathbf{a}(\mathbf{P}^{\text{M}})}{\partial \mu^j} = \frac{\partial \mathbf{a}(\mathbf{P}^{\text{M}})}{\partial \mathbf{P}^{\text{M}}} \cdot \frac{\partial \mathbf{P}^{\text{M}}}{\partial \mu^j} = \frac{1}{\|\mathbf{P}^{\text{M}}\|} [\mathbf{I} - \mathbf{a}(\mathbf{P}^{\text{M}}) \otimes \mathbf{a}(\mathbf{P}^{\text{M}})] \cdot \frac{\partial \mathbf{P}^{\text{M}}}{\partial \mu^j}. \quad (\text{B.11})$$

Similarly, the sensitivity of the third-order piezoelectric tensor $\mathbf{e}(\mathbf{a}(\mathbf{P}^{\text{M}}))$ with respect to the individual laminate volume fractions μ^j is derived as

$$\begin{aligned} \frac{\partial \mathbf{e}(\mathbf{P}^{\text{M}})}{\partial \mu^j} &= -\beta_1^{\text{e}} \left[\frac{\partial \mathbf{a}}{\partial \mu^j} \otimes \mathbf{I} \right] \\ &\quad - \beta_2^{\text{e}} \left[\frac{\partial \mathbf{a}}{\partial \mu^j} \otimes \mathbf{m} + \mathbf{a} \otimes \frac{\partial \mathbf{a}}{\partial \mu^j} \otimes \mathbf{a} + \mathbf{m} \otimes \frac{\partial \mathbf{a}}{\partial \mu^j} \right] \\ &\quad - \frac{\beta_3^{\text{e}}}{2} \left[\mathbf{I} \otimes \frac{\partial \mathbf{a}}{\partial \mu^j} + \mathbf{I} \overline{\otimes} \frac{\partial \mathbf{a}}{\partial \mu^j} \right]. \end{aligned} \quad (\text{B.12})$$

B.2 Derivatives of Fischer–Burmeister functions

The set of Fischer–Burmeister functions (4.41) considering the definitions of the additional constraints (4.36) are re-written as

$$\xi_I^j = \sqrt{[\mu^j]^2 + [\Gamma_I^j]^2} - \mu^j - \Gamma_I^j \quad \text{and} \quad (\text{B.13})$$

$$\xi_{II}^j = \sqrt{[\mu^j - 1]^2 + [\Gamma_{II}^j]^2} + \mu^j - 1 - \Gamma_{II}^j. \quad (\text{B.14})$$

The derivatives of, for example, Fischer–Burmeister function ξ_I^1 with respect to solution variables $\mathbf{v} = [\boldsymbol{\mu}, \boldsymbol{\Gamma}_I, \boldsymbol{\Gamma}_{II}]^t$, see Equation (4.38), are given as

$$\frac{d\xi_I^1}{d\mu^1} = \frac{\mu^1}{\sqrt{[\mu^1]^2 + [\Gamma_I^1]^2}} - 1, \quad \frac{d\xi_I^1}{d\mu^2} = \frac{d\xi_I^1}{d\mu^3} = \frac{d\xi_I^1}{d\mu^4} = \frac{d\xi_I^1}{d\mu^5} = 0, \quad (\text{B.15})$$

$$\frac{d\xi_I^1}{d\Gamma_I^1} = \frac{\Gamma_I^1}{\sqrt{[\mu^1]^2 + [\Gamma_I^1]^2}} - 1, \quad \frac{d\xi_I^1}{d\Gamma_I^2} = \frac{d\xi_I^1}{d\Gamma_I^3} = \frac{d\xi_I^1}{d\Gamma_I^4} = \frac{d\xi_I^1}{d\Gamma_I^5} = 0, \quad (\text{B.16})$$

$$\frac{d\xi_I^1}{d\Gamma_{II}^1} = \frac{d\xi_I^1}{d\Gamma_{II}^2} = \frac{d\xi_I^1}{d\Gamma_{II}^3} = \frac{d\xi_I^1}{d\Gamma_{II}^4} = \frac{d\xi_I^1}{d\Gamma_{II}^5} = 0. \quad (\text{B.17})$$

The total derivatives of, for example, Fischer–Burmeister function ξ_{II}^1 with respect to solution variables $\mathbf{v} = [\boldsymbol{\mu}, \boldsymbol{\Gamma}_I, \boldsymbol{\Gamma}_{II}]^t$ read

$$\frac{d\xi_{II}^1}{d\mu^1} = \frac{\mu^1 - 1}{\sqrt{[\mu^1 - 1]^2 + [\Gamma_{II}^1]^2}} + 1, \quad \frac{d\xi_{II}^1}{d\mu^2} = \frac{d\xi_{II}^1}{d\mu^3} = \frac{d\xi_{II}^1}{d\mu^4} = \frac{d\xi_{II}^1}{d\mu^5} = 0, \quad (\text{B.18})$$

$$\frac{d\xi_{II}^1}{d\Gamma_I^1} = \frac{d\xi_{II}^1}{d\Gamma_I^2} = \frac{d\xi_{II}^1}{d\Gamma_I^3} = \frac{d\xi_{II}^1}{d\Gamma_I^4} = \frac{d\xi_{II}^1}{d\Gamma_I^5} = 0, \quad (\text{B.19})$$

$$\frac{d\xi_{II}^1}{d\Gamma_{II}^1} = \frac{\Gamma_{II}^1}{\sqrt{[\mu^1 - 1]^2 + [\Gamma_{II}^1]^2}} - 1, \quad \frac{d\xi_{II}^1}{d\Gamma_{II}^2} = \frac{d\xi_{II}^1}{d\Gamma_{II}^3} = \frac{d\xi_{II}^1}{d\Gamma_{II}^4} = \frac{d\xi_{II}^1}{d\Gamma_{II}^5} = 0. \quad (\text{B.20})$$

Analogously, the other Fischer–Burmeister functions $\xi_I^{2,3,4,5}$ as well as $\xi_{II}^{2,3,4,5}$ are derived with respect to the solution variables $\mathbf{v} = [\boldsymbol{\mu}, \boldsymbol{\Gamma}_I, \boldsymbol{\Gamma}_{II}]^t$.

Bibliography

- [1] H. Allik and T. J. R. Hughes. Finite element method for piezoelectric vibration. *International Journal for Numerical Methods in Engineering*, 2(2):151–157, 1970.
- [2] G. Arlt and P. Sasko. Domain configuration and equilibrium size of domains in BaTiO_3 ceramics. *Journal of Applied Physics*, 51(9):4956–4960, 1980.
- [3] A. Arockiarajan and C. Sansour. Micromechanical modeling and simulation of rate-dependent effects in ferroelectric polycrystals. *Computational Materials Science*, 43(4):842–854, 2008.
- [4] A. Arockiarajan, B. Delibas, A. Menzel, and W. Seemann. Studies on rate-dependent switching effects of piezoelectric materials using a finite element model. *Computational Materials Science*, 37(3):306–317, 2006.
- [5] A. Arockiarajan, A. Menzel, B. Delibas, and W. Seemann. Computational modeling of rate-dependent domain switching in piezoelectric materials. *European Journal of Mechanics-A/Solids*, 25(6):950–964, 2006.
- [6] A. Arockiarajan, A. Menzel, B. Delibas, and W. Seemann. Micromechanical modeling of switching effects in piezoelectric materials—a robust coupled finite element approach. *Journal of Intelligent Material Systems and Structures*, 18(9):983–999, 2007.
- [7] A. Arockiarajan, S. M. Sivakumar, and C. Sansour. A thermodynamically motivated model for ferroelectric ceramics with grain boundary effects. *Smart Materials and Structures*, 19(1):015008, 2010.
- [8] F. Auricchio, E. Bonetti, G. Scalet, and F. Ubertini. Theoretical and numerical modeling of shape memory alloys accounting for multiple phase transformations and martensite reorientation. *International Journal of Plasticity*, 59:30–54, 2014.
- [9] J. M. Ball and R. D. James. Fine phase mixtures as minimizers of energy. In *Analysis and Continuum Mechanics*, pages 647–686. Springer, 1989.
- [10] T. Bartel and K. Hackl. A micromechanical model for martensitic phase-transformations in shape-memory alloys based on energy-relaxation. *Zeitschrift für Angewandte Mathematik und Mechanik*, 89(10):792–809, 2009.
- [11] T. Bartel and K. Hackl. Multiscale modeling of martensitic phase transformations: on the numerical determination of heterogeneous mesostructures within shape-memory alloys induced by precipitates. *Technische Mechanik*, 30(4):324–342, 2010.

- [12] T. Bartel, A. Menzel, and B. Svendsen. Thermodynamic and relaxation-based modeling of the interaction between martensitic phase transformations and plasticity. *Journal of the Mechanics and Physics of Solids*, 59(5):1004–1019, 2011.
- [13] E. Bassiouny and G. A. Maugin. Thermodynamical formulation for coupled electromechanical hysteresis effects – III. Parameter identification. *International Journal of Engineering Science*, 27(8):975–987, 1989.
- [14] E. Bassiouny and G. A. Maugin. Thermodynamical formulation for coupled electromechanical hysteresis effects – IV. Combined electromechanical loading. *International Journal of Engineering Science*, 27(8):989–1000, 1989.
- [15] E. Bassiouny, A. F. Ghaleb, and G. A. Maugin. Thermodynamical formulation for coupled electromechanical hysteresis effects – I. Basic equations. *International Journal of Engineering Science*, 26(12):1279–1295, 1988.
- [16] E. Bassiouny, A. F. Ghaleb, and G. A. Maugin. Thermodynamical formulation for coupled electromechanical hysteresis effects – II. Poling of ceramics. *International Journal of Engineering Science*, 26(12):1297–1306, 1988.
- [17] K.-J. Bathe. *Finite element procedures*. Englewood Cliffs, New Jersey: Prentice-Hall., 1996.
- [18] K. Bhattacharya. Comparison of the geometrically nonlinear and linear theories of martensitic transformation. *Continuum Mechanics and Thermodynamics*, 5(3): 205–242, 1993.
- [19] K. Bhattacharya and J.-Y. Li. *Fundamental Physics of Ferroelectrics*, chapter Domain patterns, texture and macroscopic electro-mechanical behavior of ferroelectrics, pages 72–81. American Institute of Physics, 2001.
- [20] E. Burcu. *Investigation of Large Strain Actuation in Barium Titanate*. PhD thesis, Graduate Aeronautical Laboratories, California Institute of Technology, 2001.
- [21] E. Burcu, G. Ravichandran, and K. Bhattacharya. Large electrostrictive actuation of barium titanate single crystals. *Journal of the Mechanics and Physics of Solids*, 52(4):823–846, 2004.
- [22] E. Burcu, G. Ravichandran, and K. Bhattacharya. Large strain electrostrictive actuation in barium titanate. *Applied Physics Letters*, 77(11):1698–1700, 2000.
- [23] R. Bustamante, A. Dorfmann, and R. W. Ogden. Nonlinear electroelastostatics: a variational framework. *Zeitschrift für angewandte Mathematik und Physik*, 60: 154–177, 2009.
- [24] H. Cao and A. G. Evans. Nonlinear deformation of ferroelectric ceramics. *Journal of the American Ceramic Society*, 76(4):890–896, 1993.
- [25] P. J. Chen. Three dimensional dynamic electromechanical constitutive relations for ferroelectric materials. *International Journal of Solids and Structures*, 16(12):

- 1059–1067, 1980.
- [26] P. J. Chen. Three dimensional constitutive relations for ferroelectric materials in the presence of quasi-static domain switching. *Acta Mechanica*, 48(1):31–42, 1983.
- [27] P. J. Chen and M. M. Madsen. One dimensional polar responses of the electrooptic ceramic PLZT 7/65/35 due to domain switching. *Acta Mechanica*, 41(3):255–264, 1981.
- [28] P. J. Chen and S. T. Montgomery. A macroscopic theory for the existence of the hysteresis and butterfly loops in ferroelectricity. *Ferroelectrics*, 23(1):199–207, 1980.
- [29] P. J. Chen and P. S. Peercy. One dimensional dynamic electromechanical constitutive relations of ferroelectric materials. *Acta Mechanica*, 31(3):231–241, 1979.
- [30] P. J. Chen and T. J. Tucker. Determination of the polar equilibrium properties of the ferroelectric ceramic PZT 65/35. *Acta Mechanica*, 38(3):209–218, 1981.
- [31] P. J. Chen and T. J. Tucker. One dimensional polar mechanical and dielectric responses of the ferroelectric ceramic PZT 65/35 due to domain switching. *International Journal of Engineering Science*, 19(1):147–158, 1981.
- [32] W. Chen and C. S. Lynch. A micro-electro-mechanical model for polarization switching of ferroelectric materials. *Acta Materialia*, 46(15):5303–5311, 1998.
- [33] P. G. Ciarlet. *Mathematical Elasticity. Volume I: Three-Dimensional Elasticity*. Studies in Mathematics and its Applications. North-Holland, Amsterdam, 1988.
- [34] A. C. F. Cocks and R. M. McMeeking. A phenomenological constitutive law for the behaviour of ferroelectric ceramics. *Ferroelectrics*, 228(1):219–228, 1999.
- [35] D. Damjanovic. Ferroelectric, dielectric and piezoelectric properties of ferroelectric thin films and ceramics. *Reports on Progress in Physics*, 61(9):1267–1324, 1998.
- [36] D. Damjanovic. Hysteresis in piezoelectric and ferroelectric materials. In I. Mayergoyz and G. Bertotti, editors, *The Science of Hysteresis – Volume 3: Hysteresis in materials*, pages 337–465. Academic Press, 2006.
- [37] B. Delibas, A. Arockiarajan, and W. Seemann. Rate dependent properties of perovskite type tetragonal piezoelectric materials using micromechanical model. *International Journal of Solids and Structures*, 43(3):697–712, 2006.
- [38] J. E. Dennis Jr and R. B. Schnabel. *Numerical methods for unconstrained optimization and nonlinear equations*, volume 16 of *Classics in Applied Mathematics*. Siam, 1996.
- [39] A. DeSimone. Energy minimizers for large ferromagnetic bodies. *Archive for Rational Mechanics and Analysis*, 125(2):99–143, 1993.
- [40] A. DeSimone and R. D. James. A constrained theory of magnetoelasticity. *Journal of the Mechanics and Physics of Solids*, 50(2):283–320, 2002.

- [41] D. K. Dusthakar, T. Bartel, B. Kiefer, A. Menzel, and B. Svendsen. Rate-dependent laminate-based approach for modelling of ferroelectric single crystals. In *Proceedings of the 5th International Congress on Computational Mechanics and Simulation*, pages 1324–1336, 2014.
- [42] D. K. Dusthakar, A. Menzel, and B. Svendsen. A laminate-based modelling approach for rate-dependent switching in ferroelectric materials. In *Proceedings in Applied Mathematics and Mechanics*, volume 15, pages 3–6, 2015.
- [43] D. K. Dusthakar, A. Menzel, and B. Svendsen. Comparison of phenomenological and laminate-based models for rate-dependent switching in ferroelectric continua. *GAMM-Mitteilungen*, 38(1):147–170, 2015.
- [44] D. K. Dusthakar, A. Menzel, and B. Svendsen. Numerical modelling of the rate-dependent polarisation switching in ferroelectric materials based on a sequential laminate approach. In *3rd Polish Congress of Mechanics and 21st International Conference on Computer Methods in Mechanics, Short Papers*, volume 2, pages 787–788, 2015. ISBN: 978-83-932107-6-3 Vol.2.
- [45] D. K. Dusthakar, A. Menzel, and B. Svendsen. Laminate-based modelling of single and polycrystalline ferroelectric materials – application to tetragonal barium titanate. *Mechanics of Materials*, 2017. doi:<https://doi.org/10.1016/j.mechmat.2017.10.005>. (In Press).
- [46] D. K. Dusthakar, A. Menzel, and B. Svendsen. Sequential laminate-based models for rate-dependent switching in single-crystalline ferroelectrics. In M. Kuczma, J. Schröder, G. Stavroulakis, and G. Szefer, editors, *Smart Material Systems and Structures*. Springer-Verlag, 2017. (submitted for publication).
- [47] A. C. Eringen. On the foundations of electroelastostatics. *International Journal of Engineering Science*, 1(1):127–153, 1963.
- [48] A. C. Eringen and G. A. Maugin. *Electrodynamics of continua. Volume 1: Foundations and solid media*. Springer-Verlag New York, 1 edition, 1990.
- [49] J. Fan, W. A. Stoll, and C. S. Lynch. Nonlinear constitutive behavior of soft and hard PZT: experiments and modeling. *Acta materialia*, 47(17):4415–4425, 1999.
- [50] A. Fischer. A special Newton-type optimization method. *Optimization*, 24(3-4): 269–284, 1992.
- [51] H. Goldstein. *Classical Mechanics*. Addison–Wesley series in Physics. Addison-Wesley Publishing Company, 1980. ISBN 9780201029185.
- [52] D. J. Griffiths. *Introduction to Electrodynamics*. Prentice Hall, 3 edition, 1999.
- [53] G. A. Holzapfel. *Nonlinear Solid Mechanics. A continuum approach for engineering*. J. Wiley and Sons, 2000.
- [54] J. E. Huber. Micromechanical modelling of ferroelectrics. *Current Opinion in Solid State and Materials Science*, 9(3):100–106, 2005.

-
- [55] J. E. Huber and N. A. Fleck. Multi-axial electrical switching of a ferroelectric: theory versus experiment. *Journal of Mechanics and Physics of Solids*, 49(4):785–811, 2001.
- [56] J. E. Huber and N. A. Fleck. Ferroelectric switching: a micromechanics model versus measured behaviour. *European Journal of Mechanics-A/Solids*, 23(2):203–217, 2004.
- [57] J. E. Huber, N. A. Fleck, C. M. Landis, and R. M. McMeeking. A constitutive model for ferroelectric polycrystals. *Journal of the Mechanics and Physics of Solids*, 47(8):1663–1697, 1999.
- [58] T. J. R. Hughes. *The Finite Element Method: Linear Static and Dynamic Finite Element Analysis*. Dover Civil and Mechanical Engineering. Dover Publications, 2000.
- [59] Y. Huo and Q. Jiang. Modeling of domain switching in polycrystalline ferroelectric ceramics. *Smart materials and structures*, 6(4):441–447, 1997.
- [60] Y. Huo and Q. Jiang. Modeling of domain switching in ferroelectric ceramics: an example. *International journal of solids and structures*, 35(13):1339–1353, 1998.
- [61] S. C. Hwang and R. M. McMeeking. A finite element model of ferroelectric polycrystals. *Ferroelectrics*, 211(1):177–194, 1998.
- [62] S. C. Hwang and R. M. McMeeking. A finite element model of ferroelastic polycrystals. *International Journal of Solids and Structures*, 36(10):1541–1556, 1999.
- [63] S. C. Hwang, C. S. Lynch, and R. M. McMeeking. Ferroelectric/ferroelastic interactions and a polarization switching model. *Acta Metallurgica et Materialia*, 43(5):2073–2084, 1995.
- [64] S. C. Hwang, J. E. Huber, R. M. McMeeking, and N. A. Fleck. The simulation of switching in polycrystalline ferroelectric ceramics. *Journal of Applied Physics*, 84(3):1530–1540, 1998.
- [65] J. D. Jackson. *Classical electrodynamics*. John Wiley & Sons, Inc., New York, 3 edition, 1999.
- [66] B. Jaffe, W. R. Cook, and H. Jaffe. *Piezoelectric Ceramics*. Academic Press, 1971.
- [67] K. Jayabal and A. Menzel. Voronoi-based three-dimensional polygonal finite elements for electromechanical problems. *Computational Materials Science*, 64:66–70, 2012.
- [68] K. Jayabal and A. Menzel. Modelling of non-linear switching effects in piezoceramics: a three-dimensional polygonal finite-element-based approach applied to oligocrystals. *Journal of Intelligent Material Systems and Structures*, 26(17):2322–2337, 2015.
- [69] K. Jayabal, A. Menzel, A. Arockiarajan, and S. M. Srinivasan. Micromechanical modelling of switching phenomena in polycrystalline piezoceramics: application

- of a polygonal finite element approach. *Computational Mechanics*, 48(4):421–435, 2011.
- [70] F. Jona and G. Shirane. *Ferroelectric Crystals*. International Series of Monographs on Solid State Physics. Pergamon Press, 1962.
- [71] M. Kamlah. Ferroelectric and ferroelastic piezoceramics – modeling of electromechanical hysteresis phenomena. *Continuum Mechanics and Thermodynamics*, 13(4):219–268, 2001.
- [72] M. Kamlah and U. Böhle. Finite element analysis of piezoceramic components taking into account ferroelectric hysteresis behavior. *International Journal of Solids and Structures*, 38(4):605–633, 2001.
- [73] M. Kamlah and Q. Jiang. A constitutive model for ferroelectric PZT ceramics under uniaxial loading. *Smart Materials and Structures*, 8(4):441–459, 1999.
- [74] M. Kamlah and C. Tsakmakis. Phenomenological modeling of the non-linear electro-mechanical coupling in ferroelectrics. *International Journal of Solids and Structures*, 36(5):669–695, 1999.
- [75] M. Kamlah, A. C. Liskowsky, R. M. McMeeking, and H. Balke. Finite element simulation of a polycrystalline ferroelectric based on a multidomain single crystal switching model. *International Journal of Solids and Structures*, 42(9):2949–2964, 2005.
- [76] C. Kanzow. Some noninterior continuation methods for linear complementarity problems. *SIAM Journal on Matrix Analysis and Applications*, 17(4):851–868, 1996.
- [77] M.-A. Keip. *Modeling of Electro-Mechanically Coupled Materials on Multiple Scales*. PhD thesis, Institute of Mechanics, Department of Civil Engineering, Faculty of Engineering, University of Duisburg-Essen, 2012.
- [78] M.-A. Keip and J. Schröder. A tetragonal switching model for ferroelectric materials. In *Proceedings in Applied Mathematics and Mechanics*, volume 10, pages 369–370, 2010.
- [79] M.-A. Keip and J. Schröder. A ferroelectric and ferroelastic microscopic switching criterion for tetragonal ferroelectrics. In *Proceedings in Applied Mathematics and Mechanics*, volume 11, pages 475–476, 2011.
- [80] M.-A. Keip and J. Schröder. On the modeling of microscopic switching phenomena in tetragonal ferroelectric materials. In *Proceedings of the 19th International Conference on Computer Methods in Mechanics*, pages 9–12, 2011.
- [81] B. Kiefer, T. Bartel, and A. Menzel. Implementation of numerical integration schemes for the simulation of magnetic sma constitutive response. *Smart Materials and Structures*, 21(9):094007, 2012.

-
- [82] B. Kiefer, T. Waffenschmidt, L. Sprave, and A. Menzel. A gradient-enhanced damage model coupled to plasticity - multi-surface formulation and algorithmic concepts. *International Journal of Damage Mechanics*, 0(0):1056789516676306, 2017.
- [83] S.-J. Kim and S. Seelecke. A rate-dependent three-dimensional free energy model for ferroelectric single crystals. *International Journal of Solids and Structures*, 44(3):1196–1209, 2007.
- [84] S. Klinkel. A phenomenological constitutive model for ferroelastic and ferroelectric hysteresis effects in ferroelectric ceramics. *International Journal of Solids and Structures*, 43(22):7197–7222, 2006.
- [85] S. Klinkel. A thermodynamic consistent 1D model for ferroelastic and ferroelectric hysteresis effects in piezoceramics. *Communications in Numerical Methods in Engineering*, 22(7):727–739, 2006.
- [86] L. D. Landau and E. M. Lifshitz. *Electrodynamics of Continuous Media*, volume 8 of *Course of Theoretical Physics*. Pergamon Press, 1960. Translated from the Russian by J. B. Sykes and J. S. Bell.
- [87] C. M. Landis. A new finite-element formulation for electromechanical boundary value problems. *International Journal for Numerical Methods in Engineering*, 55(5):613–628, 2002.
- [88] C. M. Landis. Fully coupled, multi-axial, symmetric constitutive laws for polycrystalline ferroelectric ceramics. *Journal of the Mechanics and Physics of Solids*, 50(1):127–152, 2002.
- [89] C. M. Landis. Non-linear constitutive modeling of ferroelectrics. *Current Opinion in Solid State and Materials Science*, 8(1):59–69, 2004.
- [90] C. M. Landis and R. M. McMeeking. A phenomenological constitutive law for ferroelastic switching and a resulting asymptotic crack tip solution. *Journal of Intelligent Material Systems and Structures*, 10(2):155–163, 1999.
- [91] J.-Y. Li and D. Liu. On ferroelectric crystals with engineered domain configurations. *Journal of the Mechanics and Physics of Solids*, 52(8):1719–1742, 2004.
- [92] J.-Y. Li, C.-H. Lei, L.-J. Li, Y.-C. Shu, and Y.-Y. Liu. Unconventional phase field simulations of transforming materials with evolving microstructures. *Acta Mechanica Sinica*, 28(4):915–927, 2012.
- [93] Y. W. Li and F. X. Li. Ultrahigh actuation strains in BaTiO_3 and $\text{Pb}(\text{Mn}_{1/3}\text{Nb}_{2/3})\text{O}_3$ - PbTiO_3 single crystals via reversible electromechanical domain switching. *Applied Physics Letters*, 102(15):152905, 2013.
- [94] Y. W. Li and F. X. Li. The effect of domain patterns on 180° domain switching in BaTiO_3 crystals during antiparallel electric field loading. *Applied Physics Letters*, 104(4):042908–042911, 2014.

- [95] Y. W. Li and F. X. Li. Domain switching criterion for ferroelectric single crystals under uni-axial electromechanical loading. *Mechanics of Materials*, 93:246–256, 2016.
- [96] M. E. Lines and A. M. Glass. *Principles and Applications of Ferroelectrics and Related Materials*. Oxford University Press, 1977.
- [97] D. Liu and J.-Y. Li. The enhanced and optimal piezoelectric coefficients in single crystalline barium titanate with engineered domain configurations. *Applied Physics Letters*, 83(6):1193–1195, 2003.
- [98] D. Liu and J.-Y. Li. Domain-engineered $\text{Pb}(\text{Mg}_{1/3}\text{Nb}_{2/3})\text{O}_3$ – PbTiO_3 crystals: enhanced piezoelectricity and optimal domain configurations. *Applied Physics Letters*, 84(19):3930–3932, 2004.
- [99] W. Lu, D.-N. Fang, C. Q. Li, and K.-C. Hwang. Nonlinear electric–mechanical behavior and micromechanics modelling of ferroelectric domain evolution. *Acta Materialia*, 47(10):2913–2926, 1999.
- [100] C. S. Lynch. The effect of uniaxial stress on the electro-mechanical response of 8/65/35 PLZT. *Acta Materialia*, 44(10):4137–4148, 1996.
- [101] C. S. Lynch. On the development of multi-axial phenomenological constitutive laws for ferroelectric ceramics. *Journal of Intelligent Material Systems and Structures*, 9(7):555–563, 1998.
- [102] S. Maniprakash. *Phenomenological modelling and simulation of ferroelectric ceramics*. PhD thesis, Institute of Mechanics, Department of Mechanical Engineering, Technical University of Dortmund, 2015.
- [103] S. Maniprakash, A. Arockiarajan, and A. Menzel. A multi-surface model for ferroelectric ceramics – application to cyclic electric loading with changing maximum amplitude. *Philosophical Magazine*, 96(13):1263–1284, 2016.
- [104] S. Maniprakash, R. Jayendiran, A. Menzel, and A. Arockiarajan. Experimental investigation, modelling and simulation of rate-dependent response of 1–3 ferroelectric composites. *Mechanics of Materials*, 94:91–105, 2016.
- [105] R. M. McMeeking and S. C. Hwang. On the potential energy of a piezoelectric inclusion and the criterion for ferroelectric switching. *Ferroelectrics*, 200(1):151–173, 1997.
- [106] R. M. McMeeking and C. M. Landis. A phenomenological multi-axial constitutive law for switching in polycrystalline ferroelectric ceramics. *International Journal of Engineering Science*, 40(14):1553–1577, 2002.
- [107] A. Menzel, A. Arockiarajan, and S. M. Sivakumar. Two models to simulate rate-dependent domain switching effects – application to ferroelastic polycrystalline ceramics. *Smart Materials and Structures*, 17(1):015026, 2008.

-
- [108] W. J. Merz. Domain formation and domain wall motions in ferroelectric BaTiO_3 single crystals. *Physical Review*, 95(3):690–698, 1954.
- [109] C. Miehe. Numerical computation of algorithmic (consistent) tangent moduli in large-strain computational inelasticity. *Computer Methods in Applied Mechanics and Engineering*, 134(3):223–240, 1996.
- [110] C. Miehe and D. Rosato. A rate-dependent incremental variational formulation of ferroelectricity. *International Journal of Engineering Science*, 49(6):466–496, 2011.
- [111] C. Miehe, B. Kiefer, and D. Rosato. An incremental variational formulation of dissipative magnetostriction at the macroscopic continuum level. *International Journal of Solids and Structures*, 48(13):1846–1866, 2011.
- [112] C. Miehe, D. Rosato, and B. Kiefer. Variational principles in dissipative electromagneto-mechanics: a framework for the macro-modeling of functional materials. *International Journal for Numerical Methods in Engineering*, 86(10):1225–1276, 2011.
- [113] C. Miehe, D. Zäh, and D. Rosato. Variational-based modeling of micro-electro-elasticity with electric field-driven and stress-driven domain evolutions. *International Journal for Numerical Methods in Engineering*, 91(2):115–141, 2012.
- [114] I. Müller. *Thermodynamics*. Interaction of Mechanics and Mathematics Series. Pitman Advanced Publishing Program, Boston, 1985.
- [115] P. R. Potnis, N.-T. Tsou, and J. E. Huber. A review of domain modelling and domain imaging techniques in ferroelectric crystals. *Materials*, 4(2):417–447, 2011.
- [116] P. W. Rehrig, G. L. Messing, and S. Trolier-McKinstry. Templated grain growth of barium titanate single crystals. *Journal of the American Ceramic Society*, 83(11):2654–2660, 2000.
- [117] J. P. Remeika. A method for growing barium titanate single crystals. *Journal of the American Chemical Society*, 76(3):940–941, 1954.
- [118] H. Romanowski. *Kontinuumsmechanische Modellierung ferroelektrischer Materialien im Rahmen der Invariantentheorie*. PhD thesis, Institute of Mechanics, Department of Civil Engineering, Faculty of Engineering, University of Duisburg-Essen, 2006.
- [119] D. Rytz, B. A. Wechsler, C. C. Nelson, and K. W. Kirby. Top-seeded solution growth of BaTiO_3 , KNbO_3 , SrTiO_3 , $\text{Bi}_{12}\text{TiO}_{20}$ and $\text{La}_{2-x}\text{Ba}_x\text{CuO}_4$. *Journal of Crystal Growth*, 99(1):864–868, 1990.
- [120] M. Schmidt-Baldassari. Numerical concepts for rate-independent single crystal plasticity. *Computer Methods in Applied Mechanics and Engineering*, 192(11):1261–1280, 2003.

- [121] D. Schrade, R. Mueller, D. Gross, T. Utschig, V. Y. Shur, and D. C. Lupascu. Interaction of domain walls with defects in ferroelectric materials. *Mechanics of Materials*, 39(2):161–174, 2007.
- [122] D. Schrade, R. Mueller, B.-X. Xu, and D. Gross. Domain evolution in ferroelectric materials: A continuum phase field model and finite element implementation. *Computer Methods in Applied Mechanics and Engineering*, 196(41):4365–4374, 2007.
- [123] D. Schrade, M.-A. Keip, H. Thai, J. Schröder, B. Svendsen, R. Müller, and D. Gross. Coordinate-invariant phase field modeling of ferro-electrics, part i: model formulation and single-crystal simulations. *GAMM-Mitteilungen*, 38(1):102–114, 2015.
- [124] J. Schröder and D. Gross. Invariant formulation of the electromechanical enthalpy function of transversely isotropic piezoelectric materials. *Archive of Applied Mechanics*, 73(8):533–552, 2004.
- [125] J. Schröder and M.-A. Keip. Two-scale homogenization of electromechanically coupled boundary value problems. *Computational Mechanics*, 50(2):229–244, 2012.
- [126] J. Schröder and H. Romanowski. A thermodynamically consistent mesoscopic model for transversely isotropic ferroelectric ceramics in a coordinate-invariant setting. *Archive of Applied Mechanics*, 74(11-12):863–877, 2005.
- [127] J. F. Scott. *Ferroelectric memories*. Springer-Verlag Berlin Heidelberg, 2000.
- [128] J. F. Scott. Applications of modern ferroelectrics. *Science*, 315(5814):954–959, 2007.
- [129] S. Seelecke, S.-J. Kim, B. L. Ball, and R. C. Smith. A rate-dependent two-dimensional free energy model for ferroelectric single crystals. *Continuum Mechanics and Thermodynamics*, 17(4):337–350, 2005.
- [130] N. Setter, D. Damjanovic, L. Eng, G. Fox, S. Gevorgian, S. Hong, A. Kingon, H. Kohlstedt, N. Y. Park, G. B. Stephenson, I. Stolitchnov, A. K. Taganstev, D. V. Taylor, T. Yamada, and S. Streiffner. Ferroelectric thin films: Review of materials, properties, and applications. *Journal of Applied Physics*, 100(5):051606, 2006.
- [131] J. Shieh, J.-H. Yeh, Y.-C. Shu, and J.-H. Yen. Operation of multiple 90° switching systems in barium titanate single crystals under electromechanical loading. *Applied Physics Letters*, 91(6):062901, 2007.
- [132] J. Shieh, J.-H. Yeh, Y.-C. Shu, and J.-H. Yen. Hysteresis behaviors of barium titanate single crystals based on the operation of multiple 90° switching systems. *Materials Science and Engineering: B*, 161(1-3):50–54, 2009.
- [133] D. Shilo, E. Burcsu, G. Ravichandran, and K. Bhattacharya. A model for large electrostrictive actuation in ferroelectric single crystals. *International Journal of Solids and Structures*, 44(6):2053–2065, 2007.

-
- [134] Y.-C. Shu and K. Bhattacharya. Domain patterns and macroscopic behaviour of ferroelectric materials. *Philosophical Magazine Part B*, 81(12):2021–2054, 2001.
- [135] Y.-C. Shu, J.-H. Yen, J. Shieh, and J.-H. Yeh. Effect of depolarization and coercivity on actuation strains due to domain switching in barium titanate. *Applied Physics Letters*, 90(17):172902, 2007.
- [136] Y.-C. Shu, J.-H. Yen, H.-Z. Chen, J.-Y. Li, and L.-J. Li. Constrained modeling of domain patterns in rhombohedral ferroelectrics. *Applied Physics Letters*, 92(5):052909, 2008.
- [137] R. C. Smith. *Smart Material Systems - Model Development*. SIAM, Philadelphia, 2005.
- [138] R. C. Smith, S. Seelecke, M. Dapino, and Z. Ounaies. A unified framework for modeling hysteresis in ferroic materials. *Journal of the Mechanics and Physics of Solids*, 54(1):46–85, 2006.
- [139] A. K. Tagantsev, L. E. Cross, and J. Fousek. *Domains in ferroic crystals and thin films*. Springer, 2010.
- [140] J. Tichý, J. Erhart, E. Kittinger, and J. Prívratská. *Fundamentals of Piezoelectric Sensorics: mechanical, dielectric, and thermodynamical properties of piezoelectric materials*. Springer-Verlag Berlin Heidelberg, 2010.
- [141] R. A. Toupin. The elastic dielectric. *Journal of Rational Mechanics and Analysis*, 5(6):849–915, 1956.
- [142] N. T. Tsou and J. E. Huber. Compatible domain arrangements and poling ability in oriented ferroelectric films. *Continuum Mechanics and Thermodynamics*, 22(3):203–219, 2010.
- [143] N. T. Tsou and J. E. Huber. Compatible domain structures and the poling of single crystal ferroelectrics. *Mechanics of Materials*, 42(7):740–753, 2010.
- [144] N. T. Tsou, P. R. Potnis, and J. E. Huber. Classification of laminate domain patterns in ferroelectrics. *Physical Review B*, 83(18):184120, 2011.
- [145] N. T. Tsou, J. E. Huber, and A. C. F. Cocks. Evolution of compatible laminate domain structures in ferroelectric single crystals. *Acta Materialia*, 61(2):670–682, 2013.
- [146] D. Viehland and Y.-H. Chen. Random-field model for ferroelectric domain dynamics and polarization reversal. *Journal of Applied Physics*, 88(11):6696–6707, 2000.
- [147] M. Šilhavý. *The Mechanics and Thermodynamics of Continuous Media*. Springer, 1997.
- [148] P. Wriggers. *Nonlinear Finite Element Methods*. Springer Berlin Heidelberg, 2010.

- [149] Y. Xu. *Ferroelectric materials and their applications*. North-Holland, Amsterdam, 1991.
- [150] T. Yamamoto and T. Sakuma. Fabrication of barium titanate single crystals by solid-state grain growth. *Journal of the American Ceramic Society*, 77(4):1107–1109, 1994.
- [151] J.-H. Yen, Y.-C. Shu, J. Shieh, and J.-H. Yeh. A study of electromechanical switching in ferroelectric single crystals. *Journal of the Mechanics and Physics of Solids*, 56(6):2117–2135, 2008.
- [152] M. Zgonik, P. Bernasconi, M. Duelli, R. Schlessler, P. Günter, M. H. Garrett, D. Rytz, Y. Zhu, and X. Wu. Dielectric, elastic, piezoelectric, electro-optic, and elasto-optic tensors of BaTiO₃ crystals. *Physical Review B*, 50(9):5941–5949, 1994.
- [153] W. Zhang and K. Bhattacharya. A computational model of ferroelectric domains. Part I: model formulation and domain switching. *Acta Materialia*, 53(1):185–198, 2005.
- [154] W. Zhang and K. Bhattacharya. A computational model of ferroelectric domains. Part II: grain boundaries and defect pinning. *Acta Materialia*, 53(1):199–209, 2005.
- [155] X. D. Zhang and C. A. Rogers. A macroscopic phenomenological formulation for coupled electromechanical effects in piezoelectricity. *Journal of Intelligent material systems and structures*, 4(3):307–316, 1993.
- [156] D. Zhou, M. Kamlah, and D. Munz. Rate-dependence of soft PZT ceramics under electric field loading. In *Proceedings of SPIE*, volume 4333, pages 64–70, 2001.
- [157] O. C. Zienkiewicz, R. L. Taylor, and J. Z. Zhu. *The Finite Element Method: Its Basis and Fundamentals*. Elsevier, 2005.

Curriculum Vitae

Personal Data

| | |
|----------------|----------------------------------|
| Name | Dinesh Kumar Dusthakar Kumar Rao |
| Date of Birth | March 11, 1985 |
| Place of Birth | Tiruchirappalli, India |
| Nationality | Indian |

Professional Occupation

| | |
|-------------------|---|
| 06/2012 – 12/2016 | Research Assistant, Institute of Mechanics, Faculty of Mechanical Engineering, TU Dortmund University, Germany. |
|-------------------|---|

University Education

| | |
|-------------------|---|
| 04/2010 – 02/2013 | International Master Studies in Computational Mechanics University of Duisburg–Essen, Germany. Academic Degree: Master of Science (M. Sc.) |
| 09/2006 – 03/2010 | Postgraduate Degree Course in Tool Engineering Nettur Technical Training Foundation, Bangalore, India. Academic Degree: Master of Engineering (M. E.) |
| 07/2002 – 04/2006 | Graduate Degree Course in Mechanical Engineering Anna University, Chennai, India. Academic Degree: Bachelor of Engineering (B. E.) |

School Education

| | |
|-------------------|---|
| 06/2000 – 03/2002 | Higher Secondary Education KRMM Higher Secondary School, Chennai, India. |
|-------------------|---|

Publication series of the Institute of Mechanics

- 2010/01 Palnau, V.: Implementierung eines netzfreien Diskretisierungsverfahrens und seine Anwendung auf die Scherbandanalyse. ISBN 978-3-921823-51-4
- 2010/02 Klusemann, B.: Application of homogenization methods and crystal plasticity to the modeling of heterogeneous materials of technological interest. ISBN 978-3-921823-53-8
- 2011/01 Hortig, C.: Local and non-local thermomechanical modeling and finite-element simulation of high-speed cutting. ISBN 978-3-921823-54-5
- 2011/02 Parvizian, F.: Modeling of microstructure evolution in aluminum alloys during hot extrusion. ISBN 978-3-921823-56-9
- 2011/03 Noman, M.: Characterization and model identification for the simulation of the forming behavior of ferritic steels. ISBN 978-3-921823-55-2
- 2011/04 Kayser, T.: Characterization of microstructure in aluminum alloys based on electron backscatter diffraction. ISBN 978-3-921823-57-6
- 2011/05 Bargmann, S.: Computational modeling of material behavior on different scales based on continuum mechanics. ISBN 978-3-921823-58-3
- 2013/01 Waffenschmidt, T.: Modelling and simulation of adaptation and degradation in anisotropic biological tissues. ISBN 978-3-921823-61-3
- 2015/01 Ostwald, R.: Modelling and simulation of phase-transformations in elastoplastic polycrystals. ISBN 978-3-921823-66-8
- 2016/01 Subramanian, M.: Phenomenological modelling and simulation of ferroelectric ceramics. ISBN 978-3-921823-74-3
- 2016/02 Clausmeyer, T.: Evolution of plastic anisotropy in metals. ISBN 978-3-921823-76-7
- 2017/01 Holtermann, R.: Computational multiscale modelling of grinding processes. ISBN 978-3-921823-86-6
- 2017/02 Bartels, A.: Modelling of evolving microstructures at different scales. ISBN 978-3-921823-93-4
- 2017/03 Dusthakar Kumar Rao, D. K.: Computational modelling of single and polycrystalline ferroelectric materials. ISBN 978-3-921823-94-1

